学位論文

Examination of the ^{30}S(α, p) thermonuclear reaction rate by ^{30}S+α resonant elastic scattering

(^{30}S+α 共鳴弾性散乱による ^{30}S(α, p) 熱核反応率の考察)

平成26年11月 博士(理学)申請

東京大学大学院理学系研究科
物理学専攻

KAHL David Miles
カール デイド マイルズ

Examination of the ^{30}S(α, p) thermonuclear reaction rate by ^{30}S+α resonant elastic scattering

David Miles Kahl

Department of Physics,
Graduate School of Science,
The University of Tokyo

A Dissertation Submitted in Partial Fulfillment of the
Requirements for the Degree of Doctor of Philosophy

Abstract

We performed the first measurement of ^{30}S+α resonant elastic scattering to experimentally examine the ^{30}S(α, p) stellar thermonuclear reaction rate in type I x-ray bursts. These bursts are a class of astronomical objects produced by thermonuclear runaway on the surface of accreting neutron star binaries. The ^{30}S(α, p) reaction plays a crucial role in x-ray bursts; however, very little is known about the compound nucleus ^{34}Ar nor the reaction rate itself. As such, the ^{30}S(α, p) reaction rate is presently estimated by the Hauser-Feshbach statistical model; yet, similar α-induced reactions near this mass region on even-even nuclei are known to be dominated by α-cluster resonances which enhance the cross-section. In this thesis, we experimentally investigate the α resonances in ^{34}Ar.

We produced a ^{30}S radioactive ion beam at 1.6 MeV/u, 30% purity, and 10^4 particles per second on-target using the Center for Nuclear Study low-energy radioactive ion beam facility CRIB. Using the thick-target, inverse-kinematics technique, we impinged the ^{30}S beam on an active target of 90% He + 10% CO_2 gas mixture. The beam was additionally tracked with standard beam-line monitors, and the outgoing α-particles were measured by a high-gain portion of the active target before depositing their residual energies in silicon telescopes, allowing us to construct an excitation function.

Using an R-Matrix analysis, we found resonances in ^{34}Ar with large alpha-widths in a region where there was no previous information concerning the nuclear level-structure. With the properties of these three new resonances, as well as preliminary results from another study by applying the insight gained from the present work, we performed the first calculation of the ^{30}S(α, p) stellar reaction rate based on experimental information on states in ^{34}Ar over 1–10 GK. We found that the experimental rate never exceeds the statistical model predictions by more than a factor of two, suggesting it may be an upper-limit for the astrophysically-relevant temperatures. As a result, ^{30}S may be a significant waiting point in x-ray bursts, possibly giving rise to rare, double-peaked morphology.

To Prof. J. Patrick Polley,
the last Renaissance man

Acknowledgments

While this thesis bears my sole authorship, reflecting that the information contained in these pages is my individual contribution to the project, the work would have been utterly impossible without a great deal of assistance from many other people.

Firstly, I would like to thank my parents Mary Lou and Joe, from answering my innumerable questions while growing up to supporting my choice to be an ex-patriot in other countries for nearly a decade in pursuit of this scientific research as a whole. Secondly, I am appreciative of my partner Sarah for putting up with me on a daily basis, which for anyone who knows me well is saying quite a lot! Among my many friends around the Tokyo area, in particular I want to express my gratitude to Chase Colburn for keeping me (almost) sane all these years, and Kazami san for innumerable conversations; I doubt I would have survived in Japan without either of them. I would also like to thank my colleagues and friends Dr. Kiana Setoodeh nia for teaching me about tolerance while living in a foreign place, and Dr. Hayakawa Seiya as my most valuable scientific peer. Finally, whether he knew it or not, Dr. Anuj Parikh was my *de facto* disinterested consultant for science (or otherwise).

Prof. Alan A. Chen proposed the original experiment which this work is based off, and not only supervised me during my M.Sc. at McMaster University but was generous enough to let me take the project with me when I transferred to the University of Tokyo. Prof. Kubono Shigeru initiated my immigration to CNS and closely advised me during my formal time as a doctoral student, and it was a serious failing of bureaucracy when he was forced to retire and I had fewer opportunities to gain his physical insight. At that time, Prof. Yamaguchi Hidetoshi took over as my guide despite his informal years in a similar role; typical to his nature, when I once commented he was the best scientist of his generation whom I knew he replied, "You need to meet more people."

As the scope of this work evolved to include an active target, Dr. Hashimoto Takashi and Dr. Ota Shinsuke made invaluable contributions from the hardware and

software sides, respectively. Dr. Dam Nguyen Binh and I shared several years together in the CRIB group, and along with him, Dr. Zhang Li Yong assisted greatly in some of the detector setups and testing. Probably only Dr. Nguyen Ngoc Duy shared with me the real pain of the GEM-MSTPC. Prof. Silvio Cherubini was a great touchstone, in particular for my coming to grips with Murphy's Law, once noting, "This was the most unlucky experiment I have ever seen." I am also grateful for the important help from some of my long-time CRIB collaborators: Dr. Chen Jun, Prof. Iwasa Naohito, Prof. Kato Seigo, Dr. Jung Hyo Soon, Dr. Kwon Young Kwan, and Prof. Teranishi Takashi. When I wanted more accelerator machine time, Dr. Nishimura Shunji, our liaison at RIKEN, encouraged my ambitious request with the quip, "It's your experiment, so if you don't fight for it, no one else will." Lastly, I want to thank Mr. Tokieda Hiroshi, Mr. Yamada Taku, and Prof. Yun Chong Cheoul for their contributions and acquiescence to grant my direct request to join the experiment.

It needs to be quite clear that the present contents of the thesis has been very substantially improved from my rather docile initial submission. This is because my dissertation committee held the work to the highest standard and insisted to me that not only could it be improved, but I knew how to do that. Prof. Hamagaki Hideki guided me through the process and was extremely kind in his conveyance of the blunt truths. The final R-Matrix fit is vastly improved by the suggestions of Prof. Hayano Ryugo and Prof. Imai Nobuaki, while the more ambitious astrophysical interpretation is largely due to the influences of Prof. Kajino Toshitaka and Dr. Tamagawa Toru.

The operation of the RIKEN Nishina Center AVF cyclotron and the ECR ion source was essential for this work, and I thank all the staff, especially the contributions of Ohshiro san. I would like to express my gratitude to all the CNS secretarial staff, in particular Endo san, Kishi san, and Yoshimura san. All the members of the CNS technical staff were also amazingly helpful, Yamazaki san in particular. Gosho san of the International Liaison Office was always helpful with questions of formality or assisting me over the language barrier.

During my nearly seven years at the Center for Nuclear Study, I made a lot of friends at CNS, around RIKEN, in Wakō, the greater Tokyo area, and other corners of the globe during experimental collaboration and conferences critical to my success; I must apologize that it would be a quite exhaustive list to name everyone, and I hope anyone omitted will forgive me as this cannot be a definitive list. Generally I mean the long-time CRIB collaborators, foreigners at RIKEN, members of Geeks' Night Out, and my personal friends from. . .around.* You all know who you are, and I sincerely thank you!

*Especially: M. Dorbin, C. C. Hatfield, J. José, E. R. Kretovics, E. Munro, J. P. Polley, P. Prosselkov, K. E. Rehm, P. H. Schury, P.-A. Söderström, W. Walsh & K. E. Wang.

Table of Contents

List of Figures

List of Tables

List of Symbols

acronym or abbreviation — What the Letters Represent(: association)

αp-process	—	$(\alpha, \mathrm{p})(\mathrm{p}, \gamma)$ sequential reaction process: nucleosynthesis
ADC	—	analog to digital converter: signal processing
AVF	—	azimuthally varying field: cyclotron
CFD	—	constant fraction discriminator: signal processing
CNO cycles	—	carbon nitrogen oxygen catalytic cycles: nucleosynthesis
CNS	—	Center for Nuclear Study, the University of Tokyo
CRIB	—	CNS Radioactive Ion Beam separator facility
D#	—	enumerated magnetic diploe: ion beams
D/S	—	downscaled beam signal: DAQ trigger
DAQ	—	data acquisition: computer routine
E7	—	experimental hall 7: RIKEN Nishina Center
ECR	—	electron cyclotron resonance: ion source
F#	—	enumerated focal plane: ion beams
FSR	—	full scale range: DAQ modules
FADC	—	flash analog to digital converter: signal processing
FWHM	—	full width half maximum: gaussian distributions
GEM	—	gas electron multiplier foil: gas detectors
HCNO cycles	—	hot carbon nitrogen oxygen catalytic cycle: nucleosynthesis
HV	—	high voltage: electrostatics
LN_2	—	liquid nitrogen: cryogenic systems
M#	—	enumerated magnetic multipole: ion beams
MSTPC	—	multiple-sampling & tracking proportional chamber: active target
NDF	—	number of degrees of freedom: statistical analysis
PID	—	particle identification
pnA	—	particle nano Amperes: beam current
PPAC	—	parallel plate avalanche counter: detector
pps	—	particles per second: ion beams

Q#	—	enumerated magnetic quadrupole: ion beams
RCNP	—	Research Center for Nuclear Physics, Osaka University
RF	—	radiofrequency: cyclotron
RI	—	radioactive ion: ion beams
RIB	—	radioactive ion beam: ion beams
RIKEN	—	The Institute for Physical and Chemical Research: laboratory
SSD-OR	—	any SSD firing by OR logic (assumed throughout with beam coincidence): DAQ trigger
SSD	—	silicon strip detector
TDC	—	time to digital converter: signal processing
ToF	—	time of flight: ion beams
TPC	—	time projection chamber; short-hand for GEM-MSTPC
WF	—	Wien (velocity) filter: ion beams
XRB	—	x-ray burst(er): accreting neutron star

Chapter 1

Introduction

1.1 A Brief History of Nuclear Astrophysics

Nuclear astrophysics is an interdisciplinary research field, which in its broadest sense aims to understand just a pair of ideas: stellar energy generation and the origin of the chemical elements. These two concepts are intimately tied to one another, as the culmination of millennia of human inquiry revealed stars to be gravitationally confined thermonuclear reactors in the mid-20^{th} century. Inside a stellar plasma, exothermic nuclear transmutations convert nuclear mass to energy* by changing one nuclear species into another, providing a hydrostatic pressure to balance the force of gravity. In consequence, stars have dynamic lives, synthesizing elements and evolving over vast epochs of time, governed by the speed at which they deplete a given form of nuclear fuel. "We may state without exaggerating that after several decades of research, stellar evolution and nucleosynthesis are among the most successful theories humans possess" [1].

The notion that the Sun is powered by conversion of hydrogen into helium *by an unknown mechanism* was first proposed by Eddington [2, 3], shortly after Aston provided experimental evidence that the mass of the helium atom is *less than* four times the mass of the hydrogen atom. While the difference is a little less than 1% or ~ 6.7 MeV/c^2 per nucleon, this is orders of magnitude larger than the typical scale of chemical reactions. Despite the recognition that hydrogen fusion is a formidable source of energy,

*Owing to Einstein's iconic mass-energy equivalence formulation $E = mc^2$, any mass excess would be released as energy.

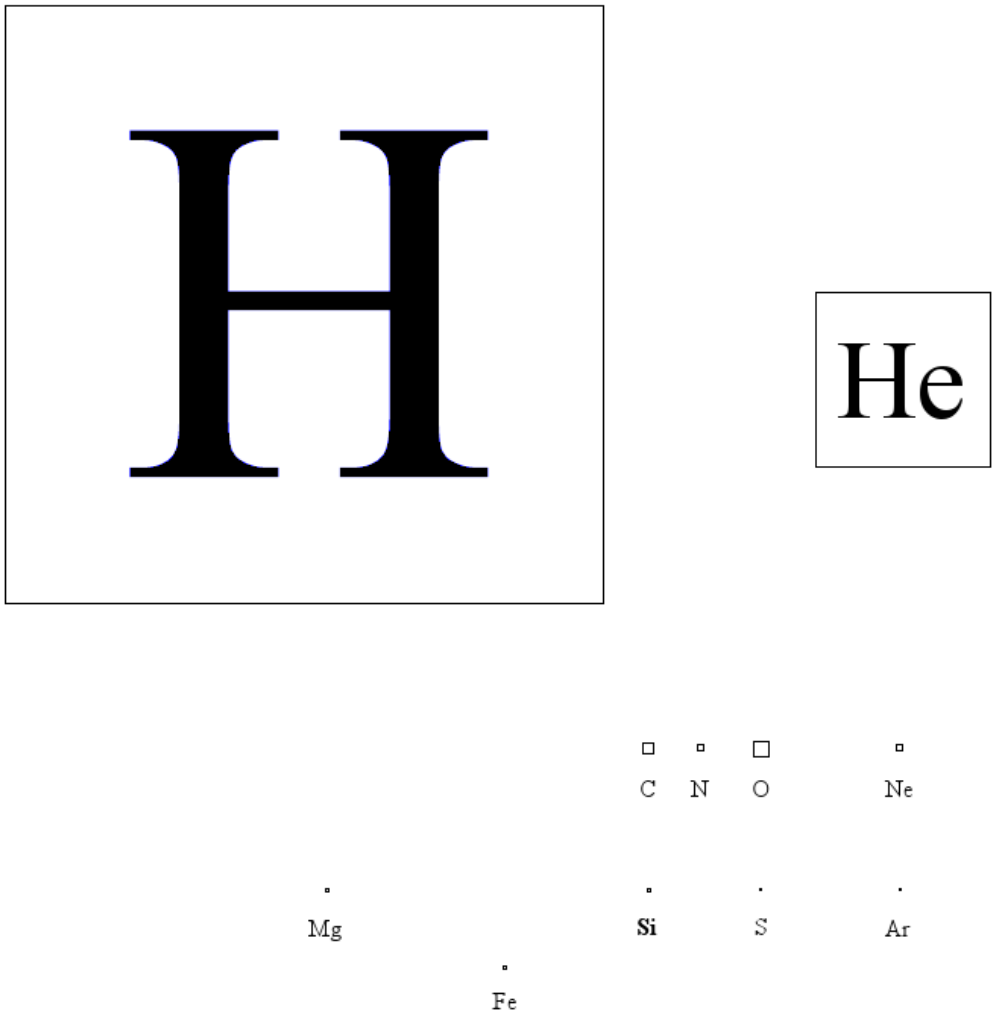

Figure 1.1: Unlike a traditional *chemist's* periodic table which represents all known elements in boxes of the same size, the above *astronomer's* periodic table represents the elements in proportion to their present abundance in the Universe. Hydrogen and helium comprise most of the chart originating from the Big Bang; there are some traces of carbon, nitrogen, and oxygen—the elements necessary for life; a few other heavier elements are barely visible; all the other elements are too small to show on the same scale.

fundamental questions remained. Rutherford's pioneering work on the interactions of α and β particles with matter showed the atomic center to be massive and highly charged with a radius vanishingly small compared to an atomic radius of 10^{-10} m [4], which was consistent with earlier mathematical models of Nagaoka on a 'Saturnian' atom [5]. However, the thermal kinetic energy of such ions in the center of the Sun, assumed to

behave as an ideal gas thus following Maxwell-Boltzmann statistics (see Equation 1.2.4), would not have individual velocities nearly high enough to approach each other's surfaces from their mutual Coulomb repulsion. The quantum tunneling effect was a major breakthrough to rectify this apparent contradiction. Discovered by Gamow [6] and Gurney & Condon [7], the tunneling theory shows that there is a small, but still finite, probability for a particle of energy E to penetrate a potential of energy U for the case when $E < U$; classical mechanics absolutely forbids such a possibility, strictly requiring that $E > U$ for the particle to overcome the barrier. Nuclear reactions involving hydrogen and helium play an important role in astrophysics not only because of the relatively lower Coulomb barriers, but because of their vast abundances, as illustrated by the cartoon in Figure 1.1.

Drawing on these influences, Atkinson qualitatively studied the source of stellar energy and concluded that it is indeed hydrogen [8, 9, 10, 11]. The first quantitative studies of stellar nuclear reaction rates by von Weizsäcker [12, 13] and Bethe [14], considered the synthesis of hydrogen into helium with carbon and nitrogen as catalysts in the Sun, now part of the so-called CNO cycles (see Section A.2.1). Bethe & Critchfield [15] also calculated the probability for the reaction of two protons directly forming a deuteron in the Sun (Equation A.1.2a), but the CN cycle (Equation A.2.1a) was favored owing to the erroneous astronomical data indicating a solar composition of $\sim$10% nitrogen, now known to be $\ll$ 1% [16]. These early works were predominantly concerned with stellar energy generation, and not necessarily the production of elements; indeed, when the CNO cycle turns over once completely, the abundances of carbon, nitrogen, and oxygen remain unchanged.

Some physicists, such as Gamow, Alpher, & Herman, described the production of all chemical elements in a hot and dense early universe [17].[†] However, the experimental discovery that ^{8}Be is unbound caused difficulties for the theory, because ^{4}He cannot capture another α particle except momentarily. Such aspects of nuclear stability also raised troubling issues in the context of stellar evolution.

The stellar burning phase after hydrogen appeared incompatible with observations,

[†]In fact, the suggestion was mocked by Hoyle, who disliked the theory, as a *big bang*. Ironically, Hoyle's pejorative term is the one employed today.

because high temperatures around 10^9 K are required to overcome the Coulomb barrier in carbon burning. Öpik proposed a three-body reaction between α-particles [18] on the basis that a statistical equilibrium of the short-lived ^{8}Be would be present; Salpeter re-calculated this value, getting a much larger fraction of ^{8}Be taking into account resonant effects of ^{8}Be [19]. Still, the known abundance of carbon was impossible to account for, so Hoyle argued that there must be a strong resonance in ^{12}C at 7.7 MeV and with an α-cluster configuration [20]. The prediction by Hoyle was made at a time of conflicting experimental work as to the existence of such a state, let alone its quantum properties of spin and parity. Cook, Fowler, and the Lauritsens performed a detailed study to investigate ^{12}C, and they were able to definitely identify a level at 7.653$\pm$0.008 MeV with a spin and parity of 0^+ [21] showing astonishing consistency with Hoyle's prediction.

Concurrent to this work, Merrill observed technetium in stellar spectra [22]; this discovery provided a major impetus, nay a catalyst, to the finalization of the burgeoning theory. Technetium is the lightest chemical element with no stable isotopes – the longest lived technetium isotope has a half-life on the order of 10^6 years, much shorter than stellar lifetimes; its observation in stars implied that stars must be actively producing heavy elements. Within several years, Cameron [23, 24, 25] and independently Burbidge, Burbidge, Fowler & Hoyle [26] presented cohesive and consistent theories on stellar nucleosynthesis. These two works, published in the same year (1957), form the essential basis for nuclear astrophysics today.

While many questions remained unanswered, an important door to an entire field of research opened. Quantum tunneling and the Coulomb barrier describe how improbable nuclear reactions play a key role in nuclear astrophysics. The history of the CNO-cycle in the Sun demonstrates the importance of accurate abundance data. Hoyle's state in ^{12}C shows not only a crucial interplay of observation, theory, and experiment, but along with Salpeter's work, the predominant role played by resonant thermonuclear reactions in astrophysics.

1.2 Stellar Reaction Rates

In order to make quantitative discussions about the role of nuclear reactions in astrophysics, it is necessary to introduce the formalism for calculating stellar nuclear reaction rates. The principle is simple, as one just needs the reaction probability, expressed in terms of the reaction cross section, normalized to the number of these particles interacting within a stellar plasma; clearly it must be so, because as either the cross section or the number of interactions go up, so too must the total reaction rate. In this section, we treat the problem in full detail.

An arbitrary two-body reaction may be schematically denoted as $A+a \rightarrow B+b$, which in nuclear experimental work it has been customary to simplify this to $\mathrm{A(a,b)B}$, with A as a target, a as a projectile, b as the ejectile and B as the recoiling nucleus. If $a = b$ and the outgoing state of A is identical to the incoming state, this is *elastic scattering*; if $a = b$ but $B = A^*$, this is *inelastic scattering* where A becomes excited. Historically the projectile was a light ion, and the ejectile also a light ion, since momentum conservation implies the lighter ejectile will more easily escape the target for detection; such a setup is now called *normal kinematics*, and if the projectile is a heavy ion on a light target, *inverse kinematics*.

In classical mechanics, the collision cross section σ for two spherical objects just depends on the radii R_i of the target A and projectile a so that $\sigma = \pi(R_A + R_a)^2$ [27]. Semi-classical notation is often employed in nuclear physics, but in reality we must not forget that nuclei are composed of quantum objects which exhibit both particle-like and wave-like properties, such as the de Broglie wavelength $\lambda\!\!\!^{-} = \lambda/2\pi$. One may obtain a quantum object's 'wavelength' by substituting the relativistic momentum of $p = E/c$ into the energy-wavelength relation $E = hc/\lambda$ yielding

$$\lambda\!\!\!^{-} = \frac{\hbar}{p}, \tag{1.2.1}$$

where $\hbar$ is Dirac's version of Planck's constant ($\hbar = h/2\pi$). As this thesis is concerned with non-relativistic nuclear reactions, for the projectile a on target A, we can write [27]

$$\lambda\!\!\!^{-} = \frac{m_a + m_A}{m_A} \frac{\hbar}{\sqrt{2m_a E_{lab}}}. \tag{1.2.2}$$

An interesting feature of quantum mechanics immediately emerges, which is that the cross section, despite still representing an area, is a function of energy, explicitly [27]

$$\sigma(E) = \pi\lambda^2 \propto \frac{1}{E}. \tag{1.2.3}$$

As introduced in Section 1.1, ions in a stellar plasma may be reasonably described by the Maxwell-Boltzmann velocity distribution

$$\phi(v) = 4\pi v^2 \left(\frac{m}{2\pi kT}\right)^{3/2} \exp\left(-\frac{mv^2}{2kT}\right) \tag{1.2.4}$$

where m is the mass of the ion of interest, k is Boltzmann's constant, and T is the gas temperature. It is customarily assumed that the function is normalized to unity ($\int_0^\infty \phi(v)dv = 1$) such that the probability for a given ion to have *some* velocity is 1. Again by assuming the non-relativistic limit relevant to this work, $E = \frac{1}{2}mv^2$, and so the velocity distribution can be simply written in terms of the energy [27]

$$\phi(E) \propto E \ \exp\left(-\frac{E}{kT}\right) \ . \tag{1.2.5}$$

Although the distinction between normal and inverse kinematics is important for the reaction nomenclature or laboratory setup, for the stellar reaction rate, the cross section depends on the properties of both interacting ions, neither of which may be treated as being at rest. Hence, it is convenient to use the *relative* velocity between two interacting particles in the center-of-mass reference frame, eliminating the need for knowledge of the *individual* velocities of the interacting particles, v_A and v_a. In the center-of-mass frame, the total mass is of course just the sum $M = m_A + m_a$, we can then introduce the reduced mass $\mu = \frac{m_A m_a}{M}$, and the center-of-mass frame velocity V depends on the total mass of the system as well as the momenta of the interacting particles by $V = \frac{p_A + p_a}{M}$ [27]. The center-of-mass energy $E_{\rm cm}$ is related to the projectile laboratory energy E_{lab} by $E_{\rm cm} = \frac{\mu}{m_A} E_{lab} = \frac{1}{2}\mu\nu^2$, where ν is the velocity of both particles approaching one another in the center-of-mass frame.[‡] Evidently, we have eliminated a degree of freedom by introducing ν in favor of v_A and v_a, which we will presently exploit.

[‡]Although the Greek letter 'μ' is customarily used for the reduced mass for the center-of-mass frame, in this work the Greek letter 'ν' is also used for the velocity of both particles in the center-of-mass.

Because of the energy dependent cross section of Equation 1.2.3 and the distribution of velocities of Equation 1.2.4, their convolution yields the reaction rate per particle pair $\langle\sigma\nu\rangle$ integrated over all velocities ν, cross sections $\sigma(\nu)$, and the velocity probability function $\phi(\nu)$ [27] as

$$\langle\sigma\nu\rangle = \int_0^\infty \phi(\nu)\nu\sigma(\nu)d\nu. \tag{1.2.6}$$

By working in the center-of-mass frame, $V \equiv 0$ and $\int_0^\infty \phi(V)dV = 1$, allowing for the circumvention of a double integral over two independent Maxwell-Boltzmann distributions, yielding [28]

$$\langle\sigma\nu\rangle = \left(\frac{8}{\pi\mu}\right)^{1/2} (kT)^{-3/2} \int_0^\infty \sigma(E)E\exp\left(-\frac{E}{kT}\right)dE. \tag{1.2.7}$$

Finally we arrive at the stellar rate r for a given thermonuclear reaction, multiplying $\langle\sigma\nu\rangle$ with the product of the number of interacting species $N_A N_a$ [28]

$$r = \frac{N_A N_a \langle\sigma\nu\rangle}{1+\delta_{Aa}} \tag{1.2.8}$$

where $\delta_{Aa} = 0$ for non-identical particles, and $\delta_{Aa} = 1$ for identical particles [27].

In order to actually calculate the stellar reaction rate r, it is evident from Equation 1.2.7 that one requires the energy-dependent cross section $\sigma(E)$, called the *excitation function*. In the simplest discussion of nuclear reaction mechanisms, two extreme cases are recognized: (1) *direct reactions* where the impact parameter is large, the timescale is short, the systems only have a glancing contact, and the excitation function is relatively smooth; (2) *compound reactions* where the impact parameter is small, the timescale is longer, the systems coalesce into an excited compound system, and the excitation function shows sharp peaks [29]. In practice, direct and compound reactions are not mutually exclusive, both of which may contribute to a particular reaction at a given energy, but the distinction is a meaningful and useful one. In particular, a sharp rise and subsequent drop in cross section is attributed to a physical resonance in the compound nucleus.

1.2.1 Nonresonant Reactions

Given the large impact parameter of direct reactions, the interaction is peripheral, including transfer reactions where one nucleon or a cluster is lost/gained, knock-out reactions, etc. Thus, only a small number of nucleons within either nucleus participates in the reaction, so the excitation function is smooth and without resonant effects arising from the full compound system.

With the exception of the neutron, all particle-bound nuclear systems have a non-zero charge Z equal to the proton number, thus one must consider the Coulomb barrier involved in nuclear reactions, and in particular the quantum tunneling probability when $E < U_{Coul}$ as is the typical case in stellar environments, as introduced in Section 1.1. When $E \ll U_{Coul}$, the probability P for tunneling through the Coulomb barrier is roughly[§] [27]

$$P \approx \exp(-2\pi\eta), \tag{1.2.9}$$

where η is the Sommerfeld parameter, defined as

$$\eta = \frac{Z_A Z_a e^2}{\hbar\nu} = \frac{Z_A Z_a e^2 \sqrt{\mu}}{\hbar\sqrt{2E}}. \tag{1.2.10}$$

Now we can more explicitly write Equation 1.2.3 including Equation 1.2.9 [27]

$$\sigma(E) = \frac{S(E)}{E} \exp(-2\pi\eta), \tag{1.2.11}$$

where the quantity $S(E)$ is called the astrophysical S-factor. Because of the exponential behavior of the Coulomb penetrability function, extrapolating the cross section down to stellar energies is a major challenge, just the region of interest where laboratory measurements are extremely difficult from the small value of $\sigma(E)$. The S-factor intends to include all variations of the cross-section due to strictly nuclear effects, which for direct reactions varies only on a small scale and allows for a much more reliable extrapolation to derive $\sigma_{E\to 0}(E)$.

One then obtains the nonresonant charged-particle reaction rate per particle pair

[§]For particular cases, or when E is not much less than U_{Coul}, one should compute the penetration factor directly from the Coulomb penetrability function [28]. Our simplification here is to elicit the general properties of stellar nuclear reactions, as described presently.

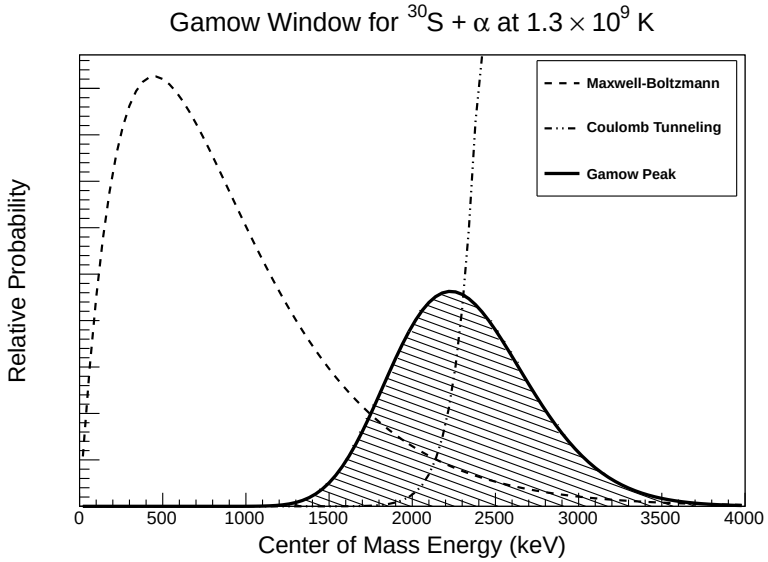

Figure 1.2: The figure shows the Gamow window (shaded region) for the interaction of $^{30}\mathrm{S} + \alpha$ at 1.3×10^9 K, plotted by the author. The center-of-mass energy is plotted along the abscissa in thousands of electron volts against arbitrary probability on the ordinate. The probability scaling spans some twenty orders of magnitude so that all three plots are simultaneously visible, as is customary in plots of the Gamow window. The Gamow peak is at E_0=2.23 MeV, with a width Δ=1.15 MeV, indicating the astrophysically important center-of-mass energies for the $^{30}\mathrm{S}(\alpha, \mathrm{p})$ reaction at 1.3 GK, the maximum energy achieved in type I x-ray bursts [30, 31].

$\langle \sigma\nu \rangle$ substituting Equation 1.2.11 into Equation 1.2.7

$$\langle \sigma\nu \rangle = \left(\frac{8}{\pi\mu}\right)^{1/2} (kT)^{-3/2} \int_0^\infty S(E) \exp\left(-\frac{E}{kT} - 2\pi\eta\right) dE. \tag{1.2.12}$$

Since the Sommerfeld parameter η itself depends on energy (Equation 1.2.10), we get

$$\langle \sigma\nu \rangle = \left(\frac{8}{\pi\mu}\right)^{1/2} (kT)^{-3/2} \int_0^\infty S(E) \exp\left(-\frac{E}{kT} - \frac{b}{\sqrt{E}}\right) dE, \tag{1.2.13}$$

where $b = \sqrt{2\mu}\pi e^2 Z_a Z_A \hbar^{-1}$ is the energy-independent Gamow factor. Inspecting the integrand of Equation 1.2.13 reveals the astrophysically-interesting nuclear reaction energy; the Maxwell-Boltzmann distribution vanishes as E diverges from kT and the Coulomb penetrability vanishes as $E \to 0$. The convolution is a single-peaked distribution as shown in Figure 1.2, called the *Gamow window*; it can be approximated with a gaussian, where the peak energy E_0 and width Δ indicate the astrophysically important energy

at a given stellar temperature. The astrophysical S-factor is not suitable for predicting changes in the cross section from resonances in the compound nucleus; thus the existence or interference of any resonances within the Gamow window should be investigated and their properties well understood, necessitating the consideration of resonant reactions.

1.2.2 Resonant Reactions

When a nuclear reaction proceeds with a small impact parameter, all the nucleons in both nuclei can participate, and a compound nucleus C will form briefly. Such a compound reaction can be represented with this intermediate state as $A + a \rightarrow C^* \rightarrow B + b$, and C^* will de-excite once sufficient energy is localized on a single nucleon or cluster [29]. C^* has been shown to decay independently of the entrance channel, with the exception of following conservation laws, such as linear and angular momenta [32]. Within the compound nucleus, there will be discrete quantum states with definite spin and parity, but the energy of a given state will have a width Γ that depends on its lifetime τ based on the time-energy uncertainty as $\Gamma \approx \hbar/\tau$. The full width at half maximum (FWHM) Γ is the sum of all the partial widths $\Gamma = \sum_i \Gamma_i$, where Γ_i represents each open reaction channel, in the example here including the incoming channel Γ_a and outgoing channel Γ_b. The cross section for such a reaction is modified from Equation 1.2.3 into the Breit-Wigner formula

$$\sigma(E) = \lambda\!\!\!^{-2}\pi\omega\frac{\Gamma_a\Gamma_b}{(E-E_R)^2 + (\Gamma/2)^2}, \tag{1.2.14}$$

where E_R is the *resonance energy* at the peak cross section and the spin statistical factor ω composed of the relevant spins J_i as

$$\omega \equiv \frac{2J_R + 1}{(2J_A + 1)(2J_a + 1)} \ . \tag{1.2.15}$$

The stellar reaction rate per particle pair $\langle\sigma\nu\rangle$ for a narrow resonance ($\Gamma \ll E_R$) is obtained by substituting Equation 1.2.14 into Equation 1.2.7 by assuming both the partial widths and the tail of the Maxwell-Boltzmann distribution (Equation 1.2.4) are

approximately constant over the resonance and found to be [28]

$$\langle \sigma\nu \rangle = \left(\frac{2\pi}{\mu kT}\right)^{3/2} \hbar^2 \omega\gamma \exp\left(-\frac{E_R}{kT}\right) \ ; \tag{1.2.16}$$

the reduced width γ is defined as

$$\gamma \equiv \frac{\Gamma_a \Gamma_b}{\Gamma_{\text{total}}}, \tag{1.2.17}$$

and the product $\omega\gamma$ is called the *resonance strength* as it is proportional to the integral of the resonance cross section.

Thus, to determine the experimental cross section of a narrow resonance, one must measure or calculate the resonance strength $\omega\gamma$ based on laboratory data, along with measuring the resonance energy E_R. The resonance energy E_R and Gamow peak energy E_0 are derived independently, but we hope to find resonances in compound nuclei in the astrophysically relevant energy regimes. As such, knowing the important burning energy regime may help identify any important resonances which likely enhance the stellar reaction rate [27].

1.3 X-ray Bursts

This thesis is motivated by a class of astronomical objects known as *x-ray bursts* (individual events) or *x-ray bursters* (the associated emission objects); both of these are interchangeably abbreviated the same way (XRBs), the context making clear which is being referred to. Observationally, these are sources where there is a sudden increase in x-ray emission within only a few seconds, with a total energy output of around 10^{40} ergs, observed to repeat with some regularity. As such high-energy photons are stopped in Earth's atmosphere, it was not until the mid-20^{th} century, when researchers first began making observations at very high altitudes, that they were discovered. Immediately prior to reports of such observations, the possibility of thermonuclear explosions on neutron star binaries giving rise to such phenomena was proposed [33, 34]; after the early observations, a more quantitative theoretical study explained these objects in a similar manner [35]. Now, more than thirty years after their discovery, about 100 galactic XRBs are known. As the thermonuclear explosions powering a given burst are not strong enough

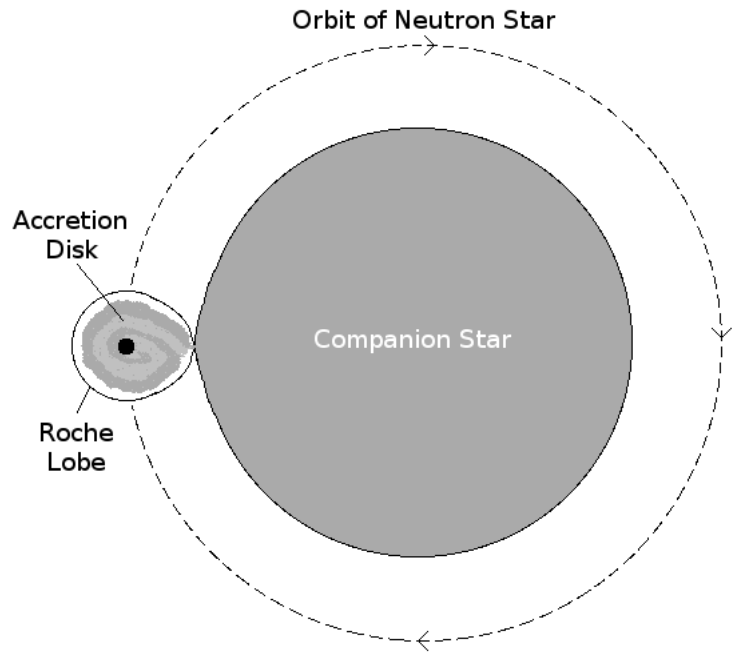

Figure 1.3: The figure shows a cartoon of accretion in a low-mass neutron star binary system, in the reference frame of the companion star. The companion star is labelled, whereas the neutron star is represented by the black dot. The mass of the two stars must be of a similar order for Roche-lobe overflow to occur, as pictured above. There are several locations, called Lagrange points, where the gravitational force acting on a test particle is zero; the most interesting one is between the two stars, called the inner Lagrange point. Although the gravitational force exerted by either star is equal at this position, matter transferred towards the neutron star—which does not fill its Roche lobe—will not return to the companion star. The companion will be largely comprised of hydrogen and helium.

to dynamically disrupt these binary star systems, they are observed to burst recurrently, usually with burst recurrence timescales on the order of hours or days. These are the "most common thermonuclear explosions in the universe" [31], and it is likely several will occur in our galaxy in the time it takes to read this chapter. Because they are not only frequent compared to other stellar thermonuclear explosions like novae and supernovae, but it is possible to observe explosive episodes from the same system many times (as well as *before* the burst begins), the study of XRBs offers a unique window to the understanding of explosive stellar nucleosynthesis.[¶]

[¶]Here, the term 'nucleosynthesis' is used to imply production of heavier nuclei by combining lighter ones, but not necessarily the ejection of that material to enrich the interstellar medium with heavier elements; XRBs are not believed to eject significant quantities of matter.

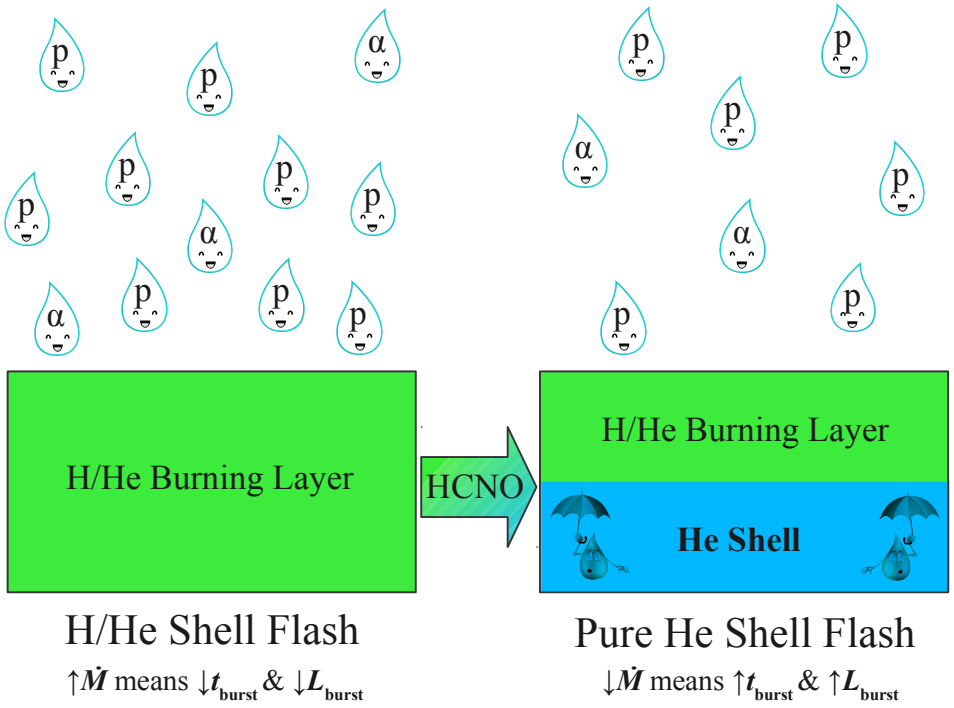

Figure 1.4: The figure is a cartoon which illustrates the effects of different accretion rates as well as operation of the HCNO cycles before an XRB, made by the author. With lower accretion rates $\dot{M}$ (right side), there is time for a shell of pure helium to be created at the base of the envelope by the HCNO cycles. Thus, systems with higher accretion rates (left side) have bursts more frequently, but they are less powerful, and thus have a lower luminosity L_{burst}, than scenarios with lower accretion rates. Although the illustration suggests the HCNO operation on the left side creates the shell on the right side, the HCNO cycle will operate in both instances. It is the time between bursts t_{burst} while the HCNO cycles operates which can create a region depleted of hydrogen which sinks below the burning layer; lower accretion rates allow enough time for the creation of such a helium shell.

Here, the goal is to paint a general picture of the XRBs themselves, as well as to show why, specifically, the $^{30}\text{S}(\alpha, \text{p})$ reaction is of interest. As there are one or two review-papers published each decade [36, 37, 38, 39], chapters in textbooks [28, 40], as well as a lengthy chapter in the author's Master's thesis dedicated to this subject [41], the interested reader is referred to those works for a more comprehensive review on the subject.

Neutron stars are the remnants of stellar cores believed to be produced in supernova

explosions. These objects are extremely dense, with typical masses similar to that of our Sun yet with radii of merely around 10 km! From their origin in the core-collapse of highly evolved progenitor stars, neutron stars have no light elements like protons or alpha particles left to further drive exothermic nuclear reactions. However, a neutron star in a close binary system may accrete material from its companion, a process that forms an extended disc around itself, and matter from the inner disc finally forms a thin envelope around the neutron star. A simplified schematic of accretion on a neutron star in such a case is shown in Figure 1.3. The main point of interest is the transfer of material rich in hydrogen and helium onto the surface of a neutron star. The environment near a neutron star has a fierce gravitational potential, so material falling towards its surface has a high velocity, and the envelope temperature is high, even before any nuclear reactions occur. Although matter inside a neutron star is neutron-degenerate (hence its name), the matter in the envelope is merely electron degenerate, which de-couples pressure and temperature from classical thermodynamics while atomic nuclei remain intact and distinct with secular neutron-to-proton ratios. In classical thermodynamics, if the local temperature increases as a result of exothermic nuclear reactions, the pressure will increase, and the system can stabilize by expanding and cooling; this is not true in a degenerate material, where a positive feedback loop can occur as the higher temperature does not cause a local change in pressure, leading to higher nuclear reaction rates which results in the release of even more energy, leading to thermonuclear runaway and finally an explosion.

As matter is accreted onto the neutron star, if there are catalysts like CNO nuclei, hydrogen burning can commence immediately via the hot CNO (HCNO) cycles outlined in Section A.2.2 [42]. While the pathway differs from quiescent stellar burning, the energy production becomes limited by beta-decays, and the turnover rate for one cycle is set by the sum of the half-lives, regardless of the temperature increases.[‖] The catalysts are the ashes of previous bursts [30] as well as possibly some accreted heavier elements, and studies have shown that between ten and twenty bursts are required in models to reproduce observation [44, 45] a phenomena called *compositional inertia* [42].

[‖]At some point, in fact, higher temperatures will photo-disintegrate the heavier nuclei that are catalysts or reaction products [43].

This is an important local effect of the nucleosynthesis of heavier elements. Although the HCNO cycle was initially proposed as the energy source for XRBs, it is now known that this is not so, and the HCNO cycles operate stably during accretion, providing the persistent flux during burst quiescence as well as no more than half of all the energy of the burst itself [46]. In our present understanding, the important action of the HCNO cycles is not so much energy generation as conversion of hydrogen to helium prior to the burst. Pure hydrogen thermonuclear burning is inherently unlikely to give rise to an explosive scenario [47, 48], as it will require many slow beta-decays; helium burning, on the other hand, may be thermally unstable [49] and can extend easily up to the calcium region or higher directly without reliance on weak interactions [50]. Still, as the accreted matter includes both hydrogen and helium, the accretion rate will generally determine the timescale between bursts, while enough material builds up in the neutron star envelope to satisfy the thermodynamic triggering conditions. The situation is illustrated in Figure 1.4.

The thermonuclear runaway is triggered by explosive helium burning in either a H/He or pure He shell flash. The explosion is triggered by a thin shell instability [33, 34]. Where during quiescence only the HCNO cycles were operating with a constant energy release, now the triple-alpha reaction creates more catalysts (or *seed nuclei*) and the burning regime breaks out from merely the HCNO cycles to synthesize heavier elements. The triple-alpha reaction causes the initial rise in luminosity, but because of the strong contribution from the Hoyle state [20], its reaction rate flattens with increasing temperature, so that its total contribution to the energy generation is small [44]. In the case of a pure-helium shell flash [51], the burning continues as a sequence of (α, γ) reactions on the ^{12}C seeds from the triple-alpha reaction up to around ^{40}Ca [52]. If hydrogen is also present in the shell flash, the ^{12}C nuclei created will immediately capture two protons to become ^{14}O [31], as any existing ^{14,15}O seed nuclei are exhausted as the thermonuclear runaway initiates. The burning then proceeds by a series of $(\alpha, \mathrm{p})(\mathrm{p}, \gamma)$ reactions on these seed nuclei, called the αp-process [53]. One such sequence in this burning pathway is

$$3\alpha \rightarrow\ ^{12}\mathrm{C}(p,\gamma)^{13}\mathrm{N}(p,\gamma)^{14}\mathrm{O}(\alpha,p)^{17}\mathrm{F}(p,\gamma)^{18}\mathrm{Ne}(\alpha,p)^{21}\mathrm{Na}(p,\gamma)^{22}\mathrm{Mg}(\alpha,p)^{25}\mathrm{Al} \quad (1.3.1)$$

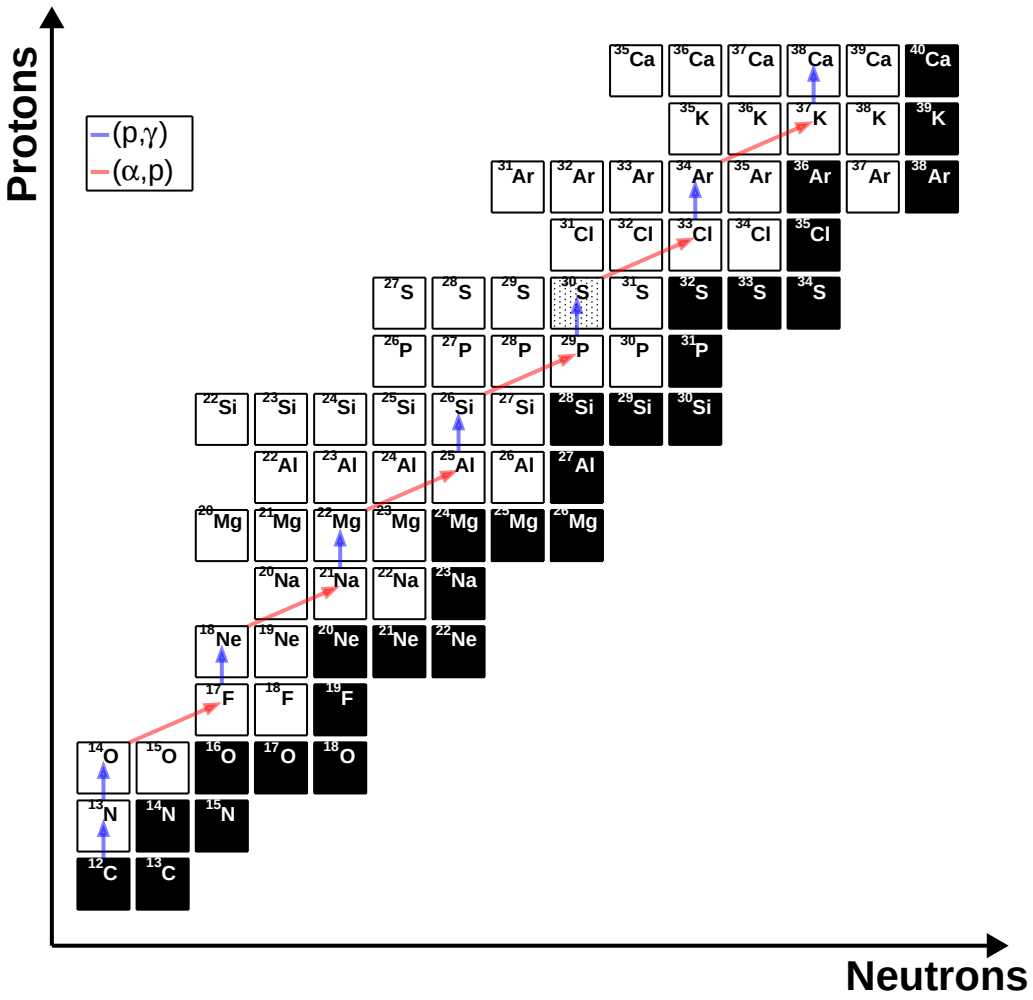

Figure 1.5: Schematic of a predominant αp-process pathway produced by the author. The plot follows the traditional chart of nuclides, where the ordinate shows the neutron number and the abscissa proton number, and each box represents a unique nuclear species. Stable species are filled in black, whereas white boxes represent β^+-unstable radioactive species (^{30}S is the partially-filled box). Arrows show different reactions linking the nuclear species and their direction. The blue arrows show (p,γ) reactions, and the red arrows show (α,p) reactions.

which continues as

$$^{25}\mathrm{Al}(p,\gamma)^{26}\mathrm{Si}(\alpha,p)^{29}\mathrm{P}(p,\gamma)\underline{^{30}\mathrm{S}(\alpha,p)^{33}\mathrm{Cl}}(p,\gamma)^{34}\mathrm{Ar}(\alpha,p)^{37}\mathrm{K}(p,\gamma)^{38}\mathrm{Ca}. \tag{1.3.2}$$

This sequence is shown in Figure 1.5. Again like in the case of a pure He shell flash,

the burning becomes increasingly inhibited by the ever-increasing Coulomb barrier and decreasing Q values with increasing mass, and this process also truncates around the calcium isotopes [43]. It is important to recognize that—with the exception of the two protons captured on ^{12}C to produce ^{14}O—despite many other (p,γ) reactions involved, this process is pure helium burning, as it does not change the overall hydrogen abundance since one proton is emitted and one proton is consumed in each αp step. Once the αp-process commences, the energy generation rate increases by as much as 3 orders of magnitude in just one second [53], which we observe as an XRB.

It can be see in Figure 1.5 that, for example, ^{30}S is not at the proton drip line, and further proton captures are possible. However, at XRB temperatures of 10^9 K, the tail of the thermal photon distribution is energetic enough to photodisintegrate nuclei with proton separations $S_p < 3$ MeV [43]. Thus, especially in this higher mass region, there is a competition between (p,γ), (γ,p), (α,p) reactions and β^+ decays. Considering the burst rise timescale and the half-life of ^{30}S is a bit more than one second, a significant mass fraction can pile up at such a particular nuclear species, which are called *waiting points*. The situation is illustrated in one burst model shown in Figure 1.6. In XRBs, where the nuclear reaction network includes hundreds of species and thousands of nuclear transmutations, it is actually only a small subset of these nuclear transmutations which need to be known precisely, as they make a predominant contribution in the nuclear trajectory to higher mass.

The $^{30}\mathrm{S}(\alpha,\mathrm{p})$ reaction is one of these important reactions in XRBs. Its contribution to the total energy generation rate is believed to be more than 5% [59], it influences the neutron star crustal composition [38] (important for sequential bursts via compositional inertia), and may even explain rare bolometrically double-peaked XRBs as shown in Figure 1.9. However, scarcely any information is known about this reaction experimentally, nor the compound nucleus ^{34}Ar above the α threshold [60], shown in Figure 1.7. Although a statistical model approach is possible to estimate such an astrophysical reaction rate [61, 62], if there are large, isolated, alpha-resonances in ^{34}Ar in the XRB Gamow window, the Hauser-Feshbach method [63] will not reliably predict the (α,p) reaction rate. For alpha-induced reactions on $T_z = \pm 1$ ($T_z = \frac{N-Z}{2}$) nuclei with $A = 18$, this was shown to be true [64, 65, 66]. This behavior was also shown to be true for $T_z = 1$ nuclei

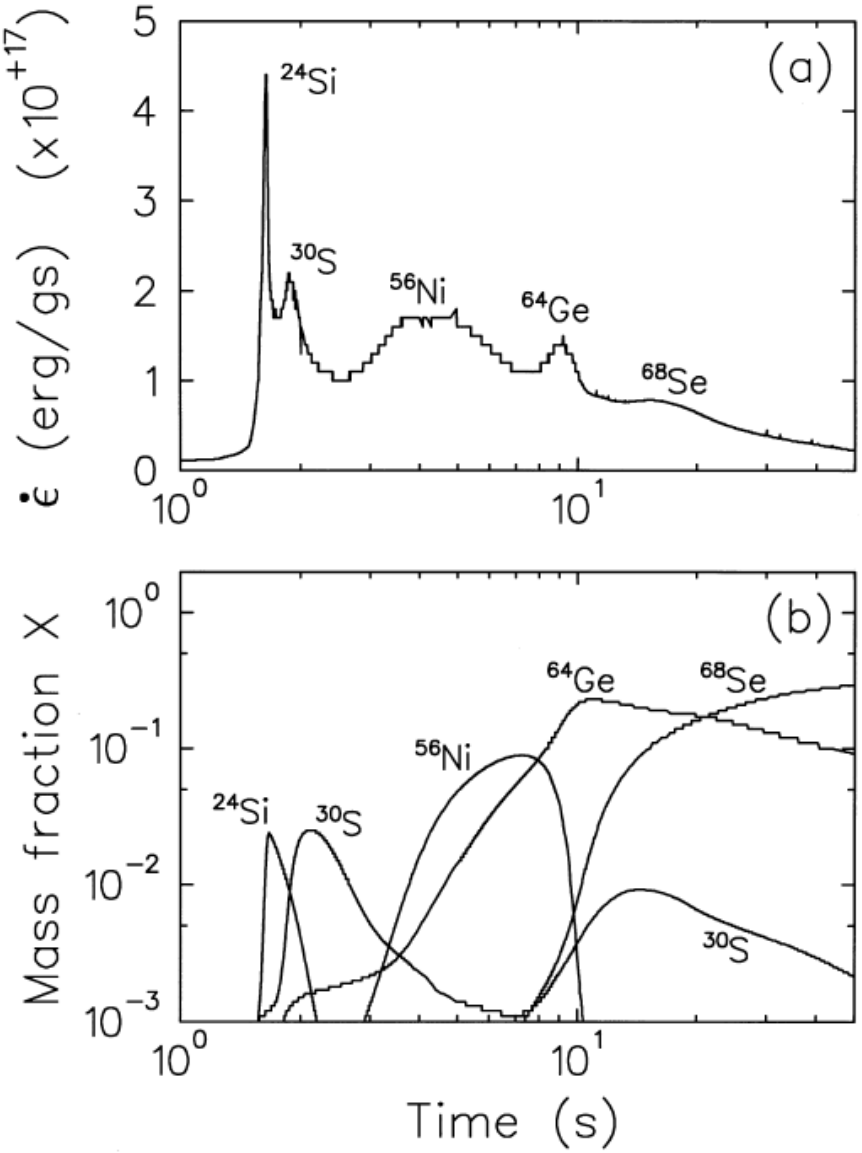

Figure 1.6: Plots of energy generation rate $\dot{\epsilon}$ in ergs per gram second and mass fraction $X \equiv \frac{N_i M_i}{\rho N_A}$ (where N_i is the number density of selected nuclei i, M_i is the relative atomic mass of species i, ρ is the mass density, and N_A is Avogadro's number [28]) on the ordinate, against logarithmic burst time in a simulation [54]. The mass fraction is high for a number of nuclei, indicating they are possible waiting points. The energy generation rate has local maxima when waiting point nuclei mass fraction varies most sharply [54].

at higher mass $20 \leq A \leq 30$ [67, 68], clearly motivating the case at hand. Indeed, it is totally unknown at present the lowest mass where reaction rates of α-induced reactions

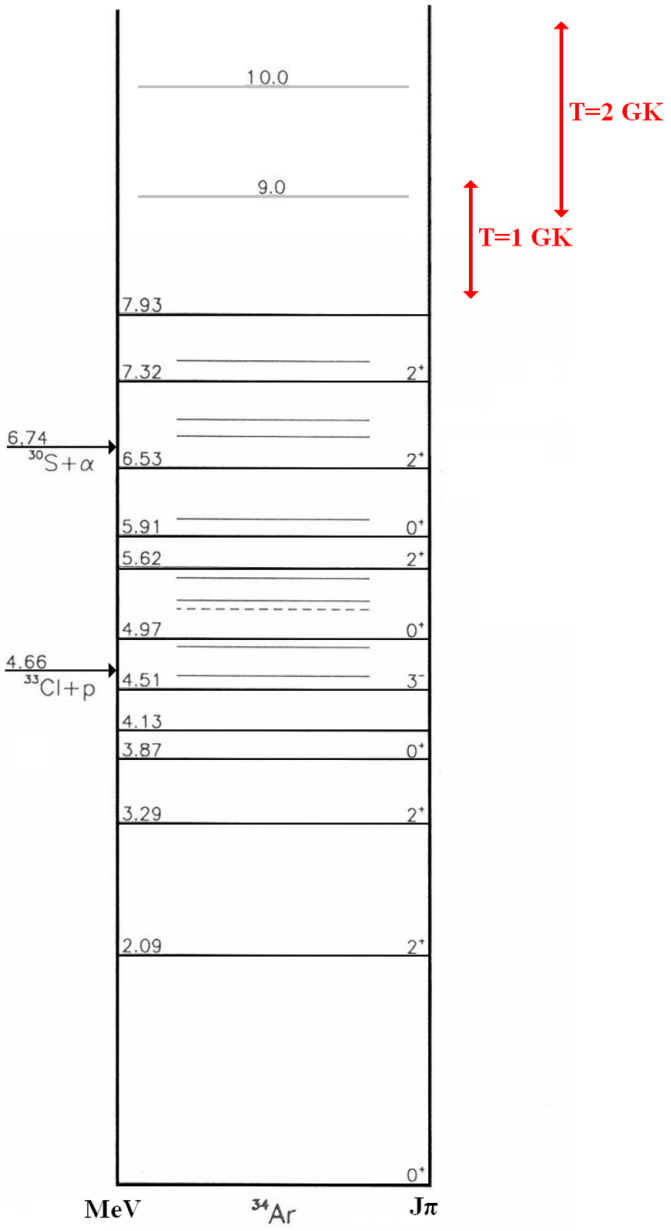

Figure 1.7: Level scheme of ^{34}Ar, the compound nucleus for the ^{30}S(α,p) reaction, modified from original [55]. The α and proton thresholds are shown on the left in black, and the important astrophysical energies in the Gamow window for XRBs are shown on the right in red. Notice how there are no known levels in the Gamow windows (the grey lines at 9 and 10 MeV are shown merely for scale). Although the original figure is quite dated, no new levels have been proposed above the α-threshold in the more than two decades since this evaluation.

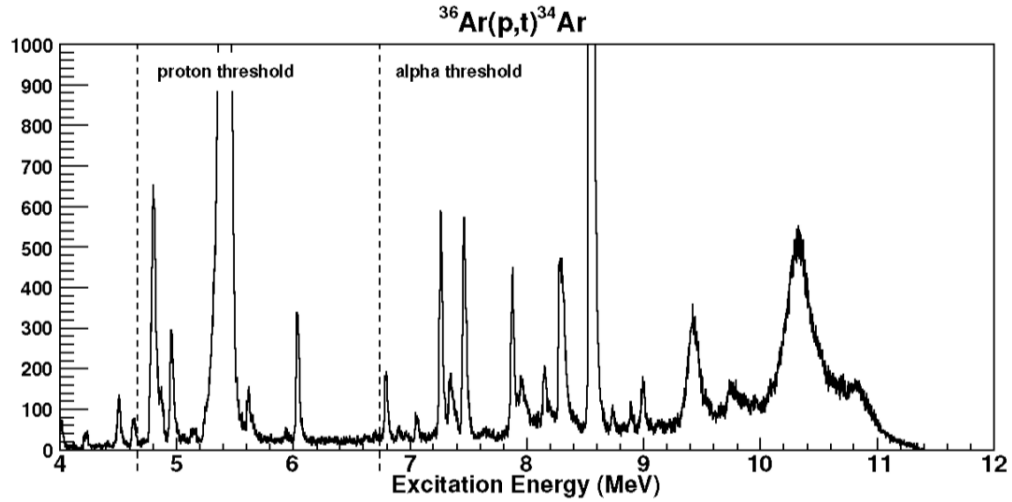

Figure 1.8: Preliminary spectrum of the ^{36}Ar(p, t) reaction [56]. A number of isolated, natural-parity resonances are observed above the α-threshold.

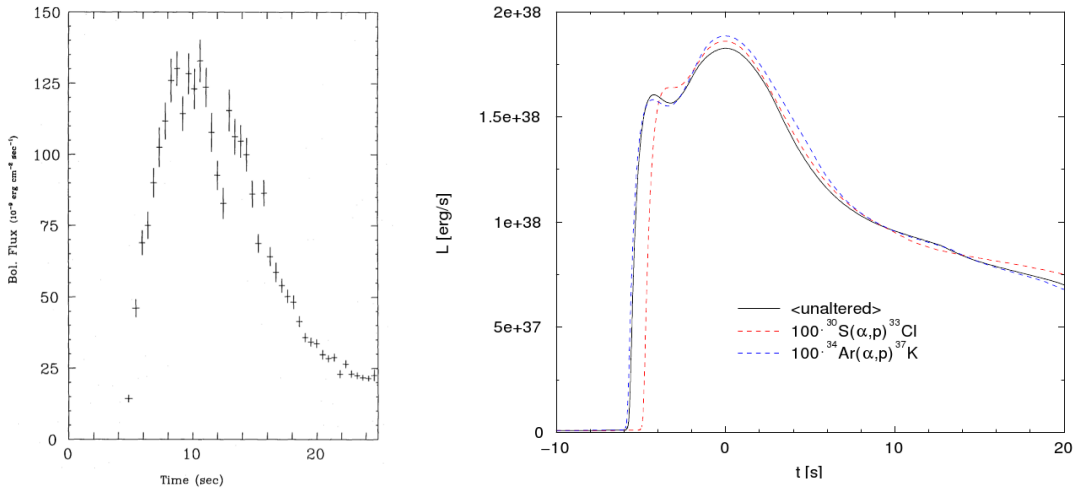

(a) Observation from [57]

(b) Model from [58]

Figure 1.9: Double-peaked x-ray bursts from observation (a) and a simulation (b). The observation is of the object 4U 1608-52, which has shown regular single-peaked bursting behavior; note the 25% decline of the luminosity for several seconds. Although the model has the peak-height hierarchy inverted, they were able to reproduce a double-peaked structure (shown as the black solid line), using standard reaction rates. When the reaction rate of ^{30}S(α, p) was artificially increased by a factor of 10^2 over the statistical model rate (shown as the dashed red line), the double-peak structure was significantly diminished, suggesting in their model that the ^{30}S waiting point was partly responsible for the double-peaked structure.

on $T_z = \pm 1$ nuclei can be reliably calculated with the statistical model.

The only relevant experimental information for the $^{30}\mathrm{S}(\alpha, \mathrm{p})$ stellar reaction rate has just become available in the last several years, with one study of the time-reversal reaction $^{33}\mathrm{Cl}(\mathrm{p}, \alpha)^{30}\mathrm{S}$ [69] and a preliminary report of a high-precision $^{36}\mathrm{Ar}(\mathrm{p}, \mathrm{t})^{34}\mathrm{Ar}$ transfer reaction at high excitation energy shown in Figure 1.8 [56]. The aim of the present work is to experimentally investigate the crucial $^{30}\mathrm{S}(\alpha, \mathrm{p})$ reaction to search for any α-resonances in $^{34}\mathrm{Ar}$ via the entrance channel $^{30}\mathrm{S} + \alpha$, a reliable approach to its study.

Chapter 2

Experimental Method

The experimental work described here was performed at the CNS low-energy radioactive ion beam separator (CRIB) [70, 71], owned and operated by the Center for Nuclear Study (CNS) of the University of Tokyo and installed in the RIKEN Nishina Center. This type of facility is presently necessary to produce the neutron-deficient isotope ^{30}S as a low-energy radioactive beam. Elements in this region of the periodic table—phosphorous, sulfur, and chlorine—react with most metals, especially at high temperatures, making production of radioactive ion beams (RIBs) of these species a challenge for two-stage, post-accelerator systems like ISOL,* which is an otherwise popular and effective way to make low-energy RIBs. Conversely, RIB production in-flight via a fragmentation method generally makes beams at high energies, and their intensity will be severely diminished by straggling and scattering if such a beam is degraded to low energies ($\lesssim$ 10 MeV/u). We use the ^{3}He(^{28}Si, ^{30}S)n reaction to produce the species of interest. The $^{30}S^{16+}$ beam produced in this work is separated at 4.0 MeV/u, and arrives on target with an intensity of about 1×10^4 particles per second (pps), a purity of about 50%, and an energy of about 2 MeV/u. Despite the importance of the ^{30}S(α, p) reaction in XRBs outlined in Chapter 1, no other RIB facility in the world has reported that they managed to produce a beam even within more than an order of magnitude of the above properties of purity and intensity with a similar energy required for this work. Indeed, from our initial experimental proposal in 2006, it took several years and three test experiments to

*Isotope separation online.

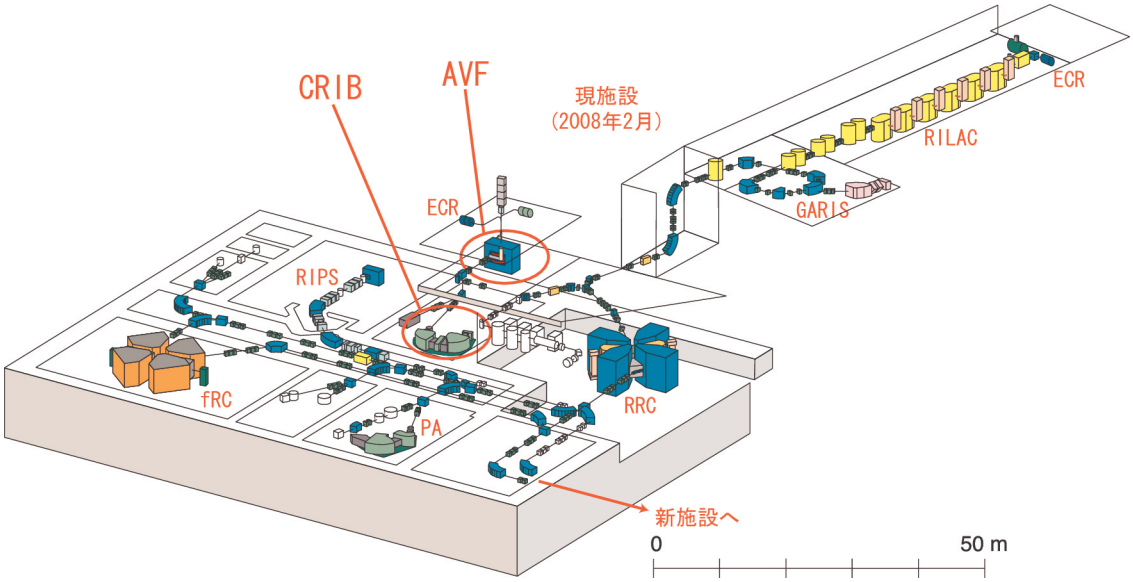

Figure 2.1: Schematic view of a portion of the RIKEN Nishina Center mainly showing facilities in the older section of the complex. The apparatuses of interest to this thesis are the ECR ion source, AVF cyclotron, and CRIB separator facility.

produce a satisfactory beam, so this work is a perfect example of the unique capabilities of the CRIB facility.

This chapter begins with an introduction of the CRIB facility, as well as an overview of the RIB production of ^{30}S. Subsequently, the active target system employed and commissioned in part by and for our experimental measurement of the $^{30}\mathrm{S} + \alpha$ system is presented in some detail from the perspective of its design and hardware; the reader can then find details of its performance in Chapter 3.

2.1 Accelerator Facility

CRIB is installed in the E7 experimental hall of the RIKEN Nishina Center at the Wakō campus in Saitama, just outside Tokyo. A cutaway schematic is shown in Figure 2.1, depicting the portion of the accelerator complex relevant to this work. The optics between the ion source, accelerator, and RIB separator should be considered carefully and from start to finish in the design of such a system, since the final RIB yield depends greatly on the primary beam optics and tuning; the RIB yield can drop an order of magnitude or more from a shift in the primary beam focal location by several mm

Figure 2.2: Photograph of CRIB with a schematic overlay created by the author; schematic overlay was modified from [71]. The schematic shows the optical and beam-line elements as closely as possible to their real positions in the photograph. The primary beam enters on the lower left side, impinging on the cryogenic production target located at the entrance focal plane to CRIB F0. The scattered beam and reaction products are dispersed by the first dipole D1, selected at the first focal plane F1 by magnetic rigidity $B\rho$ and re-focused by the second mirror dipole D2. The second focal plane F2 is achromatic and the location where most measurements to optimize the RIB of interest are performed. Next is the Wien filter ($\vec{E} \times \vec{B}$) which further purifies the cocktail beam by velocity. Many electromagnetic focusing elements can be seen along the beam-line at various places. The experiment is conducted past the upper left corner at F3, which could not be simultaneously photographed owing to a large cement bulkhead. However, various practical items are seen clearly, such as a large dewar for liquid nitrogen on the D1 magnet and the metal shielding around the Wien filter high voltage insulators. See the text.

or a slightly off-axis trajectory. The hyper ECR ion source is capable of extracting highly-charged heavy ions of many elements; the fact that this type of ion source can provide highly-charge ions is especially important given that we use a small cyclotron for acceleration. The azimuthally varying field (AVF) cyclotron has a nominal rating of $K \approx 80$, where the $\vec{B}$-field varies to correct for small relativistic effects of the ion motion.

In the non-relativistic limit, the energy E of a particle extracted from a cyclotron is

$$E = NqeV = \frac{(qeRB)^2}{2m}, \tag{2.1.1}$$

after N times crossing the electrode gap with potential V, at extraction radius R, magnetic field B, and ion charge qe and mass m. It can be seen that the final energy is proportional to the square of the charge and also the extraction radius. During this work, several modifications to the AVF cyclotron were made, effectively increasing R so that the $^{28}Si^{9+}$ primary beam energy was increased from 6.9 MeV/u to nearly 7.4 MeV/u; even this apparently small difference significantly improved the ^{30}S RIB. Another notable improvement critical to the success of this work was the increased extraction of $^{28}Si^{9+}$ from the ion source; the improvement was so great that finally we could use only 50% of the available beam current!

2.1.1 Primary beam conditions

The primary beam conditions are shown in Table 2.1, where the energies and intensities are quoted as the highest available at the time; note that the primary beam intensity quoted in 2009 and 2010 is limited by the 2 W safety limit for breaking the CRIB cryogenic target exit window and not the ion source yield or cyclotron transmission efficiency. We finally adopted the primary beam intensity of 80 pnA in 2010 as the ^{30}S RIB intensity decreased at higher primary beam intensities from heating of the production target along the beam-axis. The AVF cyclotron improvements in the ^{28}Si beam energy are clearly evident between 2006 and 2009; the initial primary beam energy delivered in 2010 was also 7.4 MeV/u, but the optics were poor, and after a re-tune of the cyclotron much better transmission could be achieved extracting one turn earlier, resulting in a slightly lower energy.

2.1.2 Radioactive Ion Beam Production

CRIB produces low-energy RIBs in-flight typically via light charge-exchange or transfer reactions such as (p, n), (d, p), (d, n) and (^{3}He, n) in inverse kinematics (see Appendix B). The cross-sections for these reactions are sufficiently high, being not less than a mb/sr

Table 2.1: Primary beam data for the CRIB experiments producing ^{30}S RIBs.

Year	Ion	Energy (MeV/u)	Intensity (pnA)
2006	$^{28}Si^{9+}$	6.9	100
2008	$^{28}Si^{10+}$	7.54	10
2009	$^{28}Si^{9+}$	7.4	144
2010	$^{28}Si^{9+}$	7.33	144

and often hundreds of mb/sr at small center-of-mass angles θ_{cm} at these center-of-mass energies. The use of inverse kinematics is particularly key, as the Jacobian transformation restricts the outgoing heavy ions to a narrow cone of merely several degrees in the laboratory, allowing for highly efficient collection, separation, and purification. By using target materials of the lightest elements such as hydrogen or helium, straggling of the secondary beam within the production target material is minimized. These are the fundamental principles that CRIB and similar RIB facilities are designed upon, and they have proven to be quite successful.

Many of the basic components of CRIB previously belonged to a decommissioned spectrometer called DUMAS in Osaka; these make up the early-stage optical focusing magnets and the two large magnetic dipoles, responsible for the selection of the RIB phase space. The selection is made according to the magnetic rigidity $B\rho$ of particles:

$$B\rho = \frac{p}{q}, \tag{2.1.2}$$

where B is the magnetic field, ρ the radius of a particle's path, p is the particle's momentum and q the particle's charge. B is set by the user, and although ρ is largely fixed by the magnet design, its precise value and width is controlled by a set of slits at the dispersive focal plane; CRIB can be set up to a rigidity of up to around 1.3 Tm. As a particle's momentum depends on the quantized nuclear mass number A and its charge is comprised of the quantized nuclear charge Z minus the number of electrons in its particular ion species. When a narrow range of $B\rho$ is selected, different nuclear and ion species will fall at distinct loci in a plot of residual energy E and time of flight (ToF), which will be distinct if its $\frac{A}{q}$ ratio is unique and overlapping otherwise.

In the early years, this was CRIB, but two later additions—a cryogenic production

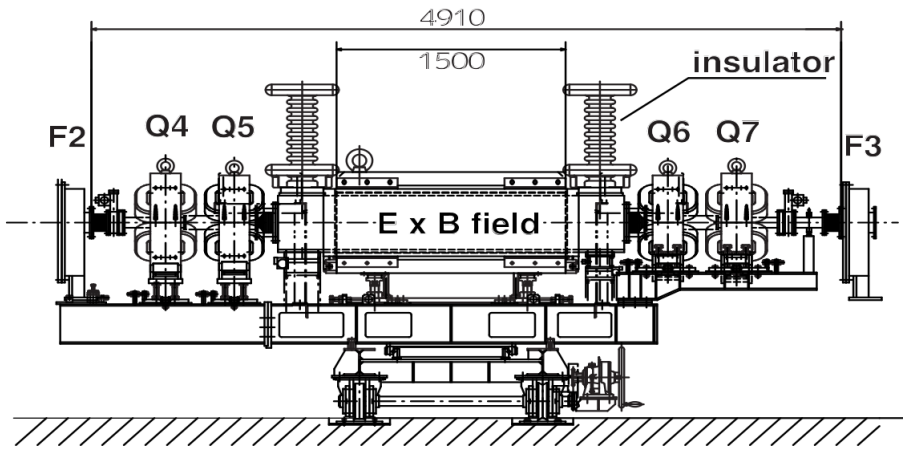

Figure 2.3: Schematic side view of the CRIB Wien filter system [72].

target system and Wien filter—are now standard in most CRIB experiments and have significantly improved its capabilities. The layout of CRIB at present is: F0, Q1, M1, D1, Q2, F1, D2, M2, Q3, F2, Q4, Q5, $\vec{E} \times \vec{B}$, Q6, Q7, and F3; here the numbers are sequential along the beam-line and F indicates a focal plane, Q is a magnetic quadrupole, D is a magnetic dipole, M is a magnetic multipole, and $\vec{E} \times \vec{B}$ is the Wien filter. CRIB is shown in Figure 2.2. Horizontal and vertical slits can be controlled before F1, F2, and F3 to aid in selecting the ions of interest.

The Wien filter significantly increases the relative purity of the species of interest by adding a velocity selection in addition to the rigidity selection of Equation 2.1.2, allowing for a true $\frac{A}{q}$ section of the beam by the time it reaches the experimental focal plane. The operation works by setting the force $\vec{F}$ exerted on a particle by an electric field $\vec{E}$ equal and opposite to the force exerted by a magnetic field $\vec{B}$:

$$F = q\vec{E} - q(\vec{v} \times \vec{B}) = 0, \tag{2.1.3}$$

where $\vec{v}$ is the velocity vector and the charge q immediately cancels out. If the electric field, magnetic field, and beam direction are mutually orthogonal, it reduces to $\frac{E}{B} = v$, a velocity filter. A schematic view of the CRIB Wien filter is shown in Figure 2.3.

As for the composition of the production target, the use of hydrogen and helium was previously motivated. However, these materials are naturally gaseous under ambient

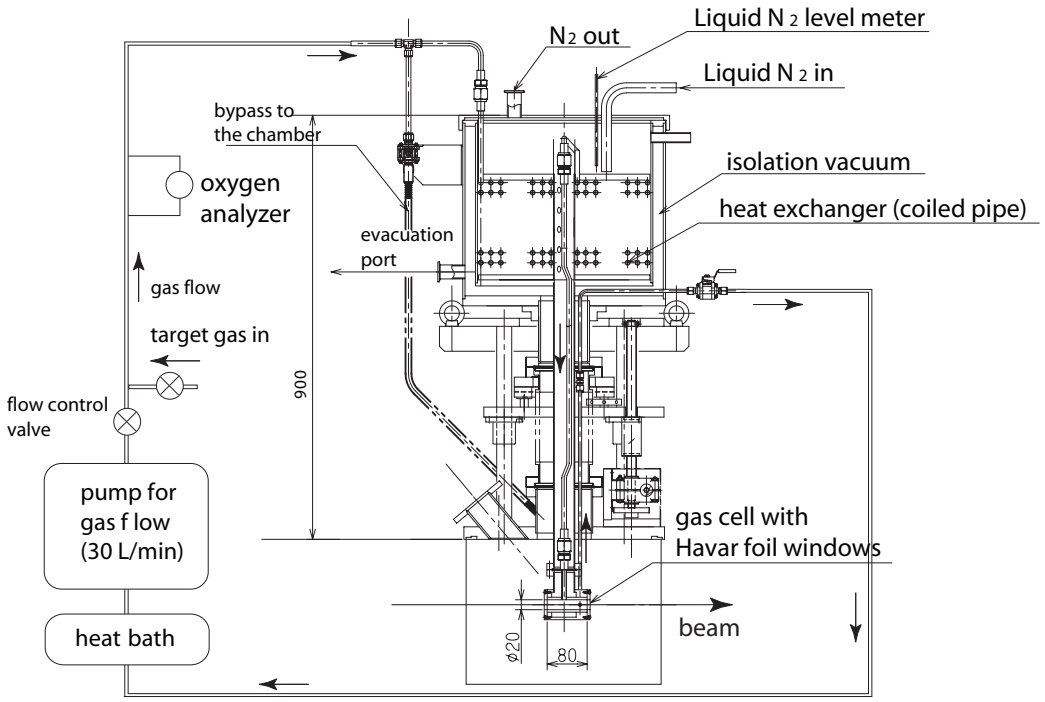

Figure 2.4: Schematic side view of the CRIB cryogenic gas target cooling system from [73].

laboratory conditions, and a windowed gas target is the most straight-forward technique to make a thick hydrogen or helium target. A popular window foil material in nuclear physics is HAVAR® composed mainly of a nickel-group alloy, as it has a high tensile strength and heat capacity even when rolled very thin; we use 2.5 μm HAVAR windows to confine the gas in the CRIB production target, and it can easily withstand differential pressures of more than one atmosphere even for a window of 2 cm diameter which we use. Keeping the window material thin minimizes energy loss and straggling. The target gas is cryogenically cooled to an effective temperature of 90 K by forced-flow through a reservoir of liquid nitrogen (LN_2), described in [73]. Firstly, this is important because it increases the density by a factor of three compared to ambient conditions, in principle allowing the beam to interact with more target nuclei traversing the same physical space. Secondly, the beam will deposit energy along its path, which can locally expand or even ionize the target gas as the beam intensity is increased, significantly decreasing the RIB yield away from a linear function of primary beam intensity; this effect in particular can

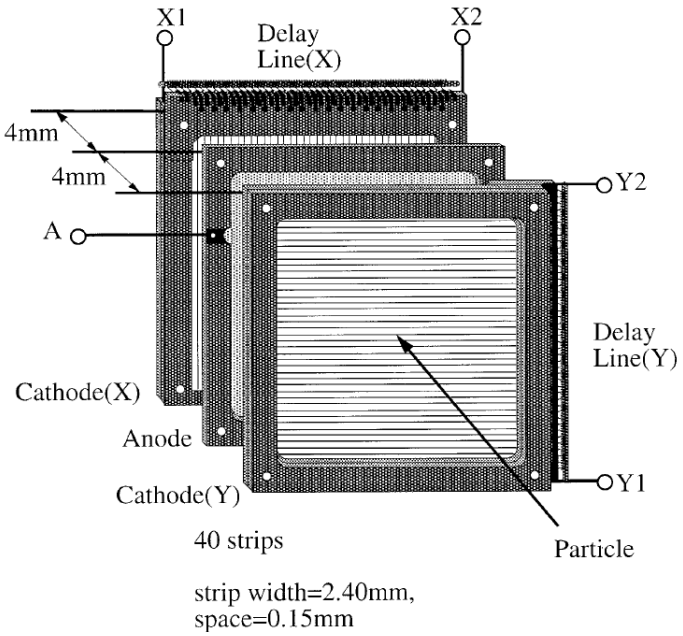

Figure 2.5: Schematic of the internal structure of the delay-line PPAC from [74].

be counteracted by forcing the flow of the target gas back into the cooling reservoir and is a feature unique to the CRIB cryogenic production target design. A schematic of the CRIB cryogenic production target system is shown in Figure 2.4; the target length is 80 mm. In the ^{30}S work, we used ^{3}He at an ambient pressure of 400 Torr, for a total effective thickness of 1.72 mg/cm^2.

2.2 Standard CRIB detectors

Experiments performed at CRIB utilize standard detectors for the RIB production, which we overview here.

2.2.1 Beam-line monitors

For monitoring the beam timing and spatial position, we use parallel plate avalanche counters (PPACs), a type of fast and thin ionization chamber. Ion chambers operate on the principle that impinging radiation will ionize the fill gas, and the charge can be collected by applying a high voltage, typically optimized for either timing or energy information. The PPACs at CRIB can all be inserted or removed from the beam-line as

required. We insert a PPAC at F1 to determine the $B\rho$ of the primary beam by measuring the beam position, for example confirming the energy reported by the cyclotron operators is consistent with the primary beam ion species considering the magnetic field we set for D1; generally, this detector is removed from the beam-line. We place a PPAC at F2 for both the primary beam tuning as well as for RIB production; this detector is removed if we send the beam to F3. At F3 we use two sequential PPACs to extrapolate the trajectory of the RIB as well as determine a beam ion's species event-by-event for experimental measurements.

The PPAC at F1 is a charge-division type with a large window size to accommodate the full range of the momentum slits, about ±60 mm. Other PPACs, at F2 and F3, are delay-line type [74], with windows measuring 50×50 mm^2 and thin 2.5 μm aluminized mylar entrance/exit foils to minimize the energy loss of our low-energy RIB ions. In recent years, all the PPACs at CRIB operate with a C_3F_8 fill gas at 8–9 Torr, which has the advantage of being non-flammable for safety. Note that these specific properties apply to the delay-line PPACs at CRIB and differ somewhat from those in the original design of Ref. [74]. A schematic of the delay-line PPAC is shown in Figure 2.5. These PPACs are capable of handling injection rates up to around 10^6 pps and achieve a spatial resolution better than 1 mm. The timing resolution is better than 1 ns. The delay-line PPAC operates on the principle that the timing signals on two sides of a cathode can be compared to one another to determine the physical position of ionizing radiation along the cathode. As we are only interested in the timing information, we use a fast amplifier and a common fraction discriminator (CFD) with an extremely short delay to process the PPAC signals. These signals are used to create the gating and trigger conditions for the data acquisition system (DAQ), as well as sent to the time to digital converter (TDC) to be recorded to disk. Two cathodes are used: one for the position in x and the other for the position in y. Further details concerning this method of position determination as well as calibration are described in Section D.1.1.

2.2.2 Silicon detectors

Silicon semi-conductor detectors (SSDs) are a practical and popular way to measure the energy deposition of charged particles, particularly in a confined geometry where

a gaseous detector would not easily fit. Impinging charged particles will lose energy by exciting electrons in the silicon lattice; the electrons and/or electron-holes can be collected and their charge measured by applying a bias across the detector, where a higher bias is required for thicker SSDs. For low-energy heavy ions, this will almost always be their total residual energy, as they quickly stop in the silicon wafer. However, for light ions like protons and alpha particles, depending on the ion energy and SSD thickness, the particles may punch through the detector, depositing only a portion of their energy.

We place one single-strip thick SSD at F2 during RIB production; for this work, it was a 1.5 mm thick model ordered from Micron Semiconductor. When the F2 SSD is inserted to the beam line, we can measure the full residual energy of the cocktail beam to assist in identifying the ions.

SSDs can typically only withstand intensities around 10^3 pps before the lattice becomes damaged (although this depends on the total energy deposition), and caution must be used whenever such a detector can be directly hit by the beam. The SSD analog output is pre-amplified and then amplified before being sent to an analog-to-digital converter (ADC) to record the data to disk. Although the timing resolution of SSDs is rarely better than several ns, the timing signals are required for gating conditions when we want to insist a given SSD fired. Thus, the output from the pre-amplifier is split, and sent also to a fast amplifier and a CFD to generate a timing signal; the CFD delay is much longer here, 150 ns. The SSDs used in the active target are described in Section 2.4.6.

2.3 ^{30}S RIB Production

We performed a total of three RIB production tests for ^{30}S, conducted in 2006, 2008 and 2009. The first two tests were the subject of the author's Master's thesis [41], while the latter was performed as a part of the present work. A fourth beam was also produced for the experimental work of interest in 2010.

2.3.1 General summary of RIB properties obtained

Results for the ^{30}S RIB at F3 are summarized in Table 2.2 over several years. Refer to Table 2.1 for the corresponding primary beam conditions. These values were all the highest achieved at the time. Although the RIB energy is typically reported as the one measured on-target, here the energy is tabulated at the dispersive focal plane for proper comparison, as the PPAC thickness and choice of target window material changed over the years. HV is the Wien filter high voltage, quoted as the *setting* as typical for CRIB works; the setting value is slightly higher than the *applied* voltage by a few kV.

However, a few additional caveats are needed for individual cases. The purity quoted for $^{30}S^{15+}$ is actually an upper limit, because it was demonstrated that some amount of $^{28}Si^{14+}$ leaks into the PPAC gating condition, making the beam entirely unusable. Although we attempted to use a thin (1.5 μm) mylar degrader at the dispersive focal plane to improve the purity of $^{30}S^{14+}$, the total yield decreased by 80%, and thus we quote the case without a degrader like all other cases. There was also some concern about the firm identification of $^{30}S^{14+}$ at F3, further calling into question the merits of employing this ion species; we attempted a half-life measurement in 2009 to confirm its identity, but unfortunately ran out of machine time. It can be seen clearly that the intensity and purity of our ^{30}S RIB improved significantly over the four years we spent on the project.

Table 2.2: Secondary beam data for the CRIB experiments producing ^{30}S RIBs.

Year	Ion	Energy (MeV/u)	Intensity (pps)	Purity (%)	HV (kV)
2006	$^{30}S^{16+}$	3.91	1.8×10^3	30	$\pm$50
2006	$^{30}S^{15+}$	3.82	3×10^3	1.7	$\pm$50
2008	$^{30}S^{16+}$	3.64	7×10^2	30	$\pm$60
2008	$^{30}S^{14+}$	3.47	1.2×10^4	2	$\pm$60
2009	$^{30}S^{16+}$	4.80	8.6×10^3	24	$\pm$60
2010	$^{30}S^{16+}$	4.00	1×10^4	88	$\pm$75

2.3.2 Identification of ^{30}S

The main particle identification (PID) is performed at the F2 focal plane by inserting one PPAC for timing information and one SSD for a residual energy measurement. The

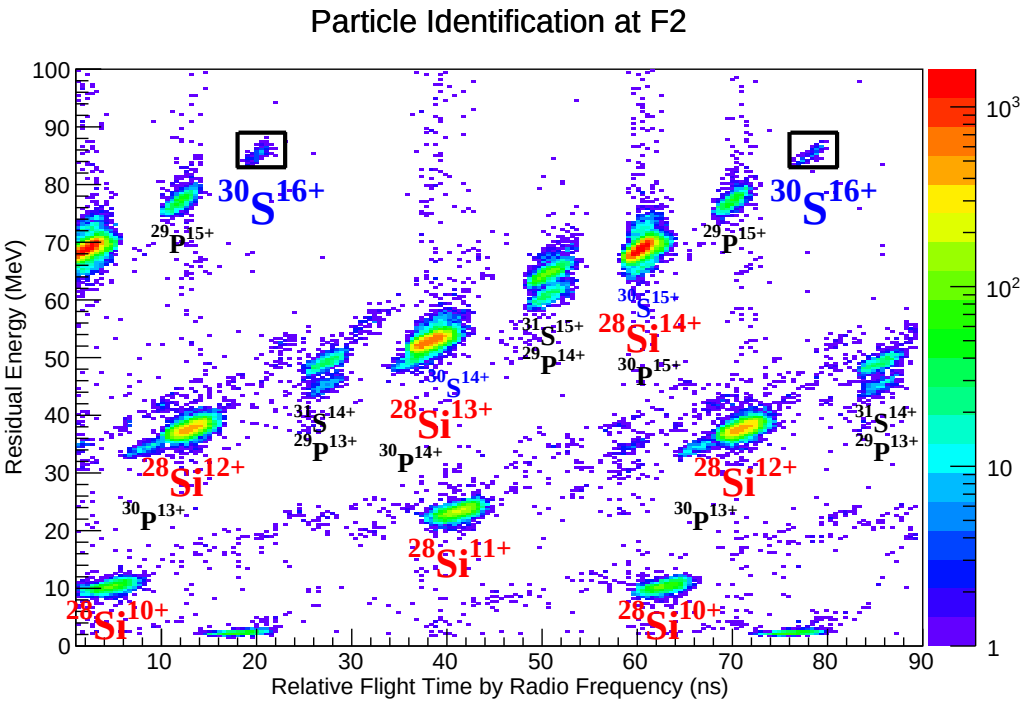

Figure 2.6: Experimental data for the identification of $^{30}S^{16+}$ in the stopped cocktail beam at F2, with $B\rho = 0.54018$ Tm and an F1 slit setting of 0 ± 10 mm. Compare to the calculation in Figure 2.7, where here several charge states of ^{30}S are labelled in blue, charge states of the scattered primary beam ^{28}Si are labelled in red, and other RI species are labelled in black (all labels are below the respective loci for clarity). The $^{30}S^{16+}$ loci are clearly separated from any contaminants. The abscissa shows the Rf time, representing an ion's ToF from the production target at F0 to the PPAC at F2 (with repetition on the order of 60 ns). The ordinate shows ion residual energy as measured by a silicon detector. The color-depth is logarithmic. Both of these detectors are removed from the beam-line during the main experimental measurement, and are used for simply optimizing the CRIB settings for selection and transmission of the RIB of interest. See the text.

PPAC, coupled with the timing signal from the cyclotron RF signal, enables a ToF measurement, described in full detail in Section D.1.2.[†] In the standard CRIB DAQ system, approximately one and a half RF cycles are measured by two TDC registers with a delay between them (Rf_0 and Rf_1), creating up to two loci for each particle species; we can choose the register where our species of interest appears twice—in the

[†]The DAQ systems are different, and so there are some minor, but trivial, differences between the Rf data in the CRIB and Active Target DAQ systems. Namely, the CRIB DAQ measures about one and a half cycles in each register, but the Active Target DAQ measures exactly one cycle.

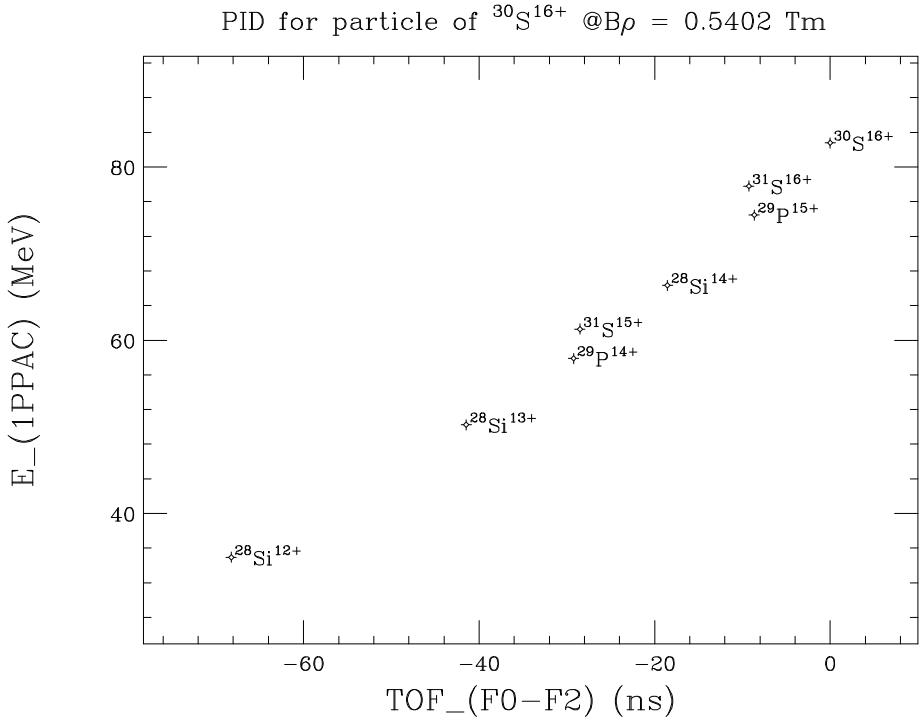

Figure 2.7: Calculated plot for identification of $^{30}S^{16+}$ in the cocktail beam at F2, produced by the `CRIB Optimizer` program written by our collaborator Dr. J. J. He. Compare to the experimental data in Figure 2.6. The abscissa shows the ToF from the production target at F0 to the PPAC at F2. The ordinate shows ion residual energy after 1 PPAC. The plot does not show all the ions one might identify in the experimental data, and instead focuses on $^{30}S^{16+}$ and other prominent loci in its vicinity for clarity; well over 16 species are seen in the data, and more might be guessed to appear by calculation.

case of $^{30}S^{16+}$ it is Rf_0. The cyclotron RF was set to 16.75 MHz, or one pulse each 59.70 ns, meaning any two loci from the CRIB DAQ, separated by about 60 ns in Rf but having otherwise identical properties, are the same species. The SSD measures a particle's residual energy, after energy loss in the PPAC. Due to the $B\rho$ selection at F1, a measurement of the ToF and residual energy separates particles into loci according to p/q as in Equation 2.1.2.

We estimated the optimum $B\rho = 0.5515$ Tm with an energy loss calculation and kinematics assuming the $^{28}Si(^3He, n)^{30}S$ reaction occurs in the center of the production target. The PID spectrum for $^{30}S^{16+}$ is shown in Figures 2.6 and 2.7 for the experimental

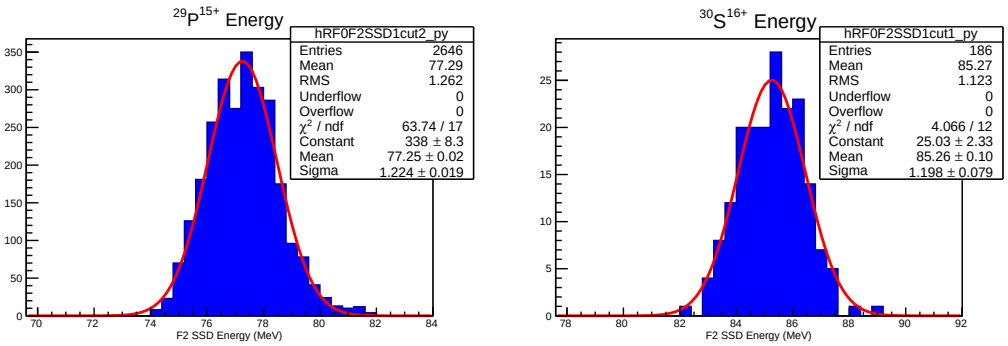

Figure 2.8: Energy projections from Figure 2.6 for $^{29}P^{15+}$ (left) and $^{30}S^{16+}$ (right), showing their energy distributions appear to be gaussian, considering the limited statistics.

data and calculation, respectively. The figures show the case after we optimized $B\rho$ by scanning the momentum-space with the F1 slits; the experimentally optimized $B\rho$ is about 2% lower than the calculated one, which is not too unusual for CRIB experiments, considering ice might build up on the production target windows. The only difference of the beam shown here and the one finally employed in the measurement is that we increased the F1 slit width to maximize the ^{30}S yield on-target. The full momentum width was $\frac{\Delta p}{p} = 1.875\%$, giving a beam energy of $E = 119.9 \pm 2.3$ MeV.

Presuming $^{30}S^{16+}$ is being produced and transmitted, and sufficient statistics are acquired, one actually does not even need to make such a sophisticated calculation to identify it, and can instead rely on simple deduction. When the primary beam and primary target—^{28}Si and ^{3}He, respectively—react once by a single-step transfer reaction, the highest nuclear charge that can be created is $Z = 16$, or sulfur. As $^{30}S^{16+}$ is in its fully stripped charge-state, $q = Z$, and this is thus the maximum q possible by this production mechanism. ^{30}S is also the lightest isotope of $Z = 16$ which can be created in a single-step transfer reaction between our beam and our target, as only two protons and zero neutrons are transferred in the $(^3\mathrm{He}, \mathrm{n})$ reaction. Although several simplifying assumptions are employed, it is easy to see that $^{30}S^{16+}$ will have the lowest possible A/q ratio from ^{28}Si+^{3}He reactions, thus implying in the p/q selection it must be the most energetic particle visible. This is consistent with the PID of $^{30}S^{16+}$ at the top of the loci chain in Figure 2.6 (where there are no meaningful data with $E > 100$ MeV).

Another useful method for performing the PID is to realize that the scattered primary

beam will nearly always be more intense than other species prior to the velocity filter, and thus charge-states of the primary beam species will be the most prominent loci. Indeed, although in the calculation of Figure 2.7 we only show three charge states of ^{28}Si, one can easily pick out the five charge states $^{28}Si^{14-10+}$ in the experimental PID data.

Of course, to be fully convinced, it is always reassuring to perform a calculation, and make a quantitative comparison between the data and theory; it is clear we successfully identified $^{30}S^{16+}$. Some other remarks can be made about the PID histogram. Although we can clearly see $^{31}S^{15+}$ and $^{29}P^{14+}$, apparently $^{31}S^{16+}$ has nearly zero intensity at this $B\rho$.[‡] Lower charge-states of ^{30}S were not plotted in the calculation, but they will be rather close to the scattered primary beam owing to similar A/q values. Indeed, directly above and below $^{28}Si^{14+}$, $^{30}S^{15+}$ and $^{30}P^{15+}$ can be seen, respectively, since they all have $A/q = 2.0$. By $^{28}Si^{13+}$, $^{30}S^{14+}$ and $^{30}P^{14+}$ have shifted slightly to relatively higher and lower Rf values, respectively.

The ease in identifying and separating $^{30}S^{16+}$ is precisely why we used this RIB charge-state for our measurements.

The energy projections from the PID plot of Figure 2.6 for the two species arriving at the experimental focal plane F3, $^{30}S^{16+}$ and $^{29}P^{15+}$, are shown in Figure 2.8. These energy distributions can be reproduced by gaussians, modeling the F2 PPAC as ≈ 14.4 μm of mylar in the energy loss calculations, which is about 5% thicker than the nominal value of 13.8 μm.[§] These distributions, as well as the effective PPAC thickness, become relevant during the more detailed discussion of heavy ion energy loss in Section 3.4.3.1.

2.3.3 Charge stripper foil

Although $^{30}S^{16+}$ is the easiest to identify and separate in our conditions, at these energies, it is not preferentially populated in the charge-state distribution emerging from the F0 exit HAVAR foil which is largely composed of species with nuclear charge $24 \leq Z \leq 28$. It seemed likely that placing a stripper foil after the F0 cryogenic target we could increase

[‡]It is worthwhile to note that there are no experiments reported in the literature employing a low-energy ^{29}P RIB, which we have easily produced at CRIB as an accidental by-product of ^{30}S production. This beam could clearly be used for future work at CRIB.

[§]This larger PPAC thickness at F2 is no longer used, and at present CRIB experiments, the F2 and F3 PPACs are all identical, nominally being 9.5 μm of mylar.

the yield of $^{30}S^{16+}$, although this is the first CRIB work to attempt such a setup. We previously tested the difference of the charge state of the degraded primary beam in HAVAR and carbon foils [41, 75], and found that the fully stripped ion $^{28}Si^{14+}$ had an order of magnitude more intensity emerging from carbon as compared with HAVAR. In the 2009 ^{30}S RIB test, we used a Be foil, although the foil was somewhat broken during preparation. In the 2010 experiment, we used both beryllium and later carbon stripper foils. This is one difference in the RIB production conditions from 2006 and 2008, and the ^{30}S yield and purity was increased as shown in Table 2.2 (although as shown in Table 2.1, the primary beam condition also changed).

One should consider the best foil thickness to employ as a stripper foil, which depends on the beam ion species and energy. In Ref. [76], the authors determine the required carbon foil thicknesses τ to achieve full charge-state equilibrium of ions of $6 \leq Z \leq 18$ at 4.3 MeV/u. Although they did not test $Z = 16$, a linear correlation between Z and τ was clearly observed. Using this data, the author estimated that a 256 μg/cm^2 carbon foil was required for sulfur to achieve full equilibrium, and 163 μg/cm^2 thickness for 3.2% of ions below equilibrium at 4.3 MeV/u—very close to our RIB energy. When the ions are out of equilibrium, more ions will be in the lower charge tail instead of near the more highly-charged peak, which are the ions of our interest. Although no useful references for Be foil charge-state equilibrium were found for $Z = 16$ in this energy region, we assumed it should be basically similar to the case of C.

The commercially available Be foils from Goodfellow could be purchased at 185 or 462 μg/cm^2, where we opted for the higher thickness (nominally 2.5 μm) considering the brittleness of Be. At the time of this experiment, we only had a 300 μg/cm^2 carbon foil similar to the above thicknesses. Normally, thin C foils are made by evaporation and thicker foils by arc-cracking, and foils around 100 to 200 μg/cm^2 can be difficult to produce; since our experiment, the ECR team has found a successful method to produce foils around 100 μg/cm^2.

When the Be foil was fresh, although we only saw about a factor of 2 increase in the ^{30}S RIB intensity, finally in 2010 with a fresh foil we achieved an astonishing 88% purity. However, the ^{30}S purity slowly decreased over the machine time, as the high-intensity primary beam eventually broke the center of the foil. When we switched to the backup

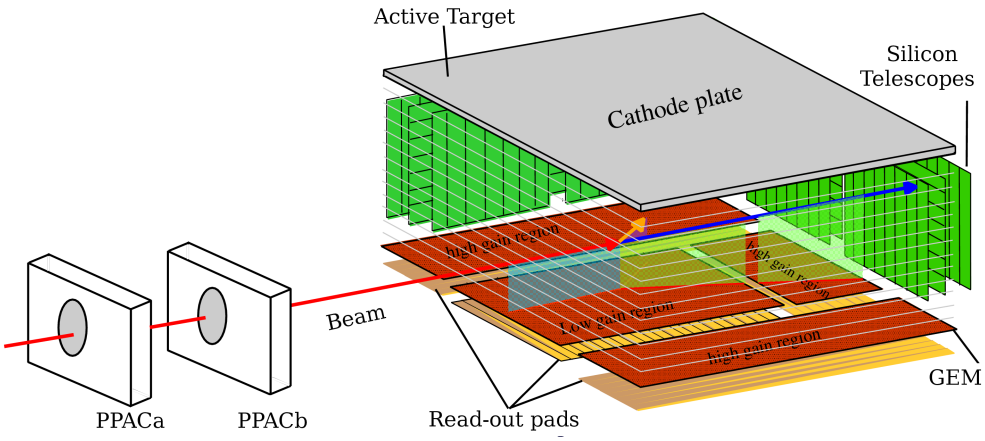

Figure 2.9: Schematic of experimental setup created by Dr. T. Hashimoto, consisting of two PPACs, the active target, and silicon telescope arrays. Note that between PPACb and the active target, the beam impinges on an entrance window, which retains the active target fill gas. The beam is tracked in the central low gain region (active target region, 19 cm), surrounded on three sides by high gain GEMs and silicon telescopes to measure outgoing light ions (right side telescope not depicted). Beneath each GEM is a readout pattern, separated into 4 mm thick backgammon pads. ΔE is simply proportional to the collected charge of each pad. The coordinate system is one where the beam axis defines positive Z, the rest following left-handed conventions. Z and X positions are determined by the pad number and comparing charge collection on either side of the backgammon, respectively. The Y position is determined by the electron drift time.

carbon foil, the purity went from 44% up to 67%. Although Be foil could offer the best purity, considering its expense, toxicity, and difficulty in etching from the copper backing, it can be difficult to use in practice; furthermore, the α particles coming through CRIB in the cocktail beam to F3 were much more intense with the Be foil, likely owing to the single-neutron removal from ^{9}Be leading to two alpha particles. For these reasons, in the future we suggest using carbon foils, which give reasonably nice results for the ^{30}S beam intensity and purity. The newly-developed 100 μg/cm^2 carbon foils might be ideal, since the beam will deposit less energy and they may have a longer lifetime.

2.4 Active Target System

We developed a new target/detector system with the aim of performing measurements for the αp-process, which so far has been used with beams of ^{18}Ne, ^{22}Mg, and the present case of ^{30}S. An active target is a device where gas serves simultaneously as a

target gas and an ion chamber fill-gas, allowing one to perform direct measurements *at a beam interaction position* rather than extrapolating or interpolating data acquired only by detectors *outside* the target region. The design we used was inspired by the gated multi-sampling and tracking proportional counter (GMSTPC) [77], where, to allow for higher beam-injection rates, gas electron multiplier (GEM) foils were incorporated to this newly-designed system, which we call the GEM-MSTPC. Of course, it is still very useful and necessary to place additional detectors outside the active region, some of which are part of the TPC system itself, and others which are separate. In this section, we introduce and outline the fundamentals of the GEM-MSTPC and its related detectors and hardware. A schematic of a portion of the experimental setup is shown in Figure 2.9.

2.4.1 Scattering Chamber and Fill-gas

The active target system is housed in a scattering chamber with 2 cm thick walls filled with 194 Torr ($\frac{1}{4}$ atm) of He + CO_2 gas. The fill-gas is 90% He as the target material with 10% of CO_2 as a quenching gas (percentages are quoted by volume). As in any gaseous detector using a noble gas for ionization, the quenching gas inhibits secondary ionization; greenhouse gasses are commonly used for this purpose to absorb photons emitted from the He atoms ionized by the radiation as they de-excite. The electrons produced by primary ionization correspond to the radiation of interest, whereas those from secondary ionization do not and should be suppressed for a clear and sharp signal.

Carbon dioxide is chosen here over methane, for example, as it does not contain hydrogen, which might easily contribute a significant background from nuclear interaction with the beam. The Coulomb barrier for ^{30}S+^{12}C is 20.5 MeV and for ^{30}S+^{16}O it is 26.2 MeV. The ^{30}S beam energy as it enters the scattering chamber is 1.6 MeV/u, giving $E_{\mathrm{cm}} = 14, 17$ MeV for ^{12}C and ^{16}O, respectively, indicating there should not be a significant contribution from reactions with the quenching gas. Thus, the contributions for interactions between ^{30}S and the quenching gas should be minimal.

During the experiment, the gas was flowed at rates between 10 and 20 standard liters per minute to reduce any leaks from the atmosphere, since even small traces of N_2 caused problems for the active target operation, in particular the pulse shape de-

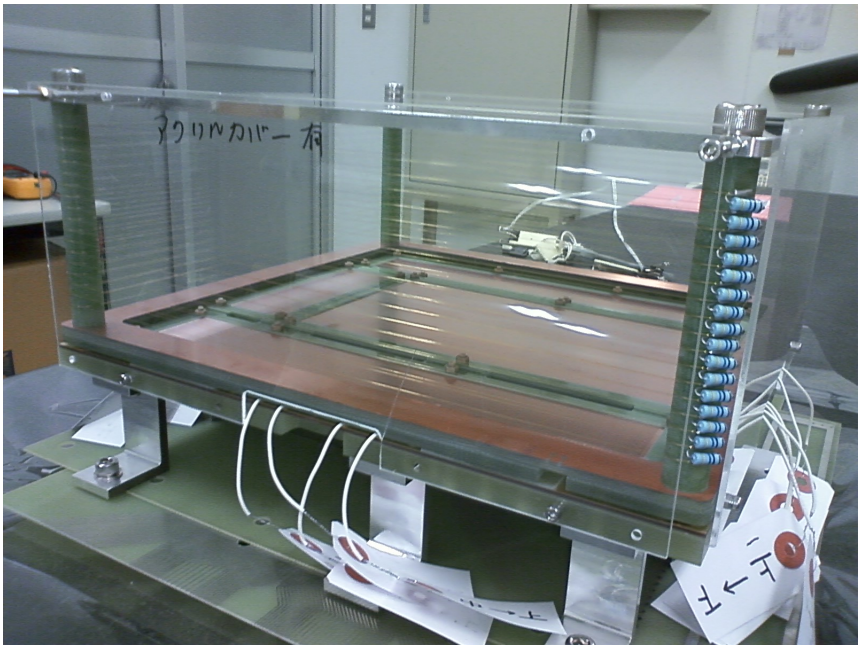

Figure 2.10: Photograph of the active target field cage. The top plate, field cage wires, and resistors are clearly visible. In the experimental setup, the beam would enter from the right side. The acrylic covers are to protect the field cage during transportation or other work, and removed after installation to the scattering chamber.

scribed in Section D.1.4. The system was always pumped down with an all-in-one turbo pumping system coupled with a rotary pump designed to prevent back-flow of oil vapors. The entrance window isolating the scattering chamber from the beam-line was 4 cm in diameter and sealed with a 7.4 μm Kapton foil.

2.4.2 Field Cage

In order to collect electrons produced by primary ionization, a smooth electric field should be applied, which we achieve with by applying a high voltage to the top cathode plate, surrounded by wires connected with resistors forming a cage. The top plate was set to -2828 V, and the frame at the bottom to -1000 V. As the scattering chamber is metallic, the field cage must be placed a sufficient distance from any chamber walls to avoid discharge. The minimum safe distanced determined by several tests for a top plate bias of -3 kV was 3 cm, and for this experiment the field cage was set 35 mm downstream of the inner surface of the upstream chamber flange. The beam optical axis nominally

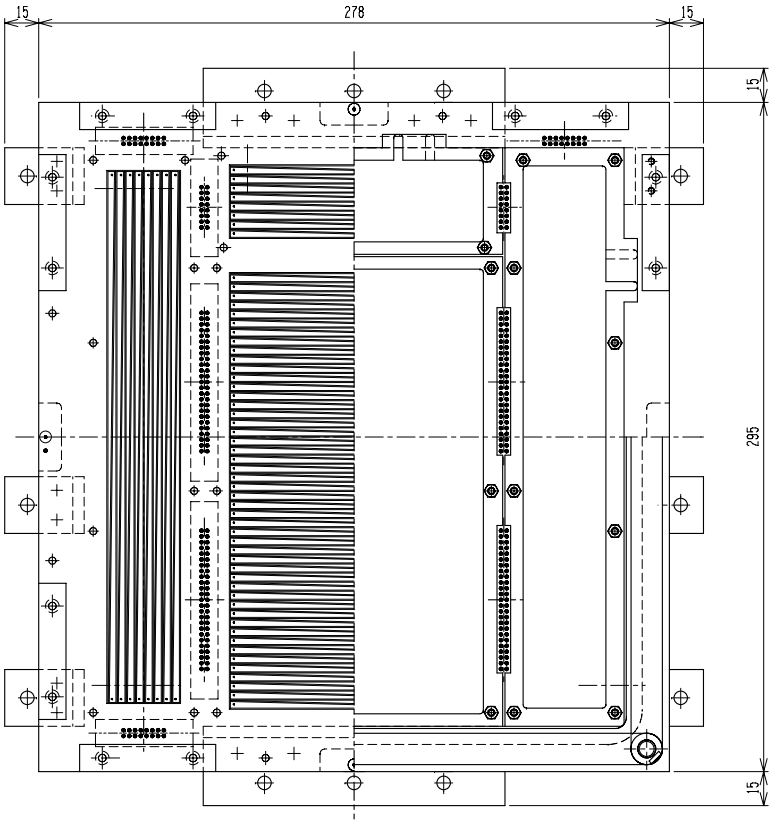

Figure 2.11: Top-down cutaway of the GEM-MSTPC GEM configuration (right) and readout pattern (left), where the electrons are accelerated and then detected. All dimensions listed are given in mm. The positions of the supporting feet and readout connections are also shown.

enters the vertical center of the field cage; the field cage itself is 100 mm from the bottom of the top plate to the top of the insulating frame at its base. A photograph of the field cage is shown in Figure 2.10.

2.4.3 Readout pads

The readout section of the GEM-MSTPC is an etched copper plate placed under the field cage, opposite to the cathode top plate, so that electrons created in the electric field of the cage by primary radiation drift towards it. The readout pads are separated into four sections: one for detecting the beam or heavy recoils and three for detecting outgoing light ions, shown in Figure 2.11.

Forty-eight pads comprise the beam readout section, while the regions for detecting

light ions are comprised of eight pads each. The pads are 3.5 mm in depth, surrounded by 0.25 mm of insulation on all sides (making 0.5 mm of insulation between the center of one pad and the next). Each pad is also bisected diagonally into two congruent right triangles, so that the collected charge can be read out from two opposing sides. The section for detecting the beam ions is the largest and located at the center, slightly shifted towards the beam upstream direction after installation in the scattering chamber. The regions for detecting light ions surround the beam section on the left, right, and downstream sides.

All the pads are separated by about 3 cm from the edge of the cage in principle so that the electric field over the pads is homogeneous. Thus, the distance from the Kapton entrance window (which is flush with the outer wall of the scattering chamber) to the beginning of the field cage is 55 mm, and including the region within the field cage before the first beam readout pad begins, there is a total of 83 mm of 'inactive' target gas. The width of the field cage is 278 mm, while its depth from the beam perspective is 295 mm. Ribbon cables connect to the underside of the readout pattern plate at the end of each set of readout pads, making efficient use of the space necessary to separate different groups of readout pads.

Generally, it is well known that light ions will deposit much less energy over the same distance in the isobaric gas of the active target than heavy ions, meaning light ions will produce many fewer electrons in the field cage. In consequence, with only the field cage and the readout pattern, the resulting signal from light ions will be relatively much weaker than for heavy ions.[¶] In order to work around this problem, we provide a relatively lower gain region over the beam pads, and a relatively higher gain region over the pads designed to detect light ions. These different gain regions are produced and controlled by the GEM foils.

2.4.4 GEM foils

GEM foils are thin, perforated insulating material coated in a conducting layer on both sides, in this case copper. We can classify them here as either low gain (for heavy ions)

[¶]With the conditions described (beam energy, gas composition & pressure, and electric field strength), even detecting the heavy ions could be difficult, but here we provide a generalized argument to segue to the next section.

or high gain (for light ions). In this work, there are three low-gain GEM foils of 200 μm each, and two high-gain GEM foils for each region detecting light ions (six in total) of 400 μm each.[‖] We used different GEMs of different thicknesses because a thicker GEM can attain higher gain. Furthermore, a frame ('cover') with a conductive layer on its upper surface is placed at the top of each GEM stack to assist in smoothing the electric field between the bottom of the field cage and the surface of the top GEM, as the base of the field cage has a 3.2 mm thick insulating material for structural support. We frequently found traces of discharge to the GEM covers, perhaps because of their sharp edges; it might be better to design a single cover etched with insulating material than using several individual covers in the future.[**]

The holes in the GEM foil are 300 μm ϕ, and their layout follows a circular pattern of six holes placed about a central hole. The center-to-center spacing between two adjacent perimeter holes is 0.6 mm; the spacing between one perimeter hole and its second neighbor is 1.04 mm; the spacing between two holes on opposite sides of the circle is 1.2 mm; the spacing between any perimeter hole and the central hole is 0.6 mm. The pattern is repeated many times to cover the GEM area.

To understand how a GEM foil operates, consider injecting some arbitrary ionizing radiation into the biased field cage and measuring the charge read out Q_0 by one pad. Now imagine we add a single GEM foil which is initially unbiased; clearly, the charge read out Q_{GEM} has decreased ($Q_{\mathrm{GEM}} < Q_0$), as many electrons produced in the drift region strike the foil and are stopped before hitting the pad. As voltage V_{GEM} is put across the GEM, the charge collected Q_{GEM} will at first increase linearly with the applied bias, as more electrons are guided through the GEM holes rather than striking the GEM foil. At some critical bias, we will have $Q_{\mathrm{GEM}} = Q_0$. As V_{GEM} is increased past the critical value, Q_{GEM} will grow exponentially as the drift electrons accelerate into the GEM hole, colliding with gas atoms in the hole, creating more electrons. Hence the name *gas electron multiplier foil*. The vertical spacing between the GEMs was 2 mm.

[‖] We place one additional GEM foil over the low-gain region compared to the high-gain region to suppress heavy-ion feedback.

[**] Since this work, we already designed such a unified cover for a different experiment which did not use the high-gain GEMs.

2.4.5 GEM-MSTPC Bias Settings

The applied voltages for various components of the active target are shown in Table 2.3. The values are all quoted in volts. The top row shows the field cage settings, while the lower portion shows the low-gain section on the left and the high-gain section on the right; recall that the low-gain section has an additional GEM compared to the high-gain section. The various GEMs are abbreviated by a number (their sequential order, from the top down) and a letter (the upper or lower face of the GEM).

Table 2.3: Bias settings for the active target in the ^{30}S experiment. See the text

Top	-2828	Bottom	-1000
Low-gain		High-gain	
Cover	-950	—	—
1U	-913	—	—
1D	-823	Cover	-992
2U	-803	1U	-899
2D	-587	1D	-694
3U	-513	2U	-655
3D	-135	2D	-135

Although these settings can be estimated considering the ionizing radiation of interest, the energy loss in the fill gas, the ionizing potential of the fill gas, the dynamic range (considering the preamplifier, ADC and physics of interest), the electric fields, and the gas gain, with this large number of parameters and several uncertainties one is unlikely to calculate the ideal practical values. For the final settings in the experiment, we considered the actual ^{30}S beam for the low-gain region as well as a proton beam produced with CRIB for the high-gain region.

2.4.6 Silicon Detectors

A basic outline of silicon semi-conductor detectors (SSDs) is given in Section 2.2.2. Here we describe the SSDs used with the active target system. Relatively large-size SSDs were required, so that two side-by-side ΔE-E stacks cover most of the field cage drift region on one side. Eight SSDs were put at the forward angles, four on the left and four on the right. Five SSDs were put on the left side of the field cage, with the downstream telescope having three SSDs and the upstream telescope having two SSDs. The remaining four

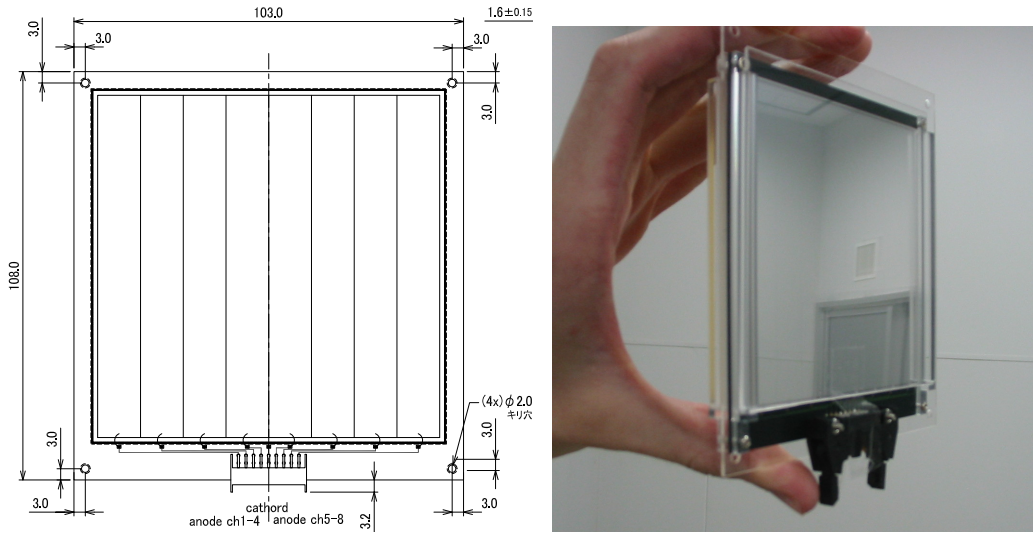

(a) SSD Technical Diagram

(b) Photograph of SSD

Figure 2.12: Figures of the SSD used in the active target. They have a relatively large area, 8 strips on one side (strip side), and a single strip on the reverse (pad side). By using two sequentially and rotating one 90° with respect to the other, it is possible to get 2D position information for a proton. Each detector is nominally 500 μm thick. These detectors were custom designed for the GEM-MSTPC by Hamamatsu Photonics. In total 17 were used in the final experiment.

SSDs were put in pairs to form the right-side telescopes at the largest angles. As each SSD is 500 μm with strips only one side, they are only ΔE-E telescopes for protons with energy larger than 7 MeV; lower energy protons and any alpha particles produced by the RIB stop in the first layer. A diagram and photograph of the SSD is shown in Figures 2.12 (a) and (b), respectively.

Chapter 3

Signal Processing & Calibration

We need to calibrate the electronic signals not only to make sense of the data, but to interpret the results in absolute terms.

3.1 DAQ Trigger

The triggering condition used during the experiment (denoted as the *physics trigger*) is

$$\left(\frac{\text{BEAM}}{n}\right) \oplus (\text{SSD-OR} \otimes \text{BEAM}),$$

where n is the downscale factor, SSD-OR is in principle the front layer of a ΔE-E silicon telescope, and BEAM is defined as

$$\text{BEAM} \equiv \text{PPACa} \otimes \text{PPACb},$$

the coincidence between two PPAC events. For convenience, the (BEAM/n) condition will be referred to as the 'D/S' trigger and the (BEAM $\otimes$ SSD-OR) as the 'SSD-OR' trigger throughout this chapter. In the actual experiment, the downscale factor was set as $n = 2.2 \times 10^4$ in order to record roughly one such event per second, and the SSD-OR signal in practice was

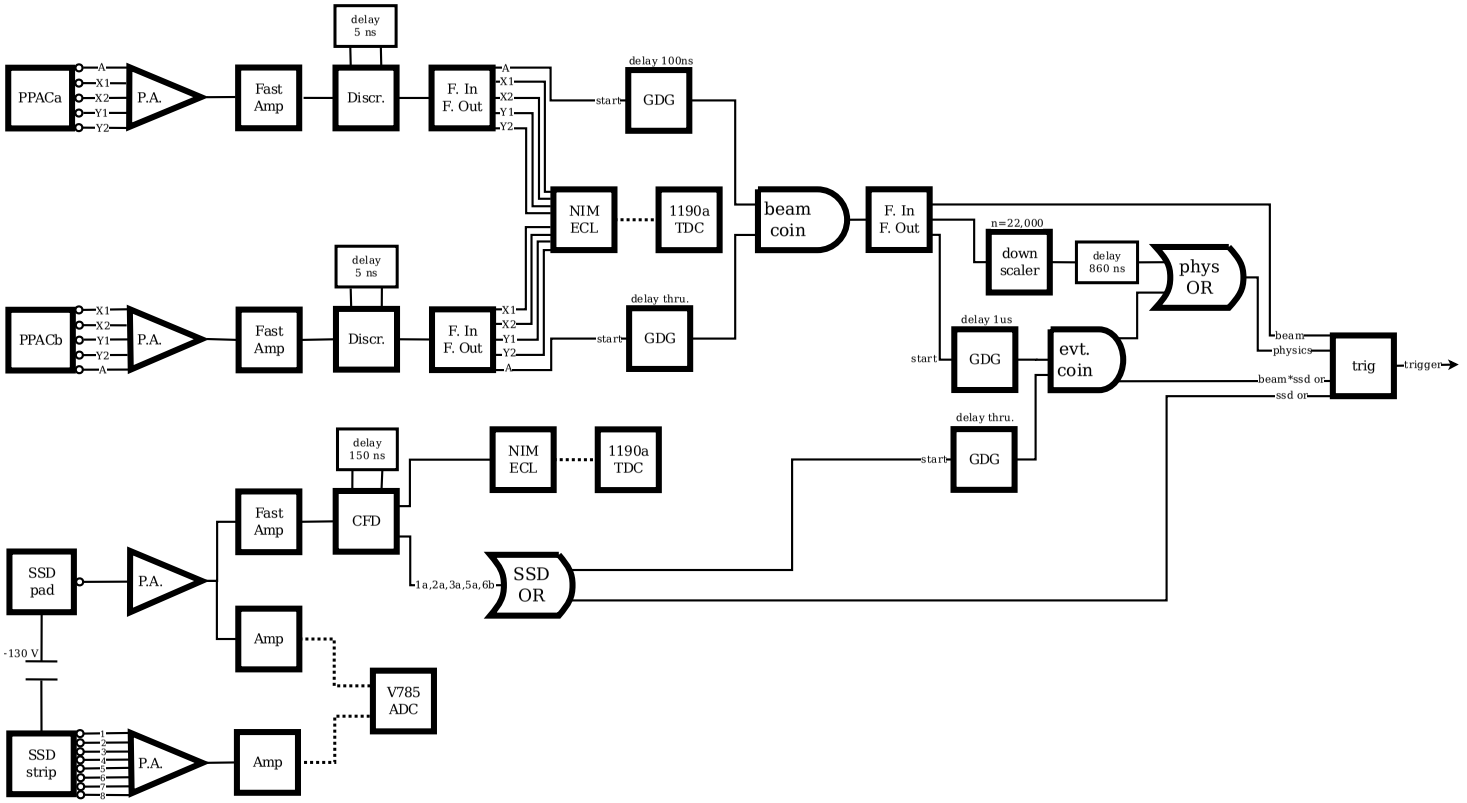

Figure 3.1: Standard triggering used for CRIB active target experiments, including all specific details for the ^{30}S+α measurement. The module labeled as 'trig' was used to select the trigger for various runs, such as beam production, active target tuning, and calibration; the trigger labelled as 'physics' was used during the main experimental runs. See the text.

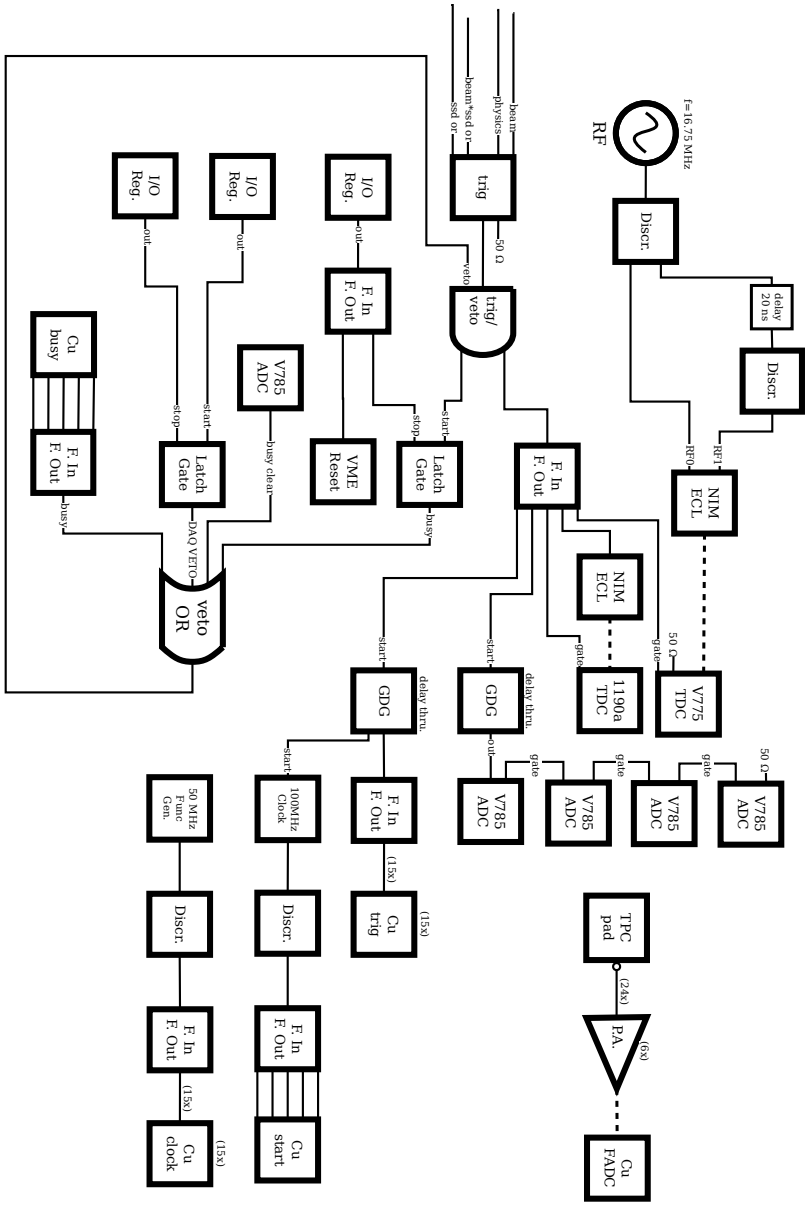

Figure 3.2: Standard veto used for CRIB active target experiments, including all specific details for the ^{30}S+α measurement.

$$\text{SSD-OR} \equiv 1a + 2a + 3a + 5a + 6b,$$

owing to an accidental swap of the 6a $\leftrightarrow$ 6b pad signals after the preamplifier, and accidental failure to include the 4a timing signal in the SSD-OR logic. The DAQ trigger and veto are shown schematically in Figures 3.1 and 3.2, respectively, while the corresponding timing charts are shown in Figures 3.3 and 3.4. Because the BEAM coincidence requirement is shared between the two portions of the physics trigger, the D/S trigger is delayed with respect to the SSD-OR trigger. Importantly, the signal processing for the SSDs takes longer than for the PPACs, which is evident from the delay time difference of more than one order of magnitude employed for their respective CFDs. The (BEAM $\otimes$ SSD-OR) trigger also involves an additional coincidence requirement, also requiring additional time. First and foremost, we want to record all the true physics events, represented by the coincidence of beam and SSD events, while the D/S trigger is used mainly for statistical purposes; for this reason we delay the D/S trigger to ensure it will always take place after any possible beam and SSD coincidences. The time delay for between the SSD-OR and D/S triggers was determined to be $\sim$860 ns with an oscilloscope and recorded in the online logbook (with an additional 80 ns between PPACa/b coincidence to be subtracted), which as we shall see is consistent with an analysis of the timing data, once it is calibrated.

3.2 Results from Calibrated Timing Signals

As we employ three different types of modules to record timing information, we need to calibrate them independently yet consistently. The PPAC and SSD timing signals are recorded by a CAEN V1190A Multihit TDC; the calibration is described in Section D.1.1. Because the RF signal is sent regularly at short intervals from the cyclotron, one should avoid using a multihit TDC for that signal or else the data size becomes quite large, and so a CAEN V775 TDC is used to record the RF signal; the cyclotron RF was set to 16.75 MHz, equivalent to beam packets extracted and delivered to CRIB separated by 59.70 ns each; the calibration is described in Section D.1.2. Finally, the COPPER Flash ADC samples the active target analog signals at a frequency determined by a Biomation

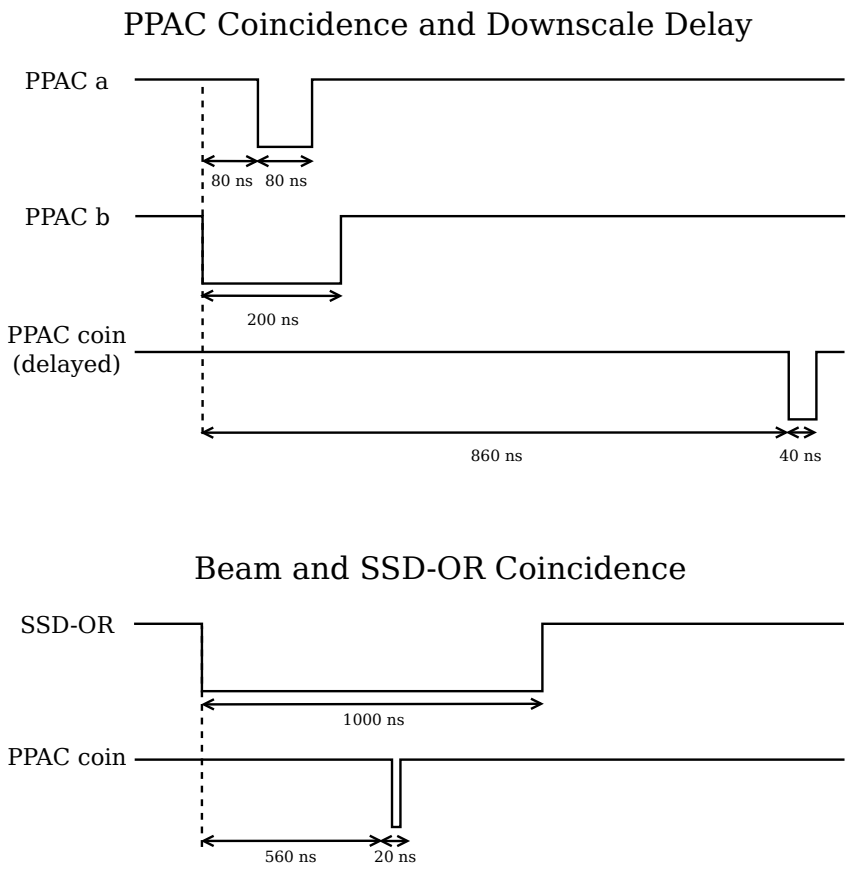

Figure 3.3: Timing chart for the trigger conditions taken with an oscilloscope. The top panel shows the PPAC coincidence condition (BEAM in the text), and the delay employed for the D/S trigger condition; it is evident the D/S data is delayed about 780 ns. The lower panel shows the BEAM and SSD-OR coincidence condition.

241 GA arbitrary waveform / function generator, set to 50 MHz, equivalent to sampling every 20 ns, which serves as the active target timing information; the calibration is described in Section D.1.3.

The PID of the cocktail beam arriving at the experimental focal plane F3 is shown in Figure 3.5, while the real-space distribution in the Y vs. Z plane of the ^{30}S beam injected into the active target and scattered alpha particles are shown in Figures 3.6 (a) and (b), respectively. The PPAC position resolution was determined to be 0.9 mm (1σ), while the active target Y position determined by drift time was found to have a resolution of 0.5 mm (1σ), as shown in Figure D.7.

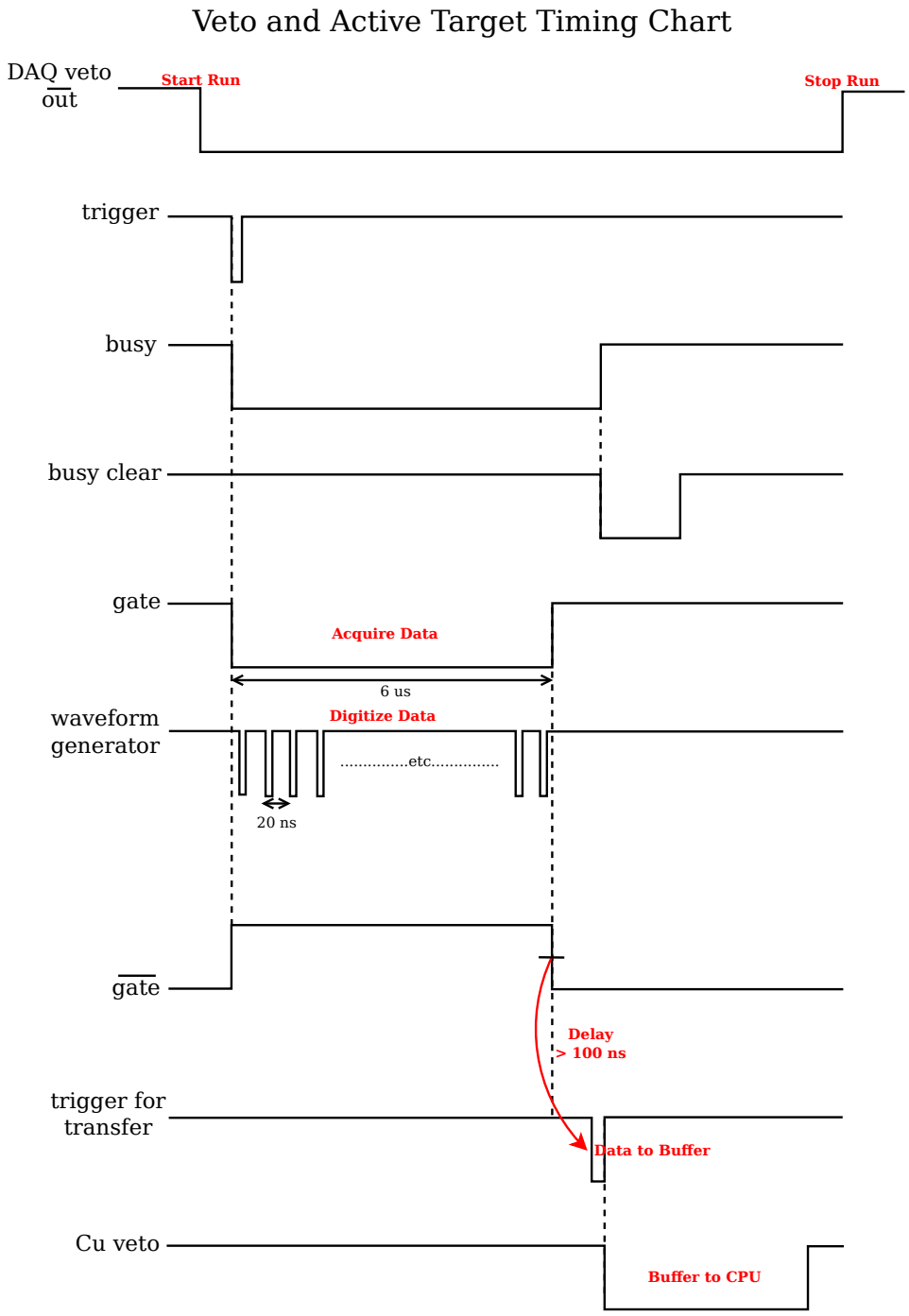

Figure 3.4: Timing chart for the DAQ veto and active target gate and sampling. Once a run is started, triggers will arrived based on Figure 3.2, and the DAQ begins sampling the active target. During this time, we must veto any new triggers as the DAQ is busy. Finally the busy signal is cleared and the COPPER buffer is sent to the CPU and cleared.

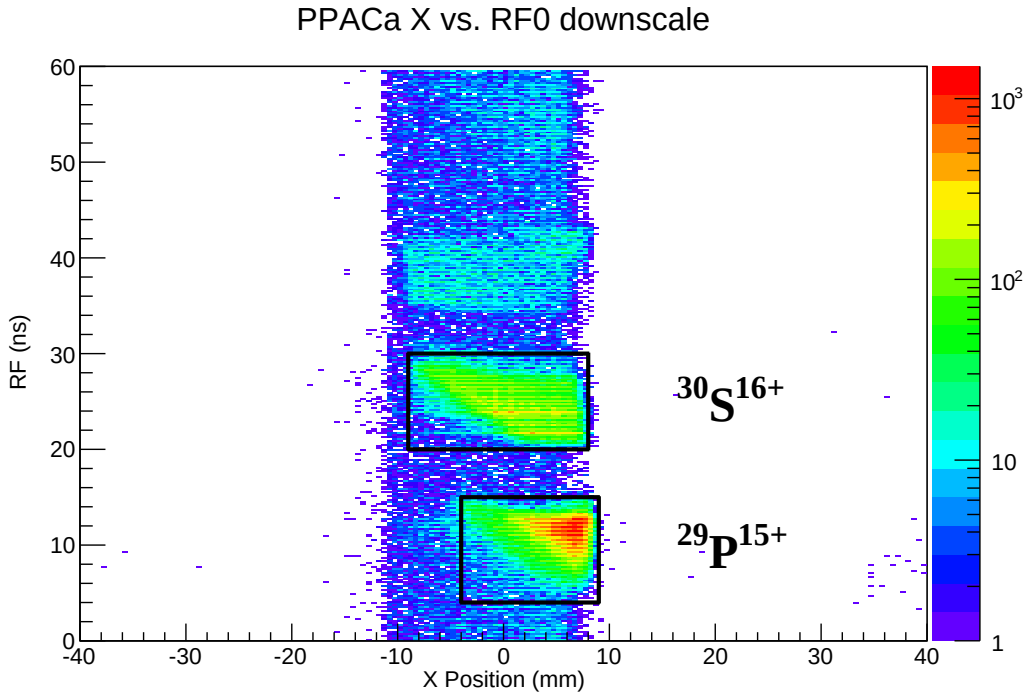

Figure 3.5: Calibrated PPACa X position versus Rf_0 for the D/S condition, showing the PID of ^{30}S and ^{29}P.

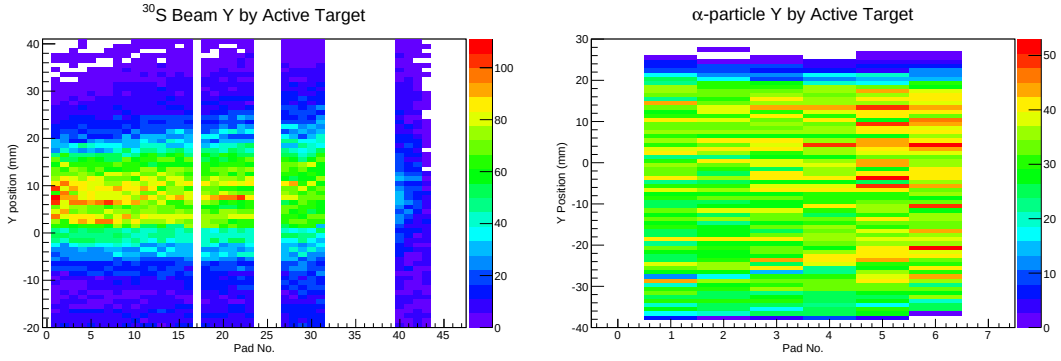

(a) GEM-MSTPC calibrated Y position for ^{30}S

(b) GEM-MSTPC calibrated Y position for α-particles

Figure 3.6: ^{30}S beam tracks (a) and scattered α-particles (b) in Y over the low-gain and high gain active target regions after calibration.

3.3 Silicon Detector Calibration

The silicon detector analog signal data are recorded by a CAEN V785 ADC, which has 4096 bins. Unfortunately, a large portion of the SSD data were not recorded during the experiment because the zero suppression mode was set to *16-bit mode* instead of the *2-bit mode* which was intended.* Normally, the pedestal for this setup might appear around channel 100, and in order to reduce the amount of disk space and simplify the data analysis, any data below a user-set threshold are discarded by the ADC. In the *2-bit mode*, to set a zero suppression of 100 for a given ADC channel, one would send the value of 50 to that register ($2 \times 50 = 100$); but when a value of 50 is sent in the *16-bit* zero suppression mode, it suppresses the lower 20% of the data ($16 \times 50 = 800$)! During the α-calibration prior to the experiment, we had disabled zero-suppression mode in case any of

*The setting for *2-bit* off is `0x4990`, *2-bit* on is `0x4980`, *16-bit* off `0x4890`, and *16-bit* on `0x4880`; it is easy to see how such a mistake might be made.

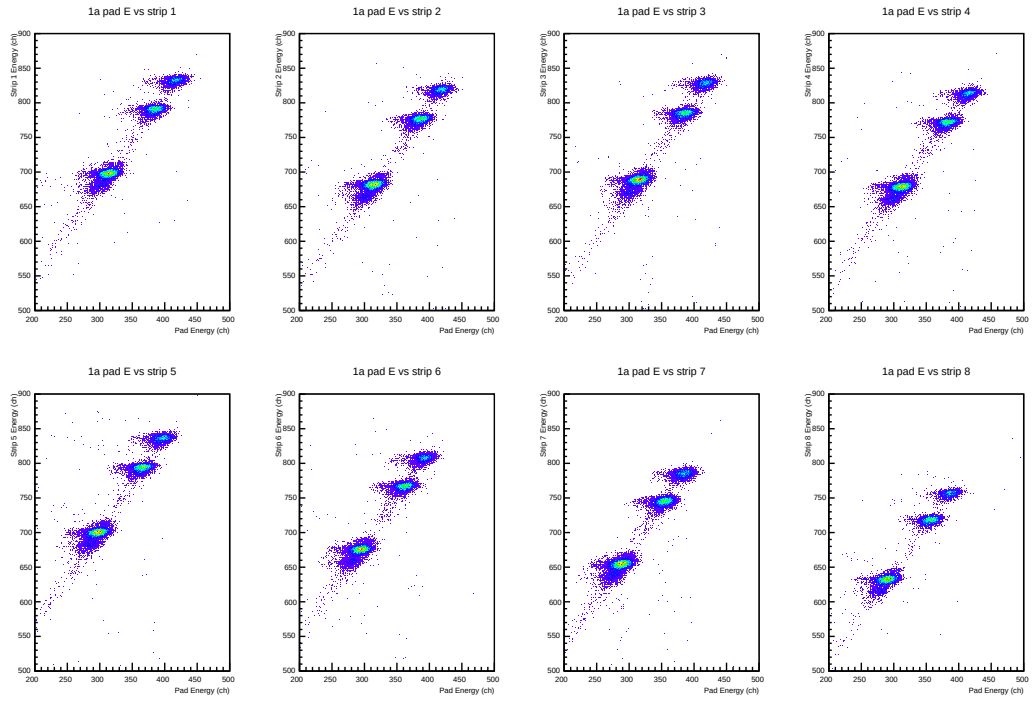

Figure 3.7: Two dimensional histograms of SSD 1a pad energy versus strip energy for all eight strips from an α-calibration run. Although the raw strip channels for a given alpha locus differ by the channel gain settings, the pad energy should be independent of which strip is hit. The projection is shown in Figure 3.8.

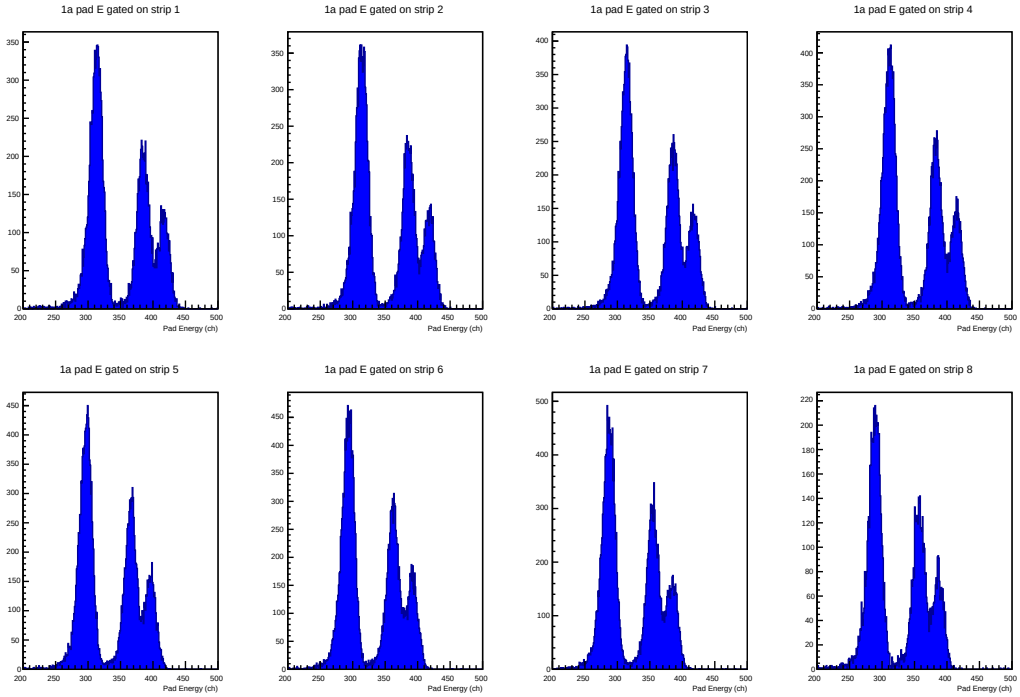

Figure 3.8: SSD 1a pad energy gated on the coincident strip, a projection from Figure 3.7. The centroids of the α peaks do not shift gating on strips $1-4$, but they decrease at strips 5 & 6, and even further for 7 & 8. Note also the number of counts for strip 8 is abnormally low compared to the other strips. See the text.

the signals were very weak and needed troubleshooting. In a conventional experiment, the SSD ADC pedestals would be determined and set at this time, after all detector signals were confirmed to be functioning correctly. However, when the SSDs are placed near the high voltage field cage of the active target, the noise level typically increases; thus we could not tune the SSD pedestals for the DAQ until the final setup was completed and the system operational. As there were many issues successfully operating the active target, this was much delayed and not enough attention was given to the silicon detector data. The fact of the matter is that the *16-bit* zero suppression mode was accidentally set and no one realized until it was too late. While the DAQ system basically worked, we had only a very limited capability to do online data analysis, and a fully functional data visualization program would have significantly improved the situation, possibly preventing this sort of simple but extremely serious error.

Luckily, the channel for the pad side of SSD 1a was set to a zero suppression of

5 (probably because of an entry error omitting the next character) meaning only data up to channel 80 were zero-suppressed, which is much closer to the typical value. The pad side of the SSD has a large area, and this detector was the first layer of a forward angle ΔE-E telescope. It was also such a forward angle detector in the active target experiment with ^{18}Ne conducted two months prior, and apparently suffered some minor radiation damage from the beam. The other forward angle, front-layer SSD 2a was also radiation damaged in the ^{18}Ne experiment, but it was swapped with 4a before the ^{30}S experiment. None of this radiation damage was realized until after the experiments, but fortunately we can correct for it.

Data from a calibration run with a triple α-source is shown for SSD 1a in Figure 3.7; the histograms show the pad energy correlation with the individual strip energies. The pad energy gated on which strip is hit is shown in Figure 3.8, a projection of the previous figure. These histograms can be easily fit with gaussians, and we can calibrate the pad energy based on which strip is hit, the exact parameters listed in Table I.4 using Equation I.0.1. The standard alpha source peak energies are 4.780, 5.480, and 5.795 MeV; the average resolution for the pad side of SSD 1a in this energy range was $\sigma = 98$ keV. However, the strip resolution was $\sigma = 29$ keV, which is useful during calibration runs to estimate the energy straggling more precisely, discussed in Section 3.4.3.2.

In the experimental setup, SSD 1a strip 8 is closest to the beam optical axis, and the data show clear evidence of detector damage towards this side. The pad energies on one half of the detector, strips $1-4$, are all basically identical to one another, but they slowly shift downwards with increasing strip number. Because during the experiment most of the strip data were zero suppressed, and we only recorded the timing information from the pad side, there is no way to know from the SSD pad data alone where the radiation struck the detector. However, using information from the other detectors (PPACs and active target) we can extrapolate the SSD hitting position to determine which calibration set to use.

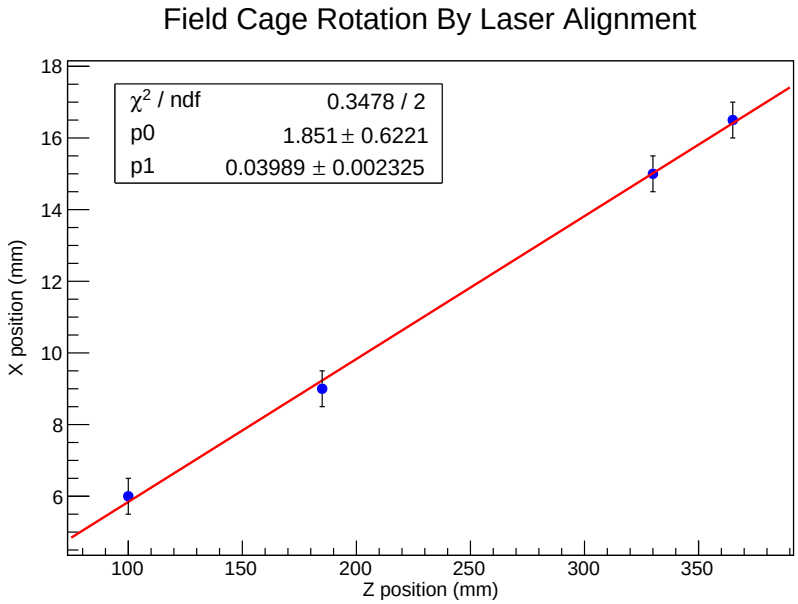

Figure 3.9: Center of the active target field cage in the frame of the beam optical axis as determined by laser alignment after the ^{30}S experiment. The abscissa Z is the beam penetration depth into the target chamber ($Z = 0$ corresponds to the active target entrance window position), and the ordinate X is the left/right position with respect to the beam axis from the beam perspective. Each data point is the interception of a line between two field cage support feet and the beam optical axis, as measured with a ruler; errors in X assume ± 0.5 mm ruler reading accuracy. The field cage foot spacing in Z is from the design diagrams and was confirmed with a ruler. This figure shows explicitly the correction required in X as a function of Z; see Figure 3.10 for a more complete view of the detector geometry. See the text.

3.4 Active Target Analog Signal Calibration

The analog data of the active target are used to determine the energy deposit ΔE as well as the relative position of the ionizing radiation over the length of the pad. The method of finding the peaks in the recorded data is discussed in Section D.1.4.

3.4.1 Active Target Geometry and Rotation

The pads, given preamplifier channel, and/or flash ADC channel will all exhibit slight individual variation, requiring calibration for consistency. One possible approach is to induce charge on all the pads by connecting the lower-most GEM to a research pulser via a charge terminator, or, similarly, sending a pulser signal to the input of each pream-

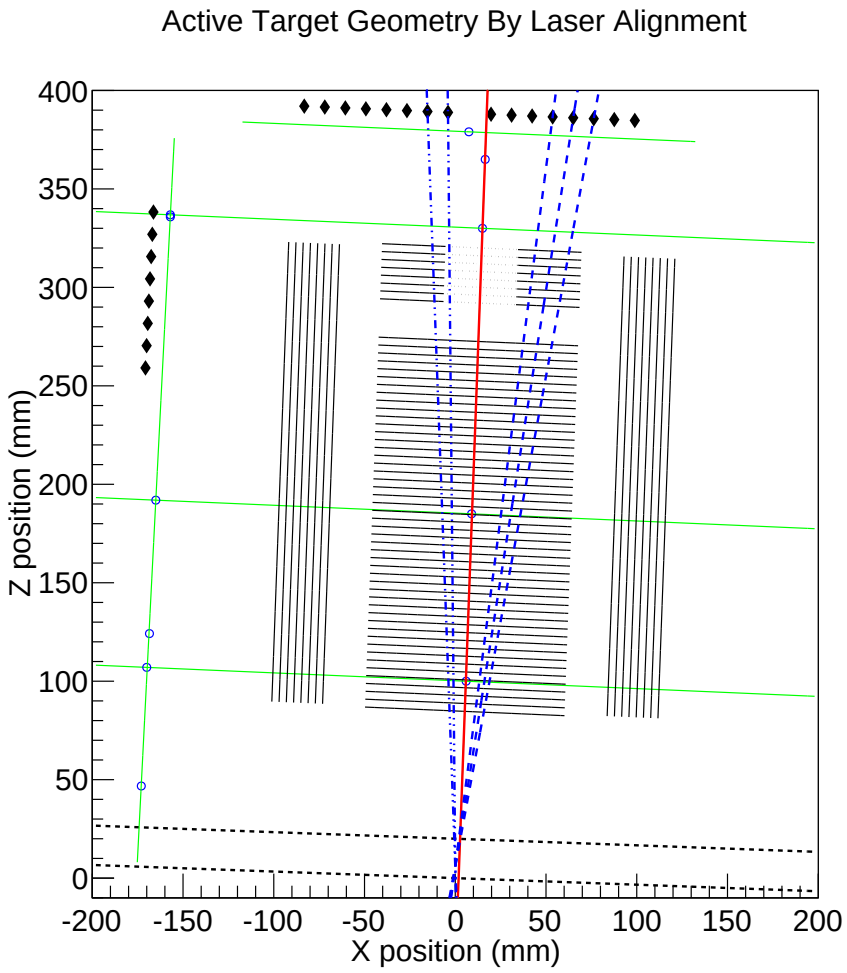

Figure 3.10: Schematic of selected portions of the active target detector geometry as setup in the ^{30}S experiment. The abscissa X is the left/right position with respect to the beam axis, and the ordinate Z is the beam penetration depth into the active target chamber ($Z = 0$ corresponds to the entrance window). The bold red line corresponds exactly with the one shown in Figure 3.9 after correction for the change of axes. The open blue circles show selected positions measured, interpolated, or extrapolated (green lines) between the beam optical axis (as determined by laser alignment) and the foot rests of detectors, all traced on the chamber floor in oil-based marker and subsequently measured precisely with a ruler; error bars are smaller than the point-size. The locations of all TPC readout pads are shown, including the location of the bridge over the central high-gain GEM. The black diamonds represent the strip positions for SSDs 1a, 2a, and 3a. For example, the blue dashed lines show the rays between the center of selected strips from SSD 1a and an alpha source mounted on the entrance window, and blue dash-dotted lines show the rays of alpha particles in the cocktail beam under different run conditions. The dotted black line shows the chamber flange. See the text.

plifier channel and recording the data to disk. Unfortunately these pulser data were not taken. Although this calibration method would allow for consistency among the cable lines, preamplifier channels, and ADC channels, it would still not account for any local variations in the drift field or inhomogeneities and/or local damage on any GEMs. Inhomogeneities in the drift field may be particularly important near the edge region, the region interfacing GEMs with different gain settings, and along the beam axis during the experiment due to space-charge effects; in fact, no pads directly adjacent to the interface regions functioned correctly. As such, the methods outlined here are generally relevant, applicable, and necessary for any such experiment. The calibration method employed is broken into two components: 1) Calibration of the low-gain GEM comparing the beam ion trajectory extrapolated from the PPACs to the one determined by the active target; 2) Calibration of the high-gain GEMs using offline data taken with known geometry and standard α-sources. We do, however, employ self-consistent and identical calibration methods between all these components whenever possible.

It is known from an alignment measurement after the experiment that while the center of both PPACs coincide with the beam optical axis, the TPC field cage was both off-center and slightly rotated with respect to the beam optical axis, as shown in Figure 3.9; more details of the active target detector geometry are shown in Figure 3.10. The unfortunate situation of the misalignment appears to have resulted from miscommunication between the author and collaborators. However, as the experimental geometry was precisely measured after the experiment by the author with a laser using known markers of the beam optical axis upstream and downstream from the experimental setup, we merely must add an additional step into the active target X position calibration to correct for the misalignment. As shown in the figures, the field cage is offset by 5.2 mm to the right of the beam axis at the start of the active region which increases at an inclination of 2.3°. We can correct the offset and rotation simultaneously by choosing the rotational point to be the one where the central axis of the field cage intercepts the beam optical axis, which is 129.2 mm upstream from the beginning of the active region (46.4 mm upstream of the entrance window). To work in the frame of the beam axis, we should add a correction factor $5 \leq X_\theta(Z) \leq 15$ mm to the X position extracted from the active target, depending on the pad Z position; the exact values are given in Tables

I.5 and I.6 for the beam and central GEMs, respectively.

3.4.2 Backgammon Pad Calibration

The position in one of the two dimensions orthogonal to the vector of the ionizing radiation can be determined by comparing the charge collected on two different sides of a readout pad. In this experimental work, for the beam and central GEMs this position is X and for the left and right GEMs it is Z; as the beam plus central pads constitute a majority of the system, when we discuss this concept generally, we shall denote a position so derived by X. Each rectangular readout pad is bisected diagonally with an insulator into two congruent right triangles, one being rotated 180° with respect to the other. As readout pads are ordered consecutively, the resulting readout pattern is somewhat akin to a long and closely spaced backgammon board, from which the name of this style of readout pattern derives.

With such a backgammon readout pattern and all other things being equal, one should be able to determine the position of ionizing radiation over the backgammon pad merely comparing the collected charge:

$$X_{\text{raw}} = \frac{W}{2}\frac{Q_1 - Q_2}{Q_1 + Q_2}, \tag{3.4.1}$$

where Q_1 (Q_2) is the charge collected on the right (left) side of the backgammon, and W is the lateral width of the pad in units of distance. $W = 109$ mm for the beam and central GEMs and $W = 234$ mm for the left and right GEMs. For reasons mentioned above, even for radiation passing normal to and over the pad's center, the measurement of the deposited charges may not be equal. Thus, what we want to do is ensure that signals from the left and right backgammon strips comprising a single pad are calibrated with respect to one another. The basic equation for calibration is as follows:

$$X_{\text{cal}} = \frac{W}{2}\frac{c_1 Q_1 - c_2 Q_2}{Q_1 + Q_2} + X_\theta(Z), \tag{3.4.2}$$

where we determine the unitless coefficients from the residual spectrum as $c_{1,2} = (1 \pm \frac{\Delta X}{W/2})$ and $X_\theta(Z)$ is the geometric offset from the misalignment.

The real-space distribution in the X vs. Z plane of the ^{30}S beam injected into

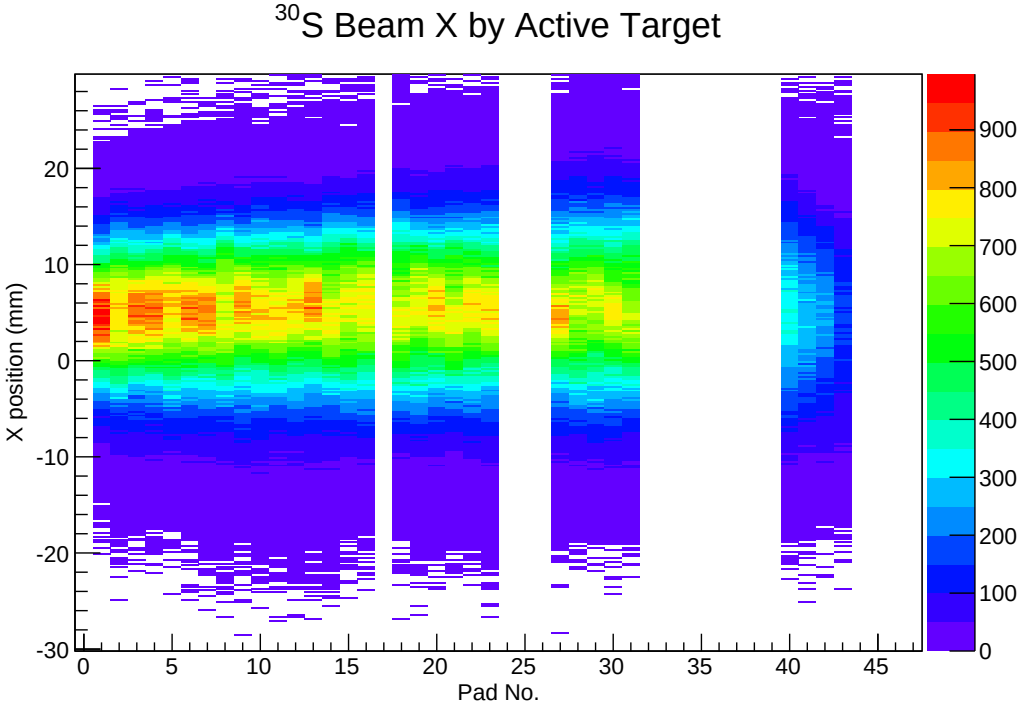

Figure 3.11: ^{30}S beam track in X over the low-gain active target region. Beam penetration depth (left to right) with pad number (4 mm) vs. left/right position derived by charge-division.

the active target is shown in Figure 3.11. The active target X position determined by charge-division was found to have a resolution of 3 to 5.5 mm (1σ) depending on ΔE, as shown in Figure D.15. The poor resolution of the active target in X by the backgammon method for the low-gain region, considering the small laboratory scattering angle of the recoiling heavy ions, was a considerable limitation in the usefulness of the active target data.

3.4.2.1 High-gain charge division

At the end of the machine time, without making any intentional changes to the experimental setup or conditions, we placed a standard triple α-source in the position of the active target entrance window, and data were acquired for approximately 40 hours. Because the α-source and SSDs were in fixed and known positions, it is possible to reconstruct the expected tracks of α particles over the central and side GEMs by gating on different strips in the SSD data. The situation was illustrated in Figure 3.10 for the 1a

detector; it is clear that only strips 3–5 are in coincidence with the central high gain GEM during this alpha-calibration.† These calibration data are crucial for understanding the active target backgammon data.

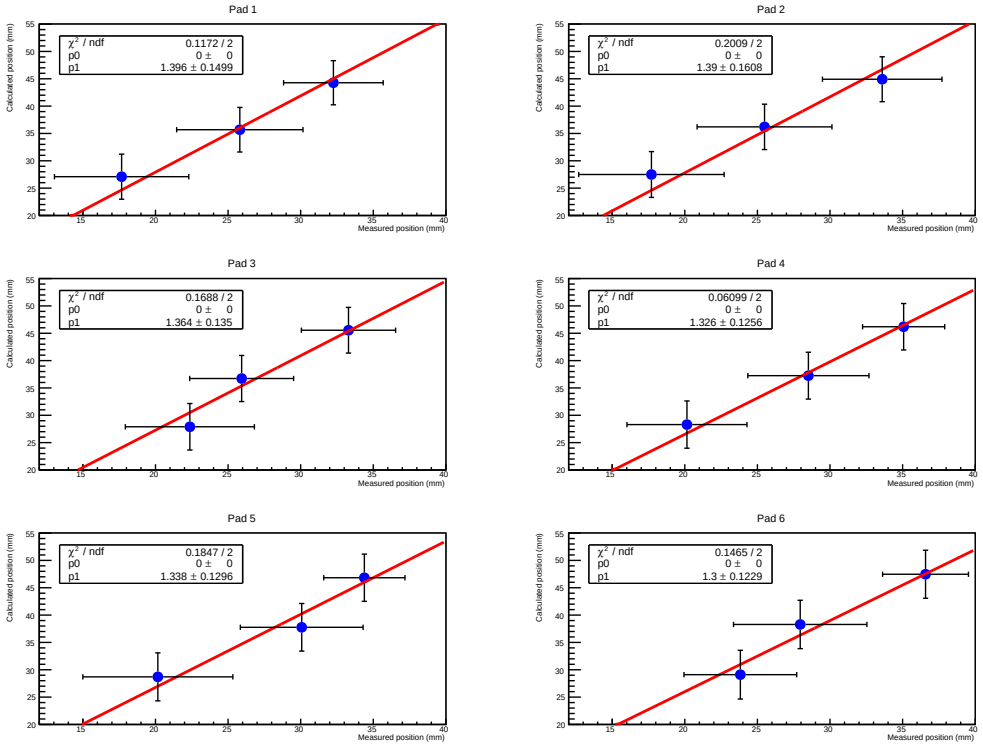

Figure 3.12: The plots show the raw measured X position from the high gain central pads $1-6$ against the expected position from geometry in the active target's own reference frame. Each data point represents a different SSD strip gate in the alpha calibration data set. For the linear fit, the offset is set to the origin. The slope $p1$ shown is the calibration parameter C. The errors in the measurement are 1σ for a gaussian fit to the data, and the error in the calculated position is determined from extrapolating the finite width of the SSD strips. See the text.

Similar to the situation with the low-gain pads described in Section D.1.4.1, it were found that the tracks determined from the active target backgammon data were contracted when compared to those expected from the geometric setup; moreover, the contraction is an increasing function of the distance from the center of the pads. The topic is analyzed in detail in Appendix F, and here we show an empirical calibration method for the central high gain GEM.

†The strips are counted right to left, starting from number 1.

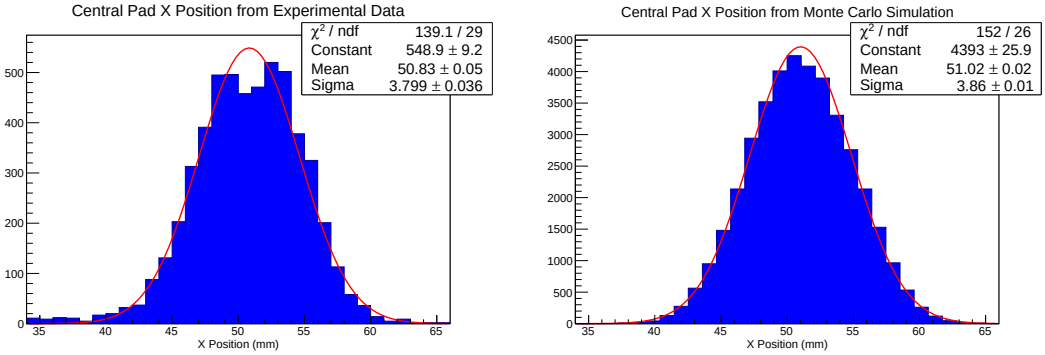

(a) (b)

Figure 3.13: Calibrated X position determined by the central high-gain GEM, gating on a single SSD strip by experiment (left) and Monte Carlo simulation (right). The simulation folded the geometrically predicted tracks with 3 mm position resolution.

The raw position derived from Equation 3.4.1 is plotted against the expected geometric position in the active target's own reference frame for each of the three coincident strips of SSD 1a hit during α-calibration. We then make a linear fit, where the slope is the calibration factor C to expand the measured position to the geometric position. The results are shown in Figure 3.12 for each pad; as usual, the first and last pads (numbered '0' and '7') did not function correctly and are thus not shown. The backgammon contraction is quite evident in the measurement, demonstrating clearly that position determination by backgammon charge division did not operate as expected. Since we know the position derived by the backgammon method is reliable at the center of the pad from Section D.1.4.1, we insisted that the linear fits have an offset of zero. The calibration is then performed using

$$X_{\text{cal}} = C\left(\frac{W}{2}\frac{Q_1 - Q_2}{Q_1 + Q_2}\right) + X_\theta(Z), \tag{3.4.3}$$

with definitions similar to Equation 3.4.1 with $X_\theta(Z)$ is from Table I.6, except C is determined from Figure 3.12. Because we could extract C in the active target's own reference frame, there is no systematic error from the order of operations in this case with the rotational correction like occurs in the low-gain case.

Unfortunately, even when calibrated, the high-gain GEM data do not appear to accurately track the light ions. That is to say, based on the calibrated backgammon results, the data cannot be reliably extrapolated to determine the known SSD hitting

position or α source locations. Thus, we average all the pad X and Y data individually, creating a single pixel over the center (in Z) of the high gain GEM. By gating on a single SSD strip in the calibration data, we are able to compare the predicted width of the sum of alpha particle tracks to the one measured by the high gain GEM. We model the geometry as a flat-top distribution, with the width of the SSD strip projected over the GEM towards the alpha source. Then, when we perform a Monte Carlo simulation assuming a position resolution of 3 mm, the experimental data are thus reproduced, as shown in Figure 3.13.

As we ultimately had no use for the side high-gain GEM data, we did not perform the calibration for those pads.

3.4.3 Pad Energy Loss Calibration

Intuitively, if an energetic charged particle impinges on a material, it will transfer some or all of its energy to the target material, depending on a variety of factors. Thus, it is often useful in nuclear physics to use analogies with conventional ballistics. If a projectile is shot into a material, it will travel some distance before coming to rest, or—if the target is thin enough or the projectile energetic enough—the projectile will punch through the target. In both nuclear physics and ballistics, higher projectile energy results in a longer path length, and higher target material density the converse. However, these physics differ in other ways, as stopping power for radiation depends, for example, on some power of the nuclear charge, whereas for ballistics one is more interested in solid state or material properties such as rigidity.

In the field of nuclear physics, *stopping power* is the amount of energy lost by charged radiation per unit distance in a given target material, and the early pioneering work on this topic was performed by Hans Bethe, where he derived classical and relativistic formulations in 1930 and 1932, respectively, using perturbation theory. The basic idea here is that as radiation travels through matter, it interacts with the electrons of the target material, transferring its own kinetic energy to target electrons. The Bethe formula is [78]

$$\frac{dE}{dx} = \frac{4\pi}{m_e c^2}\frac{nZ^2}{\beta^2}\left(\frac{e^2}{4\pi\epsilon_0}\right)^2\left[\ln\left(\frac{2m_e c^2\beta^2}{I(1-\beta^2)}\right)\beta^2\right], \tag{3.4.4}$$

where the variables represent the following physical quantities:

E Energy of the projectile

x Distance the projectile traverses within the target material

m_e Electron rest mass

n Electron number density of the target

Z Nuclear charge of the projectile

β The relativistic velocity parameter[‡]

e The fundamental charge

ϵ_0 The permittivity of free space (vacuum)

I Mean excitation potential of the target material

This equation is often mistakenly called the *Bethe-Bloch formula*. Bethe's approach with perturbation theory gave a squared term for dependence on the nuclear charge Z, and although there are further corrections by others, such as Bloch's Z^4 correction, these are obviously not present in the above equation. While there are such higher-order corrections to this pioneering formulation, the equation itself has not been modified in any fundamental way, and it essentially remains in use to this day in this form. Ziegler has done considerable work in recent decades on algorithms, tables and computer programs to calculate the stopping power of radiation in matter [79], and while these add important empirical corrections for various materials and several higher order terms alluded to earlier, the essential method traces its origin to Bethe's formulation.

In this thesis, we use a Fortran program written by Y. Watanabe based on Ziegler's method called `enewz` to perform energy loss calculations, as well as a fork of that program implemented as a subroutine for use in other programs by S. Hayakawa[§]. The program `enewz` takes several inputs for the ionizing radiation (Z, A, and E) and the

[‡]This is often mistakenly called the relativistic *velocity*, but as a unitless parameter, it cannot properly be called a *velocity* without units of distance per time.

[§]The ability to use it as a subroutine is particularly important to this work, as virtually all programming is done in the C++ language, which would otherwise require inefficient shell calls.

stoichiometry of the target material. Although Ziegler has his own program called SRIM [80], which is very widely used, is quite inconvenient for practical use in a computer program; furthermore, SRIM was entirely unable to reproduce the shape of the beam Bragg curves discussed next, giving a very rigid and flat-topped type Bragg curve rather than the smoother one we observed experimentally, perhaps because it is very near to the stopping region and the tabulated data binning is far too large for such an application.

3.4.3.1 Energy loss of heavy ions

From the RIB production, we know the energies of ^{29}P and ^{30}S at the dispersive focal plane. However, we need to know the beam energy at a given scattering location within the active target fill-gas after any and all energy loss, since it determines the center-of-mass energy which plays a critical role in extracting the physics of interest. As the cocktail beam will traverse both PPACs, the TPC entrance window, and some quantity of He+CO_2 gas before such a scattering, we must handle the energy losses in all these materials with high precision and accuracy. Using the forward angle SSD 1a with an attenuator placed after the amplifier, we made several measurements of the cocktail beam residual energy at different TPC gas pressures. We performed one measurement with the PPACs and TPC entrance window removed, but the preamplifier was saturated in this case. We also performed calibration with a triple alpha source, but the derived offsets for heavy ions and alpha particles can be quite different for SSDs, and thus these data were not useful.

The strategy for optimizing the energy loss parameters is as follows. We plot the raw channel values from the SSD against the calculated residual energy under a given set of material thicknesses for the PPACs, Kapton window, and fill-gas, and check the goodness of fit by calculating χ^2_ν. For the beam energy loss measurement experimental runs, we acquired data at vacuum as well as four different gas pressures: 0, 22, 40, 59 and 72 Torr; either no triggers were received at any higher pressures we tested or the energy distributions were non-gaussian and very low energy, meaning the beam is nearly, but not quite, stopped at 72 Torr when traversing the entire system. These runs thusly yield five data points for each of the two species, ^{29}P and ^{30}S.

However, as discussed in Appendix H in a similar experiment with ^{22}Mg where abso-

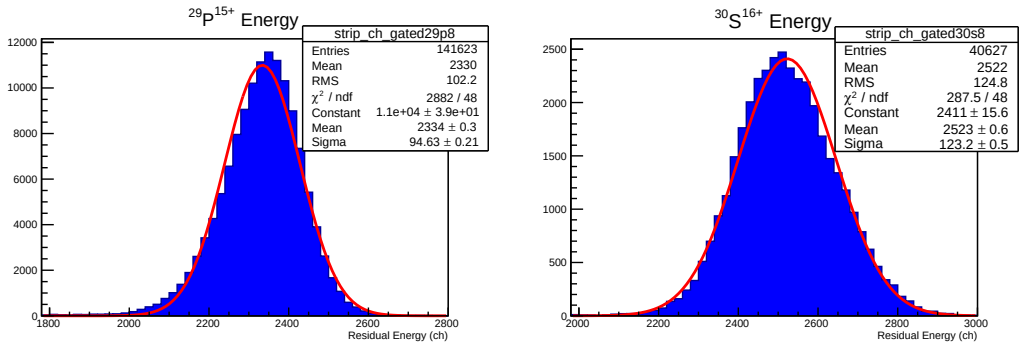

Figure 3.14: Energy distributions for $^{29}P^{15+}$ (left) and $^{30}S^{16+}$ (right) on-target at F3 when the gas was evacuated from the target. Note that the distributions are skewed from gaussian shapes towards each other (roughly $\pm 1\%$ from the centroid value), evidently by the Wien filter selection. Compare with Figures 2.8 and H.3.

lute calibration of the SSD was performed using heavy ions over an appropriate energy, we found that the RIB energies are skewed slightly from their centroid $B\rho$ values by the Wien filter selection, shown to be similar with the ^{30}S experiment in Figure 3.14. The tabulated values of the energies after the Wien filter are shown in Table 3.1, and are seen to be $\pm 1\%$ for ^{29}P and ^{30}S, respectively, but this minor deviation is allowed for within the energy spread of the momentum selection at the dispersive focal plane. The values in the last column of the table are the incident beam energies used for the energy loss calculations, which otherwise could not yield self-consistent results between the two RI species.

Table 3.1: Comparison of RIB energies at F1 and F3. The 'Peak Maximum' and the 'Gaussian Centroid' in the first and second columns, respectively, are derived from Figure 3.14. The optimized $B\rho = 0.5402$ Tm as noted in Figure 2.6, is used for calculating the third column energies at F1, with a 1.9% energy spread. The last column is the first column divided by the second column, times the third column (where all the raw channel values are corrected for the offset of -129 channels).

Ion Species	Peak Maximum	Gaussian Centroid	F1 Energy (MeV)	F3 Energy (MeV)
$^{29}P^{15+}$	2350	2334	109.1 ± 2.1	109.8
$^{30}S^{16+}$	2500	2523	119.9 ± 2.3	118.9

Each PPAC at F3 is known to have an effective thickness of ~ 9.5 μm mylar, but as described in Section 2.3.2, we found that the effective thickness of the PPAC was almost

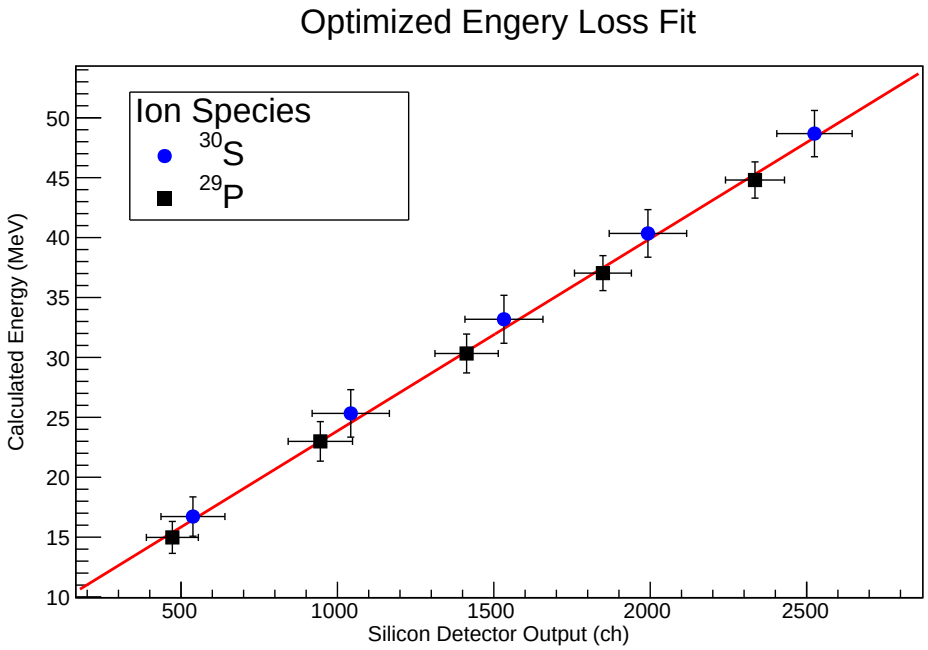

Figure 3.15: Optimized energy loss fits for ^{29}P and ^{30}S. The abscissa shows the raw SSD channel, and the ordinate the calculated energy. The material thicknesses extracted from this plot are adopted in the thesis: 19.8 μm mylar for the 2 PPACs, 7.4 μm for the Kapton, and 194 Torr of He+CO_2 gas at 293 K; all these are the nominal values, except the PPACs are 5% thicker reflecting our calibrated data at the F2 focal plane with a similar detector. See the text.

5% thicker with the absolutely calibrated silicon detector for both species at F2; thus we adopted the total thickness of 19.8 μm of mylar for these two detectors. The Kapton foil was purchased commercially at 7.4 μm thickness, which we adopted in the calculation. We also adopted the nominal pressure of 194 Torr and the standard temperature of 293 K in the energy loss calculations.

The resulting energy loss fit is shown in Figure 3.15. The error bars are 1σ for a gaussian fit to the raw data, simply propagated to the energy loss calculation. As seen in the figure, the fit is very satisfactory. The calibrated ^{30}S beam energy on-target, as well as the correlation with Rf_0, are shown in Figure 3.16 (a) and (b), respectively. The experimental Bragg curves are shown in Figure 3.17; although the Bragg curves of ^{29}P and ^{30}S are overlapping due to straggling effects, their centroid values are still distinctly different. When preparing for the experiment, we chose the active target gas pressure of 194 Torr (about 1/4 atmosphere) to scan down to 1.5 MeV in the center-of-mass over

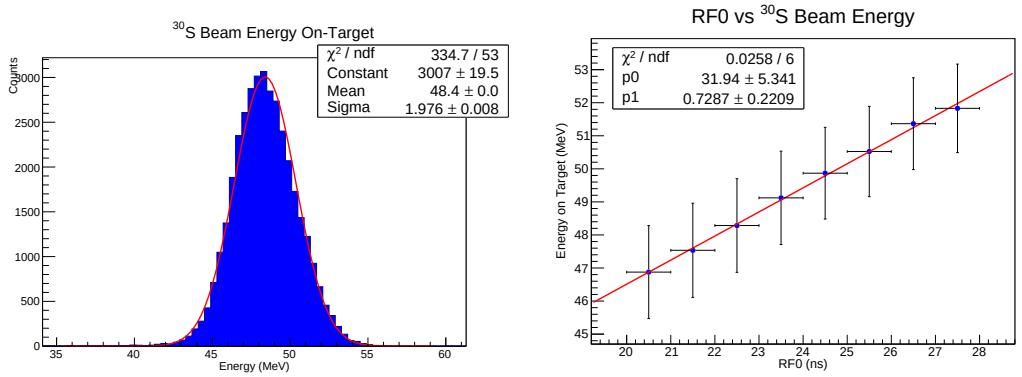

(a) ^{30}S energy on-target

(b) ^{30}S Energy vs. Rf_0

Figure 3.16: ^{30}S calibrated beam energy on-target (a) and energy vs. Rf_0 (b). Although the gaussian fit in (a) is imperfect as noted above, it is about 48 MeV or 1.6 MeV/u. To remove some effects of the energy spread, the beam energy can be determined event-by-event based on Rf_0 as shown in (b).

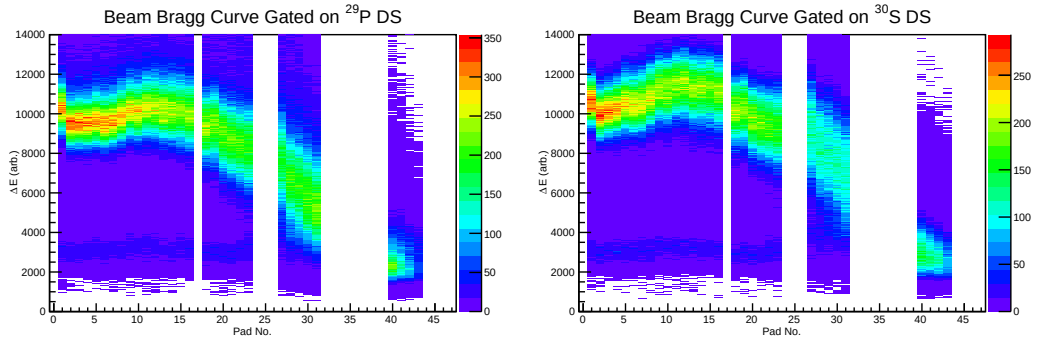

Figure 3.17: Experimental Bragg curves for the active target gated on ^{29}P (left) and ^{30}S (right). The pad number is show on the abscissa, where the beam penetrates the target beginning on the left side. The ordinate shows the energy loss, when the FADC peaks are integrated and backgammon corrected. Compare to Figure 3.18.

the active region, meaning the ^{30}S beam would still have remaining energy, requiring the bridge over the high-gain region near the beam line. This was the pressure used during all the preparation and tuning of the GEM-MSTPC prior to the experiment, which required a significant amount of time. It should be noted that, as shown in Table 2.3.2, we anticipated a slightly higher ^{30}S beam energy, thus in the actual experiment, the beam stopped somewhat sooner, just before the end of the low-gain region. The calculated Bragg curves are shown in Figure 3.18, showing the best-fit to the energy loss

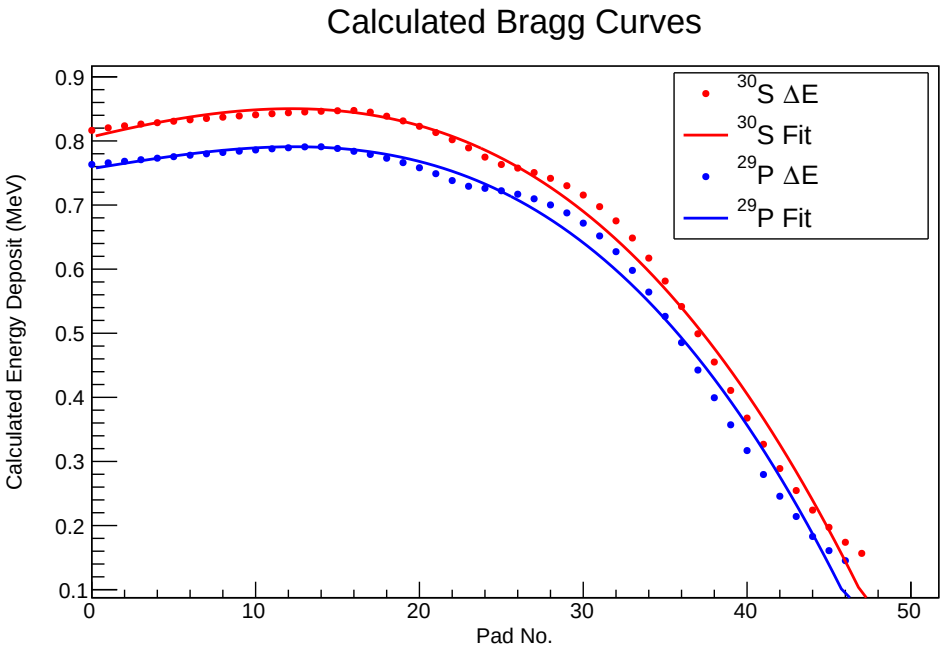

Figure 3.18: Bragg curves calculated via `enewz` for the optimized energy loss parameters corresponding to ^{30}S (red) and ^{29}P (blue). The ions lose energy in the PPACs, Kapton window, and inactive region of the active target before the calculation of ΔE, shown on the ordinate, is performed each 4 mm to simulate the active target pads on the abscissa. Third-order polynomial fits are used to smooth out the calculations. Compare to Figure 3.17. The polynomial fit in red is adopted for ^{30}S in the experiment, employed to produce Figure 3.19.

above reproduces the stopping position of both species, considering that the sensitivity of the low gain region cuts off around 200 keV.

In the comparison between the measurements and the calculations, one general point to note is that there appears to be some edge effect, and the collected charge decreases at either end versus what is expected. This effect is consistent with the observation that pads near the interface regions basically failed to operate at all, and indicates a non-trivial flaw in the active target design, which was also observed in the high-gain pads.

To perform the final ^{30}S energy loss calibration, we fit the experimental Bragg curve in the right side of Figure 3.17 to the polynomial function of Figure 3.18; the fit function

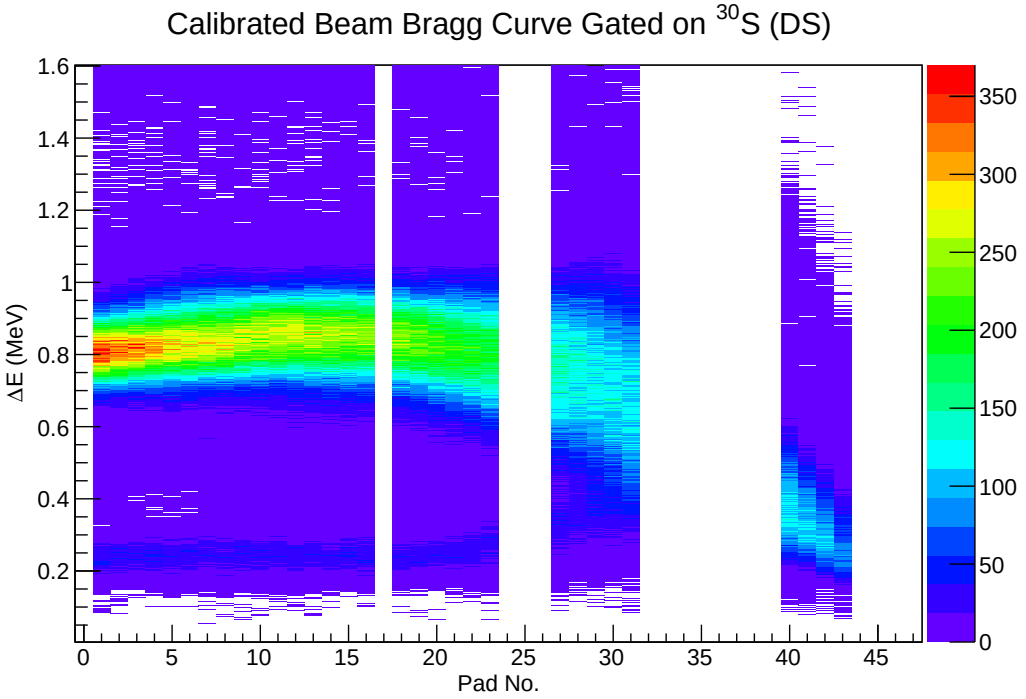

Figure 3.19: Calibrated Bragg curve of ^{30}S over the low-gain region of the active target.

is

$$\Delta E = -7.02427 \times 10^{-6} z^3 + -0.000123645 x^2 + 0.00615596 z + 0.806366, \tag{3.4.5}$$

where ΔE is in units of MeV/pad and z is the pad number. Calibrating the pads past #40 is obviously difficult; however, any alphas scattered at these low energies will not be able to reach an SSD to initiate a trigger, so we omit any data past pad 31. The calibrated Bragg curve is shown in Figure 3.19. Since the pad size of 4 mm is inconvenient for the calculation of stopping power, we also plot the stopping power for ^{30}S in the He+CO_2 gas mixture in Figure 3.20. To fit the stopping power, we use two polynomial functions:

$$S(E)_{\text{low}} = 0.0101792E^3 - 0.742609E^2 + 18.4721E + 59.8761 \tag{3.4.6}$$

$$\begin{aligned} S(E)_{\text{high}} = &- 6.74502 \times 10^{-10} E^7 \times 6.1841110^{-8} E^6 - 4.55813 \times 10^{-8} E^5 \\ &- 0.000102548 E^4 - 0.000611156 E^3 \\ &+ 0.17968 E^2 - 4.33163 E + 244.782 \end{aligned} \tag{3.4.7}$$

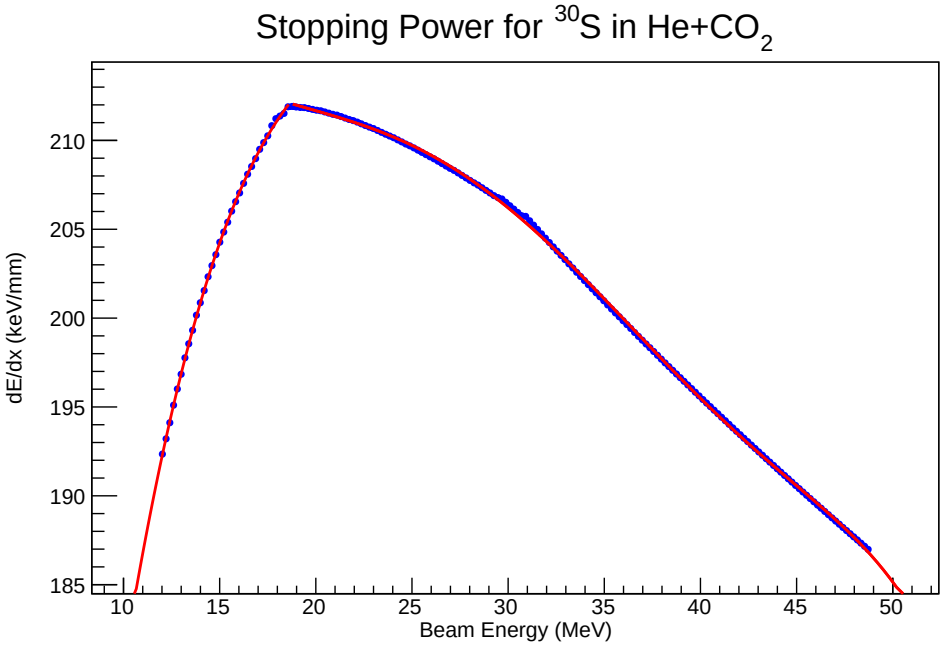

Figure 3.20: Stopping power of ^{30}S in the He+CO_2 gas mixture, using the material thickness optimized in Figure 3.15. The blue points are from `enewz` and the red lines are two polynomial fits, split at roughly 19 MeV. Points are calculated beginning at $E_{\text{beam}} \approx 48$ MeV taken from Figure 3.16(a): the energy of the beam after the PPACs and Kapton foil. Points for $E_{\text{beam}} < 12$ MeV are omitted since any scattered alpha particles below this energy cannot reach an SSD.

where $S(E)$ is the stopping power of He+CO_2 in keV/mm as a function of ^{30}S beam energy in MeV, split at 18.6367 MeV, so that their disagreement at this value is less than 1×10^{-4}.

3.4.3.2 Energy loss of light ions

As described in Section 3.4.2.1, we performed an alpha calibration of the full system directly after the experiment. We select SSD 1a strip #4 to determine the energy loss, since considering the location of the alpha source, the track of ionizing radiation passes roughly over the center of the right side of the central high-gain GEM pads in this case, as shown in Figure 3.10. ΔE-E plots are made for each of the six functioning pads, shown in Figure 3.21. Two loci corresponding to alpha particles with different parent nuclei are clearly observed and separated. We can gate on each locus and make a projection to the SSD energy to get the alpha residual energy spectrum from two species individually.

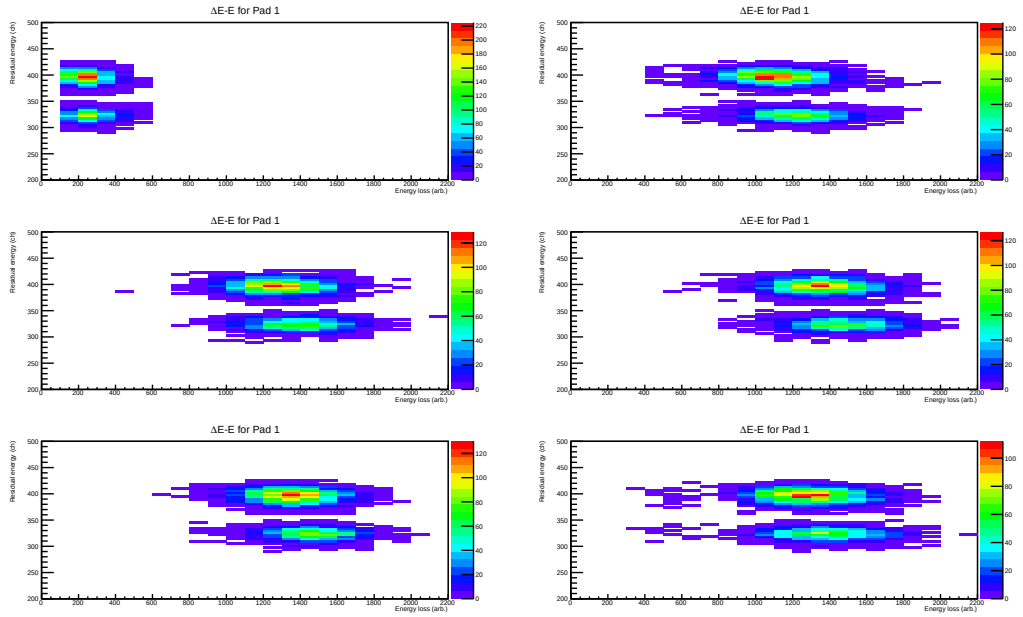

Figure 3.21: ΔE-E plots from the alpha calibration. ΔE is from the high gain central GEM pads 1-6 and the residual energy E is from SSD 1a strip # 4. We see clearly two loci, corresponding to the higher energy alpha decays in the alpha source; the lower energy alpha particles were unable to reach the SSD. The gain of pad 1 is clearly lower than the rest.

With the zero-suppression turned off, we also calibrated all the SSD strips with the TPC chamber evacuated via the same alpha source, and found that the offset for strip #4 was 98.50233 and its gain 0.0081805995 to be used in Equation I.0.1, with the output in MeV. A geometric calculation from the program used to produce Figure 3.10 determined the distance between the center of the alpha source and the center of strip #4 is 385 mm. Finally, knowing the nominal alpha energy from the standard source, we can determine the necessary energy loss parameters for alpha particles in the He+CO_2: 194 Torr at 293 K. It can be seen that, just like the case of the heavy ions in the gas mixture, light ions are modeled well with the nominal parameters, giving confidence in the overall analysis due to the self-consistency.

As mentioned in Section 3.3, the intrinsic resolution of SSD strip #4 was quite good at 29 keV under vacuum. The width broadened to $\sigma = 70$ keV when the He+CO_2 gas was filled and we gated on alpha particles in the high-gain GEM data. Convoluting the energy loss straggling (assumed as a gaussian shape) with the intrinsic detector

resolution, we found a contribution of 64 keV uncertainty from straggling to the measured width. Considering the alpha particles from the source were originally around 5-6 MeV, and lost about 3 MeV over the full length of the active target chamber, this can be considered the maximum uncertainty for straggling, with higher energy alpha particles straggling much less and originating much closer to the detectors.

Chapter 4

Data Analysis and Results

Having calibrated the detector system so that we can extract physically meaningful quantities from the data, we are finally able to analyze the data and extract physics of interest. A table of the scalers for the physics run is shown in Appendix G. In particular, we want to extract the excitation function (introduced in Section 1.2) of ^{30}S alpha elastic scattering. We applied two different methods: one is a vertex-finding method which was unsuccessful (Section J.1) and the other is the standard kinematic solution (Section 4.1, discussed presently).

4.1 Kinematic Solution

The pad side of SSD 1a was not zero suppressed at an unreasonably large value, and for some alpha particles we measured and recorded to disk their residual energies over a large energy range. Thus, for a portion of the events, we can solve the kinematic equation to deduce the scattering energy, with a simple example shown in Figure 4.1. Using the PPAC data, we can extrapolate the beam trajectory into the target via Equation D.1.1, and we know the location of the scattered alpha particle from the high-gain GEM, allowing us to determine θ_α for the measured alpha particle. Using `enewz` and the energy loss parameters determined in Section 3.4.3, we can calculate E_{beam} after energy loss up to the scattering location and convert it to E_{cm} via Equation B.0.1. Once we determine θ_α, we can calculate θ_{cm} via Equation B.0.5. Furthermore, using θ_α and E_{cm} we can

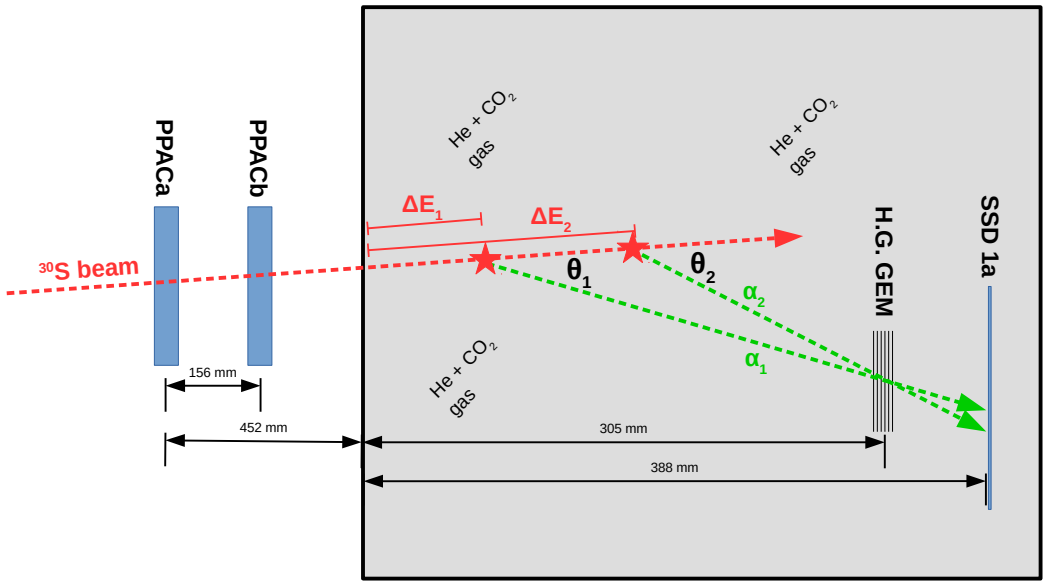

Figure 4.1: Schematic view of the scattering point determination; note it is not drawn to scale, but key distances are shown. In the cartoon, two distinct scattering positions are depicted, where the geometrical measurements of the detectors are identical. However, it is clear the energy loss of the ^{30}S beam $\Delta E_1 \neq \Delta E_2$ (changing the center-of-mass energy), as well as the laboratory alpha scattering angle $\theta_1 \neq \theta_2$, and thus the scattering energy differs, hence the residual alpha particle energy measurement by the SSD cannot be the same. By considering all possible scattering positions and comparing the calculated residual alpha particle energy with the measurement, a unique solution is found within the uncertainties.

also calculate the alpha laboratory energy E_α via Equation B.0.6. We then calculate the alpha particle energy loss up to the SSD and compare this energy with the measured residual energy. The actual kinematic calculations are performed with full relativity using the KaliVeda library written in the ROOT framework; the author has not only checked the source code for accuracy, but even filed several bug reports with the development team to improve the software. We perform this check at each 1 mm of target depth for $1 < Z < 280$, after which point any scattered alpha particles can never have enough energy to reach the SSD; we insist the difference between the calculated and measured alpha residual energy is less than 50 keV and minimize it by testing multiple values of Z.

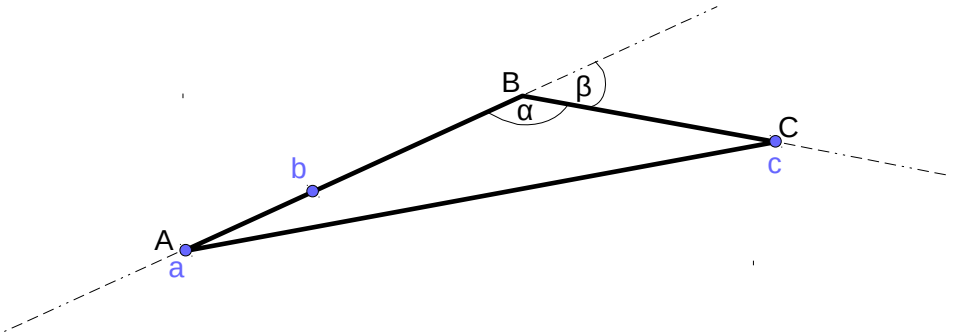

Figure 4.2: The simple triangle ABC is constructed from points a, b and c; although a coincides with A and c with C, b and B do not coincide. We extrapolate a line $\overline{ab}$ to a potential point B to construct the lines $\overline{AB}$ and $\overline{BC}$, and hence the triangle ABC. Point a represents PPACa, b represents PPACb, and c represents the high-gain GEM. B is a possible scattering location, with laboratory scattering angle β. The law of cosines would normally instruct one how to calculate the angle α, which is of no interest, but $\beta = \pi - \alpha$ which is of interest. See the text.

4.1.1 Determination of the scattering angle

We can determine the laboratory scattering angle θ_α from simple geometry. Consider the situation illustrated in Figure 4.2, where the spatial coordinates are determined by PPACa, PPACb, and the high-gain GEM, represented in the figure by the points a, b, and c, respectively. An arbitrary length between two points A and B with known Cartesian coordinates (x, y, z)—represented here as subscripts—can be calculated as

$$\overline{AB} = \sqrt{(B_x - A_x)^2 + (B_y - A_y)^2 + (B_z - A_z)^2}; \tag{4.1.1}$$

of course, the same is true for the lengths $\overline{BC}$ and $\overline{AC}$ with the appropriate substitutions. Calculating the angle α at vertex B between the lines $\overline{AB}$ and $\overline{BC}$ is then

$$\alpha = \arccos\left(\frac{\overline{AB}^2 + \overline{BC}^2 - \overline{AC}^2}{2(\overline{AB} \cdot \overline{BC})}\right), \tag{4.1.2}$$

and then the angle β between the projection of $\overline{AB}$ past B and $\overline{BC}$ is just

$$\beta = \pi - \alpha. \tag{4.1.3}$$

The angle β is the laboratory angle θ_α for a scattering at B; note that for a gas target such as this case, the position of B is depends strongly on Z and thus the same is true of β, unlike an experiment with a solid target. The coordinates of $B(x, y, z)$ are determined by extrapolation from the coordinates of $a(x, y, z)$ and $b(x, y, z)$ which are measured. It is important to keep in mind that as $\overrightarrow{AB}$ is constructed from the beam heavy ion ^{30}S but the vector $\overrightarrow{BC}$ is constructed for the scattered light ion (the non-beamlike ejectile), conversion of θ_α to the conventional θ_{cm} reported in the literature requires an additional deflection by 180° afterwards, as discussed in Appendix B; in a raw calculation this can appear confusing as the angle α is firstly deflected by π to β, transformed, and deflected yet again by π, but these operations are necessary to obtain the θ_{cm} of interest. These two deflections are entirely unrelated to one another: one arises from simple geometry to obtain β while the other arises from a reversal of the axes from kinematic definitions.

4.1.2 Ion track length determination

We calculate the length of the track of the ^{30}S beam using a method like Equation 4.1.1, starting from directly after the entrance window of the TPC chamber and up to the scattering point B. We extrapolate the line $\overrightarrow{BC}$ to the SSD surface according to the geometry of Figure 3.10; this not only gives us the length of the alpha particle's track for calculating its energy loss, but also the hitting position of the SSD, which is necessary to know the appropriate calibration parameters to use for the SSD 1a pad data, as discussed in Section 3.3.

4.1.3 Excitation Function

Summing all the scattering events we found by this method at a binning of 100 keV yields the energy spectrum shown in Figure 4.3. However, more work is required to construct the excitation function, because the solid angle for detecting alpha particles depends on the scattering position—the scattering depth especially—which in turn affects E_{beam} and hence E_{cm}.

To calculate the laboratory solid angle Ω_{lab}, we model it as a rectangular pyramid, in which case

$$\Omega_{\text{lab}} \cong 4 \arcsin\Big(\sin\frac{\alpha}{2}\sin\frac{\beta}{2}\Big), \tag{4.1.4}$$

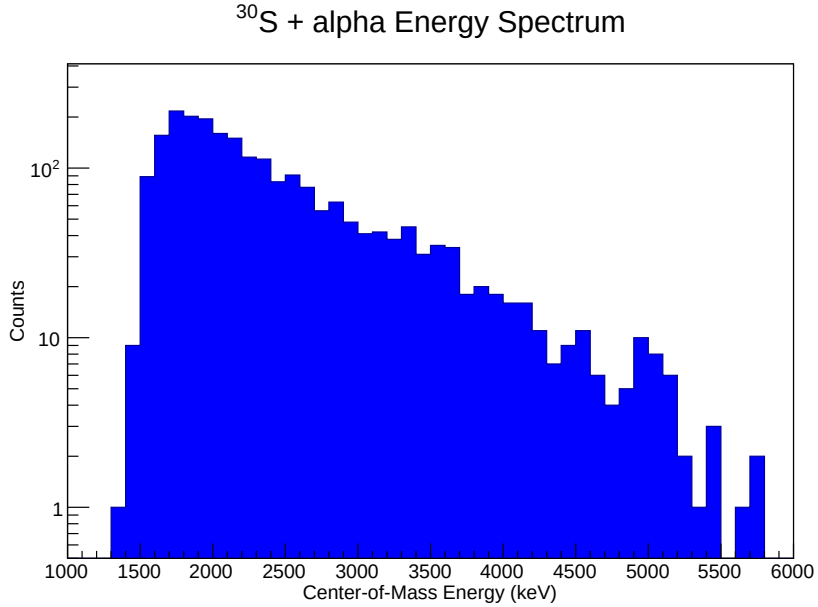

Figure 4.3: Energy spectrum of scattered alpha particles gating on the ^{30}S RIB determined by the kinematic solution. As the high-gain GEM and SSD 1a must both be hit, it is only a portion of the total events which are analyzed. Hints of several resonances can be seen.

where α and β are the angles at the vertex between the two opposite sides. Using the depth of the center of the high-gain GEM, we calculate α and β using the effective observed range for the distribution of alpha-particle tracks in X and Y, respectively. We also calculate the angles α and β using the physical size of the SSD, and for each event, the limiting acceptance was always chosen. Based on the known geometry, Ω_{lab} can be calculated event-by-event at the actual scattering locations. However, we wish to know the center-of-mass solid angle which is

$$\Omega_{\text{cm}} = 4\cos(\theta_\alpha)\Omega_{\text{lab}}. \tag{4.1.5}$$

Ω_{cm} is shown in Figure 4.4 against the center-of-mass energy; unfortunately, the solid angle is just one part of the calculation of the differential cross-section, and the event-by-event Ω itself is not very useful because one firstly needs to know the total number of counts at an energy bin, and dividing each contribution's bin size to the energy spectrum by its own solid angle would not be meaningful. Thus, instead we sum them all together

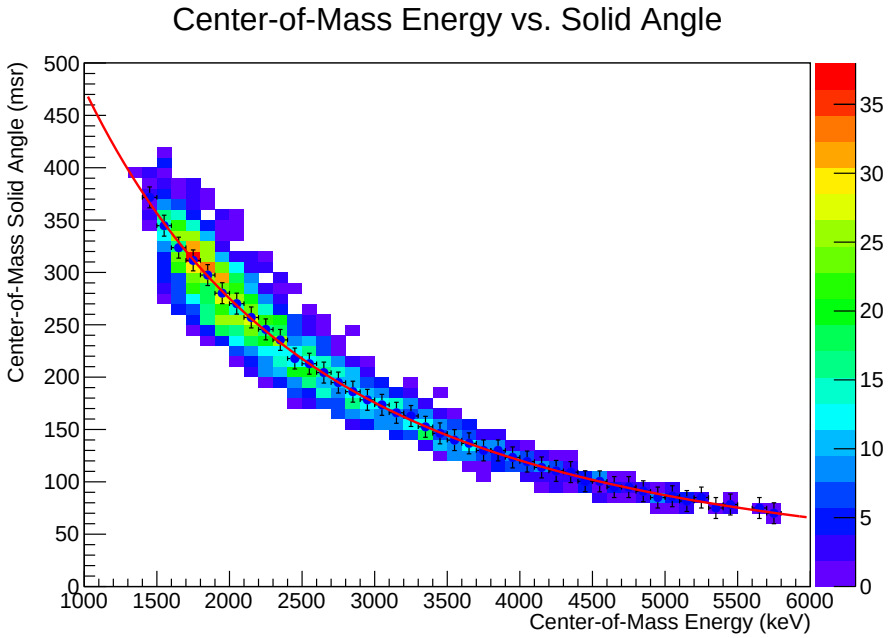

Figure 4.4: Center-of-mass energy vs. solid angle, calculated event-by-event. The data points are drawn at each 100 keV bin for the center-of-mass energy, and simply averaged for the solid angle. The error bars are derived from the binning size. To fit the data, a Landau probability distribution function is shown as the solid red line.

and fit the average solid angle projected for each energy bin with a Landau probability density function to give an empirical function for $\Omega_{\mathrm{cm}}(E_{\mathrm{cm}})$. Although the data clearly show that the scatter increases with smaller E_{cm}, the trend is well-behaved, and as we use an average, any discrepancies from the mean will cancel each other out.

To construct the excitation function itself, we finally need to calculate $\frac{d\sigma}{d\Omega}$, which can be expressed as

$$\frac{d\sigma}{d\Omega} = \frac{Y_\alpha S(E_{\mathrm{beam}})}{I_{\mathrm{beam}} n \Delta E \Delta\Omega} \frac{m_\alpha}{m_\alpha + m_{^{30}S}}, \tag{4.1.6}$$

where

$Y_\alpha =$ Yield of alpha particles at each energy bin, from Figure 4.3.

$S(E_{\mathrm{beam}}) =$ Stopping power of He+CO_2 for ^{30}S from Figure 3.20.

$I_{^{30}\mathrm{S}} =$ Number of ^{30}S beam ions injected. See below.

$n =$ Number density of ^{4}He in the active target. See below.

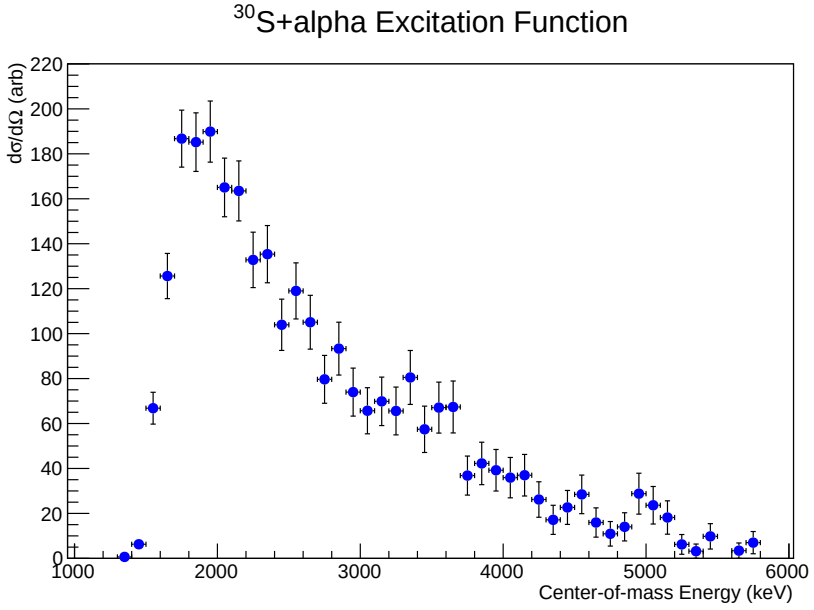

Figure 4.5: Experimental excitation function for ^{30}S alpha elastic scattering. The error bars are only statistical, assuming a Poisson distribution, thus the relative errors are $\sqrt{N}/N$, where N is the alpha particle yield Y_α at a given energy bin. See the text.

$\Delta E =$ Energy bin size, 100 keV.

$\Delta\Omega =$ Solid angle at a given energy bin from Figure 4.4.

The number of injected ^{30}S ions $I_{^{30}\mathrm{S}}$ is derived from the scalers for the PPACa,b coincidence multiplied by the purity of ^{30}S derived from the PPACa vs. Rf_0 downscale histogram (Figure 3.5), which includes a cut for the TPC entrance window for successful injection into the target; it is about one and half billion total ^{30}S ions, for an aggregate purity of 29% and an intensity of 8×10^3 pps. The number density n of ^{4}He in the active target fill-gas can be calculated from the ideal-gas law. The density ρ of the He+CO_2 mixture can be calculated as

$$\rho = \frac{P}{R_s T}, \tag{4.1.7}$$

where P is the gas pressure, $R_s = \frac{R}{M}$ is the specific gas constant with R the ideal gas constant and M as the effective molar mass, and T is the gas temperature. To calculate M we just need the molar mass of ^{4}He (4.003) and CO_2 (44.009) multiplied by their ratios in the gas mixture (by volume) and summed. As the mixture is 90% He and 10% CO_2, then we get effective molar masses of 3.6027 and 4.4009, respectively,

for a summation of 8.0036. We then find the specific gas constant R_s is 1038.833; the pressure is 194.0 Torr or 25860 Pa; the laboratory temperature is 293 K, consistent with the parameters used in the energy loss calculations. The result is $\rho = 0.000085$ g/cm^3; incidentally, it is worth noting this value agrees very well with the one calculated by `enewz` under the same conditions. We then take the mass fraction of ^{4}He in the gas mixture multiplied by its own molar mass multiplied by Avogadro's number yielding a particle density $n = 5.754 \times 10^{18}$.

With all quantities in Equation 4.1.6 known, it is possible to construct the excitation function, the results shown in Figure 4.5. It must be stated that the figure was produced without the active target part of the data, and only the central high-gain GEM data were used from the GEM-MSTPC; however, we demonstrated that it was quite difficult to extract meaningful information event-by-event from the active target beam data acquired in this experiment.

4.1.4 Energy Resolution

A number of different factors can influence the determination of the center-of-mass energy E_{cm}:

- Beam energy spread by $B\rho$: ± 2.3 MeV; see Section 2.3.2.
- Beam energy on-target from straggling: $\sigma = 2.5$ MeV; see Section 3.4.3.1.
- Residual energy of alpha particle, from SSD resolution: ~ 100 keV near 5 MeV; see Section 3.3.
- Straggling of alpha particle: < 64 keV; see Section 3.4.3.2.
- Position determination of out-going alpha in X: 3 mm; see Section 3.4.2.1.
- Position determination of out-going alpha in Y: 0.5 mm; see Section D.1.3.

However, since we use the measurement of the position and residual energy of the out-going alpha particle to impose the kinematic solution, these have the most profound effect on the determination of E_{cm}. For example, as the beam energy varies within its uncertainty, the effect in the calculation is that the determined scattering position

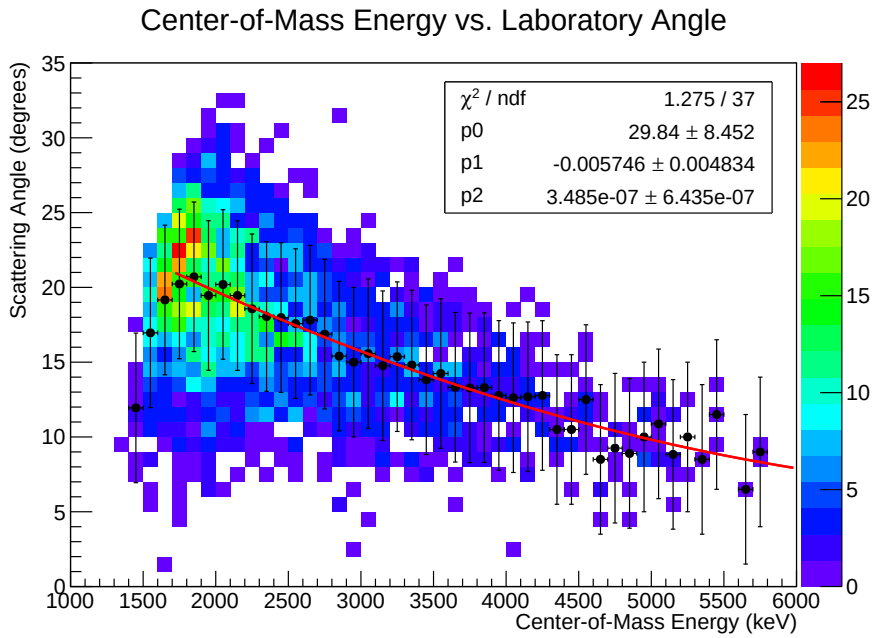

Figure 4.6: Laboratory scattering angle is shown to anti-correlate with the center-of-mass angle, which is expected from the change in scattering depth. Although there is a spread of about ±5°, the average value of θ_{lab} for the projection of each energy bin can be easily fit with a second-order polynomial to give a rough estimate.

shifts according to the measurements of the alpha particle. The kinematic equation for the determination of E_{cm} can be written to only depend on the laboratory energy and scattering angle of the alpha particle, as seen in Equation B.0.6. Considering our case of elastic scattering and only one possible kinematic solution, the kinematic equation yields the relation:

$$E_{\text{cm}} \propto E_{\alpha} \cos^{-2}(\theta_{\text{lab}}). \tag{4.1.8}$$

In order to estimate the uncertainty in θ_{lab} arising from the determination of the alpha particle's position, we need to first estimate the average θ_{lab} as a function of E_{cm}. The laboratory scattering angles for kinematically-selected events as a function of center-of-mass energy is shown in Figure 4.6, which yields a function for $\theta_{\text{lab}}(E_{\text{cm}})$. We then estimate the new angle θ'_{lab} by changing the assumed position of the alpha particle by 3 mm for 1 MeV increments in E_{cm} from 2–6 MeV; the range of $|\theta_{\text{lab}} - \theta'_{\text{lab}}| = \Delta\theta_{\text{lab}}$ was found to be 0.5–1°, increasing with decreasing E_{cm}. Using the outgoing and residual energies of the emitted alpha particles under these kinematic conditions, we estimate the

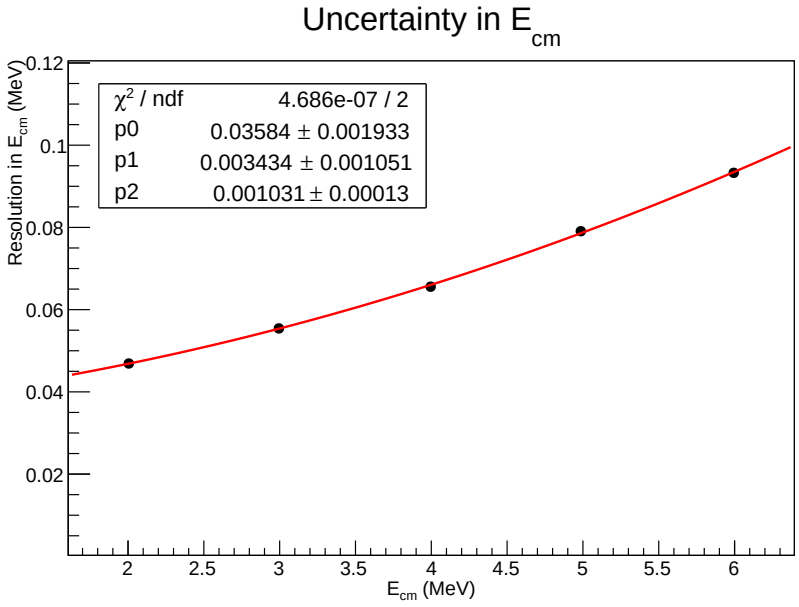

Figure 4.7: Uncertainty in the center-of-mass energy estimated for the present experiment. See the text.

applicable SSD energy resolution and straggling effects contributing to the uncertainty in the measured alpha particle energy ΔE_α. Based on Equation 4.1.8, the uncertainty in the center-of-mass energy $\Delta E_{\rm cm}$ can be expressed as

$$\Delta E_{\rm cm} = E_{\rm cm}\sqrt{\left(\frac{\Delta E_\alpha}{E_\alpha}\right)^2 + 4\left(\frac{\cos(\theta_{\rm lab}) - \cos(\theta'_{\rm lab})}{\cos(\theta_{\rm lab})}\right)^2}. \tag{4.1.9}$$

Finally, we obtained an estimate for the uncertainty of the center-of-mass energy of about 50–100 keV as shown in Figure 4.7; the intrinsic resolution of the SSD had the predominant effect, which was more pronounced at the higher energies. Thus, it can be seen that the energy binning choice of 100 keV is consistent with our achieved resolution.

4.2 R-Matrix Analysis

The R-Matrix method has been widely used in CRIB experiments of elastic scattering to extract resonance parameters from the excitation function [81, 82, 83, 84, 85, 86, 87, 88]. The seminal paper of Lane & Thomas [89] expounded the theory, which significantly im-

proves upon, among other reaction theories, the Breit-Wigner formula given in Equation 1.2.14. Succinctly, the R-Matrix method calculates the interference between the regular and irregular Coulomb functions with the resonances. The resonances are parameterized by their energy E_r (the same as E_cm from elastic scattering), channel i width Γ_i, and the angular momentum transfer ℓ_i. The resonance shape is determined by the entrance channel ℓ_α, the resonance height from the entrance channel Γ_α, and the resonance width depends on total width Γ. The total width is a sum of the proton and alpha widths, as both channels are open; the gamma widths Γ_γ are negligibly small for these highly excited, particle-unbound states. For the case of ^{30}S+α elastic scattering the situation is extremely simplified for the entrance channel, as both the nuclei have a ground-state spin-parity $J^\pi = 0^+$, and so the quantum selection rules dictate a unique resonance J^π for each ℓ_α value—namely that $J = \ell_\alpha$ and the parity is always natural for populated states in ^{34}Ar. For the proton channel, we assumed the lowest ℓ_p allowed would have the predominate contribution. The spin of the proton s_1 is $\frac{1}{2}$ and the spin of the ^{33}Cl ground state s_2 is $\frac{3}{2}$, which can align or anti-align. An example of the lowest-ℓ_p coupling schemes are shown in Table 4.1 up to 4^+ natural-parity states in ^{34}Ar.

Table 4.1: Coupling schemes for states in ^{34}Ar for $J^\pi \leq 4^+$ for the channel ^{33}Cl+p. The lowest ℓ_p is assumed, and not all possible linear combinations are denoted. The spins of the proton and ^{33}Cl $s_1 \oplus s_2 = s$ can align ($\uparrow\uparrow$) or anti-align ($\uparrow\downarrow$), and the same is true for the resulting spin s coupling with ℓ_p to sum $J = \ell_\mathrm{p} \oplus s$.

J^π	ℓ_p	s	$s_1 \oplus s_2$	$s \oplus \ell$
0^+	1	1	$\uparrow\downarrow$	$\uparrow\downarrow$
1^-	0	1	$\uparrow\downarrow$	—
2^+	0	2	$\uparrow\uparrow$	—
3^-	1	2	$\uparrow\uparrow$	$\uparrow\uparrow$
4^+	2	2	$\uparrow\uparrow$	$\uparrow\uparrow$

However, one difficulty encountered in elastic scattering is that the Rutherford cross section is very large at low energies, which is compounded by the fact that the widths shrink as resonance energy approaches the particle separation energy of the compound nucleus. The maximum width of a resonance can be estimated with the Wigner limit [27]

$$\Gamma_{Wi} = \frac{3\hbar^2}{\mu_i R_i^2 P_{\ell_i}}, \tag{4.2.1}$$

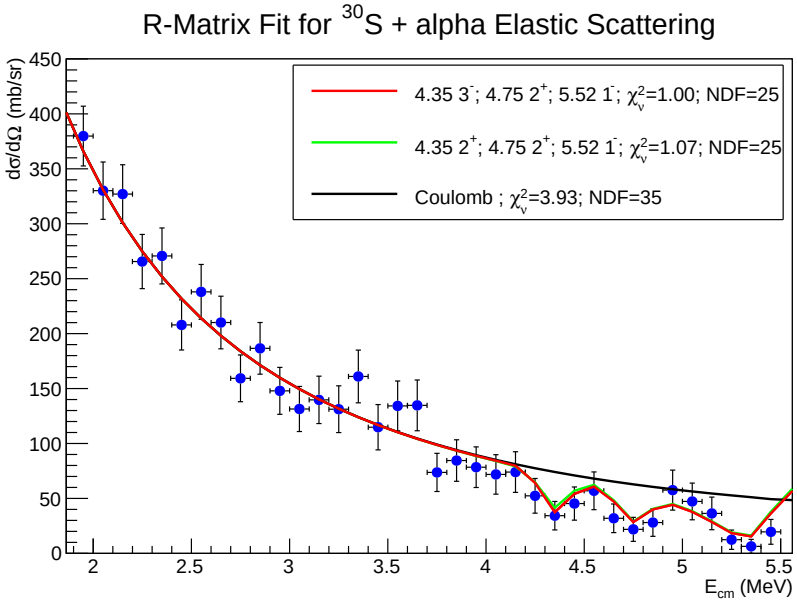

Figure 4.8: ^{30}S+α elastic scattering excitation function. The energy range displayed is the entire set of continuous data in the raw excitation function, except at the lower energy side where the plot is terminated at the point where all the α particles can no longer reach the detector from stopping in the fill gas. The bumps observed around 3.5 MeV correspond to a region of large alpha-background, as depicted in Fig. 4.10. Three resonant-like structures are seen between $4 < E_{\rm cm} < 5.5$ MeV. The data are fit with a multi-channel (α and p), multi-level R-Matrix formalism, and the results for a selected combination of ℓ_α transfers are shown (though all combinations up to $\ell_\alpha \leq 4$ were tested, and $\ell_\alpha = 5, 6$ never gave good fits). The adopted parameters of these three newly-discovered resonances are shown in Table 4.2. Several other fits for various permutations of ℓ_α with poor fits are shown in Figure 4.9. See the text.

where μ_i is the channel reduced mass (see Section 1.2), $R = 1.2(A_1^{1/3} + A_2^{1/3})$ fm is the parameterized channel radius, and P_ℓ is the channel penetrability.

In practice, it means that without high energy resolution and/or statistics, many features will be obscured by the Coulomb peak, as seen in our excitation function in Figure 4.5 below 3–4 MeV. Any resonances we introduced in this region even with Γ_α at is maximum near the Wigner limit made no observable change to the spectrum in the R-Matrix calculation of the excitation function unless we also set $\Gamma_p = 0$. Conversely, higher than about 5.6 MeV, our solid angle has become very small and very few events were detected, and they fail to be continuous as seen in Figure 4.3. In conclusion, we focus our analysis on the region between 4–5.6 MeV.

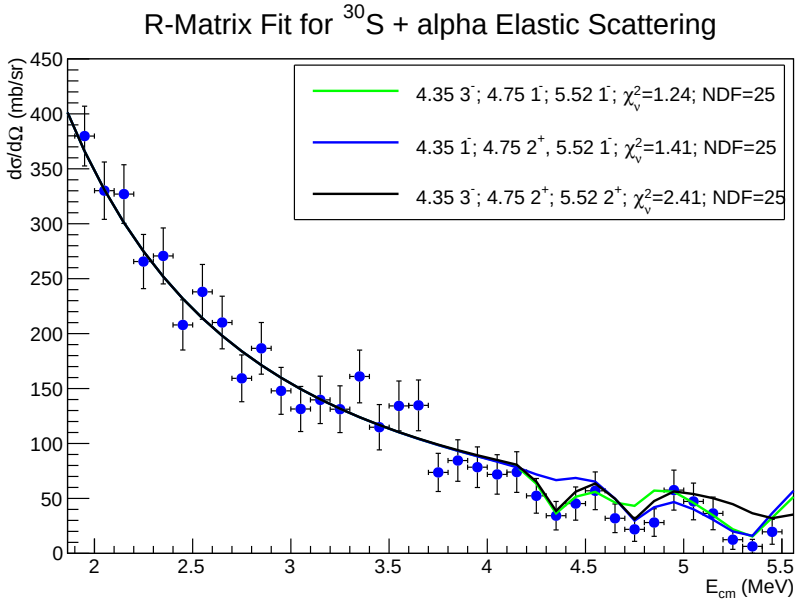

Figure 4.9: ^{30}S+α elastic scattering excitation function, showing several combinations of ℓ_α not shown in Figure 4.8 which give poor fits. See the text.

Table 4.2: Adopted level parameters for new states in ^{34}Ar along with calculations of the Wigner limit from the present work, derived from the best fit in Figure 4.8. The relationship between E_r and E_ex is the Q-value of 6.739 MeV for the $^{30}\mathrm{S}(\alpha,\mathrm{p})$ reaction; the uncertainty is from Figure 4.7, except for the 5.52 MeV resonance where we added the resolution uncertainty in quadrature with a systematic uncertainty of 100 keV for possible effects of not including higher-energy resonances. The uncertainty in the alpha-widths is assumed to be 50% from systematics, except for the 5.52 MeV resonance which has a much larger uncertainty. The uncertainty for the proton-width is unquoted owing to the model-dependence introduced with the parameterisation of ξ. See the text.

E_r (MeV)	E_ex (MeV)	ℓ_α	J^π	Γ_α (keV)	Γ_p (keV)	θ^2_α %
4.35 ± 0.07	11.09 ± 0.07	2, 3	$(2^+, 3^-)$	$0.8^{+0.4}_{-0.4}$	1.3	15
4.75 ± 0.08	11.49 ± 0.08	2	2^+	12^{+6}_{-6}	9.7	30
5.52 ± 0.13	12.26 ± 0.13	1	(1^-)	290^{+0}_{-200}	65	> 99

We used the SAMMY8 code [90] to perform multi-channel, multi-level R-Matrix calculations, folding the resulting theoretical excitation function with the achieved energy resolution (Figure 4.7) using $\theta_\mathrm{cm} = 160°$ with a 10° spread. As was shown in Figure 1.7, since there are no known resonances in this region, we initially attempted to fit the data with pure Coulomb scattering; we found $\chi^2_\nu = 3.93$ with 35 degrees of freedom (see

Appendix C). It was necessary to universally scale the experimental cross section by a factor of 2.0 to match the calculated Rutherford cross section in the lower energy region, as discussed next in Section 4.3. Three resonance-like structures can be identified. To estimate the proton width $\Gamma_{\rm p}$, we considered the spectroscopic factor θ_i^2 for each channel,* and introduce a universal spectroscopic ratio ξ for the three resonances:

$$\theta_\alpha^2 = \Gamma_\alpha / W_{\Gamma\alpha}, \tag{4.2.2}$$

$$\theta_{\rm p}^2 = \Gamma_{\rm p} / W_{\Gamma p}, \tag{4.2.3}$$

$$\xi \equiv \theta_{\rm p}^2 / \theta_\alpha^2, \tag{4.2.4}$$

$$\therefore \Gamma_{\rm p} = \xi \theta_\alpha^2 W_{\Gamma p}. \tag{4.2.5}$$

A similar approach was taken in the analysis of ^{21}Na+α elastic scattering performed at CRIB [91]. Although the value of $\Gamma_{\rm p}$ derived this way may have a large uncertainty and model-dependence, it is physically unrealistic to perform a single-channel analysis when the proton width is known to be non-zero so far above the proton separation energy.

For the three resolved resonances, the goodness-of-fit was evaluated with χ_ν^2. A computer algorithm written by the author was employed to co-vary all input parameters ($E_{\rm r}$, ℓ_α, & Γ_α for each resonance, and ξ) in a wide range of sets to find the global minimum of χ_ν^2 within the parameter space, indicated by the solid red line in Figure 4.8. The best fit for $\xi = 0.8\%$, and the value of θ_α^2 was found to correlate with $E_{\rm r}$ (15%, 30%, and $> 99\%$, respectively, for the three resonances), as shown in Table 4.2. The resonance energies were co-varied with each other over 200 keV as well as against all other parameters. θ_α^2 was varied in 1% steps, and ξ was varied from very small values up to 10%.

The best fit with $\chi_\nu^2 = 1.00$ is distinct from pure Coulomb scattering by more than 12 standard deviations,† indicating bona fide discovery of these three resonances. For 25 NDF, one expects $\chi_\nu^2 \approx 0.8 \pm 0.28$; however this theoretical limit may be smaller than the practical experimental limit, considering the error bars are only statistical and do not include any systematic uncertainties. As we had no way to subtract the background

*The reader is advised to be cautious, as θ_α^2 is the standard notation for the alpha spectroscopic factor, but θ_α is used as the scattering angle of the alpha particle in other portions of the thesis.

†Recall standard deviation of the reduced chi-square quantity is $\sqrt{2/\nu}$.

near 3.5 MeV, a larger systematic uncertainty in this region would tend to reduce our experimental χ^2_ν towards the direction of the theoretical limit, but we have no way to quantify the magnitude of the systematic uncertainty outside the overlaying statistical uncertainty. Removal of any single resonance (not depicted) can cause deviations 5σ or higher, if the full energy scale shown is used (*e.g.* if we don't cut out higher energy data). The resonance at 4.35 MeV can be tentatively assigned as $J^\pi = (2^+, 3^-)$; the resonance at 4.75 MeV can be firmly assigned as $J^\pi = 1^-$; the resonance at 5.52 MeV is tentatively assigned as $J^\pi = (-1)$. Confirmation on these assignments for ℓ_α can be seen in Figure 4.9, where the fits deviate by 1σ or more from the expectation.

The parameters deduced for the highest-energy resonance via R-Matrix analysis are subject to systematic uncertainties, owing to the inability to include the interference from higher energy resonances outside the experimental measurement; we expect that the resonance energy may shift down by as much as 100 keV, fits in the range of $\ell_\alpha = 1\pm1$ might be acceptable (or even preferred), and θ^2_α may decrease by a factor 2–3, which we consider as systematic errors for this last resonance. These systematic uncertainties for the 5.52 MeV resonance are estimated from the case when the data were fit with only two resonances and the data were cut at 5.1 MeV; in that case, the 4.75 MeV resonance had $\theta^2_\alpha \approx 1$, was 90 keV higher, and had only one possibility for ℓ_α, namely $J^\pi = 1^-$. Certainly, the widths for the 5.52 MeV resonance shown in Table 4.2 are not realistic with our adoption of ξ since it cannot both have $\theta^2_\alpha \approx 1$ and $\Gamma_p \neq 0$. Another possibility is the 5.52 MeV resonance is comprised of more than one unresolved resonances that all have large alpha-widths, consistent with an unphysical R-Matrix calculation test allowing the spectroscopic factor to exceed unity, which was optimized as $\theta^2_\alpha = 1.5$.

4.3 Scaling factor

As mentioned above in Section 4.2, a scaling factor of 2.0 was applied universally to the experimentally-deduced cross-section in Figure 4.5 to match the Coulomb scattering cross-section from the R-Matrix calculation, shown in Figure 4.8. As the use of this scaling factor may raise doubts about the validity of the analysis and the resonances introduced, we carefully investigate its origin.

4.3.1 Reliability of experimental inputs

Each term used in calculating the differential cross section in equation 4.1.6 was carefully checked for any possible errors, namely the number density of helium atoms n, the stopping power of the beam $S(E_{\text{beam}})$, the number of injected beam ions $I_{^{30}\text{S}}$, the changing solid angle $\Delta\Omega$, the energy bin size ΔE, and the yield of alpha particles Y_α.

The number density of ^{4}He atoms in the target employed cannot be changed by any physical argument, unless we are willing to accept the gas was at 600 K or that pressure reading from the gauge was overestimated by 100% (which is unlikely because it was consistent with two other pressure gauges), which are both preposterous. We reiterate that the gas density calculated from the nominal laboratory conditions by standard thermodynamic methods by hand is consistent with the density utilized in all energy loss calculations. A factor of two error here would have significant effects on the energy loss calculations as well as the resulting Bragg curves inconsistent with the experimental data, particularly considering the same change for helium would apply equally to CO_2 which induced significant energy loss for the heavy ions. Although our mixed research gas was delivered by percent volume (which we have confirmed with the company), some research gases are also delivered by percent mass; should we be mistaken and the gas was in fact 10% CO_2 by mass, there would be even more helium atoms in the target, reducing the experimental cross section by yet another factor of two.

These arguments for the accuracy of the number density of helium atoms apply similarly for several inputs to the calculation of the energy loss of ^{30}S used to deduce the stopping power. These kinds of energy loss calculations are generally known to be accurate to the order of 10% or better; a much lower stopping power for ^{30}S in He+CO_2 gas would be required, yet from the Bragg curve we experimentally determined its stopping position. Moreover, we found that the methods for calculating energy loss in this thesis were consistent with the ^{22}Mg experiment discussed in Appendix H, where the silicon detector was absolutely calibrated for heavy ions with no known sources of systematic error.

The determination of the number of incident ^{30}S ions is determined by the recorded PPAC scalers for each run, multiplied by the measured ^{30}S purity including a cut on the successful injection into the target, which should be the most reliable method. It is also

possible to integrate the number of ^{30}S ions in the downscaled spectrum for each run, and multiply by the downscaling factor of 2.2×10^4, although the downscaling module with such a large setting may not give an accurate result; nevertheless, a discrepancy of merely 7% was found between the two methods, which cannot account for the required factor of two. We also monitored the ^{30}S beam intensity during the experiment using the standard CRIB DAQ system which is entirely independent of the DAQ used for the present analysis; the ^{30}S beam intensity and purity have a good agreement between the two systems.

We checked the method of calculating the solid angle, as well as the absolute efficiency of the silicon detector and high-gain GEM, considering the known intensity of the standard alpha source used in off-line calibration runs; within the errors of these calculations, we found $\eta > 99\%$ for the silicon detector (except strip 8 that was radiation damaged and has $\eta \approx 50\%$ but is never in coincidence with the high-gain GEM anyway), and $\eta > 90\%$ for the high gain GEM. The high-gain GEM pad multiplicity is consistent with its high efficiency determined here; that is, when an event is seen, all six functioning backgammon pads provide a signal in nearly all cases. It is noted that several geometries were employed in offline testing, with a variety of different distances between the detector and the alpha source, and the solid angles calculated agree with those used in the analysis of the physics data.

The energy bin size is simply a user-set input for the histogramming; it is confirmed to be 100 keV bin size, which is easily seen by an inspection of Figure 4.3.

4.3.2 Detected number of α particles

Ruling out the other possibilities leads us to inspect the yield of alpha particles measured, Y_α. One interesting observation is that in the time of flight of the scattering system (ToF: SSD stop, PPACa start) versus SSD energy spectrum, a clear locus of elastic scattering events are selected in the kinematic solution, but there are about four times more particles in the same locus if one only requires the SSD to trigger in coincidence with ^{30}S ions in the PPACs, as shown in Figure 4.10. The solid angle of the right side of the central high gain GEM is about 50% that of the SSD 1a, and the Rutherford cross section is known to go as $(\sin^4 \frac{\theta}{2})^{-1}$, indicating it does not change appreciably over a

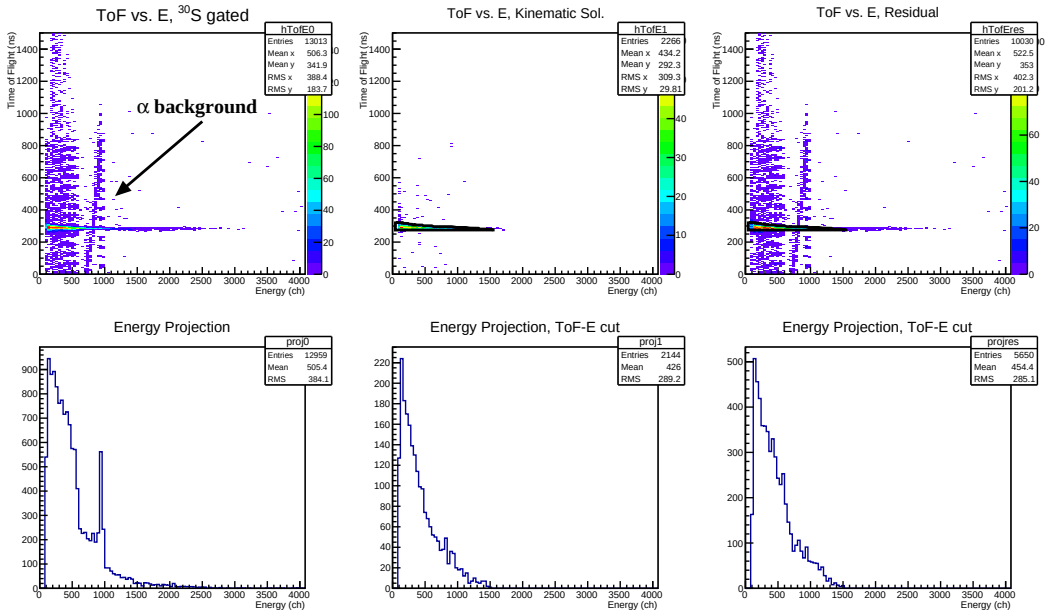

Figure 4.10: The top panels show the residual light ion energy as measured by SSD 1a on the abscissa and the ToF with PPACa as the start and the SSD as the stop on the ordinate. The left panels show only the case when the SSD 1a is hit and the PPAC is gated on ^{30}S; the center panels show the events selected by the kinematic solution, which includes virtually all events with more than one pad firing in the central high gain GEM; the *upper* right panel is a residual of the two (left minus center). The lower panels are energy projections of the upper panels, respectively, where the center and right projections are also gated on the cuts drawn in the ToF-E spectra. A clear background is seen near 1000 ch in the SSD energy, corresponding to light ions in the cocktail beam or created as beam background. The upper left panel, in particular, shows the light ions at a spacing corresponding to the cyclotron RF setting. There are no remarkable differences between the lower right projection and the central projection besides some features which are attributed to background contributions. See the text.

small change ($\approx 10°$) in θ. This implies that about half of the events in the ToF-E locus should be in coincidence with the high gain GEM. Comparing the energy projections of this locus in the case with and without the kinematic solution shows no obvious difference in the structure (besides some additional background events seen clearly in the raw spectrum). However, a similar projection to the ToF shows a depletion of events with slightly lower ToF inconsistent with merely a small change in scattering angle.

In one calibration run, we shifted the alpha particles coming in the cocktail beam with the Wien filter directly over the high gain GEM. However, the number of events with high gain GEM data were only about 50–60% the number of alpha beam events

recorded in the SSD. Again in this case, the timing structure of events with and without the high gain GEM data showed drastically different patterns.

We find that the yield of alpha particles used in the calculation of the experimental differential cross section is lower by a factor of 2 owing to a deficiency in the high gain GEM, which only recorded data for around 1/4 of the events in the ToF-E locus, which should be about 1/2, and a similar situation with the alpha beam. The cause may be a problem of the flash ADC buffer filling/readout for a given module which is supersensitive to the event timing.

Finally, we observed that the recorded Bragg curves were often mismatched with the PPAC beam data in the ^{22}Mg experiment, which used the same setup. The situation appears rather complicated, but suggests there is a very critical relationship between the beam triggering condition with the PPACs and how the active target system and DAQ obtain and record the data — sometimes the event-by-event data looked perfectly normal, and sometimes there was clearly no relationship between the PPAC data and the active target beam data in a given event. While this problem does not occur in the ^{30}S beam data set, the origin is unclear as the triggering conditions and DAQ circuits were schematically the same.

It is concluded that all contributions to the differential cross section were checked carefully for their accuracy, and there does not appear to be a significant systematic error introduced in the above correction to the alpha particle yield to match the Rutherford cross section; the statistical error was scaled accordingly.

4.4 Possible sources of background

The main sources of background could be alpha particles produced at F0 satisfying the $B\rho$ selection as well as contributions from inelastic scattering, since as discussed in Section 2.4.1 the ^{30}S beam is well below the Coulomb barrier of the quenching gas in the active target. The bumps seen in the excitation function around 3.5 MeV in Figure 4.5 correspond to a region with a significant background of beam-like alpha particles, which are clearly observed in the ToF-E spectrum of Figure 4.10, and as discussed in Section 4.2 could not be reproduced by introducing resonances, as the widths at this excitation

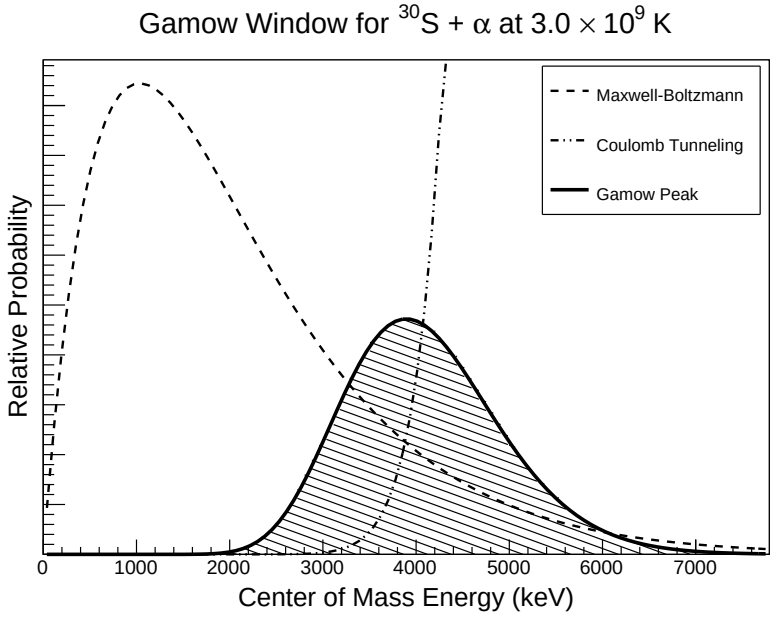

Figure 4.11: Gamow window for ^{30}S+α at a temperature of 3 GK. Resonances near 4.5 MeV should have a strong contribution to the reaction rate at these stellar energies.

energy are too small. During the experiment, no background runs were taken (since this would necessitate changing the active target fill-gas and subsequently its operational conditions), and so this source of background cannot be subtracted in a straightforward manner. However, most of these beam-like alpha-particles are confined to this particular energy region, and the main effect is to pull the best-fit experimental χ^2_ν away from the theoretical limit. As for possible contributions from inelastic scattering, the first excited state of ^{30}S is relatively high at $E_{1x} = 2.21$ MeV and with a spin-parity of 2^+. The increased scattering threshold as well as the requirement for $\ell \geq 2$ from the angular momentum selection rules indicates that the widths, which decrease with increasing ℓ as shown in Equation 4.2.1, suggesting a significantly lower cross-section than elastic scattering. For example, in other studies of alpha elastic scattering, this contribution was found to be less than 10% [81, 86].

4.5 Calculation of the ^{30}S(α, p) reaction rate

As we extracted the resonance energies E_r, spin-parities J^π, alpha widths Γ_α, and proton widths Γ_p for several states as shown in Table 4.2, we can calculate the resonant reaction

rate given in Equation 1.2.16. For our new states, we calculate the resonant reaction rate exactly, using the reduced widths precisely via Equation 1.2.17. Although the resonances we found are outside the Gamow window of 1.3 GK near the peak energy of X-ray bursts, as shown in Figure 1.2, they are near the center of the Gamow window at 3 GK as shown in 4.11.

However, we should take advantage of new data from the ^{36}Ar(p, t) experiment detailed in Appendix K. As the RCNP data only provide resonance energies, some artificial assumptions are required about the quantum properties; we set $J^\pi = 0^+$ and $\gamma = \Gamma_\alpha = 0.5W_\alpha$, considering this a best-case scenario based on the present experimental results. This latter assumption is justified considering that it is normal to assume $\gamma = \frac{\Gamma_\alpha \Gamma_p}{\Gamma_\alpha + \Gamma_p} \approx \Gamma_\alpha$ when $\Gamma_\alpha \ll \Gamma_p$, which we can infer from the Wigner limits calculated in Table K.1 and our value of $\xi = 0.8$, and it would be unrealistic to assume every resonance they observed had the full alpha width. While the contribution from an individual resonance calculated in this manner will be unreliable, the sum of these contributions can be considered an upper limit under an extreme assumption. It should be noted that $\omega\gamma$, the resonance strength, is to first-order independent of the spin-parity when parameterizing the widths based on the Wigner limit (as the penetrability includes the transfer of ℓ), decreasing the width γ while increasing the spin factor ω in the reaction rate. This implies that our arbitrary selection of $J^\pi = 0^+$ does not have a significant effect on the calculated reaction rates.

The calculated rates are plotted and compared against the NON-SMOKER [92] Hauser-Feshbach statistical model in Figure 4.12. The XRB model of the double-peaked structure required a reaction rate a factor of 10^2 greater than the statistical model to quench the proposed waiting point near ^{30}S, as was shown in Figure 1.9. Our new reaction rate evaluated with all known level structure of ^{34}Ar is inconsistent with a reaction rate deviating more than a factor of around 2 larger than the statistical model rate. The work demonstrates that while strong alpha resonances exist above the alpha-threshold in ^{34}Ar, they do not cause the stellar reaction rate to increase in a significant manner, vindicating the ^{30}S waiting point evidenced in many models assuming the statistical reaction rate. This finding is contrary to the observation that in the lower mass regions, thermonuclear rates of (α, p) and (α, n) reactions on $T_z = \pm 1$ nuclei are dominated by

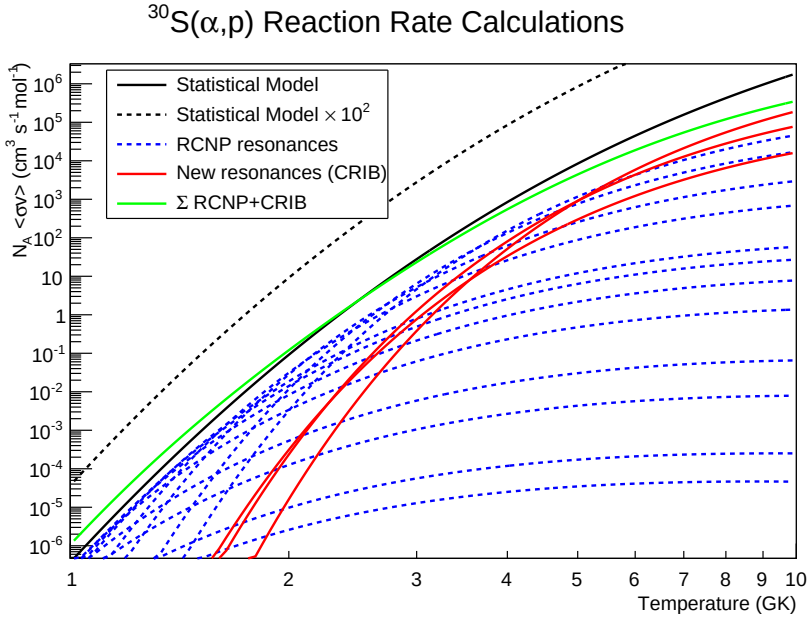

Figure 4.12: Calculation of the reaction rate from the $E_R = 4.36, 4.86$ resonances (red and blue, respectively) compared with the statistical model (black). Despite the fact that the resonances have Γ_α approaching the Wigner limit, their contribution to the stellar reaction rate is much lower than the total rate predicted by the statistical model of [92].

isolated, alpha-cluster resonances, and the statistical model may be considered reliable for $A \geq 30$ for such situations. These are the first experimental results to verify the statistical model reaction rate for $^{30}\mathrm{S}(\alpha, \mathrm{p})$, consistent with many XRB models using that rate to indicate ^{30}S is a critical waiting-point nucleus in the nuclear trajectory to higher mass.

4.6 Discussion

The present work is the first to experimentally determine the quantum properties of highly excited states above the alpha-threshold in ^{34}Ar, which all had large alpha-widths. Our finding is consistent with the expectation from the cluster-threshold rule [93]. In the future, the experimental observation of further excited states above the alpha-threshold may lead to an understanding of macroscopic band structure.

However, the stellar reaction rate calculated based on all known level-structure of ^{34}Ar did not deviate appreciably from the statistical model. This result is in stark

contrast to the measurement of the time-reversal $^{33}\mathrm{Cl}(\mathrm{p},\alpha)$ reaction which found the cross section to significantly exceed the statistical model calculation at energies above the XRB stellar energies [69], although only an upper limit was placed near the energy region overlapping with our study.[‡] Our results are consistent with the presently-accepted $^{30}\mathrm{S}(\alpha,\mathrm{p})$ reaction rate, indicating that it is a significant waiting point nucleus. We found that even resonances at high excitation energy with large alpha widths approaching the Wigner limit do not cause the stellar reaction rate to significantly deviate from the statistical model predictions.

[‡]Preliminary and unpublished results of other similar time-reversal studies for other reactions involved in the αp-process all showed rates lower than the statistical model calculation, and it would be very interesting if the $^{30}\mathrm{S}(\alpha,\mathrm{p})$ reaction is exceptionally different.

Chapter 5

Conclusions

We performed the first measurement of ^{30}S+α resonant elastic scattering to investigate the astrophysically interesting ^{30}S(α, p) stellar reaction rate. The ^{30}S(α, p) reaction is important to type I x-ray bursts (XRBs), where burst models indicate that it contributes more than 5% of the total energy generation, influences the crustal composition which in turn affects subsequent bursts, and may explain rare bolometrically double-peaked bursts as a result, all depending on its precise rate. Thus far, only the statistical model could be used to estimate the ^{30}S(α, p) thermonuclear reaction rate, without supporting knowledge of the level structure of the compound nucleus ^{34}Ar, where alpha resonances were expected to play a key role.

We conducted a measurement of ^{30}S+α in inverse kinematics using a radioactive ion beam (RIB) and an active target in search of resonances with large alpha widths. It was the first ^{30}S RIB ever produced for such a measurement, arriving on-target at 1.6 MeV/u, 30% purity, and 10^4 particles per second. Although the GEM-MSTPC drift time was found to provide better than 1 mm position resolution, we found fundamental issues with the total charge collection of the backgammon-type readout pattern, where the charge collection had an unexpectedly strong dependence on ionizing radiation position and inclination angle. Despite the fact that the active target beam energy-loss and backgammon data had too large an uncertainty to produce a reliable elastic scattering excitation function event-by-event, we can be very confident in the derived ^{30}S stopping power in the He+CO_2 active target fill-gas and thus the deduced center-of-mass energies.

The high-gain region of the active target provided energy-loss and three-dimensional position information for outgoing α particles, albeit over a limited angular range. Using that data along with the PPAC and SSD data, we solved the kinematic equation to produce the first excitation function for alpha resonant elastic scattering of ^{30}S, and several new resonances were observed with large alpha spectroscopic factors.

We performed the first calculation of the $^{30}\mathrm{S}(\alpha,\mathrm{p})$ stellar reaction rate based on experimental level-structure of ^{34}Ar and found it did not deviate from the statistical model calculation by more than a factor of two over astrophysical temperatures 1–3 GK, despite the inputs having sizable alpha widths. However, very little is known about the resonances within the XRB stellar energies, and we could only estimate their possible contributions to the total stellar reaction rate; furthermore, there may be yet unknown resonances not strongly populated by the $^{36}\mathrm{Ar}(\mathrm{p},\mathrm{t})$ reaction. Resonances in this region should be explored in the future to determine their possible impact on the $^{30}\mathrm{S}(\alpha,\mathrm{p})$ stellar reaction rate. There was also a large discrepancy between our results and the time-reversal study, which should be elucidated. Ideally, improvements in RIB production and detector technology will enable a direct measurement of the $^{30}\mathrm{S}(\alpha,\mathrm{p})$ reaction rate near stellar energies in the future.

Appendix A

Stellar Hydrogen Burning

Hydrogen burning in stars is generally accomplished via various cycles which have the net result of converting protons into helium nuclei; which cycles operate depend not only on the thermodynamic conditions such as pressure and density, but also the mass fraction Z of heavier nuclei in the cases of catalytic burning. Figure A.1 shows the contribution to stellar luminosity for a main sequence star by the pp-chains (introduced in Section A.1) and the CNO cycles (introduced in Section A.2.1) depending on stellar mass and metallicity. Regardless of the particular reaction sequence, schematically hydrogen burning occurs either as

$$4\mathrm{p} \rightarrow {}^{4}\mathrm{He} + 2e^{+} + 2\nu_e \quad (Q = 25.71 \text{ MeV}) \tag{A.0.1}$$

or

$$4\mathrm{p} + 2e^{-} \rightarrow {}^{4}\mathrm{He} + 2\nu_e \quad (Q = 26.73 \text{ MeV}). \tag{A.0.2}$$

The first reaction A.0.1 is much more typically encountered and involves two β^{+} decays; reaction A.0.2 only takes place at high density and involves two electron captures. The second case is omitted in this discussion, as investigations have shown it to have little bearing on the present work.

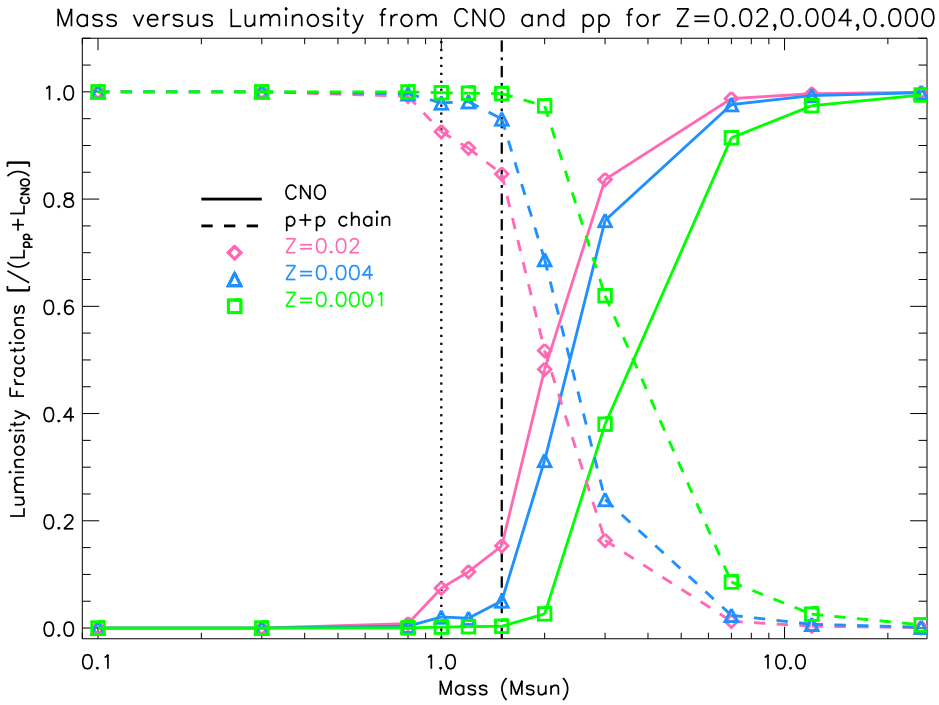

Figure A.1: The plot shows stellar mass (in units of solar mass) versus the luminosity fraction for main-sequence hydrogen burning for various metallicities, produced by Dr. S. E. Malek. For many years, $Z = 0.02$ was considered solar metallicity [94], although this is now believed to be an over-estimate by a factor of two [16]. It can seen that for a star like our Sun (the black dotted line), the pp-chains dominate the contribution to luminosity, but for a star of the same metallicity at higher mass, the CNO cycles quickly make a significant contribution (1.5 $M_\odot$ is shown as the black dash-dotted line, where the CNO contribution is already nearly 20% of the total for $Z = 0.02$). Data to create the plot are taken from EZ-Web [95].

A.1 The Proton-Proton Chains

When the mass fraction of catalytic material is too low or the temperature is not sufficiently high to overcome the Coulomb barrier between protons and the catalysts, hydrogen burning proceeds via the *pp-chains*. The pp-chains begin by converting hydrogen into ^{3}He via

$$p(p, e^+\nu_e)d(p, \gamma)^3\mathrm{He}, \tag{A.1.1}$$

and ^{4}He is then produced through a number of competing branches:

$$^3\mathrm{He}(^3\mathrm{He}, 2p)\alpha, \tag{A.1.2a}$$

$$^3\mathrm{He}(^4\mathrm{He}, \gamma)^7\mathrm{Be}(e^-, \nu_e)^7\mathrm{Li}(p, \gamma)\alpha, \tag{A.1.2b}$$

$$\text{and } ^3\mathrm{He}(^4\mathrm{He}, \gamma)^7\mathrm{Be}(p, \gamma)^8\mathrm{B}(e^+\nu_e)^8\mathrm{Be} \rightarrow 2\alpha, \tag{A.1.2c}$$

which are called the *pp I branch* (A.1.2a), *pp II branch* (A.1.2b), and *pp III branch* (A.1.2c), respectively. Hydrogen burning in the core burning of massive stars or in shells, however, occurs mainly via the CNO cycles.

A.2 The CNO Cycles

The CNO cycles utilize carbon, nitrogen, oxygen, and fluorine as catalysts to synthesize hydrogen into helium. These reaction chains can generally be grouped into two sets according to the temperature regimes in which they turn on. The cold CNO cycles occur in static stellar hydrogen burning, whereas the hot CNO cycles generally occur in explosive hydrogen burning. These cycles, as well as some relevant alpha-induced reactions, are shown schematically in Figure A.2.

A.2.1 Cold CNO Cycles

The cold CNO cycles take place on timescales where β^+ decays are faster than proton capture rates. Thus, the individual cycles have timescales set by the proton capture with the smallest cross-section—usually the one with the lowest Q_p. The cold CNO reaction network is:

$$^{12}\mathrm{C}(p, \gamma)^{13}\mathrm{N}(e^+\nu_e)^{13}\mathrm{C}(p, \gamma)^{14}\mathrm{N}(p, \gamma)^{15}\mathrm{O}(e^+\nu_e)^{15}\mathrm{N}(p, \alpha)^{12}\mathrm{C}, \tag{A.2.1a}$$

$$^{15}\mathrm{N}(p, \gamma)^{16}\mathrm{O}(p, \gamma)^{17}\mathrm{F}(e^+\nu_e)^{17}\mathrm{O}(p, \alpha)^{14}\mathrm{N}, \tag{A.2.1b}$$

$$^{17}\mathrm{O}(p, \gamma)^{18}\mathrm{F}(e^+\nu_e)^{18}\mathrm{O}(p, \alpha)^{15}\mathrm{N}, \tag{A.2.1c}$$

$$\text{and } ^{18}\mathrm{O}(p, \gamma)^{19}\mathrm{F}(p, \alpha)^{16}\mathrm{O}. \tag{A.2.1d}$$

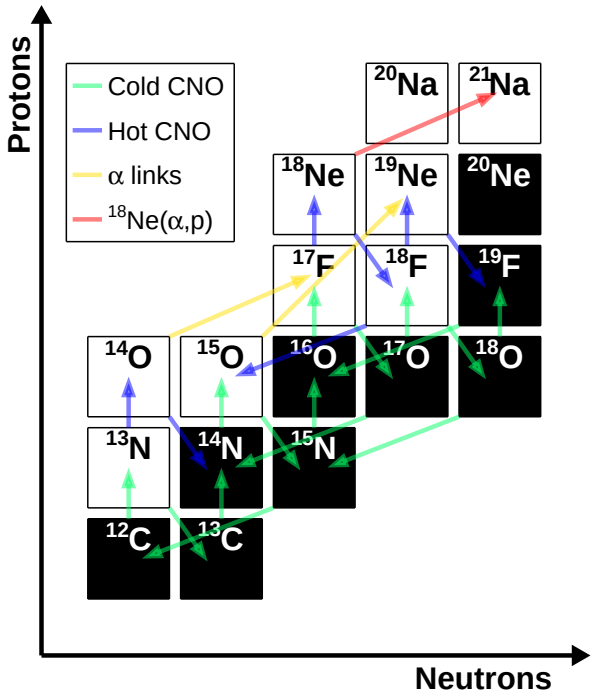

Figure A.2: Schematic of the CNO cycles and associated helium-induced reactions, produced by the author. The plot follows the traditional chart of nuclides, where the ordinate shows the neutron number and the abscissa proton number, and each box represents a unique nuclear species. Stable species are filled in black, whereas white boxes represent β^+-unstable radioactive species. Arrows show different reactions and decays linking the nuclear species and their direction. The green arrows show nuclear transmutations in the cold CNO cycles, the blue arrows reactions and decays in the hot CNO cycles, and alpha-induced reactions are in yellow and red. The colors correspond somewhat with the temperature-density conditions of Figure A.3, although transmutations at lower temperature or density are always possible, although they may not dominate the flow.

The limiting reaction in the CN cycle A.2.1a is ^{14}N(p,γ) [96], which is about two orders of magnitude stronger than the limiting reaction in the ON cycles A.2.1b-d ^{16}O(p,γ) [97]. The branching ratio between the CN and ON cycles is thus determined by the ratio of the rates of the reactions ^{15}N(p,γ)^{16}O/^{15}N(p,α)^{12}C [98], and an equilibrium is established [99].

Material can breakout from the CNO cycles via

$$^{19}\mathrm{F}(p,\gamma)^{20}\mathrm{Ne}, \tag{A.2.2}$$

because the reaction flow past ^{20}Ne is irreversible under the thermodynamic conditions under which the cycles operate. The conditions for the cold CNO cycles are $T \approx 2-13\times 10^7$ K in main sequence stars with densities $\rho \approx 2\times10^3 - 2\times10^5$ kg m^{-3} [96, 100], and $T \approx 5-8\times10^7$ K in hydrogen shell burning at densities $\rho \approx 20$ kg m^{-3} [101]. At higher temperatures, the cold CNO cycles extend to include further sequences of reactions—the hot CNO cycles.

A.2.2 β-Limited Hot CNO Cycles

The hot CNO (HCNO) cycles typically take place in electron degenerate gases in hydrogen-rich, runaway thermonuclear explosive environments found in x-ray bursts (and also novæ, which this thesis does not cover). The triggering conditions of x-ray bursts are $T \approx 1-2\times10^8$ K at extreme densities $\rho \approx 10^9 - 10^{10}$ kg m^{-3} [102]; less than half the energy released in x-ray bursts originates from the HCNO cycles [53], which is why the triggering conditions (instead of peak conditions) are provided here for x-ray bursts. A plot of temperature and density for the HCNO cycles and related breakout reactions is shown in Figure A.3. Because of the thermodynamic conditions of x-ray bursts, the fusion takes place on timescales where β^+ lifetimes are much slower than proton capture reactions, hence the rate of hydrogen burning is limited mainly by β-decays. Although weak decays are insensitive to temperature, proton capture rates are highly temperature dependent. When the temperature is high enough, the proton capture rates exceed the decay half-lives of radioactive nuclei in the cycles. Thus, the individual cycles have timescales set by the slowest β^+ decays in the sequence, called *waiting point nuclei*, ^{14}O ($t_{1/2}$=70.641 seconds), ^{15}O ($t_{1/2}$=122.24 seconds), and ^{18}Ne ($t_{1/2}$=1.672 seconds). As a result, the hydrogen burning rate is a fixed function of the CNO mass fraction $Z_{\rm CNO}$

$$\epsilon_{\rm CNO} = 4.6\times10^{11} Z_{\rm CNO}, \tag{A.2.3}$$

expressed in units of (J kg^{-1} s^{-1}), as detailed in [97, 103]. The time to consume all the hydrogen is then about $\frac{790\text{s}}{Z_{\rm CNO}}$, which is only one day for solar metallicity [104], indicating the HCNO cycle is not a form of quiescent hydrogen burning. Although the above equation quantifies $Z_{\rm CNO}$, in x-ray burst models, it is not unusual to place all of

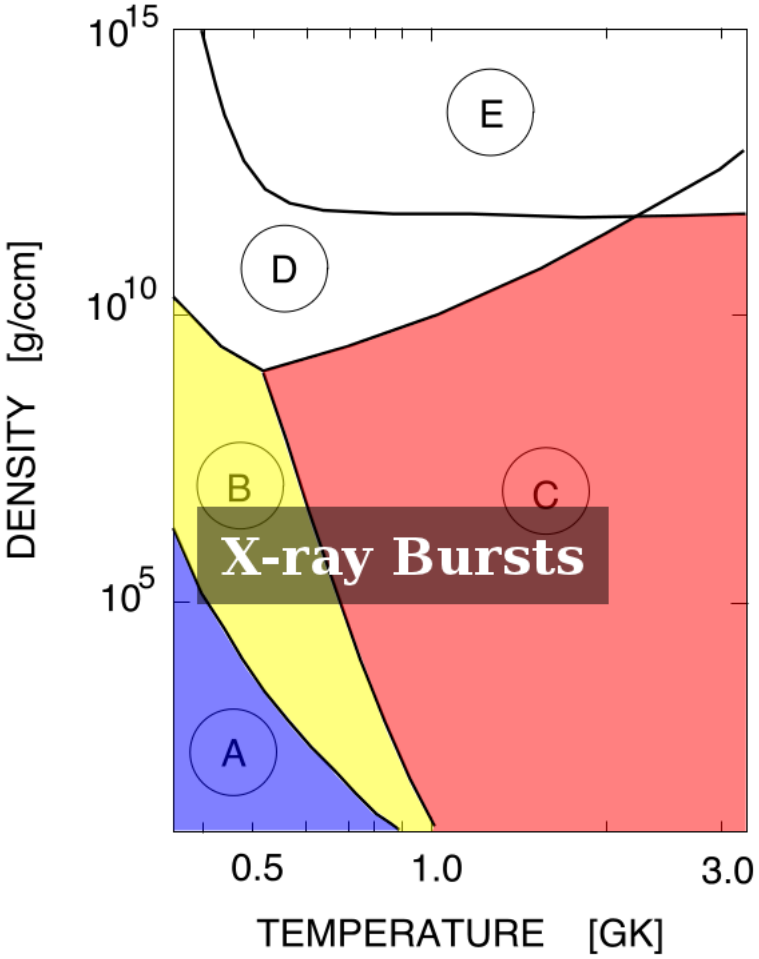

Figure A.3: The plot shows the temperature vs. density regions for various reactions in the CNO cycles and breakout reactions, as well as the region corresponding to x-ray bursts. The HCNO cycles operate in Ⓐ. $^{14}\mathrm{O}(\alpha,p)^{17}\mathrm{F}$ and $^{15}\mathrm{O}(\alpha,\gamma)^{19}\mathrm{Ne}$ operate in Ⓑ. $^{18}\mathrm{Ne}(\alpha,p)^{21}\mathrm{Na}$ breakout operates in Ⓒ. The other zones represent di-proton capture. The colors correspond to those of Figure A.2. Modified from original [97].

the metallicity into the nuclei ^{14}O and ^{15}O at the beginning of the burst [105], since if one were to instead operate the HCNO cycles leading up to the burst conditions with a variety of CNO species, a large fraction of the catalysts would be quickly converted into these two species. This exemplifies their role as waiting point species.

The HCNO reaction network is, in addition to the catalytic cycles A.2.1a-d:

$$^{12}\mathrm{C}(p,\gamma)^{13}\mathrm{N}(p,\gamma)^{14}\mathrm{O}(e^{+}\nu_e)^{14}\mathrm{N}(p,\gamma)^{15}\mathrm{O}(e^{+}\nu_e)^{15}\mathrm{N}(p,\alpha)^{12}\mathrm{C}, \qquad \text{(A.2.4a)}$$

$$^{15}\mathrm{N}(p,\gamma)^{16}\mathrm{O}(p,\gamma)^{17}\mathrm{F}(p,\gamma)^{18}\mathrm{Ne}(e^{+}\nu_e)^{18}\mathrm{F}(p,\alpha)^{15}\mathrm{O}(e^{+}\nu_e)^{15}\mathrm{N}, \tag{A.2.4b}$$

$$\text{and } ^{18}\mathrm{F}(p,\gamma)^{19}\mathrm{Ne}(e^{+}\nu_e)^{19}\mathrm{F}(p,\alpha)^{16}\mathrm{O}. \tag{A.2.4c}$$

Unlike the cold CNO cycles, helium burning may also take part in the HCNO cycles, because of the high densities and temperatures found in neutron star envelops. Thus, the ^{14}O(α,p)^{17}F reaction at a temperature of $T = 4 \times 10^8$ K [42] may also link the cycles [104] via

$$^{14}\mathrm{O}(\alpha,p)^{17}\mathrm{F}(p,\gamma)^{18}\mathrm{Ne}(e^{+}\nu_e)^{18}\mathrm{F}(p,\alpha)^{15}\mathrm{O}(e^{+}\nu_e)^{15}\mathrm{N}. \tag{A.2.5}$$

As the HCNO waiting point species ^{14}O, ^{15}O, and ^{18}Ne are at the proton drip line, there are no alternative burning paths circumventing the cycles outlined above. However, there are many more possible break-out paths than the cold CNO cycle, via alpha-induced reactions or di-proton capture:

$$^{15}\mathrm{O}(\alpha,\gamma)^{19}\mathrm{Ne}(p,\gamma)^{20}\mathrm{Na}, \tag{A.2.6a}$$

$$^{14}\mathrm{O}(\alpha,p)^{17}\mathrm{F}(p,\gamma)^{18}\mathrm{Ne}(\alpha,p)^{21}\mathrm{Na}, \tag{A.2.6b}$$

$$^{15}\mathrm{O}(2p,\gamma)^{17}\mathrm{Ne}, \tag{A.2.6c}$$

$$\text{and } ^{18}\mathrm{Ne}(2p,\gamma)^{20}\mathrm{Mg}, \tag{A.2.6d}$$

where the latter two reactions A.2.6c-d involve proton-unbound intermediary compound nuclei [97, 106]. These di-proton captures on radioactive nuclei are extremely difficult to investigate experimentally and are generally believed to be unimportant as shown in Figure A.3, and thus have not received much attention in the literature. However, alpha-induced reactions on CNO waiting point nuclei, and the subsequent burning pathways after breakout, is a very active area of research, including the present work.

Appendix B

Inverse Kinematics

Although kinematics are frequently taught in first-year physics, and the specific nuances of kinematics of nuclear reactions are covered briefly in most introductory nuclear text books, and there are even entire books dedicated to the subject [107], it is still pertinent to outline the kinematics relevant to this thesis. We are particularly interested in two different reference frames: the laboratory and the center-of-mass. The *laboratory* reference frame is the practical one where nuclear experiments are performed, and all quantities measured take place in this reference frame. However, as will be demonstrated below, depending on the experimental setup—even for two apparently similar measurements—the measured quantities may not be directly comparable; that is to say, their laboratory measurement values might differ significantly even if the center-of-mass, or physics, quantities are the same. Furthermore, certain conservation laws are not as obvious or as simple to apply in the laboratory frame. For these and other reasons, it is convenient and useful to work in the center-of-mass system for calculations of physical quantities related to nuclear structure and reactions; this reference frame is the one where the center of gravity is fixed and where the velocity vectors of the two particles are equal in magnitude and opposite in direction.

Although the analysis itself is performed using full relativity, for the outline presented here it is sufficient to treat the problem classically so the important relationships are readily apparent and quick to demonstrate. Of course, one must justify this non-relativistic assumption; the radioactive ^{30}S beam employed for this experiment has a

laboratory energy at maximum of 4 MeV/u, which is only a fraction of the mass of ^{30}S of some 30 GeV. Hence why this thesis is categorized as a study in low-energy nuclear physics.

As introduced in Section 1.2, let an arbitrary two-body reaction be schematically written $A + a \rightarrow B + b$, which in nuclear experimental work we simplify to A(a, b)B, with A as a target, a as a projectile, b as the ejectile and B as the recoiling nucleus. In the case of a solid target, the target nucleus A is obviously at rest. In the case of a gas target, the target nucleus has a finite but negligible energy. Thus, we treat the target as at rest and only concern ourselves with the energy E_a of the beam particle a. The center-of-mass energy E_{cm} is then related by the masses of the target M_A and the beam M_a to the laboratory beam energy as

$$E_{\mathrm{cm}} = E_a \frac{M_A}{M_A + M_a}. \tag{B.0.1}$$

Now, if $M_A \gg M_a$, then $E_{\mathrm{cm}} \approx E_a$. For several historical and practical reasons* this was often always the case, and beams of the isotopes of hydrogen and helium were most commonly used. We now refer to this situation as *normal kinematics*. At that time, typically a thin target was used, so that E_a hardly changed before and after the target. Thus, to make an excitation function, one varied the beam energy (and consequently E_{cm}) by re-tuning the accelerator condition and made a multitude of measurements.

However, in the case that one wishes to make measurements involving radioactive nuclides with short lifetimes ('short' here generally meaning less than a day), it is impractical or impossible to fabricate a target, since the nuclei of interest would surely decay before a measurement could be performed. If this is a heavy nucleus, then one has no choice but to use the radioactive species as the beam. As astrophysical reactions of interest will often involve hydrogen and helium, then we now have an *inverted* situation where $M_A \ll M_a$ and the center-of-mass energy is significantly less than the bombarding energy. This situation has hence been named *inverse kinematics*.

In experimental work, one follows the notation custom that for A(a,b)B a is always the beam, whereas in astrophysical parlance, a is always the lighter nuclide.

*The ease of creating ion sources of hydrogen and helium, the low energy loss of light ions in matter, etc.

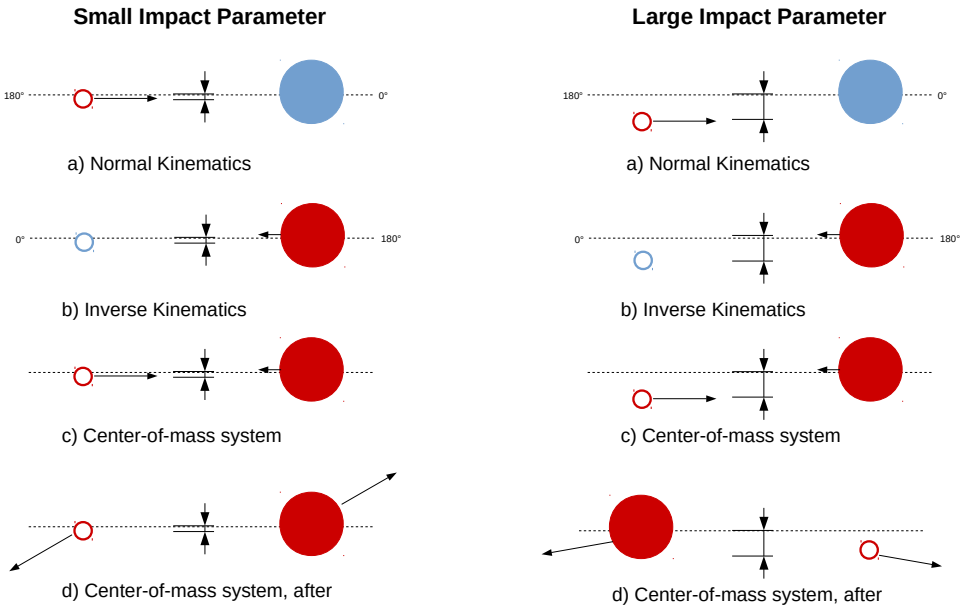

Figure B.1: The cartoon shows the situation with normal kinematics in the laboratory frame (a), inverse kinematics in the laboratory frame (b), the center of mass frame before (c) and after (d) the collision, made by the author. The left side shows the situation of a small impact parameter, whereas the right side illustrates the case of a large impact parameter; the cartoon is drawn assuming a direct, rather than, compound, reaction or scattering takes place. In all cases, the color red is used to indicate a particle treated as in motion, and the color blue to indicate a particle at rest. When the impact parameter is small, the momentum vector of a particle is always rotated by a large angle ($> 90°$) in the center-of-mass system, whereas the momentum vector of a particle is only rotated by a small angle when the impact parameter is large. Note that it is the beam direction which conventionally defines $0°$, which could be to either side in the center-of-mass system, depending on the laboratory setup. In the literature, θ_{cm} is reported as that of the beam-like ejectile or equivalently the angle of either particle with regard to the transformation of its own center-of-mass momentum vector. The target particle's momentum vector is initially at $180°$ in the center-of-mass frame. See the text.

Although the light beam and heavy target may be inverted, it is typically still the light ion ejectile that is measured; in some cases a coincidence measurement including the heavy recoil may be performed, but it is rare to only detect the heavy recoil (this may happen if the outgoing light ion is a neutron, for example). The lighter ion will always have a larger range of laboratory angles and of course suffers less from effects of energy loss. However, θ_{cm} refers strictly to the angle of the beam-like ejectile, which may not be the particle measured in an inverse kinematics experiment. One may either transform

the target-like ejectile's angle θ to the beam-like ejectile's angle (a rotation of 180°) or redefine 0° to match the target-like particle's momentum vector in the center-of-mass reference frame (also a rotation of 180°) to obtain the proper value of θ_{cm}. The situation of the angular axis definition is exemplified with small and large impact parameters for various kinematic reference frames in Figure B.1.

Finally, we are interested in the calculations of θ_{cm} and E_b. For convenience, define the parameter γ as [108]

$$\gamma = \sqrt{\frac{m_a m_b}{m_A m_B} \frac{E_a}{E_a + Q(1 + m_a/m_A)}}. \tag{B.0.2}$$

For elastic scattering, $Q = 0$, thus Equation B.0.2 reduces to

$$\gamma = \sqrt{\frac{m_a m_b}{m_A m_B}}. \tag{B.0.3}$$

The laboratory angle of the ejectile θ_b is related to its center-of-mass angle θ_{cm} simply via [108]

$$\tan\theta_b = \frac{\sin\theta_{\mathrm{cm}}}{\cos\theta_{\mathrm{cm}} + \gamma}. \tag{B.0.4}$$

However, as we measure θ_b and wish to calculate θ_{cm}, the equation can be rearranged as:

$$\theta_{\mathrm{cm}} = \arctan\left(\frac{\tan\theta_b\left(1 \pm \sqrt{1 + (1-\gamma^2)\tan^2\theta_b}\right)}{1 - \gamma^2\tan^2\theta_b}\right). \tag{B.0.5}$$

As for the energy of the ejectile

$$E_b = E_{\mathrm{cm}} \frac{m_A m_b}{m_a(m_a + m_A)}\left(\cos\theta_b \pm \sqrt{\gamma^{-2} - \sin^2\theta_b}\right)^2. \tag{B.0.6}$$

Appendix C

Statistical Analysis

In this thesis, the goodness-of-fit is generally performed using the *chi-square test* of the distribution. Firstly, we define the value χ^2 as:

$$\chi^2 \equiv \sum_{i=1}^{n} \frac{(x_i - c_i)^2}{\sigma_i^2}, \tag{C.0.1}$$

for a data set with n data points, indexed by i, x_i is the experimental measurement of the i^{th} datum, c_i is the calculated value from a theoretical model of the phenomenon at the i^{th} datum, and σ_i is the experimental error, typically represented as the standard deviation σ if x_i was the centroid extracted from a gaussian fit, for example. The basic concept is to quantify how closely the experimental data are reproduced by a model considering the error. The closer the model is to the measurement at a given datum, the smaller the contribution to χ^2. The larger the error bar, the less we are able to distinguish one model from another model. The values are customarily squared since it is not important whether the model overestimates or underestimates the experimental data.

However, it is clear that the more data points an experiment has (for instance, perhaps reflecting the binning or resolution), the larger χ^2 will necessarily become, all other things being equal. Similarly, the more free parameters introduced to the model, the easier it will generally be for the model to reproduce the experimental data; as John von Neumann once quipped, "With four parameters I can fit an elephant, and with five I

can make him wiggle his trunk." Thus, the concept of the number of degrees-of-freedom (denoted either as NDF or ν) is introduced; if the model has m free parameters and there are n experimental data points, $\nu = n - m$. In that case, we can denote $\chi^2_\nu = \chi^2/\nu$, called the *reduced chi-square*. One can then vary the parameters in the model and check the results of each test by computing χ^2_ν, which should be approximately equal to unity for a good fit, depending on the NDF. Specifically, the expectation value of chi square is $\nu \pm \sqrt{2\nu}$ for one standard deviation and for the reduced chi-square is then $1 \pm \sqrt{2/\nu}$, when ν becomes arbitrarily large. Two different models with the same χ^2_ν and the same NDF are statistically indistinguishable, and the experimental data cannot prefer one model over the other.

Appendix D

Supplementary Material for Signal Processing & Calibration

In this Appendix, each step of the signal processing for the experimental setup as well as the calibration of those signals are carefully elucidated step-by-step, as a supplement to Chapter 3. Specifically, some portions of the calibration are not used for the physics results presented in Chapter 4, and thus their inclusion in the main text may distract the reader from the most important aspects, while other aspects are highly technical.

D.1 Timing Signal Calibration Details

D.1.1 CAEN V1190A Multihit TDC Calibration

The multihit TDC has an internal clock which samples at 40 MHz, or every 25 ns, and has $2^8 = 256$ bits, meaning that nominally its calibration parameter is $\frac{25}{256}$ ns/bin; this was calibrated more precisely channel-by-channel using a research pulser to ensure not only the precision of the internal clock but the consistency of each channel, but the deviation from the nominal value was found to be negligible compared to the employed detector timing resolution. The raw PPAC timing data for a sum of the ^{30}S+α runs are shown in Figures D.1 and D.2 for PPACa and PPACb, respectively. Two peaks prominently appear for each channel, the first peak corresponding to the SSD-OR trigger condition, while the second peak corresponds to the D/S trigger condition, consistent

with our requirement that the SSD-OR trigger should always arrive first. The distance between these two timing peaks $\Delta t = 8246$ bins averaged over the eight PPAC timing signals, corresponding to a calibrated time difference of 805 ns. The delay offsets are shown in Table I.2. As meaningful SSD timing information only appears within the data acquired during the SSD-OR condition, we omit any analysis or discussion of the SSD timing data in relation to the trigger timing offset.

To calibrate the PPACs, we begin by adjusting the raw timing data for the trigger condition (if necessary) and then convert the raw timing information into nanoseconds as above. As we read the timing signal from two sides of the PPAC for position determination in one dimension, suppose we now have two timing signals t_1 and t_2, which we take the difference of $\Delta t = t_1 - t_2$. Firstly, we subtract from Δt the offset *inside* the PPAC provided by the manufacturer. Subsequently, we subtract any offset *outside* the PPACs, which depends on any minor differences of timing in cabling or electronics for the signals t_1 and t_2. At this point Δt is calibrated in ns, so we use a gain factor to convert from ns to mm, also provided by the company. Finally, we subtract any geometric offset which is known from the setup compared with laser alignment or the optical slits. This yields the position of ionizing radiation in physical space with respect to the beam optical axis. The calibration parameters described above are listed in Table I.1.

It is also useful to extrapolate the beam's position based on the position determined by the PPACs. Let us denote the X position determined by PPACa and PPACb as X_a and X_b, respectively, and the distance between the PPACs as Z_0. In that case, the X position of the ion is a function of distance $X(Z)$, as long as $Z > Z_0$, can be written as:

$$X(Z) = X_a + \left(\frac{Z}{Z_0} \Big(X_b - X_a \Big) \right). \tag{D.1.1}$$

In our experiment, $Z_0 = 156$ mm. The equation is, of course, applicable to the Y position and $Y(Z)$ can be constructed by simple substitution of the appropriate quantities Y_a and Y_b.

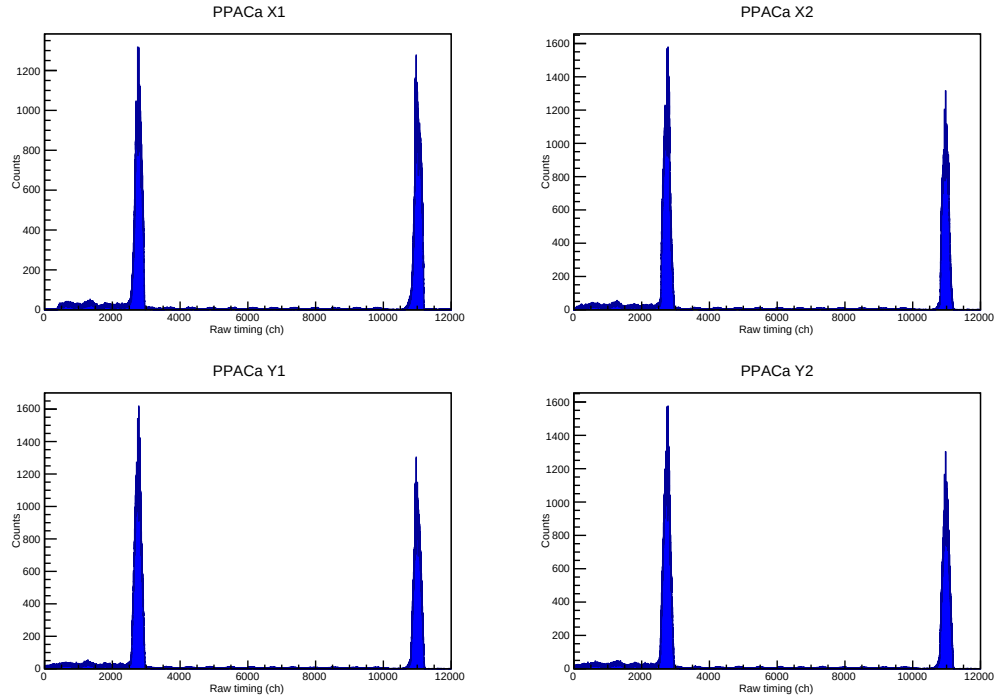

Figure D.1: PPACa raw timing data. Notice there are two prominent peaks.

D.1.2 CAEN V775 TDC Calibration

There are a few approaches one may employ for a calibration of the V775 TDC, which as we shall see, give consistent results. The module driver used is from BAQ [109], and one parameter specified is sent to the Full Scale Range (FSR) register. This relationship is non-linear, as shown in Figure D.3, and because small changes in the setting value, particularly for smaller settings, can result in large differences for the FSR, this method is not very reliable for time calibration. Since we know the AVF cyclotron typically operates with an RF with an inverse of $\sim$60 ns, and the V775 TDC here is only used to measure the RF signal, a larger FSR setting corresponding to a smaller FSR is appropriate for the best timing resolution. While the intended setting was for an FSR of 150 ns, there was a mistake in the hexadecimal entry, such that the actual FSR was roughly 500 ns; this FSR setting gives a timing calibration of $\sim$0.1221 ns/bin; however, as shown later in Figure D.4, the full 4096 bins are also not all used, which suggests this calibrated value is too small.

Another approach is to consider the meaning of the *Rf* time and calibrate the data

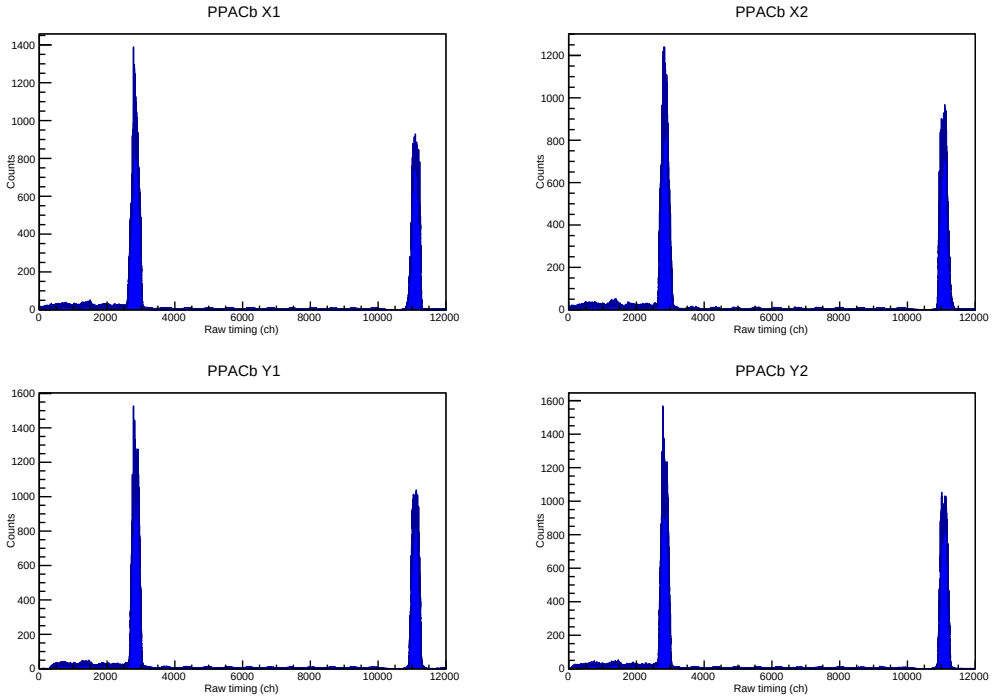

Figure D.2: PPACb raw timing data. Notice there are two prominent peaks.

internally. Most generally, the *Rf* time is started by the PPACa trigger and stopped by the RF signal; we do not use the RF as the start signal for the same reason we do not measure the RF with a multihit TDC—there are simply too many RF signals, many of which are meaningless to us. Because the cyclotron accelerates and ejects the primary beam in discrete packets, the difference of the flight time of individual ions within one beam pulse from extraction to arrival at the F0 target is constant, within the pulse width of the beam bunch (about $2 \sim 3$ ns). However, different ion species arriving at the focal plane of CRIB were selected based on their A/q values, and despite that we filter them for their velocities, there is still some velocity spread Δv, implying a time of flight spread ΔToF. In summary, a comparison of two ions' *Rf* times is a comparison of their F0 to F3a ToF, only the sign of Δv is inverted because a true ToF measurement would necessitate RF start and PPAC stop.

As we previously performed the PID of the major components of the RIB, a natural way to get a calibration for the V775 TDC is to compare the calculated ΔToF between $^{29}\mathrm{P}^{15+}$ and $^{30}\mathrm{S}^{16+}$ to the measured ones. Two RF signals are recorded, Rf_0 and a signal

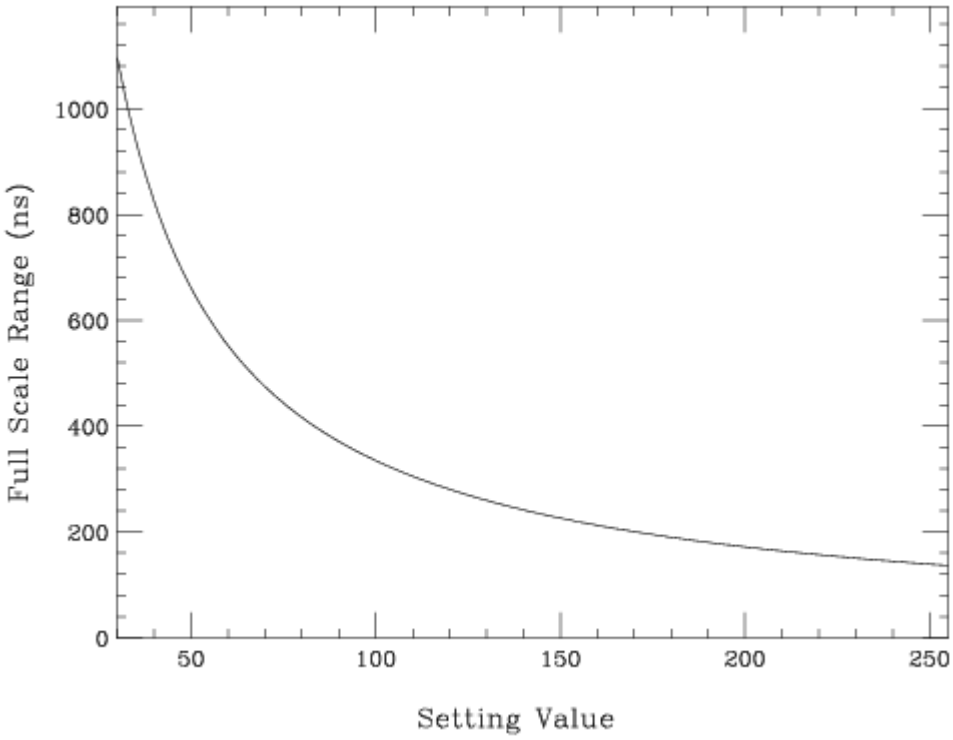

Figure D.3: V775 module driver setting value versus resulting full scale range. As the FSR shows a strong dependence on the precise setting at low setting values, it is unsuitable for calibration purposes under such conditions.

delayed by 20 ns, Rf_1. The experimental $B\rho = 0.5402$ Tm, yielding $E_{beam} = 109.1$ MeV for $^{29}P^{15+}$ and $E_{beam} = 119.9$ MeV for $^{30}S^{16+}$. Using the known optical flight path distance of 12.82875 m from the center of F0 to F3a, we get ToF= 476.8 ns for ^{29}P and ToF= 461.8 ns for ^{30}S, or $|\Delta\text{ToF}| = 13.7$ ns. The raw Rf signals under the D/S condition are shown in Figure D.4. We get $|\Delta\text{ToF}_0| = 98.6$ and $|\Delta\text{ToF}_1| = 98.7$ bins, giving the timing calibrations of 0.1389 and 0.1388 ns/bin, respectively. This method, however, involves a few systematic uncertainties. Firstly, we do not know where within the F0 target ions are made, and previous tests using a scintillator at F0 to measure the beam burst indicated a spread of a few nanoseconds. We have assumed $dE/dx = 0$ for the F0 target and entirely neglected it for PPACa; as energy loss goes as Z^2, the velocity difference is thus proportional to Z, and we expect a calculation of ΔToF between ions with different Z to be systematically smaller than its true value. Furthermore, although we fit the centroids of the Rf time by gaussians for the above comparison, there is no

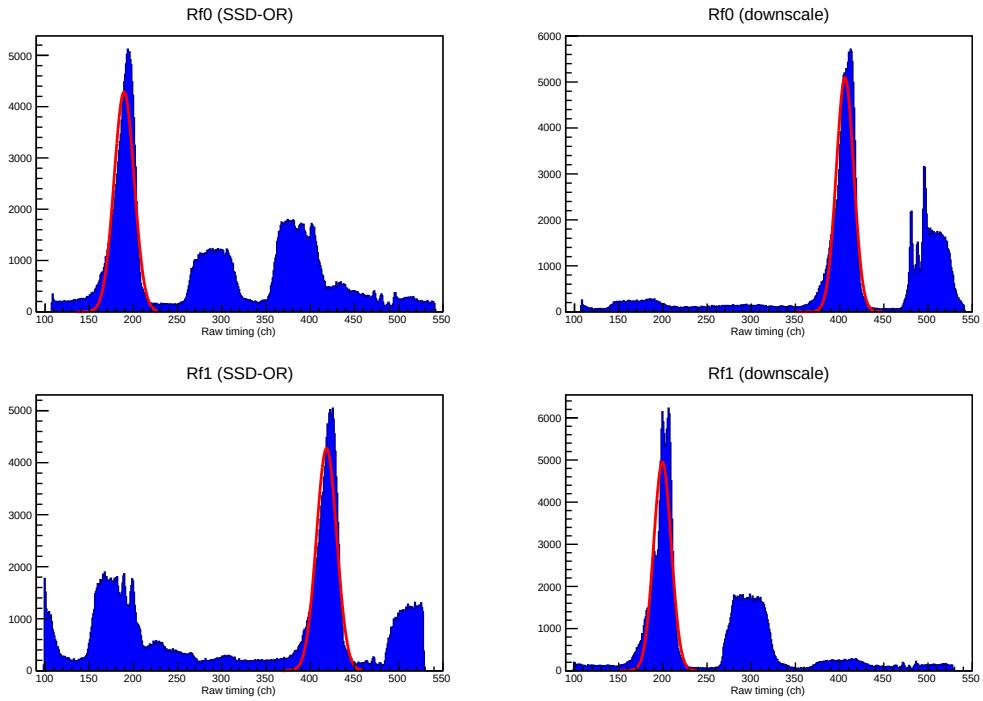

Figure D.4: Raw data for Rf_0 (top panels) and Rf_1 (bottom panels), with the left and right panels showing the SSD-OR and D/S conditions, respectively. The fitted peak is ^{29}P and the next peak after that is ^{30}S. The third peak appearing only prominently in the SSD-OR data is a much lighter ion in the cocktail beam with a very low intensity, yet it is able to self-trigger for SSD-OR by directly striking a silicon detector.

guarantee *prima facie* that this should be true. CRIB was optimized for the transmission of $^{30}S^{16+}$, which we might expect to have a gaussian (or at least symmetric) distribution in $B\rho$ about its maximum, but the same cannot be said for $^{29}P^{15+}$, which as we already know does not arrive perfectly at the optical center of PPACa, nor with a symmetric distribution in X (and thus neither in velocity space).

A final approach we might consider is to derive a TDC calibration simply from the known cyclotron RF value in comparison with the observed difference between the minimum and maximum values within the Rf data (Figure D.4). We observe $\Delta Rf_0 =$ 433 bins and $\Delta Rf_1 = 428$ bins, and as stated above the inverse of the true cyclotron RF is 59.7 ns, leading to calibration gains of $g_0 = 0.1376$ and $g_1 = 0.1388$ ns/bin for Rf_0 and Rf_1, respectively. These values are in close agreement with the ones derived from the RIB ToF, and yet suffer none of the systematic uncertainties.

For the SSD-OR zero-offset, we merely use the observed minima bin values, which are 108 bins for Rf_0 and 99 bins for Rf_1. To determine the offset of the D/S data from the SSD-OR data, we can simply determine the time difference between ions of the same species under the SSD-OR and D/S conditions; we choose $^{29}P^{15+}$ as it has a narrower *Rf* spread and better statistics than our ion of interest $^{30}S^{16+}$. We fit these peaks with gaussians* as shown in Figure D.4. For Rf_0 it is straight forward and we get $\Delta t_0 = 216.8$ bins. For Rf_1 we should subtract the minimum bin and add the maximum bin to the D/S data so their timing values are larger than the SSD-OR data, and we get $\Delta t_1 = 209.1$ bins. The D/S offsets are these Δt_i plus the minima bins above.

We can check that the calibration is self-consistent. If we multiply the trigger delay Δt_i by the gain g_i, we get 29.8 ns and 29.0 ns for Rf_0 and Rf_1, respectively; the meaning of these values is simple to understand. For the true D/S offset, we can consider the measured timing difference of 805 ns from the Multihit TDC compared with the inverted cyclotron frequency of 59.7 ns. It is evident that the D/S trigger delay is not an integer number of RF cycles, because $\frac{805 \text{ ns}}{59.7 \text{ ns}} = 13.4$; from this we can calculate that the *Rf* data under the two trigger conditions should be separated by 40% of an RF cycle, or 28.9 ns. This is in good agreement with the trigger delays calculated considering the PPAC uncertainty of ±1 ns. An example of the *Rf* calibration results was shown in Figure 3.5.

D.1.3 COPPER Flash ADC Timing Calibration

The vertical position of ionizing radiation traversing the active target is determined by the electron drift time. The ionising radiation creates ion and electron pairs (*ion pair*) along its track; if the track is further from the readout pad, the electrons take a longer time drifting in the applied field to reach the pad and vice versa if the track is closer. Once the triggering condition is satisfied, the flash ADC begins sampling the data; as stated previously, the sampling frequency is 50 MHz or every 20 ns. When a given sample's height first crosses the threshold, the number of discarded samples is recorded

*Although it was previously stated that fitting the *Rf* peaks with gaussian functions is a possible source of systematic error, it is mainly a problem when comparing the derived centroids of two different species whose *Rf* spectra may differ in shape; although the fits in Figure D.4 demonstrate the non-gaussian nature of the peaks, we can expect this systematic equally affects the derived centroids for ions of the same species, and any skew is cancelled out by subtraction of one centroid from the other.

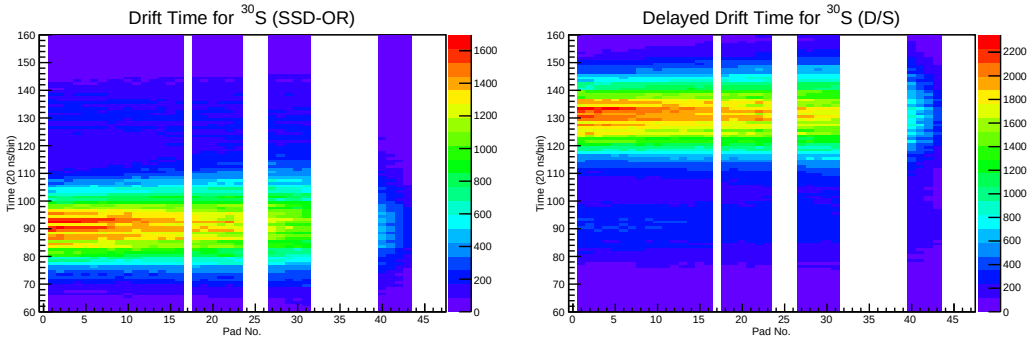

Figure D.5: Raw drift time in the low-gain portion of the GEM-MSTPC for ^{30}S ions. The abscissa is the pad number (increasing target depth) and the ordinate is the measured time. The left panel shows the SSD-OR trigger condition (the true drift time), while the right panel shows the D/S trigger condition (drift time is offset by the delay).

as *fTime*, and it is simple to count the number of consecutive samples j where the height exceeds the baseline, which is an array we call $fClock_j$. Here one only needs the $fClock$ value when j corresponds to a peak position (as described in Section D.1.4). As each backgammon pad has two sides, there are the crossing times $fTime_L$ & $fTime_R$ as well as the sampling times preceding the peak $fClock_L$ & $fClock_R$, both for the left and right sides, respectively. The total drift time is thus an average of these sums as

$$\frac{1}{2}\Big(\big(fTime_L + fClock_L\big) + \big(fTime_R + fClock_R\big)\Big). \tag{D.1.2}$$

Just as in the other cases of timing calibration, the raw drift time data for the ^{30}S beam shows loci at different times for the SSD-OR and D/S trigger conditions, shown in Figure D.5. Projecting each pad and subtracting the drift time for the SSD-OR case from the D/S case gives an average of $\Delta t = 39.1$ bins or $\Delta t = 782 \pm 20$ ns, very close to the value of 805 ± 1 ns obtained with the Multihit TDC and in excellent agreement with the trigger time chart value of 780 ns (Figure 3.3). The individual values of Δt are applied to each channel to correct for the trigger timing delay. Although the D/S data are not used for any physics, for the calibration of the drift time (ns) into position (mm), it is best to use the unscattered beam which will have a straight track, which in turn necessitates firstly removing this timing offset between the two trigger conditions.

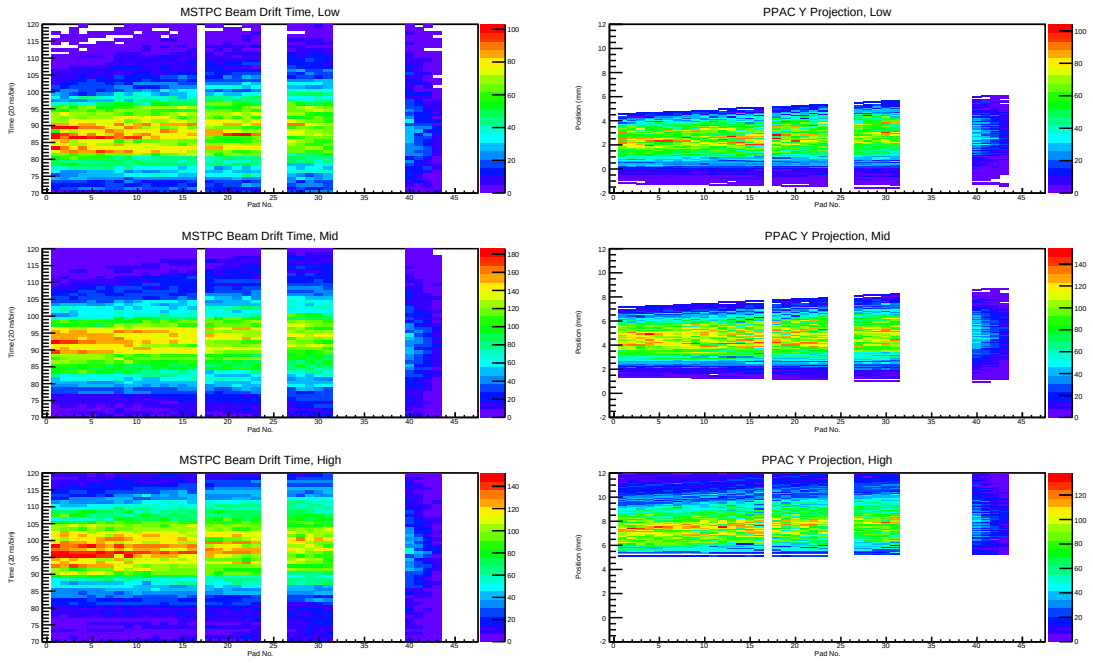

Figure D.6: The histograms show the results of three narrow software gates in the PPAC Y data to simulate planar beams at various heights. The left panels show the MSTPC drift time on the ordinate whereas the right panels show the PPAC extrapolated Y position; all the panels have the pad number along the abscissa. See the text.

In order to perform the absolute calibration, three narrow gates are made in the PPACa and PPACb Y data, and the centroids of the drift time data are compared to the centroids of the PPAC extrapolation for each pad. These software gates emulate a planar beam produced with a sequence of physical collimators, which were defined as follows:

Low Gate: -0.5 mm $<$ PPACa Y $<$ 0.5 mm & 0.0 mm $<$ PPACb Y $<$ 1.0 mm

Mid Gate: 2.0 mm $<$ PPACa Y $<$ 3.0 mm & 2.5 mm $<$ PPACb Y $<$ 3.5 mm

High Gate: 4.0 mm $<$ PPACa Y $<$ 5.0 mm & 5.0 mm $<$ PPACb Y $<$ 6.0 mm

As the beam has a slightly upward trajectory, we cannot get a reasonable result by using the same gate in PPACa and PPACb. Although we define its size to be 1 mm, the extrapolation is nearly half a meter downstream of PPACa and the PPAC separation was merely 156 mm. The results of the gate are shown in Figure D.6. With three data points (one from each gate condition), we can perform a reliable linear fit to extract the

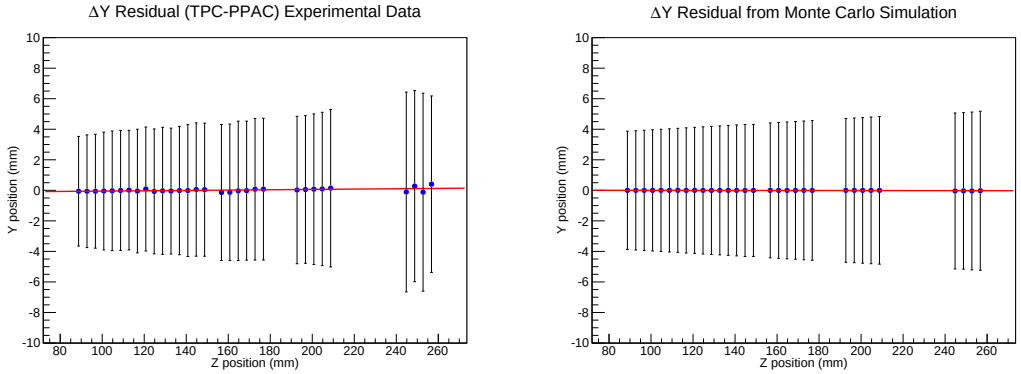

(a) ΔY Residual by Experiment

(b) ΔY Residual by Simulation

Figure D.7: Projection and fit of the beam residual data for Y position. ΔY is determined by the active target position minus the PPAC extrapolation, and the Z position is the distance from the entrance window to the center of each pad. The error bars are 1σ for a gaussian fit.

offset (about 1.7 μs) and electron drift speed (about 25 μm/ns); note that with this drift speed, it should take electrons about 2 μs to drift the 50 mm from the field cage center to the pads, suggesting that after the delays involved in the trigger processing, electrons were already drifting for around 300 ns. The order of these values are all consistent with the of values in the trigger and gating time charts. The exact calibration parameters are listed in Table I.3. The final calibrated spectrum for the ^{30}S beam from the drift time was shown in Figure 3.6(a).

To estimate the resolution, we performed a Monte Carlo simulation, taking the PPAC and TPC drift time position resolution as free parameters. Results of the simulation are shown in Figure D.7, where the simulation shown has used a PPAC position resolution of 0.9 mm and a resolution from the TPC drift time of 0.5 mm. The agreement is quite good, except near the end region where straggling effects are observed in the experimental data but not included in the simulation. The adopted PPAC resolution was fixed to be the same in Y as in X in the simulation; the simulation of X is discussed in Section D.1.4.1 and shown in Figure D.15.

For the high-gain GEMs, we have no relevant data for calibrating the Y position from drift time. This is because the silicon strips in the first layer of the ΔE-E telescopes have vertical strips, and can only be used to calibrate the X position. It would have

been a good idea to also take α-calibration data after switching the orientation of the first SSD layer. Instead, we adopted universal offset (83) and gain (0.5) values for the high gain data from the low gain data shown in Table I.3. Although the GEM settings were different, the electrons spend most of their time drifting in the field cage, which has the same electric field throughout, so the systematic error introduced should be small. The calibrated spectrum was shown in Figure 3.6(b).

D.1.4 Peak Finding within Flash ADC Data

In order to analyze the data, the first and most important step is finding peaks within the flash ADC data. An example pulse is shown in Figure D.8. Naïvely, a peak is simply defined as a sample whose value is larger than neighboring samples. Let us define N to be the number of samples in a given channel for a given event, and denote an arbitrary individual sample within that set by S_j. For the j^{th} sample to be a local peak, it should be greater than all of $\pm n$ samples, where $2n+1$ is the peak-searching window (number of samples). If we insist that the peak is smooth, this algorithm can be written as:

$$\begin{aligned} S_{j-n} &< S_{j-(n-1)} \\ &\vdots \\ S_{j-1} &< S_j \\ S_j &> S_{j+1} \\ &\vdots \\ S_{j+(n-1)} &> S_{j+n}. \end{aligned} \tag{D.1.3}$$

Note that the term $(S_j \geq S_{j+1})$ is used rather than the more strict $(S_j > S_{j+1})$ for the raw data, because in the ^{30}S data, it was found about $\sim 10\%$ of peaks had a flat top; such a case is shown in Figure D.8.

The peak window parameter n should be optimized for the data set, and naturally $(2n+1) \ll N$ for typical values of N, since the above criteria for a peak cannot be satisfied if the window is larger than the number of samples.[†] Evidently from the algorithm, the

[†]It is possible to relax the constraint on n for small N; but in the case of small N, the data are typically junk (resulting from noise, discharge, etc) and it is difficult to extract useful information.

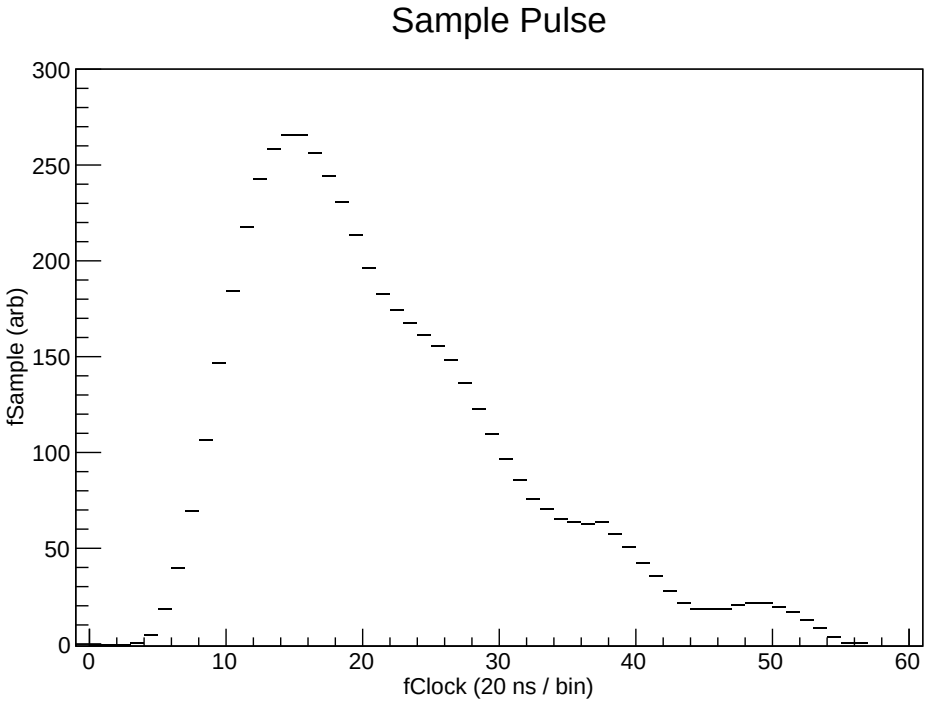

Figure D.8: Typical pulse exhibiting a flat top and jitter in the tail region. The peak itself is located at $fClock = 14$, while a false peak might be identified near $fClock = 50$. Sampling time is 50 MHz and sample height is in channels after baseline subtraction. In the text, the sample number $fClock$ is represented by j and its sample value $fSample$ by S_j.

samples are scanned beginning at $j = n$ and finishing at $j = (N - n)$ for any peaks, which precludes identification of any peaks very near to the beginning or end of the sampling time. Such a constraint is chosen to match the sampling procedure, where the DAQ trigger and gate logic timing was tuned to properly record pulses associated with the trigger; the tuning must be done based on the experimental conditions, such as the particle flight times and the electron drift time (depending on fill gas, electric field, etc). With the DAQ gate open, the flash ADC records the five samples prior to the one that first exceeds the threshold setting, which not only provides the baseline (zero-point) data, but also insists that there are no peaks above the noise level for $j < 5$. A single pulse typically exceeds the threshold value for ∼800 ns (its full width), while as was shown in Figure 3.4, the sampling time is 6 μs; pulses associated with the triggering

condition should all return to the baseline value well before the sampling is truncated.[‡] This method is thus capable of locating peaks in smooth pulses associated with the triggering condition, although additional factors play a role in constraining the choice of n.

Practically speaking, the pulses are not perfectly smooth, and so the value of n inversely correlates with the number of peaks the algorithm may identify. Most commonly, there is jitter in the tail of the signal, so in this respect a larger value of n will decrease the number of false positives obtained with the algorithm. In contrast, the window size must not only be less than or equal to the typical width of a peak, but smaller than the scale size of fluctuations in sample height near the peak; here the efficiency of finding true peaks decreases with increasing n. A representative group of five hundred pulses were examined manually with various values of n to quantify the efficiency and false positives. With $n = 3$ (140 ns window width), the method showed better than 99.8% efficiency but had one or more false positives in ∼20% of pulses.

As it is undesirable to decrease the efficiency by further increasing n, instead the data are rebinned and averaged by a factor w before processing by the peak-finding algorithm to smooth out the jitter. For clarity, denote the parameters associated with the rebinned data by primes: the total number of rebinned samples is $N' = \frac{N}{w}$; the number of samples included in the peak searching window is then $w(2n'+1) = (2n+1)$; an arbitrary sample $S'_{j'}$ is given by

$$S'_{j'} = \frac{1}{w} \sum_{j=(j'-1)w}^{j=j'w} S_j. \tag{D.1.4}$$

When employing the rebinned data in the algorithm of D.1.3, we can consider this as a *moving average* peak finder. The moving average algorithm was optimized with $n' = 2$ and $w = 4$ (400 ns window width), considering the same group of five hundred pulses, and showed the same efficiency with zero false positives. By rebinning, the jitter was smoothed out to eliminate false positives, while using a small value of n' such that the efficiency remained high; the flat-top is also removed in the rebinned data. To finally extract the true peak position j we search for the maximum value S_j within the rebinned

[‡]In the case where a small quantity of contamination, such as nitrogen, is introduced to the active target fill gas, one can easily find pulses with tails extending several microseconds. This is a key reason for the chamber to have good vacuum seals and/or to circulate the target gas.

sample $S'_{j'}$ identified as the peak.

Integration of the deposited charge in a pad is not only simple but useful. The integration is performed by summing the values of each sample pulse after subtracting the baseline. Although the algorithm can recognize the instance of multiple separate peaks in the same pulse, it cannot de-convolute them yet; for most of our experiments, the event rate is low enough that the instance of such events is less than 1% and they can be discarded. Furthermore, suppose two identical ions are injected to the active target within a very short interval from one another. In this case, the active target pulse will appear not as two separate pulses, but as one larger pulse. The exact timing of their overlap will allow the pulse height to vary from one which is nearly the same as a single pulse to about two times this value. In the case that the pulse is integrated, however, the pulse will always indicate twice as much charge was deposited as for the case of one ion. Thus, peak integration allows us to easily reject pileup events, which is more difficult otherwise, for instance requiring a sophisticated pulse shape analysis algorithm. We used the integrated peaks for the beam data, and the peak heights for the light-ion data (which are unlikely to suffer pileup effects).

D.1.4.1 Low-gain charge division

For the low-gain region of the active target, as we are tracking the beam ions with a pair of PPACs, we can compare the measured active target X position with the PPAC projection, and insist that each data point in the residual spectrum fall at zero. The raw residual spectrum is shown in Figure D.9a, and the result of applying the geometric corrections listed in Table I.5 is shown in Figure D.9b. Jitter is evident in the active target backgammon data in Figure D.9, clearly justifying our interest to perform this calibration. The uncorrected residual data also show a systematically negative slope and offset from zero, both qualitatively consistent with the alignment measurements; whereas the geometrically corrected data show a nearly flat slope significantly closer to zero. However, even after the geometric correction the residual data are still clearly offset from zero. Naïvely, one may consider merely Equation 3.4.1, the PPAC calibration, and/or the geometric measurements to be in error; however, it is instructive to first further investigate the data for other systematic anomalies.

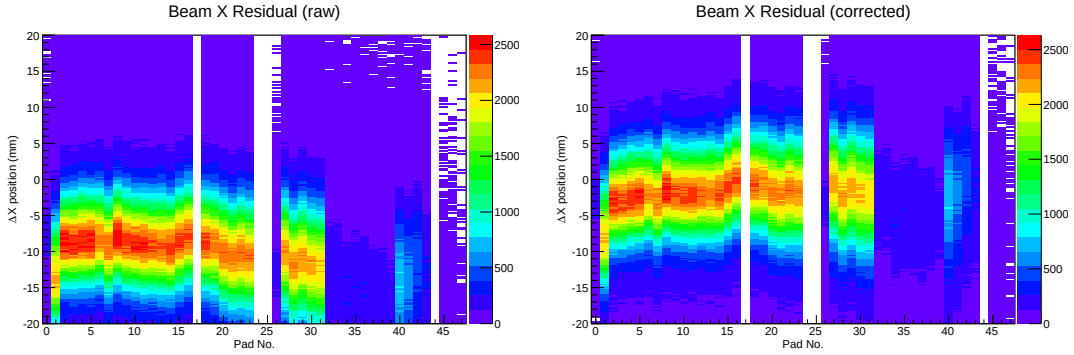

(a) ΔX Residual vs. Z position.

(b) Corrected ΔX Residual vs. Z position.

Figure D.9: Residual position of beam ions within the active target compared with the PPAC extrapolation, uncorrected (a) and corrected for geometry (b) both against target depth (each pad is 4 mm). Horizontal position X from the active target is first determined by comparing the collected charge at the left and right side of the backgammon for the active target as calculated by Equation 3.4.1 with and without the $X_\theta(Z)$ correction; to obtain ΔX, we subtract from this the extrapolated X position measured by two consecutive beam monitors (PPACs).

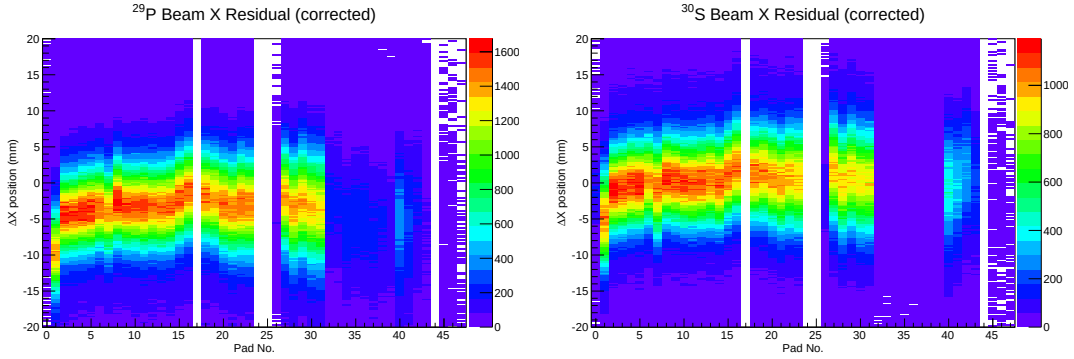

(a) ΔX Residual vs. Z position for ^{29}P.

(b) ΔX Residual vs. Z position for ^{30}S.

Figure D.10: Same as Figure D.9b but gated on the loci for the ion species of (a) ^{29}P and (b) ^{30}S. The beam ion species gates are made in the *Rf* vs. PPAC X position data (see *e.g.* Figure 3.5). A clear difference of behavior is observed between the two histograms.

For example, if we de-construct Figure D.9b into its component ions of ^{29}P and ^{30}S, shown in Figure D.10, evidently some other confounding factor is at work and exhibits itself in the species-gated ΔX residual. Errors in geometry are immediately ruled out, as they should affect both species in the same manner. It is not obvious *prima facie* precisely what cause manifests itself as this behavior; the mass number, incident charge states and energies, and intensities of these two species are comparable. However, as

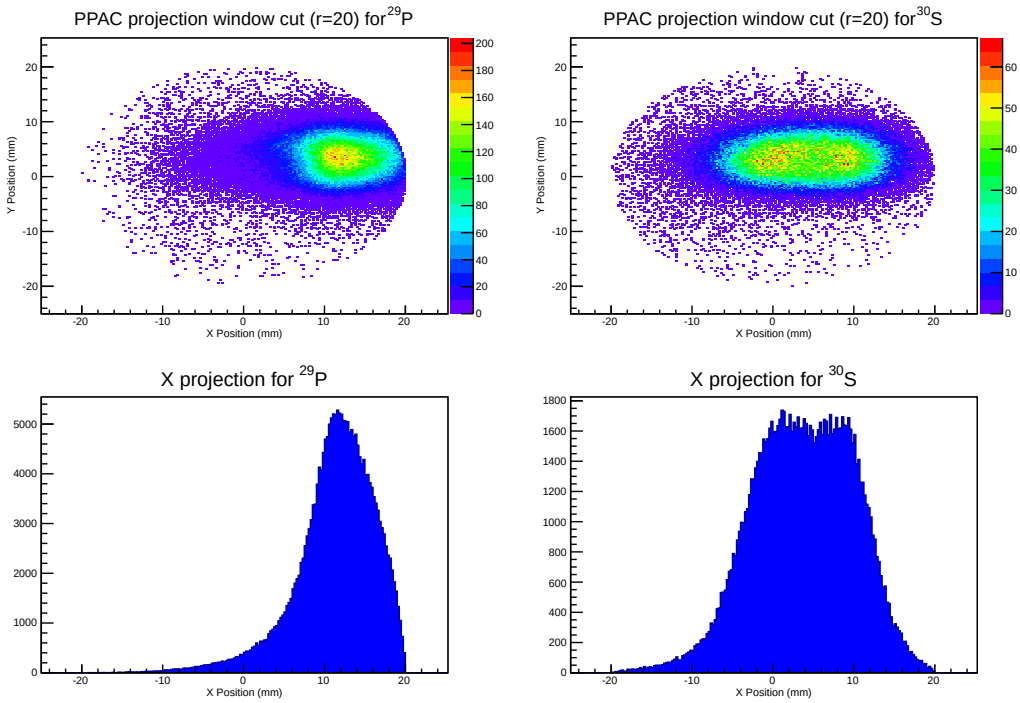

Figure D.11: PPAC projection to the entrance window plane with cut for $r = 20$ mm. Note that the apparent bi-modal distribution in the ^{30}S profile is a result of this region between the two peaks of PPACb becoming radiation damaged and unresponsive as the experiment progressed.

shown in Figure 3.5, the two species have different trajectories in the X direction owing to the velocity dispersion of the Wien filter.

Although a cut is applied to the PPAC projection data to produce Figs. D.9 and D.10 to simulate the TPC chamber entrance window, in that case the window was supposed to have its true physical size ($r = 20$ mm), as shown in Figure D.11. If instead one further restricts the window-cut to half its true value ($r = 10$ mm), as shown in Figure D.12 in order to remove any contribution to the ΔX residual spectrum from ions which are non-central or are not injected at a normal inclination to the active target, a surprising result is obtained, shown in Figure D.13. The spectrum is tightened, loses a small negative slope contribution, and the residual is centered about zero for both ion species. As their respective X profiles at the TPC chamber window still vary considerably within the narrow window-cut with respect to one another, it suggests the calibration method itself works as anticipated. However, the X position of ^{29}P beam ions which travel in

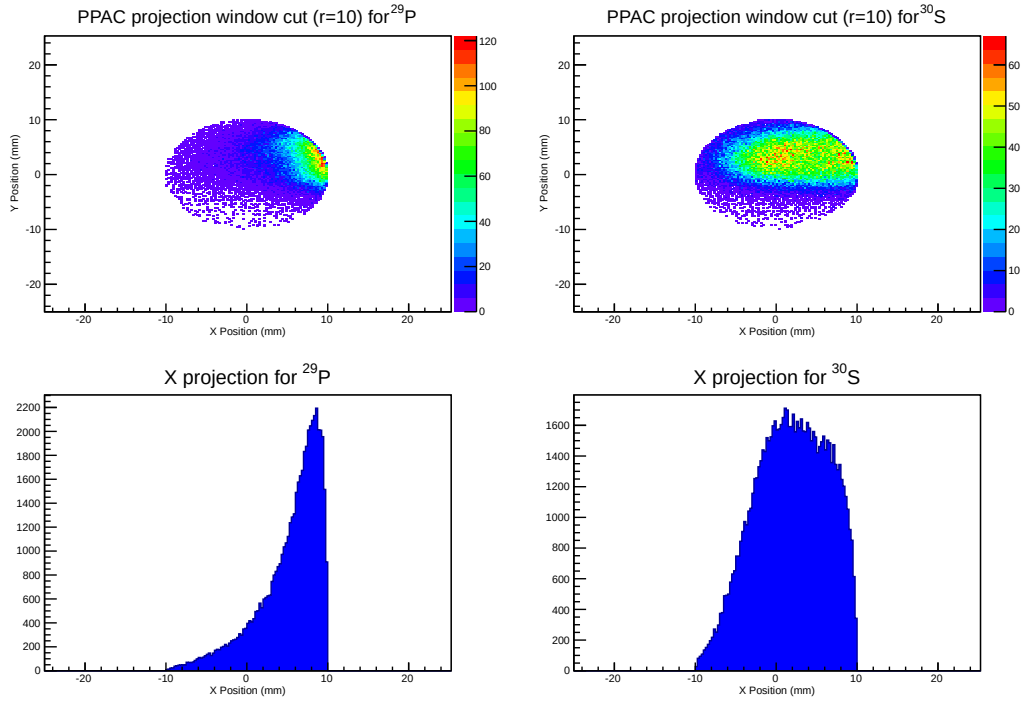

Figure D.12: PPAC projection to the entrance window plane with cut for $r = 10$ mm.

an outward-inclined trajectory and further from the optical axis cannot be accurately determined by the backgammon charge-division data. As discussed in Appendix F, the backgammon pad data show a non-linearity of the charge collected away from the center of a pad as well as an unexpected strong dependence on the incident angle of the ionizing radiation. However, fortunately although the ^{30}S beam does not converge to the center of the beam optical axis, owing to the field-cage misalignment, it does pass over the center of the beam GEM, and as the beam optics were tuned for ^{30}S, its trajectory is perpendicular to the readout pads. Because the focus of this thesis is on the interaction of the ^{30}S+α system, it is not necessary to calibrate the system for ^{29}P.

It is now possible to perform the backgammon calibration for ^{30}S according to Equation 3.4.2. One minor issues arises, since so far we showed the residuals *after* the geometric correction, but clearly we need to extract $c_{1,2}$ based on ΔX *before* rotation, but the data cannot be in units of distance before the geometric correction is applied. If the linear fit to the residual after rotation was perfectly flat with no offset, we could use the linear fit before rotation to extract c_i. Figure D.14a shows the projection of the

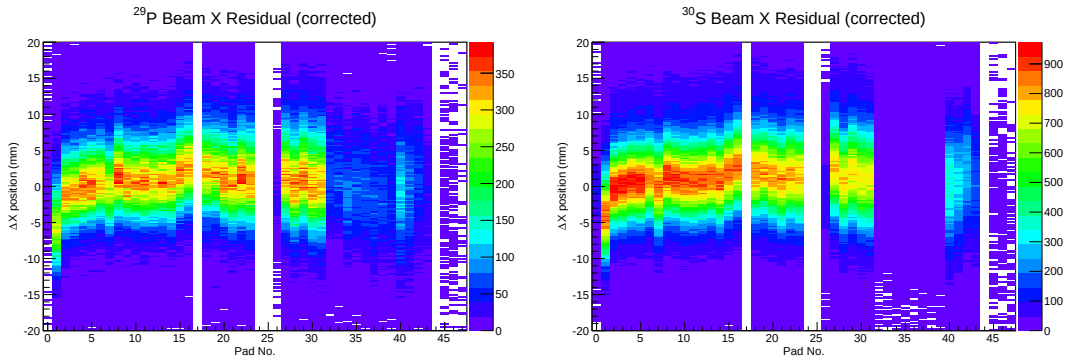

(a) ΔX Residual vs. Z position for ^{29}P. (b) ΔX Residual vs. Z position for ^{30}S.

Figure D.13: Same as Figure D.10 but with a narrow window-cut to ensure the ions do not scatter off the window flange. The window-cut is imposed within the PPAC projection data for $r = 10$ mm rather than the true window size of $r = 20$ mm. The disagreement between the two species observed in Fig D.10 disappears, as does the offset from zero or non-zero slope seen in Figure D.9b.

data from Figure D.10b, where the projection from each pad is fit with a gaussian to determine its centroid and the error bars are $\pm 1\sigma$. The projections are subsequently fit with a linear function, its parameters shown in the inset; pads #0 and #26 did not function correctly for most of the experiment, and pad #1 requires a correction greater than 5% for most of the data sets (and pad #7 for a small subset), and are thus not included for the determination of the best linear fit as they would skew the results. As shown in Figure D.14a, the rotated residual shows a slightly nonzero slope and offset, which we can subtract from the linear fit to the unrotated residual. Figure D.14b shows the ^{30}S residual ΔX data before the geometric correction with its best fit in red, and the subtraction of the best fit in (a) from the best fit of (b) in green, from which the values for ΔX are extracted. Although this method also introduces a systematic error from the order of operations, it is acceptable given the minuscule slope and offset in the rotated residual compared with the error bars.

The final calibrated active target X position from the pad charge division against pad number was shown in Figure 3.11. The adopted calibration coefficients are summarized in Table I.7. To estimate the resolution, similar to the case of Y we performed a Monte Carlo simulation, taking the PPAC and TPC backgammon position resolution as free parameters. Results of the simulation are shown in Figure D.15, where the simu-

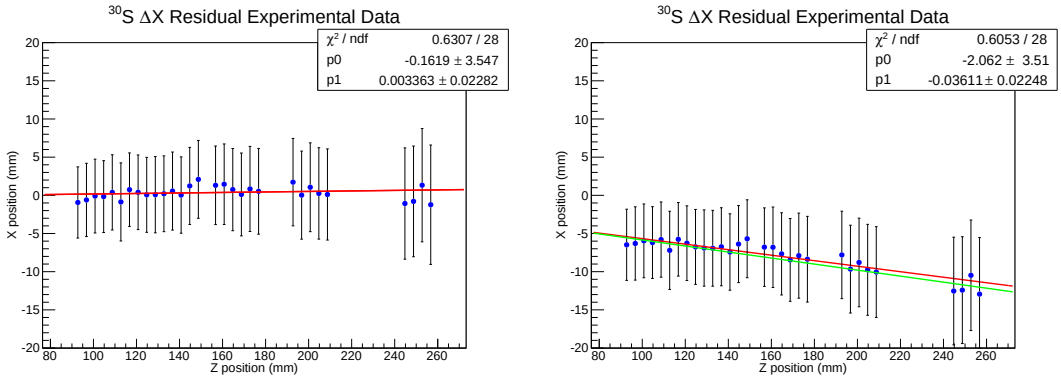

(a) ΔX Residual vs. Z after rotation

(b) ΔX Residual vs. Z before rotation

Figure D.14: Projection and fit of the beam residual data for ^{30}S. The red lines show the best linear fits for the data in each plot (with corresponding fit parameters in the inset), whereas the green line in (b) is the subtraction of the fit in (a) from the fit in (b). ΔX is determined by each data point's difference from the green line.

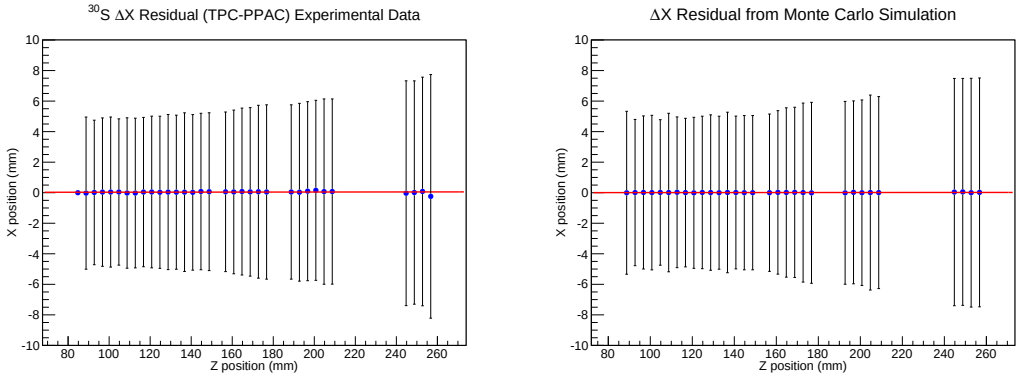

(a) ΔX Residual by Experiment

(b) ΔX Residual by Simulation

Figure D.15: Projection and fit of the beam residual data for X position. ΔX is determined by the active target position minus the PPAC extrapolation. TPC resolution by charge-division ranges from 3 mm to 5.5 mm depending on ΔE. PPAC resolution is 0.9 mm. Errors are 1σ.

lation shown has used a PPAC position resolution of 0.9 mm and a resolution from the TPC backgammon ranging from 3–5.5 mm; the backgammon resolution depends on the amount of energy deposited. The agreement is quite good, except near the end region where straggling effects are observed in the experimental data but not included in the simulation.

Appendix E

Readout Pad Channel Mapping

To properly decode and interpret the data, it is necessary to know the correspondence between the physical signal lines and assigned channel numbers. For most cases in this thesis, such technical details are omitted owing to the fact that it is arbitrary and specific to the experiment; however, the feedthrough cabling for the low-gain pads of the GEM-MSTPC show some systematic inversions which affect all the experiments conducted with the apparatus. The swapping of these neighboring channels was not noticed until the preparation for the fourth experiment using this TPC (with ^{30}S + α being the second such experiment). The author determined these inversions by use of a digital multimeter channel-by-channel for the entire system. Because the readout cables connect to the TPC with a definite polarity (making the left and right channel mappings mirror images of one another in principle), but the neighbor-swapping does not have mirror symmetry, deducing the correct mapping is not entirely trivial. However, the erroneous inversions are identical for each such feedthrough, suggesting some global mistake in their production. The mapping scheme is shown in Figure E.1. Note that the counting indices for the channel begin with the first element as number 0, because this is the standard method used for accessing array elements in C++.

The preamplifiers each have 24 channels, thus the mapping scheme is divided according to one block per preamplifier (denoted by the numbers 1–4). As each flash ADC board has three 8-channel flash ADC modules, each block is subdivided into three parts. The subdivision helps to visually group the local inversions which occur between the

preamplifier (24-channel output) and the flash ADC (8-channel input); although these inversions are illustrated for clarity, they should not be confused with the neighbor-swapping in the feedthrough which exist by pure accident rather than design simplicity.

Left Upstream – 1

Physical Readout	L23	L22	L21	L20	L19	L18	L17	L16	L15	L14	L13	L12	L11	L10	L9	L8	L7	L6	L5	L4	L3	L2	L1	L0
Feedthrough Input	1A	1B	1C	1D	1E	1F	1G	1H	1I	1J	1K	1L	1M	1N	1O	1P	1Q	1R	1S	1T	1U	1V	1W	1X
Feedthrough Output	1A	1B	1C	1D	1F	1E	1H	1G	1J	1I	1L	1K	1M	1N	1O	1P	R1	Q1	1S	1T	1U	1V	1W	1X
Pad Correspondence	L23	L22	L21	L20	L18	L19	L16	L17	L14	L15	L12	L13	L11	L10	L9	L8	L6	L7	L5	L4	L3	L2	L1	L0
FADC Input Channel	7	6	5	4	3	2	1	0	15	14	13	12	11	10	9	8	23	22	21	20	19	18	17	16
Data Channel	**0**	**1**	**2**	**3**	**4**	**5**	**6**	**7**	**8**	**9**	**10**	**11**	**12**	**13**	**14**	**15**	**16**	**17**	**18**	**19**	**20**	**21**	**22**	**23**
Pad Mapping	**L17**	**L16**	**L19**	**L18**	**L20**	**L21**	**L22**	**L23**	**L8**	**L9**	**L10**	**L11**	**L13**	**L12**	**L15**	**L14**	**L0**	**L1**	**L2**	**L3**	**L4**	**L5**	**L7**	**L6**

Right Upstream – 2

Physical Readout	R0	R1	R2	R3	R4	R5	R6	R7	R8	R9	R10	R11	R12	R13	R14	R15	R16	R17	R18	R19	R20	R21	R22	R23
Feedthrough Input	2A	2B	2C	2D	2E	2F	2G	2H	2I	2J	2K	2L	2M	2N	2O	2P	2Q	2R	2S	2T	2U	2V	2W	2X
Feedthrough Output	2A	2B	2C	2D	2F	2E	2H	2G	2J	2I	2L	2K	2M	2N	2O	2P	2R	2Q	2S	2T	2U	2V	2W	2X
Pad Correspondence	R0	R1	R2	R3	R5	R4	R7	R6	R9	R8	R11	R10	R12	R13	R14	R15	R17	R16	R18	R19	R20	R21	R22	R23
FADC Input Channel	31	30	29	28	27	26	25	24	39	38	37	36	35	34	33	32	47	46	45	44	43	42	41	40
Data Channel	**24**	**25**	**26**	**27**	**28**	**29**	**30**	**31**	**32**	**33**	**34**	**35**	**36**	**37**	**38**	**39**	**40**	**41**	**42**	**43**	**44**	**45**	**46**	**47**
Pad Mapping	**R6**	**R7**	**R4**	**R5**	**R3**	**R2**	**R1**	**R0**	**R15**	**R14**	**R13**	**R12**	**R10**	**R11**	**R8**	**R9**	**R23**	**R22**	**R21**	**R20**	**R19**	**R18**	**R16**	**R17**

Left Downstream – 3

Physical Readout	L47	L46	L45	L44	L43	L42	L41	L40	L39	L38	L37	L36	L35	L34	L33	L32	L31	L30	L29	L28	L27	L26	L25	L24
Feedthrough Input	3A	3B	3C	3D	3E	3F	3G	3H	3I	3J	3K	3L	3M	3N	3O	3P	3Q	3R	3S	3T	3U	3V	3W	3X
Feedthrough Output	3A	3B	3C	3D	3F	3E	3H	3G	3J	3I	3L	3K	3M	3N	3O	3P	3R	3Q	3S	3T	3U	3V	3W	3X
Pad Correspondence	L47	L46	L45	L44	L42	L43	L40	L41	L38	L39	L36	L37	L35	L34	L33	L32	L30	L31	L29	L28	L27	L26	L25	L24
FADC Input Channel	55	54	53	52	51	50	49	48	63	62	61	60	59	58	57	56	71	70	69	68	67	66	65	64
Data Channel	**48**	**49**	**50**	**51**	**52**	**53**	**54**	**55**	**56**	**57**	**58**	**59**	**60**	**61**	**62**	**63**	**64**	**65**	**66**	**67**	**68**	**69**	**70**	**71**
Pad Mapping	**L41**	**L40**	**L43**	**L42**	**L44**	**L45**	**L46**	**L47**	**L32**	**L33**	**L34**	**L35**	**L37**	**L36**	**L39**	**L38**	**L24**	**L25**	**L26**	**L27**	**L28**	**L29**	**L31**	**L30**

Right Downstream – 4

Physical Readout	R24	R25	R26	R27	R28	R29	R30	R31	R32	R33	R34	R35	R36	R37	R38	R39	R40	R41	R42	R43	R44	R45	R46	R47
Feedthrough Input	4A	4B	4C	4D	4E	4F	4G	4H	4I	4J	4K	4L	4M	4N	4O	4P	4Q	4R	4S	4T	4U	4V	4W	4X
Feedthrough Output	4A	4B	4C	4D	4F	4E	4H	4G	4J	4I	4L	4K	4M	4N	4O	4P	4R	4Q	4S	4T	4U	4V	4W	4X
Pad Correspondence	R24	R25	R26	R27	R29	R28	R31	R30	R33	R32	R35	R34	R36	R37	R38	R39	R41	R40	R42	R43	R44	R45	R46	R47
FADC Input Channel	79	78	77	76	75	74	73	72	87	86	85	84	83	82	81	80	95	94	93	92	91	90	89	88
Data Channel	**72**	**73**	**74**	**75**	**76**	**77**	**78**	**79**	**80**	**81**	**82**	**83**	**84**	**85**	**86**	**87**	**88**	**89**	**90**	**91**	**92**	**93**	**94**	**95**
Pad Mapping	**R30**	**R31**	**R28**	**R29**	**R27**	**R26**	**R25**	**R24**	**R39**	**R38**	**R37**	**R36**	**R34**	**R35**	**R32**	**R33**	**R47**	**R46**	**R45**	**R44**	**R43**	**R42**	**R40**	**R41**

Figure E.1: Pad mapping diagram for the low-gain section of the GEM-MSTPC. The four blocks represent the left-upstream, right-upstream, left-downstream, and right-downstream sections, respectively. The physical readout enumeration runs from 0 to 47 for a total of 48 pads, with the prefix ('L' or 'R') corresponding to the left or right side, respectively. The signals are grouped in sets of 24 because this is the capacity of the preamplifiers, which are identified in the feedthrough via numbers 1–4, respectively. For distinction, the feedthrough channels are enumerated by letters A–X rather than numbers. Inversions are highlighted in color. The inversion between the *FADC Input Channel* and the *Data Channel* merely occurs in the cabling which splits the 24 channel preamplifier output into the sets of 8 channel flash ADC inputs. However, the feedthrough neighbor-swapping has a unique effect on each block. The final two rows of each block show the mapping between the raw data channel (in sequential order) and the corresponding pad. See the text.

The principle of chiral symmetry in the mapping is exhibited by comparing the *Physical Readout* and *Feedthrough Input* rows in the upstream or downstream cases. For example, input A of preamplifier 1 ('1A') is L23 and input A of preamplifier 2 ('2A') is R0; conversely, input X of preamplifier 2 ('2X') is R23 whereas input X of preamplifier 1 ('1X') is L0. As the neighbor-swapping in the feedthrough does not have chiral symmetry, the result is that the *Pad Mapping* of the left and right sides of the same pad in the raw data are not necessarily in the same order. Consider the first eight pads, where the left side is mapped as L0, L1, L2, L3, L4, L5, L7, L6 whereas the right side is mapped as R6, R7, R4, R5, R3, R2, R1, R0; specifically, L4 & L5 are in the correct order ('S' and 'T' are not swapped), but R4 & R5 are inverted ('E' and 'F' are swapped). So long as the mapping shown here is provided to the analysis routine, these neighbor-swapping problems are resolved. Once this was done, some jitter in the Bragg curve was removed, giving confidence in this mapping structure.

The high-gain pad mapping is not shown here because there is no neighbor-swapping in the feedthrough (again, determined with a multi-meter). The high-gain feedthrough cables connecting to the TPC have a different layout, because the high-gain pads are split into six sets of 8 channels each. Thus, we conclude it is at this point that the low-gain pad feedthrough has the cable order mixed up.

It is, of course, possible to fabricate new low-gain feedthrough cabling for future experiments with the GEM-MSTPC. However, since we now know the proper mapping to use, this is unnecessary and could introduce further problems that are not immediately recognized. Figure E.1 shows clearly that, even without neighbor-swapping, determining the proper channel mapping takes some careful consideration.

Appendix F

Position Determination from Backgammon Pad

The design concept of the backgammon readout pattern is that the lateral position can be determined by comparing the charge collected on opposite sides, Q_1 and Q_2, respectively. If we assume that the amount of energy deposited is constant over the pad ($dE/dx = 0$), then the charge collected is directly proportional to the length of the track of ionizing radiation. The difference of charges Q_1 and Q_2 over the sum of the two charges yields a *charge ratio* which represents how far the pad crossing point is from the center of the pad, either laterally or in depth. In order to convert this unitless ratio into a distance, one merely needs to multiply it by half the width of the pad W as stated previously:

$$X_{\text{raw}} = \frac{W}{2}\frac{Q_1 - Q_2}{Q_1 + Q_2}, \tag{3.4.1}$$

which can just as easily yield the depth of the pad crossing position if one instead uses the pad size S instead of the width. It is simple to demonstrate that if one fixes the pad crossing position, the charge ratio so derived does not depend on the incident angle θ of the ionizing radiation, illustrated in Figure F.1.

For convenience, the figure labels the *projected* distance the radiation travels over each side of the pad as $Q_{1,2}$. The actual distance traveled by the radiation over each pad are the hypotenuses of the yellow triangles, equal to $Q_1/\cos(\theta)$ and $Q_2/\cos(\theta)$,

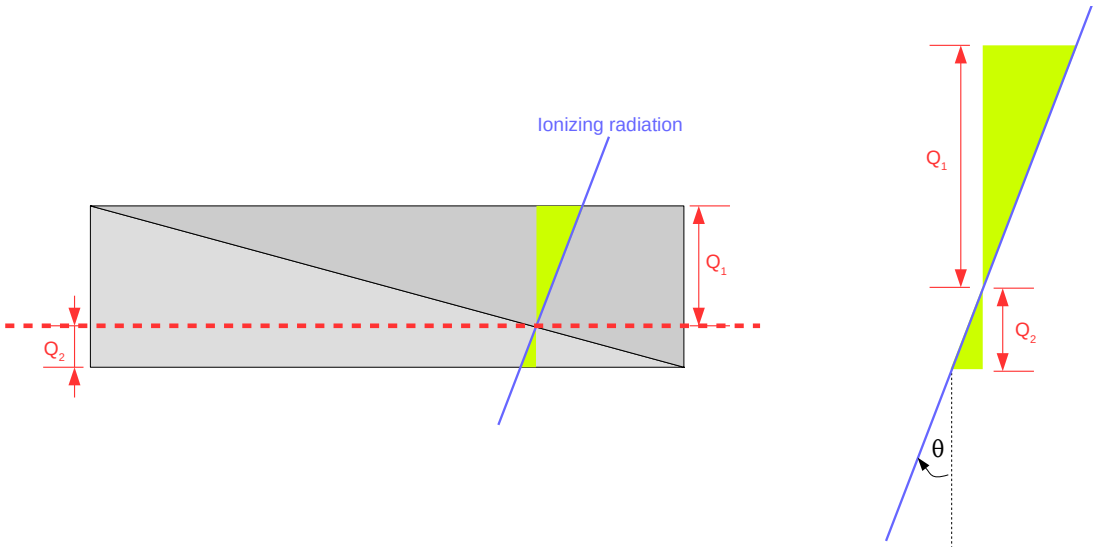

Figure F.1: Illustrated example of the geometry of ionizing radiation passing over a backgammon-type readout pad. The left side shows the backgammon configuration in grey-scale; the inclined ionizing radiation is the blue line; the pad crossing point is shown as a red dashed line; the collected charges $Q_{1,2}$ are proportional to the projected distances the radiation travels over each pad; yellow triangles allow one to compare the path of radiation at an inclined angle to radiation normal to the backgammon pad. The right side is an expanded view near the radiation track, including the incident angle θ. See the text.

respectively. If these modified values are inserted to Equation 3.4.1,

$$X_{\text{raw}} = \frac{W}{2}\frac{(Q_1/\cos(\theta)) - (Q_2/\cos(\theta))}{(Q_1/\cos(\theta)) + (Q_2/\cos(\theta))}, \tag{F.0.1}$$

it is clear to see that the dependence on θ cancels out. Thus, the determination of the pad crossing point does not depend on the incident angle of the radiation, so long as all the charge is collected. However, the pad crossing position is not the value of interest; the position one wishes to extract is defined as the position where the radiation crosses the center of the pad, not the position where the radiation crosses from one pad to another that is measured.

The relation between the pad crossing position and the defined position ΔX is illustrated in Figure F.2. As stated above, the charge ratio easily yields the pad crossing depth

$$Z_{\text{raw}} = \frac{S}{2}\frac{Q_1 - Q_2}{Q_1 + Q_2}, \tag{F.0.2}$$

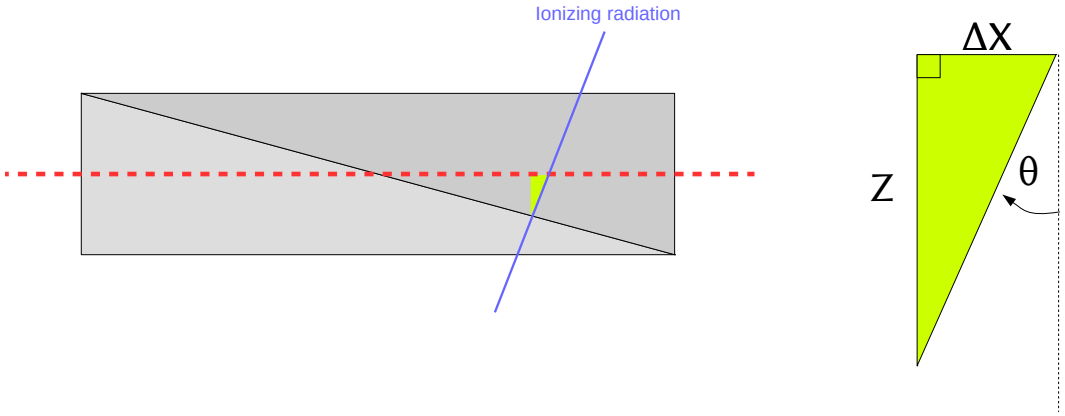

Figure F.2: Illustrated example of the geometry of ionizing radiation passing over a backgammon-type readout pad. The left side shows the backgammon configuration in grey-scale; the inclined ionizing radiation is the blue line; the red dashed line bisects the backgammon pad; the yellow triangle allows one to compare the path of radiation at an inclined angle to radiation normal to the backgammon pad. The right side is an expanded view near the radiation track, including the incident angle θ, the difference ΔX between the pad crossing point and the defined position, and the depth Z of the pad crossing position. See the text.

which does not depend on θ. The correction ΔX is clearly a function of angle and pad crossing point as

$$\Delta X = \frac{Z}{\tan(90^\circ - \theta)}. \tag{F.0.3}$$

As $\theta \to 0^\circ$ the denominator goes to infinity so $\Delta X \to 0$, because for normal radiation of course the lateral pad crossing position and the defined position are equal. Conversely, for a relatively large inclination angle (considering the experimental setup) such as $\theta = 45^\circ$, $\Delta X = Z$, some fraction times half the pad size $S/2$. As such, the equation also indicates that the correction factor increases as the radiation becomes more non-central, as $0 \leq Z \leq S/2$. Because the pad size S is merely 4 mm, this correction so derived should be typically of the order of 2 mm or less, which is certainly smaller than the practical position resolution achieved of around 5 mm. The correction is difficult to implement in practice, because without additional information θ is unknown. It also indicates that the effect results from the finite size of the backgammon pad. In general, the correction should be negligible unless the radiation is highly inclined **and** non-central.

As discussed in Sections D.1.4.1 and 3.4.2.1, despite extensive attempts, variations of any of the parameters in Equation 3.4.2—W, $c_{1,2}$, and $X_\theta(Z)$—could not yield satisfactory and globally consistent results. Thus we decided to examine the behavior of the raw charges $Q_{1,2}$. Here we present the raw active target data from the post-experimental α-calibration runs for the central GEM in coincidence with SSD 1a. For this GEM, the distance between the edge of the bridge and the edge of the GEM is 24.5 mm, and as the SSD strip size is approximately 11 mm, three distinct α-particle tracks can be created gating on one of three individual SSD strips. α-particles from this source hitting other strips of SSD 1a do not traverse an active region of the target. The SSD strips are enumerated increasing from right to left, so that for SSD 1a which is located downstream and to the right side of the beam axis, a smaller strip number is further from the beam axis. Explicitly in relation to the central GEM from beam's perspective, strip 3 is near its right edge, strip 4 is over the center of its right side, and strip 5 is near to the right side of the bridge. Thus, when comparing the charge collected on the left and right side of a central pad, we expect the largest charge disparity when gating on strip 3 and a lesser degree of disparity when gating on strip 5. This disparity is observed; however, as the charge in the left side increases, the charge in the right side should decrease, because the total charge deposited should be conserved,* considering that the inclination of the track changes only a small amount as a function of the strip gate. Although the charge collected by the far side of the pad in relation to the ion track shows the anticipated behavior, the charge collected by the side of the pad near to the ion track appears somehow diminished.

The data are shown in Figures F.3–F.8 organized by pad number. The left (right) panels show the charge collected by the left (right) side of a pad, and the gate for the SSD strip increases from top to bottom within the set of histograms in each figure. The charge collected by the left side of each pad always increases with the SSD strip gate, as expected. In contrast, the charge collected by the right side of each pad shows no clear dependence on the SSD strip gate; pad 1 in Figure F.3 shows a similar trend more like one expects, but pad 6 in Figure F.8 shows the opposite effect!

*Although the α-source contains three radionuclides and energy loss is a random process, the statistics collected are great enough to make this general discussion.

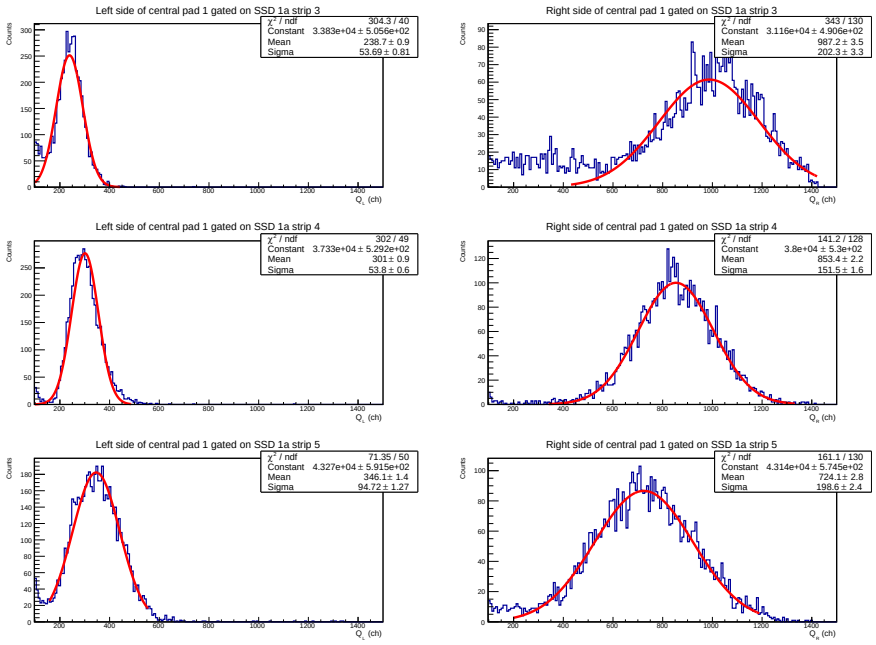

Figure F.3: Comparison of the charge collected at the left and right side of central pad 1 during alpha calibration gated on different SSD strips. See the text.

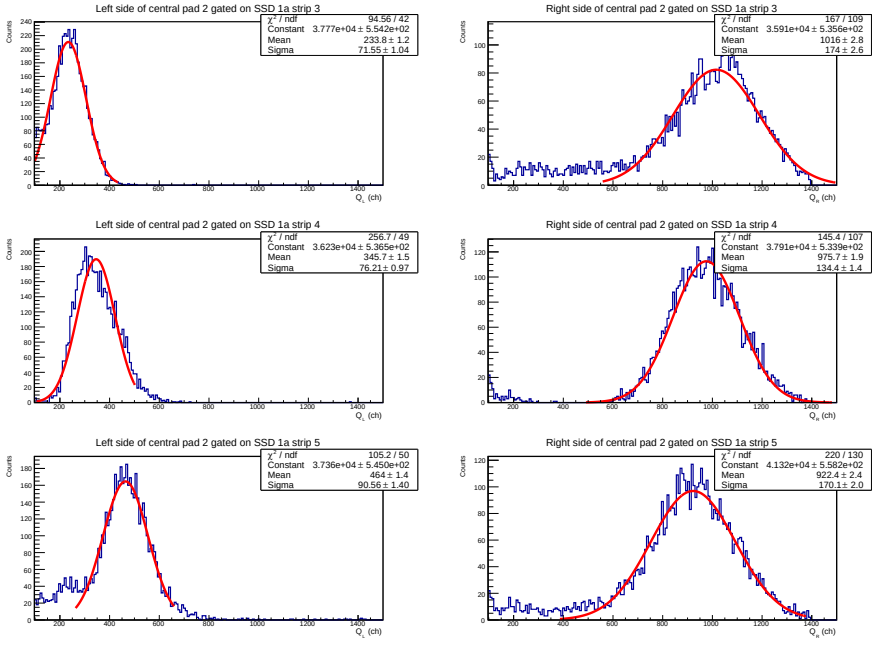

Figure F.4: Comparison of the charge collected at the left and right side of central pad 2 during alpha calibration gated on different SSD strips. See the text.

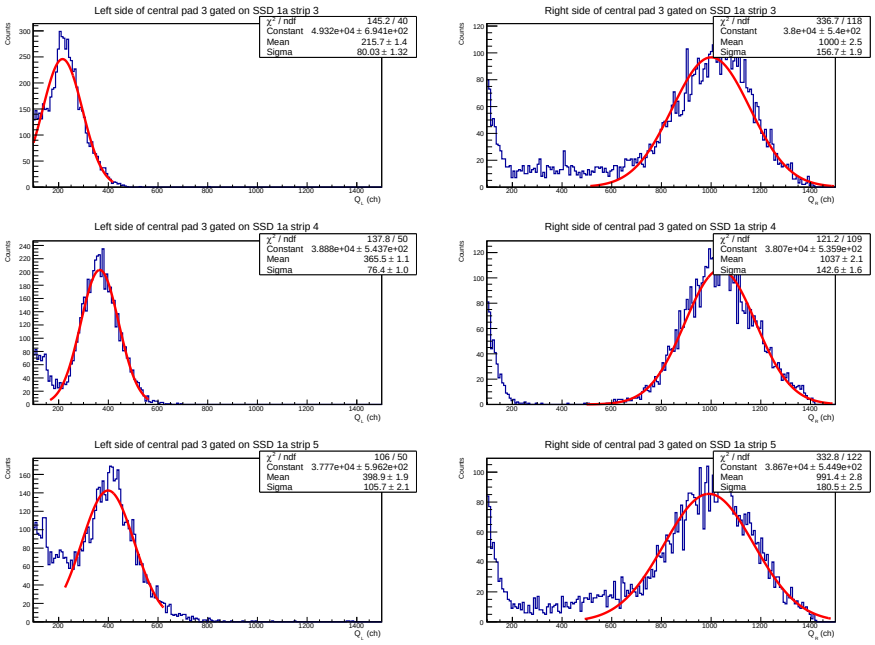

Figure F.5: Comparison of the charge collected at the left and right side of central pad 3 during alpha calibration gated on different SSD strips. See the text.

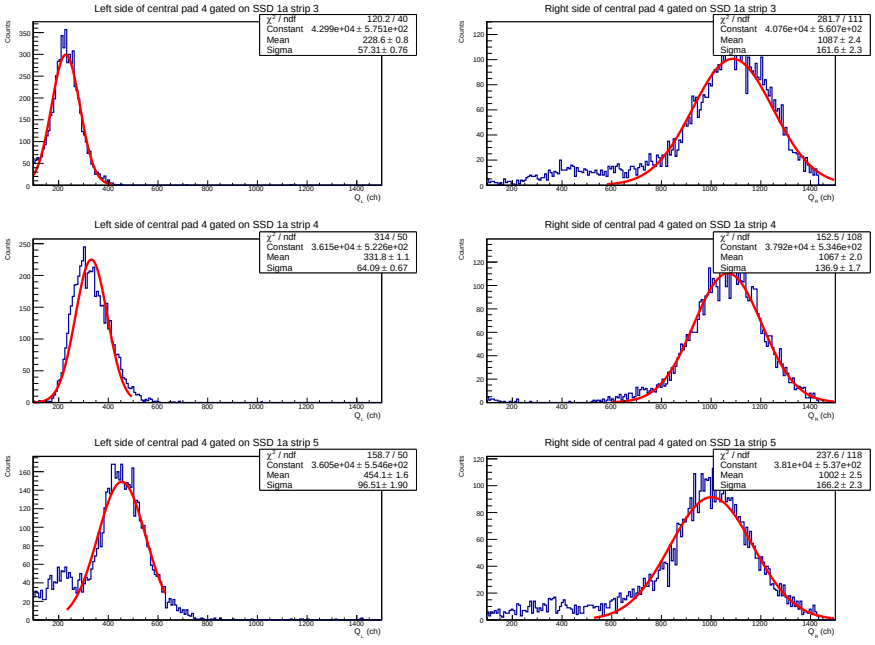

Figure F.6: Comparison of the charge collected at the left and right side of central pad 4 during alpha calibration gated on different SSD strips. See the text.

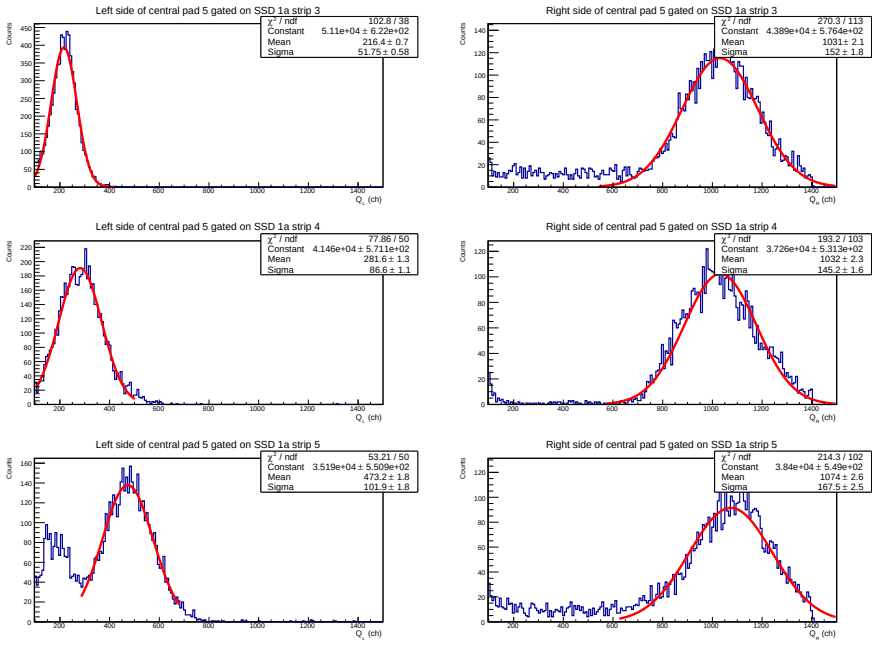

Figure F.7: Comparison of the charge collected at the left and right side of central pad 5 during alpha calibration gated on different SSD strips. See the text.

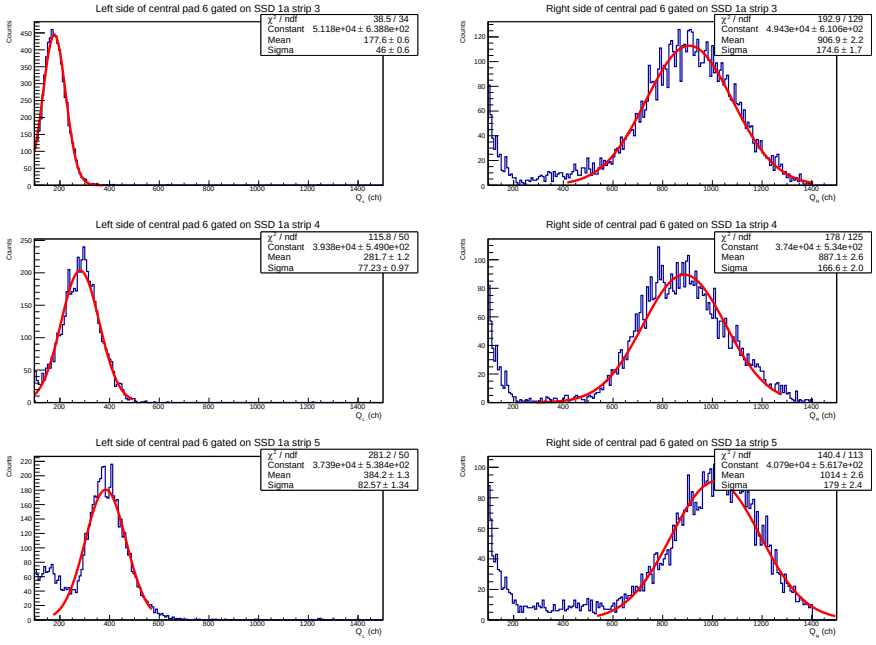

Figure F.8: Comparison of the charge collected at the left and right side of central pad 6 during alpha calibration gated on different SSD strips. See the text.

Appendix G

Physics Run Scalers

This appendix contains a table with selected scalers from the physics runs for the ^{30}S+α experiment. The triggering conditions D/S and SSD-OR were defined in Section 3.1. 'Ungated' is the number of triggers presented to the system, whereas 'Gated' are the ones which are not vetoed by a busy signal. Not all the runs are used in the physics analysis, mostly because of tuning the active target or a discharge, except for runs 1024 and 1027 where we changed the beam optics for calibration purposes. Data were accumulated for approximately 60 hours.

G.1 Tabulated physics run data

The scalers are shown in Table G.1.

Table G.1: Table of selected scalers for the physics runs.

Run N°	Ungated	Gated	D/S	SSD-OR	Seconds	Used?
1001	7445	7420	2630	4815	6870.9	Yes
1002	4152	4140	1330	2822	3121.7	Yes
1003	11658	11602	6026	5632	7205.6	Yes
1004	8817	8789	4757	4060	5723.3	Yes
1005	2418	2402	1341	1077	1024.1	Yes
1006	779	779	360	419	400.7	No

Table G.1: Table of selected scalers for the physics runs.

Run N°	Ungated	Gated	D/S	SSD-OR	Seconds	Used?
1007	1021	1013	493	528	536.1	No
1008	13444	13353	6384	7060	7215.0	No
1009	11584	11517	6061	5523	5659.7	No
1010	1390	1374	756	634	349.2	No
1011	24001	23845	6912	17089	7869.4	Yes
1012	13406	13341	4209	9197	7331.8	Yes
1013	11557	11505	3864	7693	6859.1	Yes
1014	3464	3442	1216	2248	2471.6	Yes
1015	6703	6650	2420	4283	1960.5	Yes
1016	269	264	116	153	126.6	No
1017	30836	30527	10893	19943	6850.6	Yes
1018	16799	16623	5932	10867	5060.3	Yes
1019	33087	32828	13933	19154	7099.8	Yes
1020	2940	2919	1568	1372	713.9	Yes
1021	18831	18728	8162	10669	8278.7	Yes
1022	28831	28646	11399	17432	9280.7	Yes
1023	67	65	32	35	32.1	Yes
1024	10179	9206	357	447	1218.7	No
1025	23262	23078	12053	11209	5622.0	Yes
1026	40849	40424	19508	21341	6997.4	Yes
1027	19936	19816	9222	10714	6782.5	No
1028	31480	31255	14115	17365	7700.0	Yes
1029	25736	25562	11255	14481	7127.0	Yes
1030	29687	29466	13612	16075	7488.6	Yes
1031	25667	25504	11759	13908	7149.5	Yes
1032	17250	17131	7822	9428	4443.1	Yes
1033	24941	24754	10793	14148	7177.5	Yes

Table G.1: Table of selected scalers for the physics runs.

Run N°	Ungated	Gated	D/S	SSD-OR	Seconds	Used?
1034	23596	23454	10922	12673	8166.7	Yes
1035	21968	21842	10407	11561	8221.5	Yes
1036	28467	28231	12903	15564	7945.1	Yes
1037	28044	27827	12374	15670	7403.2	Yes
1038	444	437	206	238	165.7	Yes
1039	25328	25123	11007	14321	6896.8	Yes
1040	3487	3461	1337	2150	649.5	Yes
1041	8766	8734	3275	5491	3608.9	Yes
1042	19932	19869	7448	12484	9336.7	Yes
1043	7287	7265	2747	4540	2886.1	Yes

Appendix H

Beam Energy of ^{22}Mg After the Wien Filter

As discussed in Section 3.4.3.1, the energy loss of the heavy beam ions employed in thick-target, inverse-kinematics experiments is a crucial quantity to the derived physics, as it determines the center-of-mass energy. Empirical models are often relied upon for the energy loss calibration, which may or may not be fit to data taken during the physics experiment of interest. Moreover, when such data are taken, the energy range explored may be limited, the detectors may not be calibrated absolutely with heavy ions, there may be additional materials inserted to the beam line (causing systematic errors), and the energy loss calibration is rarely performed using more than one RI species in the cocktail beam self-consistently.

In this Appendix, we show an ideal example of precisely measuring the beam energy from a CRIB experiment using a ^{22}Mg RIB with the GEM-MSTPC active target, performed in 2011 roughly one year after the present work. A notable difference between the ^{30}S and ^{22}Mg experiments as relevant to this topic is the author derived and acquired data in a simple manner to absolutely calibrate the silicon detectors with heavy ions over an energy range comparable to the RIB.

Figure H.1 shows a tailor-made primary beam cocktail for absolute energy calibration for heavy ions. A relatively thick degrader (30 μm of Al) was inserted as the primary target at F0, while an arbitrarily low $B\rho$ was selected with a tight momentum selection

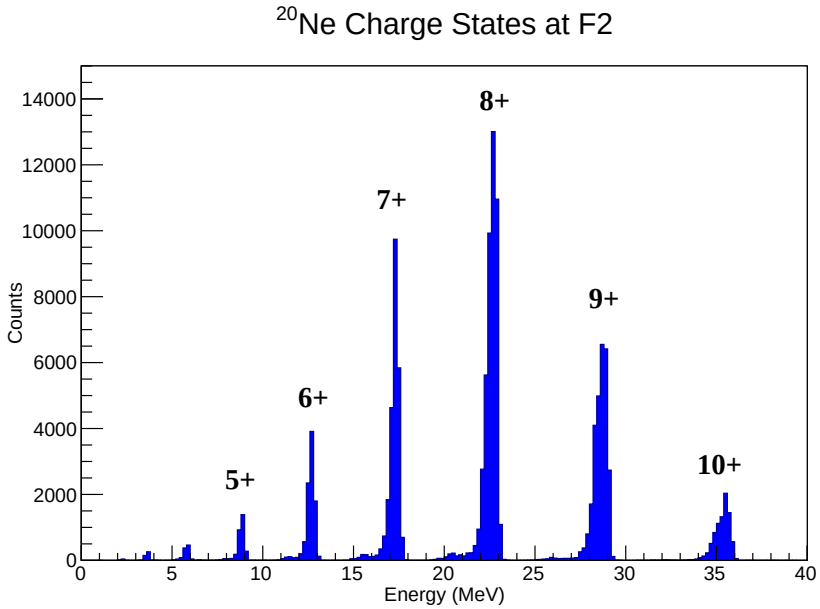

Figure H.1: An array of charges states for the heavily-degraded primary beam ^{20}Ne at the achromatic focal plane F2, as measured by a previously calibrated silicon detector with no intervening materials between the momentum selection and the residual energy measurement. Nearly all charge states of the primary beam are observed in a single short run of merely 126 seconds (apparently from 10+ down to 3+), providing ample calibration points in a minimum of beam time.

($\frac{\Delta p}{p} \approx 0.1\%$); the result was a low-energy array of charge-states of the primary beam.

We then sent the resulting charge-state cocktail beam to the experimental focal plane, F3, and used the Wien filter to select the charge-states one-by-one. An advantage of this method is that the exact species of the beam ion striking the silicon detector can be known without any beam-line monitors inserted, allowing for absolute calibration with no systematic uncertainties. Several charge-states at the experimental focal plane are shown in Figure H.2. The statistics are significantly lower not only because of the Wien filter selection, but because the strip of the silicon detector making the measurement is not at the ion-optical center of the beam axis. In fact, the beam appeared to predominately strike a neighboring strip with the beams of $^{20}Ne^{10+}$ and $^{20}Ne^{9+}$, and it was necessary to remove the phantom events on the strip of interest where charge was induced by the neighbor.*

*The strip predominately struck in those cases did not have the necessary electronics for a heavy-ion energy measurement.

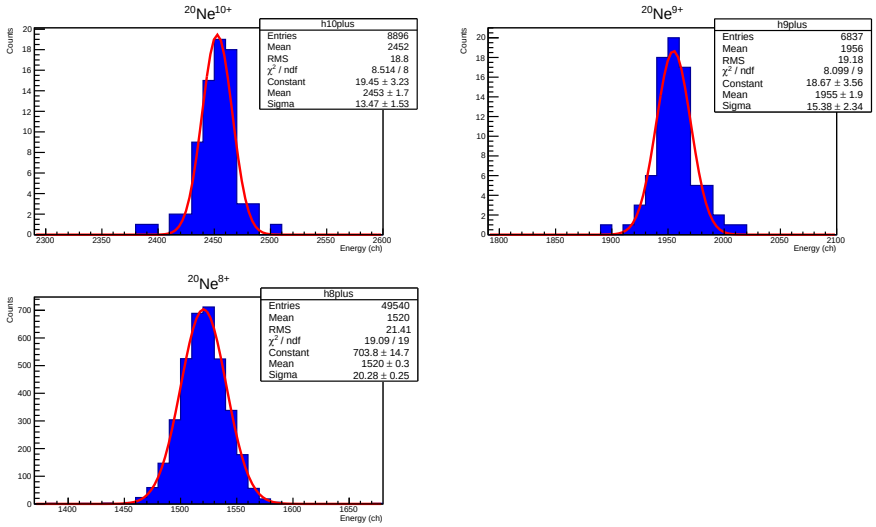

Figure H.2: Three charge-states of ^{20}Ne collected during separate runs using the Wien-filter selection to calibrate a silicon strip for heavy ions at the experimental focal plane.

We then calibrated the heavy-ion energy loss of the RIBs using the heavy-ion calibrated SSD. The results for ^{21}Na and ^{22}Mg after two PPACs is shown in Figure H.3, as one example. An unexpected feature is observed: namely, the modestly non-gaussian shape of the energy distributions, with the RI energies skewed towards one another. Using the nominal beam energies as determined by $B\rho$, it was not possible to reproduce the calibrated beam energies derived from the gaussian fits; in that case, we required to change the nominal PPAC thickness of 19 μm of mylar by $-1\,\mu m$ for ^{21}Na and $+1\,\mu m$ for ^{22}Mg. However, when we instead used the rebinned maxima from the experimental measurements (similar to the mean value over the energy range), the calculations were reproduced with an identical nominal thickness when we similarly skewed the incident beam energy by $\pm 1\%$, respectively, for each ion.[†]

These two RI species were produced by the ^{3}He(^{20}Ne, ^{21}Na)^{2}H and ^{3}He(^{20}Ne, ^{22}Mg)n reactions, and the fully stripped ions ^{21}Na^{11+} and ^{22}Mg^{12+} arrived at the experimental focal plane. This is in analogy to the present experiment, where two RI species were produced by the ^{3}He(^{28}Si, ^{29}P)^{2}H and ^{3}He(^{28}Si, ^{30}S)n reactions, and the fully stripped ions ^{29}P^{15+} and ^{30}S^{16+} arrived at the experimental focal plane. Thus the primary beams

[†]These skews are easily allowed for in the momentum selection at the achromatic focal plane. They are also consistent with the relatively poor historical Wien filter transmission of $\approx 25\%$.

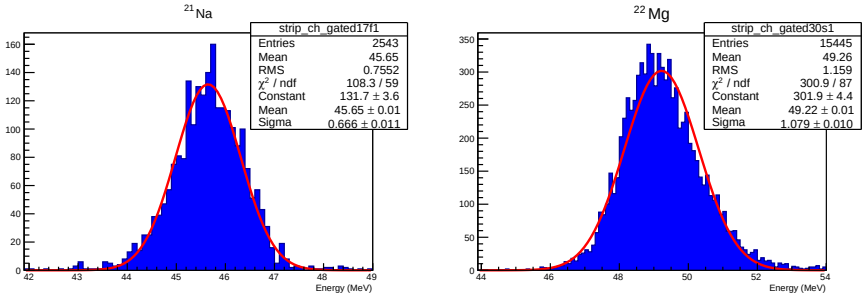

Figure H.3: Calibrated beam energies of ^{21}Na (left) and ^{22}Mg (right) after two PPACs. Note that the distributions are skewed from a gaussian shape, the energies of the two ions being shifted towards each other. Although the statistics are low, the high-statistics run in ^{30}S shows the behavior very clearly in Figure 3.14.

were alpha-nuclei (^{20}Ne and ^{28}Si), the RI beams of interest were $T_z = -1$ nuclei (^{22}Mg and ^{30}S) produced by di-proton transfer, and the main contaminants were $T_z = -\frac{1}{2}$ nuclei (^{21}Na and ^{29}P) produced by single-proton transfer. Thus we can expect the ion-optical behavior between the two experiments to exhibit analogous behavior, which can be seen by a comparison of Figures H.3 and 3.14.

Using these modestly skewed incident beam energies, measured with the absolutely calibrated SSD, it was possible to reproduce the energy losses measured in the ^{22}Mg experiment self-consistently for both RI species using the nominal material thicknesses with `enewz`.

Appendix I

Calibration Parameters

Tabulated calibration parameters are listed here for reference. If a specific calibration equation is not referenced and the parameters are tabulated as 'offset' and 'gain,' the standard calibration equation

$$\text{Calibrated} = \text{Gain}(\text{Raw} - \text{Offset}) \tag{I.0.1}$$

is used; note that because offsets are usually expected to be positive, the linear equation itself has a negative sign, and that the zeroth order linear term is actually −Offset/Gain. Such a linear fit is simply extracted from a plot of the raw vs. calibrated data.

Table I.1: PPAC calibration parameters. Here PPACa and PPACb are abbreviated as 'a' and 'b,' respectively.

	aX	aY	bX	bY
PPAC Offset (ns)	0.92	1.58	0.17	0.11
Line Offset (ns)	0.0	-0.22	-4.3	-1.0
Position Gain (mm/ns)	0.6200	0.6210	0.6205	0.6125
Geometry Offset (mm)	-0.60	0.0	0.0	0.0

Table I.2: PPAC delay parameters for the downscale trigger. Units are in channels.

	X1	X2	Y1	Y2
PPACa	8246	8244	8244	8242
PPACb	8247	8246	8250	8248

Table I.3: Active target low-gain Y calibration coefficients, extracted from Figure D.6 and used to produce Figure 3.6(a). The offset is in bins of 20 ns, and the gain can be considered the average electron drift velocity in units of mm/20 ns.

Pad (#)	Offset	Gain
0	0.	1.
1	82.7561	0.49569
2	82.6844	0.492829
3	82.6175	0.489467
4	82.8402	0.49753
5	82.855	0.499552
6	82.7769	0.498452
7	82.6236	0.499131
8	83.1335	0.495347
9	82.8258	0.497693
10	83.1452	0.497068
11	83.215	0.495938
12	83.042	0.494658
13	83.1391	0.497776
14	83.3684	0.508436
15	83.2467	0.504777
16	83.1503	0.50153
17	0.	1.
18	83.4992	0.504669
19	83.4803	0.504848
20	83.3935	0.503347
21	83.2244	0.500503
22	83.2044	0.498747
23	83.1135	0.496826

Pad (#)	Offset	Gain
24	0.	1.
25	0.	1.
26	0.	1.
27	83.6659	0.499885
28	83.2716	0.492709
29	83.3184	0.495124
30	83.1966	0.496732
31	83.229	0.506069
32	0.	1.
33	0.	1.
34	0.	1.
35	0.	1.
36	0.	1.
37	0.	1.
38	0.	1.
39	0.	1.
40	83.7742	0.618299
41	82.5666	0.59743
42	83.7187	0.637739
43	81.2353	0.556725
44	0.	1.
45	0.	1.
46	0.	1.
47	0.	1.

Table I.4: SSD 1a pad energy calibration parameters, depending on which strip is hit.

Strip	Offset	Gain
1	-175.146863845	0.009805
2	-176.3853942927	0.009777
3	-170.2845865803	0.009881
4	-181.0720526262	0.009729

Strip	Offset	Gain
5	-172.0350774054	0.010206
6	-168.3535821039	0.010371
7	-169.2308132329	0.010489
8	-171.0663206459	0.010404

Table I.5: Extracted geometric corrections for field cage alignment for the beam GEM.

Pad (#)	Z (mm)	X_θ (mm)	Pad (#)	Z (mm)	X_θ (mm)
0	84.75	5.21587	24	180.75	9.04549
1	88.75	5.37543	25	184.75	9.20505
2	92.75	5.535	26	188.75	9.36462
3	96.75	5.69457	27	192.75	9.52419
4	100.75	5.85414	28	196.75	9.68376
5	104.75	6.0137	29	200.75	9.84332
6	108.75	6.17327	30	204.75	10.0029
7	112.75	6.33284	31	208.75	10.1625
8	116.75	6.49241	32	212.75	10.322
9	120.75	6.65197	33	216.75	10.4816
10	124.75	6.81154	34	220.75	10.6412
11	128.75	6.97111	35	224.75	10.8007
12	132.75	7.13068	36	228.75	10.9603
13	136.75	7.29024	37	232.75	11.1199
14	140.75	7.44981	38	236.75	11.2794
15	144.75	7.60938	39	240.75	11.439
16	148.75	7.76895	40	244.75	11.5986
17	152.75	7.92851	41	248.75	11.7581
18	156.75	8.08808	42	252.75	11.9177
19	160.75	8.24765	43	256.75	12.0773
20	164.75	8.40722	44	260.75	12.2368
21	168.75	8.56678	45	264.75	12.3964
22	172.75	8.72635	46	268.75	12.556
23	176.75	8.88592	47	272.75	12.7155

Table I.6: Extracted geometric corrections for field cage alignment for the central GEM.

Pad (#)	Z (mm)	X_θ (mm)	Pad (#)	Z (mm)	X_θ (mm)
0	292.25	13.4934	4	308.25	14.1317
1	296.25	13.653	5	312.25	14.2913
2	300.25	13.8126	6	316.25	14.4508
3	304.25	13.9721	7	320.25	14.6104

Table I.7: Active target low-gain X calibration coefficients, extracted from Figure D.14b and used in Equation 3.4.2 to produce Figure 3.11.

Channel	c_1	c_2
0	0	0
1	1.0598	0.94018
2	0.99809	1.0019
3	0.99459	1.0054
4	0.97469	1.0253
5	0.99992	1.0001
6	0.98231	1.0177
7	0.97762	1.0224
8	0.97919	1.0208
9	0.99799	1.002
10	0.98537	1.0146
11	0.98989	1.0101
12	0.97818	1.0218
13	1.0051	0.99486
14	0.99036	1.0096
15	1.0016	0.99842
16	0	0
17	0.9585	1.0415
18	0.97374	1.0263
19	0.97923	1.0208
20	0.97693	1.0231
21	0.99971	1.0003
22	0.98715	1.0128
23	0.98697	1.013

Channel	c_1	c_2
24	0	0
25	0	0
26	0	0
27	0.98547	1.0145
28	1.0175	0.98246
29	0.98844	1.0116
30	1.0117	0.98835
31	1.0071	0.99294
32	0	0
33	0	0
34	0	0
35	0	0
36	0	0
37	0	0
38	0	0
39	0	0
40	1.0254	0.97461
41	1.0241	0.9759
42	0.95379	1.0462
43	1.0824	0.91758
44	0	0
45	0	0
46	0	0
47	0	0

Appendix **J**

Vertex Searching in the Active Target

This Appendix presents a method of searching for scattering vertices within the active target data. However, the poor resolution for the X position as determined by the charge-division of 3 to 5.5 mm, as presented in Sections 3.4.2 & D.1.4.1, caused the method to fail owing to the small laboratory scattering angle of the heavy recoils.

J.1 Vertex Searching Method

As most of the SSD data were zero-suppressed, the first place one can begin is attempting to locate the scattering vertex of the ^{30}S beam and heavy recoil within the active target beam data. When a scattering occurs within the active target, the trajectory of the ^{30}S ion will change, and the Bragg curve should show a modest localized change in the energy deposit, since some energy is taken away by the scattered α particle, and the recoiling heavy nucleus will lose energy according to the stopping power as shown in Figure 3.20, where the 'beam' energy (actually the recoil energy) has suddenly changed.

If a scattering event occurred, it could either take place upstream of the active region or within the active region. These two possibilities are distinct:

1) *Upstream scattering* (in the 83 mm of target gas before the active region)

- We should find a good single linear fit in X vs. Z and Y vs. Z

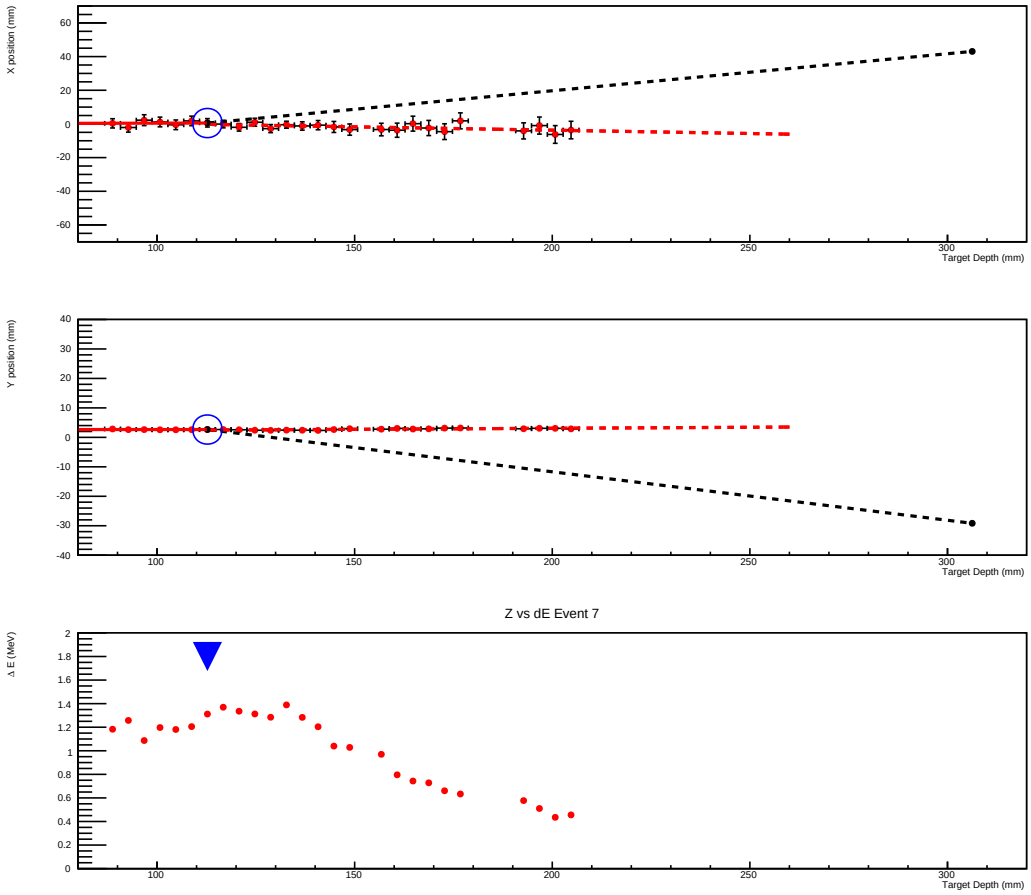

Figure J.1: Sample event where a vertex is identified in blue. The ordinate is always the target depth Z, derived from the pad number. The abscissa in the top panel is the X position derived from the backgammon. The abscissa in the middle panel is the Y position derived from the drift time. The abscissa the lower panel is the energy loss ΔE. Data points from the low-gain pads are in red. The solid red lines shows the linear fits in the region before the vertex, including the upstream PPAC data (not shown here from the scale), the dashed red lines show the linear fits after the vertex. The data point from the high gain region is shown in black. The dashed black line shows the inferred alpha particle track, with a slope of opposite sign to the dashed red line.

– There is no relation with the PPAC data

2) *Active target scattering*

– We should find two pairs of linear fits in X vs. Z and Y vs. Z

– The vertex must be the same

– The first sets of linear fits include the PPAC data

– There should be a local change in the ΔE shape at the vertex

In both cases, the slopes must go opposite to the direction of the α particle detected in the high-gain GEM to conserve momentum, since the beam axis region is blocked by the high-gain bridge. We then compute and compare χ^2_ν (see Appendix C) to distinguish the scattering cases **1)** and **2)**. For *upstream scattering*, we have only one fit in each of X and Y yielding ${}_{\mathbf{1}X}\chi^2_\nu$ and ${}_{\mathbf{1}Y}\chi^2_\nu$, respectively, and the sum of these we denote ${}_{\mathbf{1}}\chi^2_\nu$. For *active target scattering*, we must firstly loop over every pad as a possible vertex. In X and Y we have two fits each, denoted a and b before and after the potential vertex, respectively. Thus we get:

$$ {}_{\mathbf{2}}\chi^2_\nu = {}_{\mathbf{2}X}\chi^2_\nu + {}_{\mathbf{2}Y}\chi^2_\nu = \frac{{}_{\mathbf{2}Xa}\chi^2 + {}_{\mathbf{2}Xb}\,\chi^2}{\mathrm{NDF}_a + \mathrm{NDF}_b} + \frac{{}_{\mathbf{2}Ya}\chi^2 + {}_{\mathbf{2}Yb}\,\chi^2}{\mathrm{NDF}_a + \mathrm{NDF}_b}. \tag{J.1.1} $$

Of course, we have a ${}_{\mathbf{2}}\chi^2_\nu$ for each pad tested, and we select the pad where this value is minimized as the most likely scattering location. Finally, we distinguish the cases **1)** and **2)** as:

If $\big(({}_{\mathbf{1}}\chi^2_\nu < {}_{\mathbf{2}}\chi^2_\nu)$ & $({}_{\mathbf{2}X}\chi^2_\nu > 1$ *or* ${}_{\mathbf{2}Y}\chi^2_\nu > 1)\big)$: *upstream scattering*

Else if $\big(({}_{\mathbf{2}X}\chi^2_\nu < 1)$ & $({}_{\mathbf{2}Y}\chi^2_\nu < 1)\big)$: *active target scattering*

Since any case where $\chi^2_\nu < 1$ cannot be distinguished from another such case, and we additionally have the ΔE constraint for *active target scattering*, we choose *active target scattering* over *upstream scattering* in such situations. A sample event is shown in Figure J.1.

Once we locate the vertex, we can perform all the ^{30}S beam energy loss up to the active target, sum the measured energy loss in each pad up to the scattering vertex, and convert the resulting beam energy to the center-of-mass energy, creating a preliminary energy spectrum, shown in Figure J.2. However, we know that Rutherford scattering physically has a large cross section, as we are exploring alpha scattering below the Coulomb barrier of 7.9 MeV. Thus, the method essentially fails somehow, likely because the laboratory angle of the ^{30}S recoil is small, thus a majority of the vertices so-identified

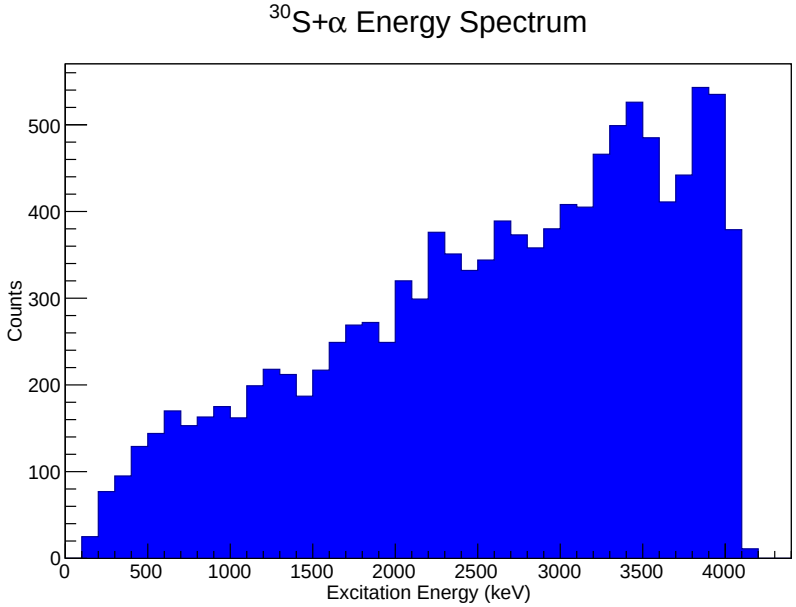

Figure J.2: Energy spectrum of scattered alpha particles gating on the ^{30}S RIB determined by the vertex finder. The gating condition requires five beam pads to fire and a hit in either SSD 1a or 2a. Although hints of several resonances can be seen, low energy events appear outside the region of sensitivity and no trace of Coulomb scattering is observed, which should be physically impossible.

represent noise within the data. The spectrum is weighted towards identifying a scattering location at early pads by including the PPAC data in the first set of linear fits; if one removes the constraint of including the PPAC data, the result is no less physical, as the energy spectrum weights instead towards the central region still without a Coulomb peak – essentially a random number generator.

Appendix K

^{36}Ar(p, t) Experiment at RCNP

As discussed in Section 1.3, a measurement of ^{36}Ar(p, t)^{34}Ar was performed with the Grand RAIDEN spectrograph up to high excitation energy with high resolution to study the ^{30}S(α, p) reaction via the states in the compound nucleus ^{34}Ar [56]. However, because the report is just a preliminary one in a conference proceeding, no analysis nor tabulation of the data were provided, merely one figure. To gain some insight from the figure, we employed a graphical extraction technique to estimate the excitation energies reported. Of course, the calibration or background subtraction may not be finalized by those researchers, and the graphical extraction technique has a systematic error for how well the user can click on the data points (estimated as 10 keV), and does not use any sophisticated fitting procedure on the real data. The states extracted in this manner generally agreed well with the energies reported in a compilation [55], except a couple higher-energy states which were 20 to 30 keV higher than the compilation, giving a basic confidence to this approach. Despite the limitations of this extraction technique, the RCNP experiment is the only other study in the literature reporting highly excited states in ^{34}Ar, and it is a good idea to take some advantage of even the preliminary result.

The graphical extraction was done with the `Graph Digitizing System (GSYS, SyGRD)` developed by the Hokkaido University Nuclear Reaction Data Centre (JCPRG) [110]; a screenshot of the method employed is shown in Figure K.1. Extracted excitation energies E_{ex} are shown in Table K.1, along with the corresponding center-of-mass energy E_{cm} for

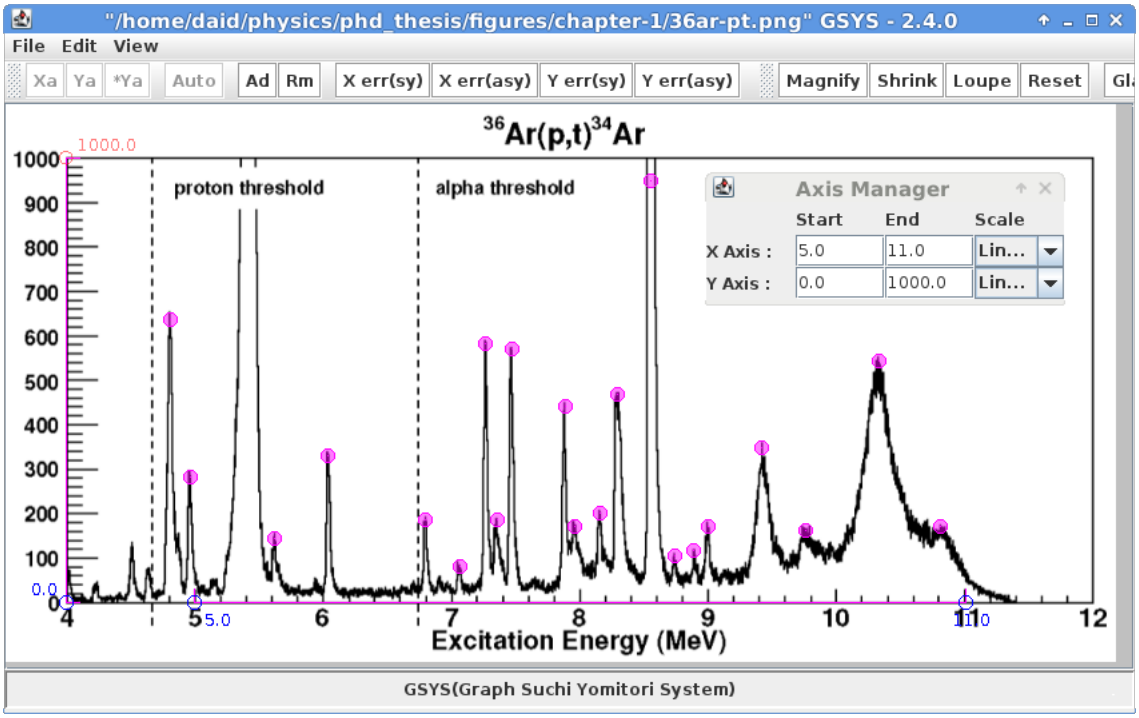

Figure K.1: Screen capture of the GSYS program used on the ^{36}Ar(p, t) spectrum, which was shown as Figure 1.8. Blue dots are the user-input to select points of interest, where it was attempted to deduce the centroids. The user must also define the ordinate and abscissa visually, and input the value for the beginning and end, which can be compared with the location of the pixels of the selected blue dots; the range of the axes is shown in the 'Axis Manager' overlaid window. These results can then be exported to a text file.

the ^{30}S(α, p) reaction, and the Wigner limit for the alpha and protons widths, $W_{\Gamma\alpha}$ and $W_{\Gamma p}$, respectively.

As the RCNP data only provide excitation energies,* some artificial assumptions are required about the quantum properties; we set $J^\pi = 0^+$ for the Wigner-limit calculations. It should be noted that $\omega\gamma$, the resonance strength (see Section 1.2.2), is to first-order independent of the spin-parity when parameterizing the widths based on the Wigner limit (as the penetrability includes the transfer of ℓ), decreasing the width γ while increasing the spin factor ω in the reaction rate. This implies that our arbitrary selection of $J^\pi = 0^+$ does not have a significant effect on $\omega\gamma$ under this picture.

*Even in a future publication with a full analysis of the data, owing to their limited angular range, any experimental determination of J^π will be tentative. There is no way to deduce Γ_α nor Γ_p from a (p, t) study.

Table K.1: Extracted excitation energies E_{ex} in $^{36}\mathrm{Ar(p,t)}^{34}\mathrm{Ar}$ from Figure K.1 above the alpha threshold, the corresponding center-of-mass energy E_{cm} for the $^{30}\mathrm{S}(\alpha,\mathrm{p})$ reaction, and the Wigner limit for the alpha and proton widths, $W_{\Gamma\alpha}$ and $W_{\Gamma p}$, respectively, assuming each state has $J^{\pi} = 0^{+}$. States well below the astrophysically relevant energies of x-ray bursts are neglected for the alpha Wigner limit calculation as they are so tiny.

E_{ex} (MeV)	E_{cm} (MeV)	$W_{\Gamma\alpha}$ (keV)	$W_{\Gamma p}$ (MeV)
6.79	0.05	—	0.4
7.06	0.32	—	0.6
7.26	0.52	—	0.8
7.35	0.61	—	0.1
7.47	0.73	5×10^{-19}	1
7.88	1.14	5×10^{-13}	2
7.96	1.22	3×10^{-12}	2
8.15	1.41	1×10^{-10}	2
8.30	1.56	1×10^{-09}	2
8.55	1.81	3×10^{-08}	2
8.74	2.0	2×10^{-07}	3
8.89	2.15	9×10^{-07}	3
8.99	2.25	2×10^{-06}	3
9.42	2.68	4×10^{-5}	4
9.75	3.01	0.0003	4
10.32	3.58	0.003	5
10.81	4.07	0.01	5

Bibliography

[1] Iliadis, C., "Introduction to Nuclear Astrophysics." *American Institute of Physics Conference Series* **1213** (2010) 3–22.

[2] Eddington, A.S., "The sources of stellar energy." *The Observatory* **42** (1919) 371–376.

[3] Eddington, A.S., "The internal constitution of the stars." *The Observatory* **43** (1920) 341–358.

[4] Rutherford, E., "The scattering of α and β particles by matter and the structure of the atom." *Philosophical Magazine* **21** (1911) 669–688.

[5] Nagaoka, H., "Kinetics of a system of particles illustrating the line and the band spectra and the phenomena of radioactivity." *Philosophical Magazine* **7** (1904) 445–455.

[6] Gamow, G., "Zur Quantentheorie des Atomkernes." *Zeitschrift fur Physik* **51** (1928) 204–212.

[7] Gurney, R.W. & Condon, E.U., "Quantum Mechanics and Radioactive Disintegration." *Physical Review* **33** (1929) 127–140.

[8] Atkinson, R.D.E. & Houtermans, F.G., "Zur Frage der Aufbaumöglichkeit der Elemente in Sternen." *Zeitschrift fur Physik* **54** (1929) 656–665.

[9] Atkinson, R.D., "Atomic Synthesis and Stellar Energy." *The Astrophysical Journal* **73** (1931) 250.

[10] Atkinson, R.D., "Atomic Synthesis and Stellar Energy. II." *The Astrophysical Journal* **73** (1931) 308.

[11] Atkinson, R.D., "Atomic Synthesis and Stellar Energy. III." *The Astrophysical Journal* **84** (1936) 73.

[12] von Weizsäcker, C.F., "Über Elementumwandlungen in Innern der Sterne I." *Physikalische Zeitschrift* **38** (1937) 176–191.

[13] von Weizsäcker, C.F., "Über Elementumwandlungen in Innern der Sterne II." *Physikalische Zeitschrift* **39** (1938) 633–646.

[14] Bethe, H.A., "Energy Production in Stars." *Physical Review* **55** (1939) 434–456.

[15] Bethe, H.A. & Critchfield, C.L., "The Formation of Deuterons by Proton Combination." *Physical Review* **54** (1938) 248–254.

[16] Grevesse, N., Asplund, M., & Sauval, A.J., "The Solar Chemical Composition." *Space Science Reviews* **130** (2007) 105–114.

[17] Alpher, R.A., Bethe, H., & Gamow, G., "The Origin of Chemical Elements." *Physical Review* **73** (1948) 803–804.

[18] Öpik, E.J., "Stellar Models with Variable Compositions II. Sequences of Models with Energy Generation Proportional to the 15th Power of Temperature." *Proceedings of the Royal Irish Academy Section A* **54** (1951) 49–+.

[19] Salpeter, E.E., "Nuclear Reactions in Stars Without Hydrogen." *The Astrophysical Journal* **115** (1952) 326–328.

[20] Hoyle, F., "On Nuclear Reactions Occuring in Very Hot STARS.I. the Synthesis of Elements from Carbon to Nickel." *The Astrophysical Journal Supplement Series* **1** (1954) 121–146.

[21] Cook, C.W., Fowler, W.A., Lauritsen, C.C., & Lauritsen, T., "B^{12}, C^{12}, and the Red Giants." *Physical Review* **107** (1957) 508–515.

[22] Merrill, P.W., "Spectroscopic Observations of Stars of Class S." *The Astrophysical Journal* **116** (1952) 21–26.

[23] Cameron, A.G.W., "Nuclear Reactions in Stars and Nucleogenesis." *Publications of the Astronomical Society of the Pacific* **69** (1957) 201–222.

[24] Cameron, A.G.W., "Stellar Evolution, Nuclear Astrophysics and Nucleogenesis.", *Chalk River Report CRL-41*, Chalk River Laboratories (1957).

[25] Cameron, A.G.W., *Stellar Evolution, Nuclear Astrophysics, and Nucleogenesis*, Dover, 2013. Editor D. M. Kahl.

[26] Burbidge, E.M., Burbidge, G.R., Fowler, W.A., & Hoyle, F., "Synthesis of the Elements in Stars." *Reviews of Modern Physics* **29** (1957) 547–650.

[27] Rolfs, C. & Rodney, W.S., *Cauldrons in the Cosmos*, the University of Chicago Press, 1988.

[28] Iliadis, C., *Nuclear Physics of Stars*, Wiley-VCH, 2007.

[29] Satchler, G.R., *Introduction to Nuclear Reactions*, Oxford University Press, 1990, 2nd edition.

[30] Woosley, S.E., Heger, A., Cumming, A., Hoffman, R.D., Pruet, J., Rauscher, T., Fisker, J.L., Schatz, H., Brown, B.A., & Wiescher, M., "Models for Type I X-Ray Bursts with Improved Nuclear Physics." *The Astrophysical Journal Supplement Series* **151** (2004) 75–102.

[31] Fisker, J.L., Schatz, H., & Thielemann, F.K., "Explosive Hydrogen Burning during Type I X-Ray Bursts." *The Astrophysical Journal Supplement Series* **174** (2008) 261–276.

[32] Ghoshal, S.N., "An Experimental Verification of the Theory of Compound Nucleus." *Physical Review* **80** (1950) 939–942.

[33] van Horn, H.M. & Hansen, C.J., "A Model for the Transient X-Ray Sources." *The Astrophysical Journal* **191** (1974) 479–482.

[34] Hansen, C.J. & van Horn, H.M., "Steady-state nuclear fusion in accreting neutron-star envelopes." *The Astrophysical Journal* **195** (1975) 735–741.

[35] Woosley, S.E. & Taam, R.E., "Gamma-ray bursts from thermonuclear explosions on neutron stars." *Nature* **263** (1976) 101–103.

[36] Lewin, W.H.G., "X-ray burst sources." *Monthly Notices of the Royal Astronomical Society* **179** (1977) 43–53.

[37] Lewin, W.H.G., van Paradijs, J., & Taam, R.E., "X-Ray Bursts." *Space Science Reviews* **62** (1993) 223–389.

[38] Schatz, H. & Rehm, K.E., "X-ray binaries." *Nuclear Physics A* **777** (2006) 601–622.

[39] Parikh, A., José, J., Sala, G., & Iliadis, C., "Nucleosynthesis in type I X-ray bursts." *Progress in Particle and Nuclear Physics* **69** (2013) 225–253.

[40] Lewin, W.H.G., van Paradijs, J., & van den Heuvel, E.P.J., *X-ray Binaries*, Cambridge University Press, 1997.

[41] Kahl, D.M., *^{30}S Radioactive Beam Development and the ^{30}S Waiting Point in Type I X-Ray Bursts*, Master's thesis, McMaster University (2008).

[42] Taam, R.E., "X-ray bursts from thermonuclear runaways on accreting neutron stars." *The Astrophysical Journal* **241** (1980) 358–366.

[43] Thielemann, F.K., Kratz, K.L., Pfeiffer, B., Rauscher, T., van Wormer, L., & Wiescher, M.C., "Astrophysics and nuclei far from stability." *Nuclear Physics A* **570** (1994) 329–343.

[44] Ayasli, S. & Joss, P.C., "Thermonuclear processes on accreting neutron stars - A systematic study." *The Astrophysical Journal* **256** (1982) 637–665.

[45] Taam, R.E., Woosley, S.E., Weaver, T.A., & Lamb, D.Q., "Successive X-ray bursts from accreting neutron stars." *The Astrophysical Journal* **413** (1993) 324–332.

[46] Wallace, R.K., Woosley, S.E., & Weaver, T.A., "The thermonuclear model for X-ray transients." *The Astrophysical Journal* **258** (1982) 696–715.

[47] Joss, P.C., "X-ray bursts and neutron-star thermonuclear flashes." *Nature* **270** (1977) 310–314.

[48] Lamb, D.Q. & Lamb, F.K., "Nuclear burning in accreting neutron stars and X-ray bursts." *The Astrophysical Journal* **220** (1978) 291–302.

[49] Taam, R.E., "Nuclear processes at neutron star surfaces." *Annual Review of Nuclear and Particle Science* **35** (1985) 1–23.

[50] Fujimoto, M.Y., Hanawa, T., & Miyaji, S., "Shell flashes on accreting neutron stars and X-ray bursts." *The Astrophysical Journal* **247** (1981) 267–278.

[51] Bildsten, L. & Cumming, A., "Hydrogen Electron Capture in Accreting Neutron Stars and the Resulting g-Mode Oscillation Spectrum." *The Astrophysical Journal* **506** (1998) 842–862.

[52] Fisker, J.L. (2008). Private communication.

[53] Wallace, R.K. & Woosley, S.E., "Explosive hydrogen burning." *The Astrophysical Journal Supplement Series* **45** (1981) 389–420.

[54] Iliadis, C., Endt, P.M., Prantzos, N., & Thompson, W.J., "Explosive Hydrogen Burning of ^{27}Si, ^{31}S, ^{35}Ar, and ^{39}Ca in Novae and X-Ray Bursts." *The Astrophysical Journal* **524** (1999) 434–453.

[55] Endt, P.M., "Energy levels of A = 21-44 nuclei (VII)." *Nuclear Physics A* **521** (1990) 1–400.

[56] O'Brien, S., Adachi, T., Berg, G.P.A., Couder, M., Dozono, M., Fujita, H., Fujita, Y., Görres, J., Hatanaka, K., Ishikawa, D., Kubo, T., Matsubara, H., Namiki, Y., Ohkuma, Y., Okamura, H., Ong, H.J., Patel, D., Sakemi, Y., Sault, K., Shimbara, Y., Suzuki, S., Suzuki, T., Tamii, A., Wakasa, T., Wantanabe, R., Wiescher, M., Yamada, R., & Zenihiro, J., "Exploring the αp-process with Grand Raiden." *American Institute of Physics Conference Series* **1090** (2009) 288–292.

[57] Penninx, W., Damen, E., van Paradijs, J., Tan, J., & Lewin, W.H.G., "EXOSAT observations of the X-ray burst source 4U 1608-52." *Astronomy & Astrophysics* **208** (1989) 146–152.

[58] Fisker, J.L., Thielemann, F.K., & Wiescher, M., "The Nuclear Reaction Waiting Points: ^{22}Mg, ^{26}Si, ^{30}S, and ^{34}Ar and Bolometrically Double-peaked Type I X-Ray Bursts." *The Astrophysical Journal, Letters* **608** (2004) L61–L64.

[59] Parikh, A., José, J., Moreno, F., & Iliadis, C., "The Effects of Variations in Nuclear Processes on Type I X-Ray Burst Nucleosynthesis." *The Astrophysical Journal Supplement Series* **178** (2008) 110–136.

[60] Endt, P.M., "Supplement to Energy Levels of A=21-44 Nuclei (vii)." *Nuclear Physics A* **633** (1998) 1–220.

[61] Rauscher, T., Thielemann, F., & Kratz, K., "Applicability of the Hauser-Feshbach approach for the determination of astrophysical reaction rates." *Nuclear Physics A* **621** (1997) 331–334.

[62] Rauscher, T., Thielemann, F., & Kratz, K., "Nuclear level density and the determination of thermonuclear rates for astrophysics." *Physical Review C* **56** (1997) 1613–1625.

[63] Hauser, W. & Feshbach, H., "The Inelastic Scattering of Neutrons." *Physical Review* **87** (1952) 366–373.

[64] Groombridge, D., Shotter, A.C., Bradfield-Smith, W., Cherubini, S., Davinson, T., di Pietro, A., Görres, J., Graulich, J.S., Laird, A.M., Leleux, P., Musumarra, A., Ninane, A., Ostrowski, A.N., Rahighi, J., Schatz, H., Wiescher, M., & Woods, P.J., "Breakout from the hot CNO cycle via the ^{18}Ne(α,p)^{21}Na reaction. II. Extended energy range $E_{c.m.} \sim$ 1.7-2.9 MeV." *Physical Review C* **66** (2002) 055802:1–10.

[65] Dababneh, S., Heil, M., Käppeler, F., Görres, J., Wiescher, M., Reifarth, R., & Leiste, H., "Stellar He burning of ^{18}O: A measurement of low-energy resonances and their astrophysical implications." *Physical Review C* **68** (2003) 025801:1–11.

[66] Berg, G.P.A., Hatanaka, K., Wiescher, M., Schatz, H., Adachi, T., Bacher, A.D., Foster, C.C., Fujita, Y., Fujita, H., Fujita, K., Görres, J., Herman, C., Kamiya, J., Sakamoto, N., Sakemi, Y., Shimbara, Y., Shimizu, Y., Stephenson, E.J., Wakasa, T., & Yosoi, M., "Resonance states in ^{22}Mg for reaction rates in the rp-process." *Nuclear Physics A* **718** (2003) 608–610.

[67] Angulo, C., Arnould, M., Rayet, M., Descouvemont, P., Baye, D., Leclercq-Willain, C., Coc, A., Barhoumi, S., Aguer, P., Rolfs, C., Kunz, R., Hammer, J.W., Mayer, A., Paradellis, T., Kossionides, S., Chronidou, C., Spyrou, K., degl'Innocenti, S., Fiorentini, G., Ricci, B., Zavatarelli, S., Providencia, C., Wolters, H., Soares, J., Grama, C., Rahighi, J., Shotter, A., & Lamehi Rachti, M., "A compilation of charged-particle induced thermonuclear reaction rates." *Nuclear Physics A* **656** (1999) 3–183.

[68] Aprahamian, A., Langanke, K., & Wiescher, M., "Nuclear structure aspects in nuclear astrophysics." *Progress in Particle and Nuclear Physics* **54** (2005) 535–613.

[69] Deibel, C.M., Rehm, K.E., Figueira, J.M., Greene, J.P., Jiang, C.L., Kay, B.P., Lee, H.Y., Lighthall, J.C., Marley, S.T., Pardo, R.C., Patel, N., Paul, M.,

Ugalde, C., Woodard, A., Wuosmaa, A.H., & Zinkann, G., "First measurement of the ^{33}Cl(p,α)^{30}S reaction." *Physical Review C* **84** (2011) 045802:1–6.

[70] Kubono, S., Yanagisawa, Y., Teranishi, T., Kato, S., Kishida, Y., Michimasa, S., Ohshiro, Y., Shimoura, S., Ue, K., Watanabe, S., & Yamazaki, N., "New low-energy RIB separator CRIB for nuclear astrophysics." *European Physical Journal A* **13** (2002) 217–220.

[71] Yanagisawa, Y., Kubono, S., Teranishi, T., Ue, K., Michimasa, S., Notani, M., He, J.J., Ohshiro, Y., Shimoura, S., Watanabe, S., Yamazaki, N., Iwasaki, H., Kato, S., Kishida, T., Morikawa, T., & Mizoi, Y., "Low-energy radioisotope beam separator CRIB." *Nuclear Instruments and Methods in Physics Research A* **539** (2005) 74–83.

[72] Yamaguchi, H., Saito, A., He, J.J., Wakabayashi, Y., Amadio, G., Fujikawa, H., Kubono, S., Yamazaki, N., Teranishi, T., Fülöp, Z., Elekes, Z., Yanagisawa, Y., Michimasa, S., Nishimura, S., & Niikura, M., "Beam Focusing and Separation Test of the Wien Filter for CRIB." *Center for Nuclear Study Annual Report 2004* **CNS-REP-66** (2005) 60–70.

[73] Yamaguchi, H., Wakabayashi, Y., Amadio, G., Hayakawa, S., Fujikawa, H., Kubono, S., He, J.J., Kim, A., & Binh, D.N., "Development of a cryogenic gas target system for intense radioisotope beam production at CRIB." *Nuclear Instruments and Methods in Physics Research A* **589** (2008) 150–156.

[74] Kumagai, H., Ozawa, A., Fukuda, N., Sümmerer, K., & Tanihata, I., "Delay-line PPAC for high-energy light ions." *Nuclear Instruments and Methods in Physics Research A* **470** (2001) 562–570.

[75] Kahl, D., Chen, A.A., Kubono, S., Binh, D.N., Chen, J., Hashimoto, T., Hayakawa, S., Kaji, D., Kim, A., Kurihara, Y., Lee, N.H., Nishimura, S., Ohshiro, Y., Setoodeh Nia, K., Wakabayashi, Y., & Yamaguchi, H., "^{30}S(α, p) in X-Ray Bursts at CRIB." *American Institute of Physics Conference Series* **1269** (2010) 424–426.

[76] Miyoshi, T., Noda, K., Sato, Y., Tawara, H., Tolstikhina, I.Y., & Shevelko, V.P., "Evaluation of excited nl-state distributions of fast exit ions after penetrating through solid foils. Part 1: Charge-state fractions for 4.3 MeV/u projectiles with atomic numbers Z = 6-26 passing through carbon foils." *Nuclear Instruments and Methods in Physics Research B* **251** (2006) 79–88.

[77] Hashimoto, T., Ishiyama, H., Ishikawa, T., Kawamura, T., Nakai, K., Watanabe, Y.X., Miyatake, H., Tanaka, M.H., Fuchi, Y., Yoshikawa, N., Jeong, S.C., Katayama, I., Nomura, T., Furukawa, T., Mitsuoka, S., Nishio, K., Matsuda, M., Ikezoe, H., Fukuda, T., Das, S.K., Saha, P.K., Mizoi, Y., Komatsubara, T., Yamaguchi, M., & Tagishi, Y., "Gated multiple-sampling and tracking proportional chamber." *Nuclear Instruments and Methods in Physics Research A* **556** (2006) 339–349.

[78] Bethe, H., "Bremsformel für Elektronen relativistischer Geschwindigkeit." *Zeitschrift fur Physik* **76** (1932) 293–299.

[79] Ziegler, J.F., Biersack, J.P., & Ziegler, M.D., *SRIM - The Stopping and Range of Ions in Matter*, Lulu Press, 2012.

[80] Ziegler, J.F., "SRIM - The Stopping and Range of Ions in Matter." `http://www.srim.org/`.

[81] Yamaguchi, H., Hashimoto, T., Hayakawa, S., Binh, D.N., Kahl, D., Kubono, S., Wakabayashi, Y., Kawabata, T., & Teranishi, T., "α resonance structure in ^{11}B studied via resonant scattering of ^{7}Li+α." *Physical Review C* **83** (2011) 034306:1–10.

[82] Chen, J., Chen, A.A., Amádio, G., Cherubini, S., Fujikawa, H., Hayakawa, S., He, J.J., Iwasa, N., Kahl, D., Khiem, L.H., Kubono, S., Kurihara, S., Kwon, Y.K., La Cognata, M., Moon, J.Y., Niikura, M., Nishimura, S., Pearson, J., Pizzone, R.G., Teranishi, T., Togano, Y., Wakabayashi, Y., & Yamaguchi, H., "Strong ^{25}Al+p resonances via elastic proton scattering with a radioactive ^{25}Al beam." *Physical Review C* **85** (2012) 015805.

[83] Jung, H.S., Lee, C.S., Kwon, Y.K., Moon, J.Y., Lee, J.H., Yun, C.C., Kubono, S., Yamaguchi, H., Hashimoto, T., Kahl, D., Hayakawa, S., Choi, S., Kim, M.J., Kim, Y.H., Kim, Y.K., Park, J.S., Kim, E.J., Moon, C.B., Teranishi, T., Wakabayashi, Y., Iwasa, N., Yamada, T., Togano, Y., Kato, S., Cherubini, S., & Rapisarda, G.G., "Experimental study of resonant states in ^{27}P via elastic scattering of ^{26}Si+p." *Physical Review C* **85** (2012) 045802.

[84] He, J.J., Zhang, L.Y., Parikh, A., Xu, S.W., Yamaguchi, H., Kahl, D., Kubono, S., Hu, J., Ma, P., Chen, S.Z., Wakabayashi, Y., Sun, B.H., Wang, H.W., Tian, W.D., Chen, R.F., Guo, B., Hashimoto, T., Togano, Y., Hayakawa, S., Teranishi, T., Iwasa, N., Yamada, T., & Komatsubara, T., "The ^{18}Ne(α,p)^{21}Na breakout reaction in x-ray bursts: Experimental determination of spin-parities for α resonances in ^{22}Mg via resonant elastic scattering of ^{21}Na+p." *Physical Review C* **88** (2013) 012801.

[85] Jin, S.J., Wang, Y.B., Su, J., Yan, S.Q., Li, Y.J., Guo, B., Li, Z.H., Zeng, S., Lian, G., Bai, X.X., Liu, W.P., Yamaguchi, H., Kubono, S., Hu, J., Kahl, D., Jung, H.S., Moon, J.Y., Lee, C.S., Teranishi, T., Wang, H.W., Ishiyama, H., Iwasa, N., Komatsubara, T., & Brown, B.A., "Resonant scattering of ^{22}Na + p studied by the thick-target inverse-kinematic method." *Physical Review C* **88** (2013) 035801.

[86] Yamaguchi, H., Kahl, D., Wakabayashi, Y., Kubono, S., Hashimoto, T., Hayakawa, S., Kawabata, T., Iwasa, N., Teranishi, T., Kwon, Y.K., Binh, D.N., Khiem, L.H., & Duy, N.N., "α-resonance structure in ^{11}C studied via resonant scattering of ^{7}Be+α and with the ^{7}Be(α,p) reaction." *Physical Review C* **87** (2013) 034303.

[87] Hu, J., He, J.J., Parikh, A., Xu, S.W., Yamaguchi, H., Kahl, D., Ma, P., Su, J., Wang, H.W., Nakao, T., Wakabayashi, Y., Teranishi, T., Hahn, K.I., Moon, J.Y., Jung, H.S., Hashimoto, T., Chen, A.A., Irvine, D., Lee, C.S., & Kubono, S., "Examination of the role of the ^{14}O(α,p)^{17}F reaction rate in type-I x-ray bursts." *Physical Review C* **90** (2014) 025803.

[88] Zhang, L.Y., He, J.J., Parikh, A., Xu, S.W., Yamaguchi, H., Kahl, D., Kubono, S., Mohr, P., Hu, J., Ma, P., Chen, S.Z., Wakabayashi, Y., Wang, H.W., Tian, W.D., Chen, R.F., Guo, B., Hashimoto, T., Togano, Y., Hayakawa, S., Teranishi, T., Iwasa, N., Yamada, T., Komatsubara, T., Zhang, Y.H., & Zhou, X.H., "Investigation of the thermonuclear ^{18}Ne(α,p)^{21}Na reaction rate via resonant elastic scattering of ^{21}Na + p." *Physical Review C* **89** (2014) 015804.

[89] Lane, A.M. & Thomas, R.G., "R-Matrix Theory of Nuclear Reactions." *Reviews of Modern Physics* **30** (1958) 257–353.

[90] Larson, N., "A Code System for Multilevel R-Matrix Fits to Neutron Data Using Bayes' Equations." (2000). ORNL/TM-9179/R5 (Unpublished).

[91] Binh, D.N., *Study of the ^{21}Na(α, p)^{24}Mg Stellar Reaction by α-scattering and (α, p) Measurements in Inverse Kinematics*, Ph.D. thesis, The University of Tokyo (2010).

[92] Rauscher, T. & Thielemann, F.K., "Tables of Nuclear Cross Sections and Reaction Rates: AN Addendum to the Paper "ASTROPHYSICAL Reaction Rates from Statistical Model Calculations." *Atomic Data and Nuclear Data Tables* **79** (2001) 47–64.

[93] Kubono, S., Binh, D.N., Hayakawa, S., Hashimoto, H., Kahl, D., Wakabayashi, Y., Yamaguchi, H., Teranishi, T., Iwasa, N., Komatsubara, T., Kato, S., & Khiem, L.H., "Nuclear Clusters in Astrophysics." *Nuclear Physics A* **834** (2010) 647–650.

[94] Anders, E. & Grevesse, N., "Abundances of the elements - Meteoritic and solar." Geochim. Cosmochim. Acta **53** (1989) 197–214.

[95] Townsend, R., "EZ-Web." `http://www.astro.wisc.edu/ townsend/static.php?ref=ez-web`.

[96] LUNA Collaboration, Lemut, A., Bemmerer, D., Confortola, F., Bonetti, R., Broggini, C., Corvisiero, P., Costantini, H., Cruz, J., Formicola, A., Fülöp, Z., Gervino, G., Guglielmetti, A., Gustavino, C., Gyürky, G., Imbriani, G., Jesus, A.P., Junker, M., Limata, B., Menegazzo, R., Prati, P., Roca, V., Rogalla, D., Rolfs, C., Romano, M., Rossi Alvarez, C., Schümann, F., Somorjai, E., Straniero, O., Strieder, F., Terrasi, F., & Trautvetter, H.P., "First measurement of the ^{14}N(p,γ)^{15}O cross section down to 70 keV." *Physics Letters B* **634** (2006) 483–487.

[97] Wiescher, M., Görres, J., & Schatz, H., "TOPICAL REVIEW: Break-out reactions from the CNO cycles." *Journal of Physics G Nuclear Physics* **25** (1999) 133–161.

[98] Redder, A., Becker, H.W., Lorenz-Wirzba, H., Rolfs, C., Schmalbrock, P., & Trautvetter, H.P., "The ^{15}N(p, α_0)^{12}C reaction at stellar energies." *Zeitschrift fur Physik A Hadrons and Nuclei* **305** (1982) 325–333.

[99] Caughlan, G.R. & Fowler, W.A., "The Mean Lifetimes of Carbon, Nitrogen, and Oxygen Nuclei in the CNO Bicycle." *The Astrophysical Journal* **136** (1962) 453.

[100] Hansen, C.J., Kawaler, S.D., & Trimble, V., *Stellar Interiors - Physical Principles, Structure, and Evolution*, Springer, 2004, 2nd edition.

[101] Forestini, M. & Charbonnel, C., "Nucleosynthesis of light elements inside thermally pulsing AGB stars: I. The case of intermediate-mass stars." *Astronomy & Astrophysics Supplement Series* **123** (1997) 241–272.

[102] Taam, R.E., Woosley, S.E., & Lamb, D.Q., "The Effect of Deep Hydrogen Burning in the Accreted Envelope of a Neutron Star on the Properties of X-Ray Bursts." *The Astrophysical Journal* **459** (1996) 271–+.

[103] Hoyle, F. & Fowler, W.A., "Report on the Properties of Massive Objects.", in "Quasi-Stellar Sources and Gravitational Collapse," eds. I. Robinson, A. Schild, & E.L. Schucking, 1965 p. 17.

[104] Schatz, H., Bildsten, L., Cumming, A., & Wiescher, M., "The Rapid Proton Process Ashes from Stable Nuclear Burning on an Accreting Neutron Star." *The Astrophysical Journal* **524** (1999) 1014–1029.

[105] Woosley, S.E. & Weaver, T.A., "Repeated thermonuclear flashes on an accreting neutron star." *American Institute of Physics Conference Series* **115** (1984) 273–297.

[106] Görres, J., Wiescher, M., & Thielemann, F.K., "Bridging the waiting points: The role of two-proton capture reactions in the rp process." *Physical Review C* **51** (1995) 392–400.

[107] Baldin, A.M., *Kinematics of nuclear reactions*, Pergamon Press, 1961.

[108] Krane, K.S., *Introductory Nuclear Physics*, John Wiley & Sons, 1987.

[109] Baba, H., "The BAQ/Data Acquisition/DAQ System/Babarl." `http://rarfaxp.riken.go.jp/ baba/acquisition/system/babarl/index.html`.

[110] Hokkaido University Nuclear Reaction Data Centre, "Graph Digitizing System (GSYS, SyCRD)." `http://www.jcprg.org/gsys/`.